Analysis of Coronal Mass Ejection Kinematics and Dependencies on Source Region Properties

Dissertation
zur Erlangung des mathematisch-naturwissenschaftlichen Doktorgrades

"Doctor rerum naturalium"

der Georg-August-Universität Göttingen

im Promotionsstudiengang ProPhys
der Georg-August-University School of Science (GAUSS)

vorgelegt von

Niclas Mrotzek

aus

Herne

Göttingen 2019

Betreuungsausschuss:

Prof. Dr. Ansgar Reiners
Sonnenphysik und Stellare Astrophysik, Institut für Astrophysik
Georg-August-Universität Göttingen

Dr. Volker Bothmer
Sonnenphysik und Stellare Astrophysik, Institut für Astrophysik
Georg-August-Universität Göttingen

Prof. Dr. Stefan Dreizler
Sonnenphysik und Stellare Astrophysik, Institut für Astrophysik
Georg-August-Universität Göttingen

Mitglieder der Prüfungskomission:

Prof. Dr. Ansgar Reiners
Sonnenphysik und Stellare Astrophysik, Institut für Astrophysik
Georg-August-Universität Göttingen

Dr. Volker Bothmer
Sonnenphysik und Stellare Astrophysik, Institut für Astrophysik
Georg-August-Universität Göttingen

Weitere Mitglieder der Prüfungskomission:

Prof. Dr. Wolfram Kollatschny
Extragalaktische Astrophysik und Kosmologie, Institut für Astrophysik
Georg-August-Universität Göttingen

Prof. Dr. Wolfgang Glatzel
Theoretische und Numerische Astrophysik, Institut für Astrophysik
Georg-August-Universität Göttingen

Prof. Dr. Karl-Henning Rehren
Halbleiterphysik, Institut für Theoretische Physik
Georg-August-Universität Göttingen

Prof. Dr. Andreas Tilgner
Geophysikalische Fluiddynamik, Institut für Geophysik
Georg-August-Universität Göttingen

Tag der mündlichen Prüfung: 07.02.2020

Niclas Mrotzek

Analysis of Coronal Mass Ejection Kinematics and Dependencies on Source Region Properties

Dissertation

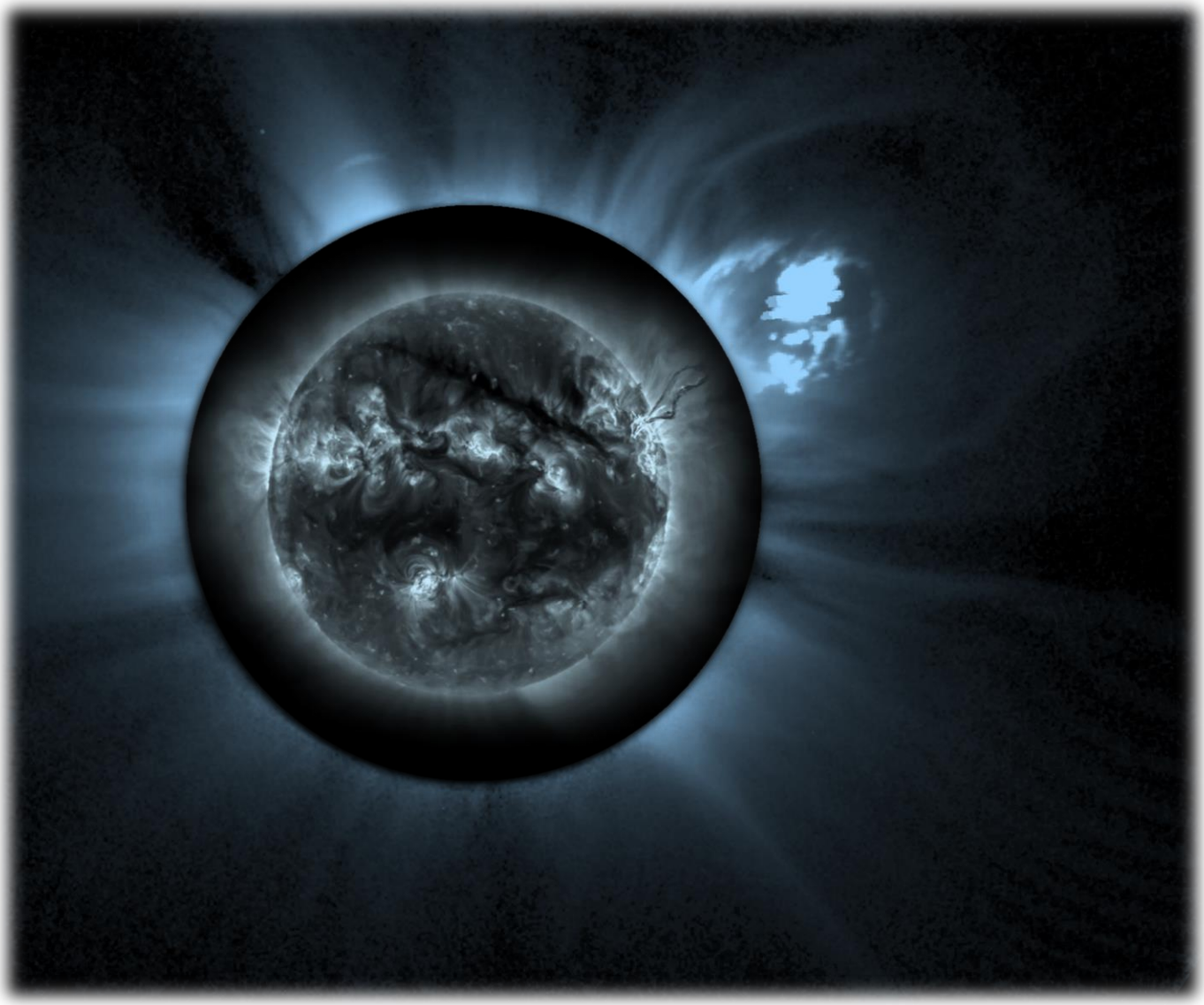

Cover Figure: Scaled composite of SECCHI/EUVI 195 B (light blue) and SECCHI/COR1 B (blue) observations of a Coronal Mass Ejection and a Filament Eruption on Spetember 9, 2011.

"Wir können den Wind nicht ändern, aber die Segel anders setzen."

Aristoteles

Abstract

Coronal Mass Ejections (CMEs) are outbursts of coronal plasma bound in magnetic structures that are explosively accelerated. Their evolution into the heliosphere can be observed with coronagraphs and heliospheric imagers, which are able to detect the photospheric light scattered by the CME's plasma through Thomson scattering. Since CME's are optically thin, multi-viewpoint observations from space-borne coronagraphs are used to reconstruct their geometry and direction of propagation. CMEs originate from magnetic active regions (ARs), primarily of bipolar nature, which are observable in magnetograms of the photosphere and extreme ultraviolet images of the lower solar atmosphere. Often the eruption of a CME is accompanied by other sudden activity phenomena located in the same AR like solar flares, filament eruptions or post eruptive arcades.

In this thesis a systematic investigation of the connection between the kinematics of CMEs and the properties of their corresponding source regions (SRs) is presented. For this purpose, a set of 21 Earth-directed CMEs between July 2011 and November 2012 was selected and analysed. The CME kinematics are obtained by applying a 3D modelling method, the Graduated Cylindrical Shell (GCS) model, to simultaneous multi-viewpoint observations taken with the SECCHI instrument suite onboard the twin STEREO spacecrafts and with the LASCO coronagraphs onboard the SOHO satellite. By using these instruments, the CME dynamics including the kinematics and geometry, are covered in high detail over a wide spatial range starting, for the majority of events, in the field of view (FOV) of EUVI below $2\,R_\odot$ and extending into the field of view of HI1 ($\sim 100\,R_\odot$). An aerodynamic drag based propagation model, including distance depending models of the solar wind and the drag coefficient as well as the CME mass determined with the GCS model and Thomson scattering theory, is used to extrapolate the measured CME trajectory to larger heliospheric distances. The extrapolated solar wind and CME characteristics are compared with in-situ measurements at L1. Furthermore, the model results are used in a torus instability (TI) Lorentz force model to describe the initial acceleration phase. The CME SRs are identified by tracking the CME trajectories back onto the solar surface and searching for ARs and related activity phenomena within in a spatial window of less than $\pm 25°$ in longitude and $\pm 10°$ in latitude and a time window of ± 8 hours to the first remote sensing observation. The ARs identified in this way as CME SRs are analysed for their magnetic and geometric properties in a time range $\sim \pm 6$ hours around the eruption time using the SMART code and line of sight magnetograms of SDO/HMI.

The results show a very good agreement between the SR and initial CME geometry with a small shift in the SR latitude towards the solar equatorial plane with respect to the CME initial latitude. A highly dynamic behaviour, including deflections and rotations in the CME geometry within the first $20\,R_\odot$, can be seen from the GCS modelling results. In the kinematic profiles, evidence for CME oscillations with periods between 29 and 93 min are found. Significant correlations are found between the CME SR magnetic flux as well as proxies of the free magnetic energy, which is provided by the CME SR, with the CME kinematic properties. The results of the drag model describe the measured CME trajectories with high accuracy and in general the predicted CME characteristics are in good agreement with the measurements in L1, while the TI Lorentz force model shows discrepancies to the observed CME accelerations.

Glossary

Roman letters

Variable	Denotation	Unit
A	Area	m^2
a	Acceleration	$\mathrm{m\,s}^{-2}$
AU	Astronimical Unit	$149597870(2)\,\mathrm{km}$ (Stix 2004, p.3)
B	Magnetic filed	nT, G, Mx
b	CME minor radius	km
C_D	Drag coefficient	
c_0	Speed of light	$299792458\,\mathrm{m\,s}^{-1}$ NIST
cv	Coefficient of variation	
E	Energy	J or eV
$\mathbf{E}$	Electric field vector	$\mathrm{V\,m}^{-1}$
F	Force	N or dyn
f	Magnetic flux	Mx
G	Gravitational constant	$6.67384(80)\cdot10^{-11}\,\mathrm{m}^3\,\mathrm{kg}^{-1}\,\mathrm{s}^{-2}$ NIST
g	Surface Gravity	$\mathrm{m\,s}^{-2}$
H	Brightness	MSB
h	Height of GCS legs	km, $\mathrm{R}_\odot$
I	Current	A
J	Electric current density	$\mathrm{A\,m}^{-2}$
k_b	Stefan-Boltzmann constant	$5.670373(21)\cdot10^{-8}\,\mathrm{W\,m}^{-2}\,\mathrm{K}^{-4}$ NIST
L_{PIL}	Length of PIL	Mm
L_{BSP}	Length of Bipolar Seperation	Mm
$L_\odot$	Solar luminosity	$3.844(10)\cdot10^{26}\,\mathrm{W}$ (Stix 2004, p.6)
l_{i}	Internal inductance	
m	Mass	kg, g or $\mathrm{M}_\odot$
m_{e}	Electron mass	$9.1093829(4)\cdot10^{-31}\,\mathrm{kg}$ NIST
m_{p}	Proton mass	$1.6726219236(5)\cdot10^{-27}\,\mathrm{kg}$ NIST
N_{e}	GCS electron density profile	cm^{-3}
n_{e}	Electron number density	cm^{-3}
n_{p}	Proton number density	cm^{-3}
n_{s}	Number of sunspots	
n_{g}	Number of Sunspot groups	
p	Momentum	$\mathrm{N\,s}$

Variable	Denotation	Unit
pa	Position angle	$^\circ$
q	Charge	C
$R_\odot$	Solar Radius	696342 km (Stix 2004 p.4)
R	Schrijver value	Mx
R^2	Coefficient of determination	
r	Heliospheric distance	km, $R_\odot$ or AU
Re	Reynolds number	
S	Solar constant	1367(3) $W\,m^{-2}$ (Stix 2004, p.6)
s	Standard deviation	
SSN	Sunspot Number	
T	Temperature	K
t	Time	a, d, h, min, s, UT
TT	Transit Time	h
u	Limb darkening coefficient	
v	Speed	$km\,s^{-1}$; $m\,s^{-1}$
v_a	Alvfén speed	$km\,s^{-1}$; $m\,s^{-1}$
W	CME angular width	$^\circ$
w	Solar wind speed	$km\,s^{-1}$
WL_{SG}	Falconer weighted integral	G

Greek letters

Variable	Denotation	Unit
α	GCS Half Angle	$^\circ$
β	Plasma β	
Γ	Tilt Angle	$^\circ$
γ	Drag parameter	km^{-1}
δ	GCS cone half angle	
Δ	Difference	
θ	Latitude	$^\circ$
κ	GCS aspect ratio	
λ	Mean-free path length	km
ν	Viscosity	$kg\,m^{-1}\,s^{-1}$
π	Pi	3.141592654
ρ	Density	$g\,cm^{-3}$
Σ	Sum	
Φ	Intensity	$W\,m^{-2}$ or SFU
ϕ	Longitude	$^\circ$
χ	Scatter angle	$^\circ$
Ω_i	Ion cyclotron plasma frequency	
ω_p	Ion plasma frequency	rad s^{-1}

Acronyms

Acronym	Denotation
3D	Three Dimensional
ACE	Advanced Composition Explorer
AFFECTS	Advanced Forecast For Ensuring Communications Through Space
AIA	Atmospheric Imaging Assembly
ATM	Apollo Telescope Mount
AR	Active Region
BC	Before Christ
BL	Babcock-Leighton (mechanism)
CCD	Charge-Coupled Device
CDAW	Coordinated Data Analysis Workshops
CH	Coronal Hole
CIR	Co-rotating Interaction Region
CME	Coronal Mass Ejection
CNO	Carbon-Nitrogen-Oxygen
DSCOVR	Deep Space Climate ObserVatoRy
DSN	Deep Space Network
EIT	Extreme ultraviolet Imaging Telescope
ESA	European Space Agency
EUV	Extrem UltraViolet
EUVI	Extrem UltraViolet Imager
FE	Filament Eruption
FLARECAST	Flare Likelihood And Region Eruption forecASTing
FOV	Field of View
FR	Flux Rope
GCS	Graduated Cylindrical Shape (Model)
GNSS	Global Navigation Satellite System
GOES	Geostationary Operational Environmental Satellite
HCM	Heliospheric Current Sheet
HELCATS	HELiospheric Cataloguing, Analysis and Techniques Service
HI	Heliospheric Imager
HICAT	Heliospheric Imager (CME) CATalogue
HMI	Helioseismic and Magnetic Imager
HXR	Hard X-Ray
IAG	Institut für Astrophysik Göttingen
ICME	Interplanetary CME

Acronym	Denotation
IMF	Interplanetary Magnetic Field
IPM	InterPlanetary Medium
KINCAT	Kinematic Database Catalogue
L1	Lagrange Point 1
LASCO	Large Angle and Spectrometric COronagraph (E)xperiment
LINKCAT	Linked Catalogue of Solar Heliospheric and In Situ EME Obervations
LH	Left Handed
LOS	Line Of Sight
LTE	Local Thermal Equilibrium
LOWCAT	Low Coronal Event Catalogue
MC	Magnetic Cloud
MDI	Michelson Doppler Imager
MHD	Magneto HydroDynamics
MVC	Multi-viewpoint CME Catalog
NASA	National Aeronautics and Space Administration
NIR	Near InfraRed
NOAA	National Oceanic and Admospheric Administration
NSWP	National Space Weather Program
OPTIMAP	Operational Tool for Ionosphere Mapping And Prediction
OSO-7	Orbiting Solar Observatory
PIL	Polarity Inversion Line
PEA	Post Eruptive Arcade
PLASTIC	PLAsma and SupraThermal Ion Composition
POS	Plane Of Sky
PSP	Parker Solar Probe
RH	Right Handed
SECCHI	Sun Earth Connection Coronal and Heliospheric Investigation
SEP	Solar Energetic Particle
SDO	Solor Dynamics Observatory
SMART	Solar Magnetic Feature Detection and Tracking for Space Weather Monitoring
SMM	Solar Maximum Mission

Acronym	**Denotation**
SR	Source Region
SSW	SolarSoft-Ware
STEREO	Solar TErrestrial RElations Observatory
STP	Solar Terestrial Probe
SOHO	SOlar and Heliospheric Observatory
SXR	Soft X-Ray
TEC	Total Electron Content
TRACE	Transition Region And Coronal Explorer
TI	Torus Instability
TT	Transit Time
UV	UltraViolet
VIS	VISual
X-ray	Röntgen radiation

Indices

Index	Denotation
$\odot$	Phys. quantity normalized to Sun units.
0	Variable in initial state
12	Variable at $r = 12\,\mathrm{R}_\odot$
Arr	Arrival
av	Average
D	Drag
diff	Difference
EO	Edge On
eff	Effective
eq	Equal
FO	Face On
G	Gravity
kin	Kinetic
L	Lorentz
mag	Magnetic
max	Maximum
mean	Mean value
min	Minimum
p	Poloidal
t	Toroidal
tot	Total
th	Thermal

Contents

List of Figures

List of Tables

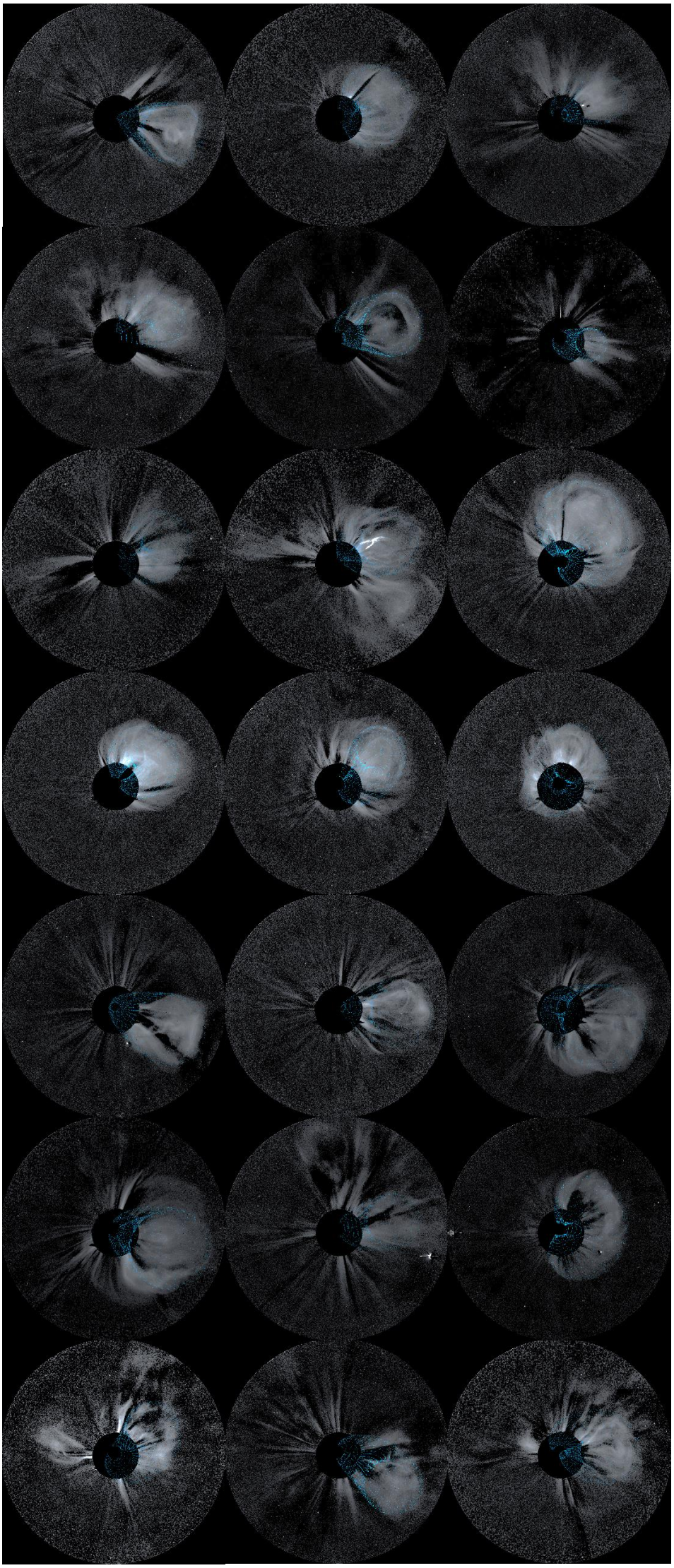

Chapter 1

Introduction

"One has to do something new in order to see something new."

Georg C. Lichtenberg

Cover Figure: Mosaic of STEREO SECCHI/COR2 B observation taken between July 8, 2011 and November 12, 2012 of all CMEs analysed in this work. The individual images represent the observation with the best white-light appearance of the event within the field of view of COR2 B.

Coronal Mass Ejections (CMEs) are impulsive eruptions of magnetised plasma originating from the solar corona. Accelerated to speeds up to a few thousand $\mathrm{km\,s^{-1}}$ in the case of extreme events (Webb and Howard, 2012), they propagate through the ambient solar wind into the interplanetary space and it is commonly believed that, for the majority of CMEs, the coronal plasma is bound in a magnetic flux rope (FR) structure (Mouschovias and Poland, 1978; Cremades and Bothmer, 2004; Vourlidas *et al.*, 2013; Marubashi *et al.*, 2015). Compared to the visible solar surface, the corona is fainter by several orders of magnitude and without technical aids only observable during a total solar eclipse. The first detection of a CME was probably made by G. Tempel in Spain during the total eclipse 1860 (Eddy, 1974), although it was not recognised as a solar transient. In order to be independent of the rare and short event of a total eclipse, coronagraphs were developed to allow more extended observations of the corona. It were the observations of the first space-borne coronagraph on board of the *seventh Orbiting Solar Observatory* (OSO-7, Tousey 1973) and the *Apollo Telescope Mount* (ATM) coronagraph on board *Skylab* (MacQueen *et al.*, 1974) that led to the discovery of CMEs in the early 1970s (Hansen *et al.*, 1971). The younger generation of coronagraphs in the NASA/ESA's heliophysics space fleet, namely the *Large Angle Spectrometric Coronagraph* (LASCO, Brueckner *et al.* 1995) on board the *Solar and Heliospheric Observatory* (SOHO, Domingo, Fleck, and Poland 1995) and the *Sun Earth Connection Coronal and Heliospheric Investigation* (SECCHI, Howard *et al.* 2008) on board the twin spacecrafts *Solar Terrestrial Relations Observatory* (STEREO, Davila *et al.* 1996), made observations with high temporal and spatial resolution available. Furthermore, with the STEREO spacecrafts simultaneous multi-viewpoint observations of the Sun were taken for the first time.

Our picture of CMEs changed substantially since their discovery. The SOHO observations revealed the basic morphology of CMEs and made it feasible to connect CME white-light observations with their photospheric source regions (SR) (Cremades and Bothmer, 2004). Figure 1.1 shows a sequence of CME observations taken with the SOHO/LASCO C3 coronagraph. CMEs are optically thin structures that appear in a coronagraph as two dimensional objects moving in the image plane. Their 3D geometry can be reconstructed by considering observations taken from different vantage points, which was first possible with the launch of the STEREO mission. An example of concurrent observations of a CME taken from different vantage points by the coronagraphs onboard the STEREO and SOHO spacecraft is shown in Figure 1.2. Thus, previously projected CME properties like angular width, propagation direction and velocity can be deprojected. Using the 3D CME quantities allows for advanced analysis and to include details that had to be neglected in early CME models. One example is the discrepancy between remote and in-situ observed CME velocities. While the near-Sun speeds range between a few hundred up to a few thousand $\mathrm{km\,s^{-1}}$ (Webb and Howard, 2012), the corresponding in-situ measurements differ in the majority of cases only by a few hundred $\mathrm{km\,s^{-1}}$ from the solar wind speed (Forsyth *et al.*, 2006). Based on single-viewpoint observations, empirical models explaining this equalisation of the CME speed to that of the solar wind were developed (Lindsay *et al.*, 1999; Dal Lago *et al.*, 2004; Gopalswamy *et al.*, 2000). Using multi-viewpoint observation from STEREO and SOHO, the 3D CME speeds can be determined and used as an input for this models. The improved data quality made it possible to show that the acceleration of slow CMEs and the deceleration of fast ones can be explained with the aerodynamic drag force between CME and the ambient solar wind. This interaction was investigated

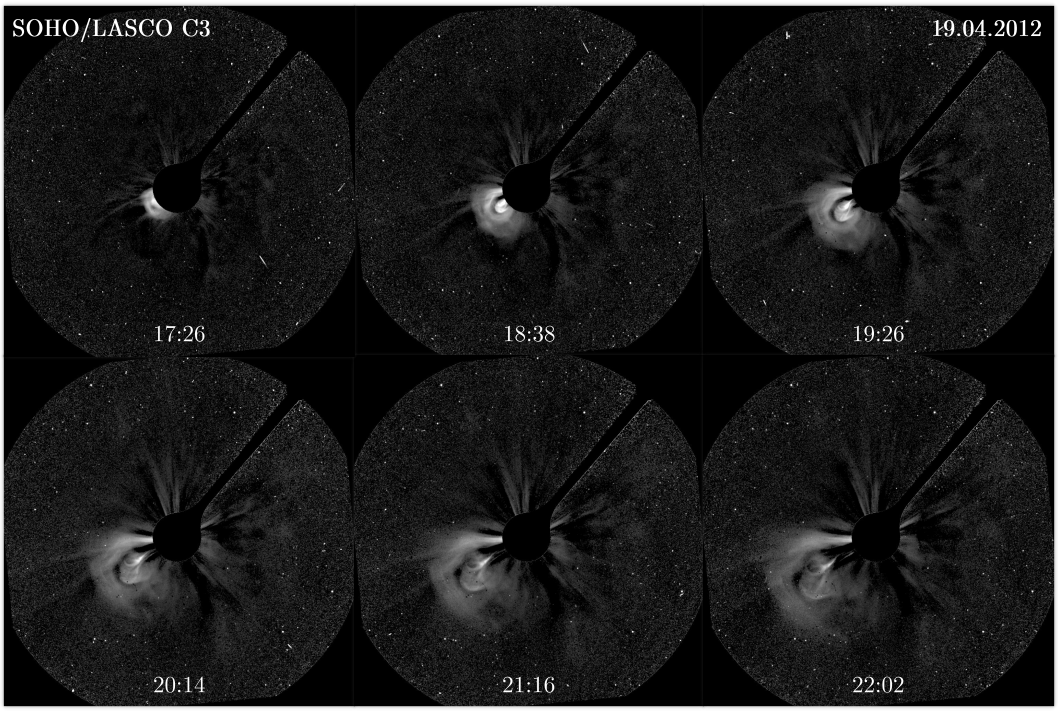

Figure (1.1) CME observation of SOHO/LASCO C3 at April 19, 2012. The observation times are given in UT. As the CME enters the FOV of C3 in the lower left quadrant of the individual images, it shows the typical morphology described by Cremades and Bothmer (2004) further explained in Section 2.2.3. The images were processed and calibrated as described in Section 4.2.2.

in magneto-hydrodynamic (MHD) simulations (Cargill, 2004), several case studies (Temmer *et al.*, 2011, 2012) and also studies using larger statistical samples (Vršnak *et al.*, 2013; Sachdeva *et al.*, 2015, 2017). Vršnak *et al.* (2014) compared observed CME transit times to the one of extrapolated CME trajectories calculated first by using an analytical one dimensional model of the drag force and again with an advanced 2.5D MHD model. They showed that, depending on the solar activity, the 1D aerodynamic drag model is as accurate as the computationally very expensive MHD simulation. However, the result of Temmer *et al.* (2011) reveals a surprisingly low momentum coupling between one of the fastest ever observed CMEs and the ambient solar wind.

The CME dynamics is influenced by several forces. In the later evolution, the CME propagation is dominated by the drag force while in the early stages magnetic forces are responsible for their initiation. Although it is generally accepted that the source of energy driving a CME must be the coronal magnetic field reconnecting at a critical point and inducting a Lorentz force (Carmichael, 1964; Sturrock, 1966; Hirayama, 1974; Kopp and Pneuman, 1976), the exact procedure of the CME initiation has led to a controversial debate resulting in a wealth of different models. Some models postulate a slowly increasing loss of the equilibrium between the participating forces, others consider a geometrical instability. The geometric and magnetic properties of CME SRs can be determined by observations of the lower corona in extreme ultraviolet (EUV) wavelengths and by mag-

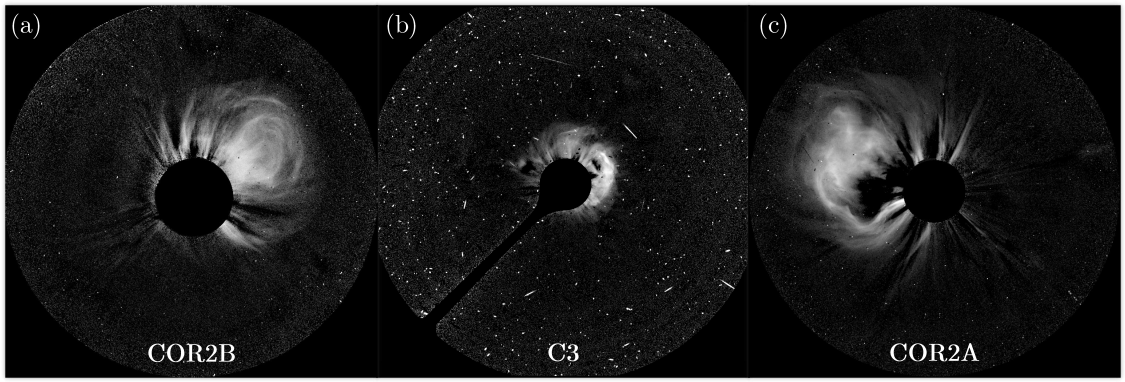

Figure (1.2) CME observation of STEREO SECCHI COR2 B (a), COR2 A (c) and SOHO LASCO C3 (b) at March 10, 2012 18:54 UT. The simulations multiviewpoint observation allow the 3D analysis of CME geometry, kinematic properties and the precise determination of the direction of propagation. The spacecraft longitudes at this date were around 118° clockwise for STEREO B and around 109° counterclockwise for STEREO A in respect to the Earth-Sun observation direction of SOHO in the libration point L1. The images were processed and calibrated as described in Section 4.2.2.

netograms of the photosphere. The agreement with the flux rope picture was proven in a number of studies (Bothmer and Schwenn, 1998; Mulligan, Russell, and Luhmann, 1998; Palmerio *et al.*, 2017, 2018). On the other hand, less analysis has been done whether this flux rope structure is preserved while propagating into the heliosphere, or if deformations, deflections and rotation with respect to the solar SR can occur (Bothmer and Mrotzek, 2017; Isavnin, Vourlidas, and Kilpua, 2014).

On its trajectory, Earth-directed CMEs can interact with Earth's magnetosphere, which dissipates energy and induces geomagnetic storms. For this reason, CMEs are the major drivers of disturbances in the magnetosphere (Bothmer and Daglis, 2007). Since the effects of solar phenomena and their impacts on Earth's ionos- and magnetosphere became aware, the question of their solar origins is strongly interlinked with the research field of *solar-terrestrial physics*. In addition to vulnerable satellite systems such as the *Global Navigation Satellite Systems*, long conductors on the ground can be heavily affected, too. Power grids, rail networks or pipelines are some of the important parts of the infrastructure being threatened (Bothmer and Daglis, 2007). By understanding how the initial conditions, especially the magnetic quantities (i.e. field strength, orientation and stored energy) of their SR on the solar surface are passed and evolve further into the heliosphere, an important step to early, pre-eruption, forecasting is made. Calculating the strength of the single magnetic field components from remote observations is a challenging task that different space weather groups and institutions all over the world are working on (Riley *et al.*, 2018; Mays *et al.*, 2018; Verbeke *et al.*, 2018; Verbeke *et al.*). In order to derive the earliest possible CME forecast, the understanding in the connection between CME SR properties and the dynamics of the corresponding CME is of special interest. Projects like the Advanced Forecast For Ensuring Communications Through Space (AFFECTS)[1], the Flare Likelihood And Region Eruption foreCASTing (FLARECAST)[2] or the OPerational

[1] https://www.affects-fp7.eu/home/ (13.12.19)
[2] http://flarecast.eu/ (13.12.19)

Tool for Ionosphere Mapping And Prediction (OPTIMAP) [3] include the scientific results of the last decades to develop accurate forecasting systems. Science projects systematically cataloguing and analysing thousands of observed events like the *Heliospheric Cataloguing, Analysis and Techniques Service* (HELCATS) [4] are fundamental to provide these results.

In this thesis, an investigation about the kinematics of CMEs, including their dynamics and geometric properties as well as their corresponding solar SR properties is presented. The results presented in this work are based on the research, outcomes and techniques developed within the HELCATS EU FP-7 project. The analysed data comprises remote sensing observations of a representative set of 21 CME events and measurements of the magnetic as well as geometric properties of their corresponding solar SR. These events were selected on the base of specific selection criteria in a time interval from July 2011 to November 2012 during solar cycle 24 and studied in detail with advanced analysis methods. In order to measure the 3D CME kinematics, the well established Graduated Cylindrical Shell model (Thernisien, Howard, and Vourlidas, 2006) was used to reconstruct the CME FR structure from multi-viewpoint observations from the SOHO and STEREO satellites, which were separated by 90° to 130° in the specified time interval. This technique is applied to observations from EUV imager at a wavelength of 195 Å, white-light coronagraphs and heliospheric imager. In this way, detailed height-time-profiles ranging from below $2\,R_\odot$ up to heliospheric distances of $\sim 100\,R_\odot$, as well as the CME geometries and CME masses of the individual events are obtained. The corresponding SRs were identified and analysed using complementary observations of the *Solar Dynamics Observatory* (SDO, Pesnell, Thompson, and Chamberlin 2012). EUV images and line of side (LOS) magnetograms within a time window of ±6 hours around the CME eruption were chosen to examine the magnetic characteristics of the CME SRs over time using the automated *Solar Magnetic Feature Detection and Tracking for Space Weather Monitoring* (SMART) algorithm developed by Higgins *et al.* (2011).

The thesis is organised as follows. Chapter 2 *Basic Knowledge* summarises the fundamentals to understand the prime source of solar activity that drives solar phenomena such as CMEs. After a brief overview about the characteristics, structure and magnetic activity of the Sun, an introduction of solar activity phenomena and the Sun-Earth-connection is given. In Chapter 3, *Theories and Observations of the CME Evolution*, the physical background of the applied analysis and models is discussed in more detail. This includes the CME initiation and propagation into the heliosphere, with a focus on the properties of CME source regions and CME kinematics. The used data-sets and the applied methods are explained in Chapter 4 *Instrumentation, Data and Methods*. A summary of the different instrument types as well as the space missions from which these data were collected is included. In Chapter 5 *Results and Discussion*, the results of this thesis are presented and critically discussed. Finally the major finding are summarised and an outlook about future investigations containing the further use of the results is given in Chapter 6 *Summary and Outlook*. Supplementary material can be found in the Appendix A.

[3] https://www.dgfi.tum.de/en/projects/optimap/ (13.12.19)
[4] https://www.helcats-fp7.eu/ (13.12.19)

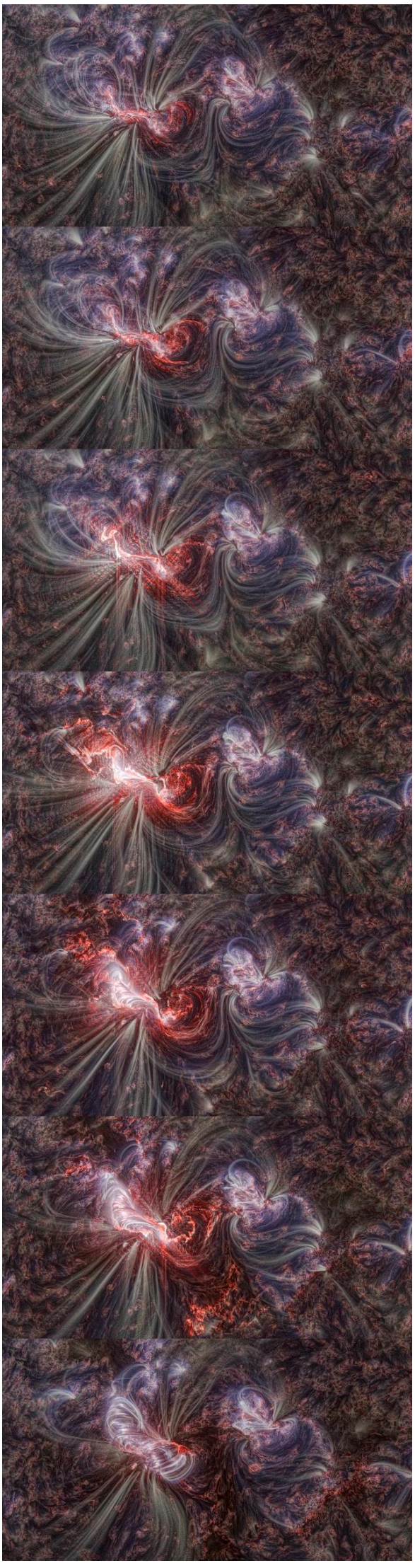

Chapter 2

Basic Knowledge

"Insufficient facts always invite danger."

Spock (Star Trek)

In this chapter, the fundamentals that are necessary to understand the solar activity and the related phenomena, which are important for the Sun-Earth connection are addressed. This phenomena are explained in detail and their dependency on the Sun as its main source is pointed out. Starting with the basic characteristics of our central star, the theory of stellar structure and the underlying processes driving the solar dynamo responsible for the changing activity of the Sun, is discussed.

Cover Figure: Time series of the source region of a CME during its eruption in March 7, 2012. The images are composites of SDO/AIA observations at the wavelengths 171 Å, 211 Å and 304 Å. For more details see Figure 3.2. Courtesy of Miloslav Druckmüller.

2.1

2.1 The Sun

In the history of mankind there are a few archetypes, which can be found in every ancient culture, presenting commonalities of which men from the past and the present are depending on. Often they occur from natural forces and were treated as Gods or mystic beings deciding on the human destiny. Less were more worshipped than our central star as *Ra* in the ancient Egypt or *Kinich Ahau* in the Mayan culture for example. The God gave light and warmth but soon it was understood, that it is also giving something more important. By observing the God rising and setting at the sky, measuring time was possible and the first clock was developed. Series of observations defined a year and with calendar systems the foundations for the modern agricultural economy, and so for the modern society, were formed. Today we can still find the first solar observatories, that were so important to know the right time for sowing and harvesting. One of these is the neolithic *Solar Observatory Goseck* (see Figure 2.1), which is even older than *Stonehenge* or the *Sky disk of Nebra* (Bertemes and Meller, 2012). Observatories of this type consist of ramparts and wooden palisades arranged in rings. Along the palisades gates mark the positions of the sunrise and sunset at the days of the summer and winter solstice.

Figure (2.1) The reconstruction of the neolithic solar observatory in Goseck, Saxony. After the archaeological excavation between 2002 and 2004, it was fully reconstructed at its location of discovery. Originally, the observatory was build in the 5^{th} millennium BC and consists out of 1675 oak poles surrounded by a circular moat and a rampart (Bertemes and Meller, 2012). Photograph taken by the author in May 2018.

With our technology we reached to some degree independence of the forces of nature but by far not of every one. The Sun is one of the factors we have no influence on, affecting our life day by day. Understanding the driving forces and underlying processes in the Sun is one of the big tasks in astrophysics. There are still a lot of open questions like the *origin of the coronal heating*, which is one of the biggest unsolved problems in stellar astronomy and astrophysics. Also the solar dynamo, responsible for the activity cycle of the Sun, is not completely understood. Giving answers to these questions is not only important for the knowledge about the solar influences on Earth, but it helps us also to study a star in high detail and to develop our picture of stars in general.

Today's solar observatories are not anymore comparable with the ancient wooden rings. Thanks to the invention of the telescope, detailed structures on the solar surface were discovered. Furthermore, within more than 400 years of observations since Galileo Galilei, it was shown that the Sun is anything but static. Through the technological progress

telescopes, became more accurate, spectral ranges beyond the visible spectrum could be observed and telescopes onboard satellites, which are not affected by Earth's atmosphere, were developed. Ground and space based telescopes opened a window for new observation making measurements of solar quantities possible. In order to investigate an object in detail, one has to be able to describe it at first before it can be classified and compared. For this reason it is essential to know fundamental physical characteristics of the Sun.

2.1.1 Basic Characteristics of the Sun

Through a single instability, a giant molecular cloud in the Orion spur of the Milky Way collapsed under its own gravity around 5 billion years ago. Due to the cooling of dust, the cloud fall into fragments. Out of one of this fragments, the Sun, and with it our solar system, was born. This process of star formation can be observed for example in the Great Orion Nebula (see Figure 2.2) which is one of the several star formation regions in our Galaxy. This emphasises the fact, that our Sun is, physically seen, one out of billions of

Figure (2.2) Wide-field exposure of a part of the constellation Orion. In the upper right corner, the Great Orion Nebula (M42) side by side with the Running Man Nebula (M43) is visible and in the bottom left corner the Flame Nebula (NGC 2024) as well as the Horsehead Nebula (Barnard 33) are shown. Photograph taken by the author in January 2018, New Zealand.

other ordinary G2 stars. Burning hydrogen to helium the Sun will stay for approximately another 5 billion years on the main-sequence of the Hertzsprung-Russel diagram before the hydrogen will run out and the star expands to a red giant.
In order to develop stellar models explaining the observations, the precise knowledge of the Sun's basic parameters like mass, size and composition is fundamental. Due to the progress

Table (2.1) List of fundamental solar parameters together with their values and the methods used for their determination. For more details see Stix (2004), p.2-9, and Carroll and Ostlie (2006), p.364.

Quantity	Value	Method
Distance	$1\,\mathrm{AU} = 149597870(2)\,\mathrm{km}$	Radar echos and Kepler's law
Mass	$1\,\mathrm{M}_\odot = 1.9889(3)\cdot 10^{30}\,\mathrm{kg}$	Kepler's law and g
Radius	$1\,\mathrm{R}_\odot = 696342\,\mathrm{km}$	Angular diameter and 1 AU
Density	$\overline{\rho} = 1.408\,\mathrm{g\,cm^{-2}}$	$1\,\mathrm{M}_\odot$ and $1\,\mathrm{R}_\odot$
Surface gravitation	$g_\odot = 274\,\mathrm{m\,s^{-2}}$	$1\,\mathrm{M}_\odot$, $1\,\mathrm{R}_\odot$ and g
Solar constant	$S = 1367(3)\,\mathrm{W\,m^{-2}}$	Measurements
Luminosity	$L_\odot = 3.844(10)\cdot 10^{26}\,\mathrm{W}$	Solar constant S pyrheliometer
Composition	92.1 % H, 7.8 % He and 0.1 % Metals	Spectroscopy
Surface Temperature	$T_{eff} = 5778(3)\,\mathrm{K}$	$L_\odot$ and $R_\odot$
Rotation period	25 d (Equator) 36 d (Poles)	Doppler effect

in technology these parameters have been determined with increasing accuracy within the last century. Their values and determination methods are summarised in Table 2.1.

2.1.2

2.1.2 The Solar Structure

By knowing the basic quantities of a star, its interior can be described by principle physical laws, which constitute the theory of stellar structure. In the solar case, neutrinos created by nuclear processes are an additional direct observable of the Sun's core. Similar to seismology on Earth, helioseismology opens a window to study the internal structure of the Sun by observing and analysing the properties of oscillations due to propagating waves.
At the first appearance the Sun is a homogeneous, fully ionised glowing sphere of gas. In detail, it consists of six regions clearly defined by the dominating type of energy transfer and basic thermodynamic as well as magnetohydrodynamic parameters. In the following, the characterising properties of these regions are pointed out. The complete solar structure, including the Sun's atmospheric layers, is illustrated in Figure 2.3.

The Core

As long as the Sun stays on the main-sequence, the *core* is the only region where the conditions are reached to ignite thermonuclear fusion. Moreover the mass of the core defines mainly the time a star remains on the main-sequence. Reaching a temperature of $\sim 1.5\cdot 10^7\,\mathrm{K}$ the core extends up to $0.25\,\mathrm{R}_\odot$. Different hydrogen burning reactions produce the majority of the energy necessary for the equilibrium between radiation pressure and the Sun's own gravity. The three proton-proton

chains contribute together with 98.8% to the total energy output while the CNO cycle is of subordinate importance in the Sun.

The Radiative Zone

Over the core up to $\sim 0.7\,R_\odot$ lays the *radiative zone*, where energy is transported primarily by radiative diffusion. The density drops about two orders of magnitude along the zone and the temperature falls off to $\sim 2 \cdot 10^6\,K$. While core and radiative zone are spinning as a rigid body, the outer parts rotate differentially. This produces an interlayer at the upper border of the radiative zone named as the solar *tachocline*.

The Convection Zone

The tachocline, as transition region between different rotation laws, has strong shear flows and a thickness of around $0.1\,R_\odot$ (Spiegel and Zahn, 1992). Because the overlaying region becomes more opaque by not fully ionised metals, the Schwarzschild criterion for stability is not valid anymore. Instabilities occur and the dominating energy transport changes from radiation to convection. This fully *convective region* reaches up to the solar "surface" at $1\,R_\odot$.

The Photosphere

A star's surface is defined by the deepest optical thin region for wavelengths of the visible light. It is the part of the convection zone in which the gas changes from completely transparent to completely opaque. The solar *photosphere* is $\sim 100\,km$ deep. Besides the hot rising and cooling convection cells, the granules, sunspots and bright faculae (see Sec. 2.1.3 and Fig. 2.4) can be observed in white light. In the H_α spectral line, filaments can be observed in the photosphere as dark lines. The photosphere is the coolest layer of the Sun with temperatures around its effective temperature $T_{eff} = 5778\,K$.

The Chromosphere

In the solar atmosphere, above the photosphere, the temperature is increasing again while the density decreases. The *chromosphere* is 10000 times fainter in brightness than the solar surface, extends to a height of $\sim 1600\,km$, and can only be seen in the visible spectrum during a solar eclipse. Due to emission lines forming in the chromosphere at temperatures around $10^4\,K$ (e.g. H, CaII and K) structures like supergranules and spicules are visible using corresponding filters. Above the chromosphere the temperature increases rapidly to $10^6\,K$ within a $\sim 100\,km$ thick transition layer (Carroll and Ostlie 2006, p. 364-365).

The Corona

The largest part of the solar atmosphere consists of the *corona*, which is even 100 times fainter than the chromosphere. Contrarily to the self emitting chromosphere and transition layer, visible light coming from the photosphere is scattered by free electrons making the corona observable during a total occultation of the solar disk. Because the corona is not in local thermodynamic equilibrium (LTE) the temperature varies around $2 \cdot 10^6\,K$. Extreme ultraviolet (EUV) radiation and X-rays are emitted from the coronal material at such high temperatures. At the same time the underlying regions are cooler and fainter in this wavelength regime making the corona directly observable across the disk. This led to the discovery of coronal holes

(CHs). The corona is categorised by different types of radiation into the components K, F and E (Carroll and Ostlie 2006, p. 366-370):

The ***K****(continuum)-corona*: The high temperature in the corona leads to two effects resulting in a continuum radiation. First, the fully ionised material of the corona scatters the light of the photosphere by Thomson scattering (see Sec. 3.4.1). Secondly, because of the large Doppler shifts the absorption lines from the photosphere are "washed out". This continuum is the primarily light source of the corona from its beginning up to a height of $2.3\,R_\odot$.

The ***F****(Frauenhofer)-corona*: Beyond $2.3\,R_\odot$ scattered light by dust particles is brighter than the one from free electrons. The dust grains are larger and moving with less speed which is why the Frauenhofer lines are still observable.

The ***E****(Emission)-corona*: Another contribution comes directly from emission lines by the ionised atoms. All parts of the corona overlap in height but the E-corona is more than two orders of magnitude fainter than the others.

Depending on the solar activity (see Sec. 2.1.3) shape and expansion of the corona changes. The quiet corona, where quiet commonly refers to solar regions that are not active or part of cornal holes, extends more at the solar equator than at the poles, while the active corona appears in a complex irregular shape.

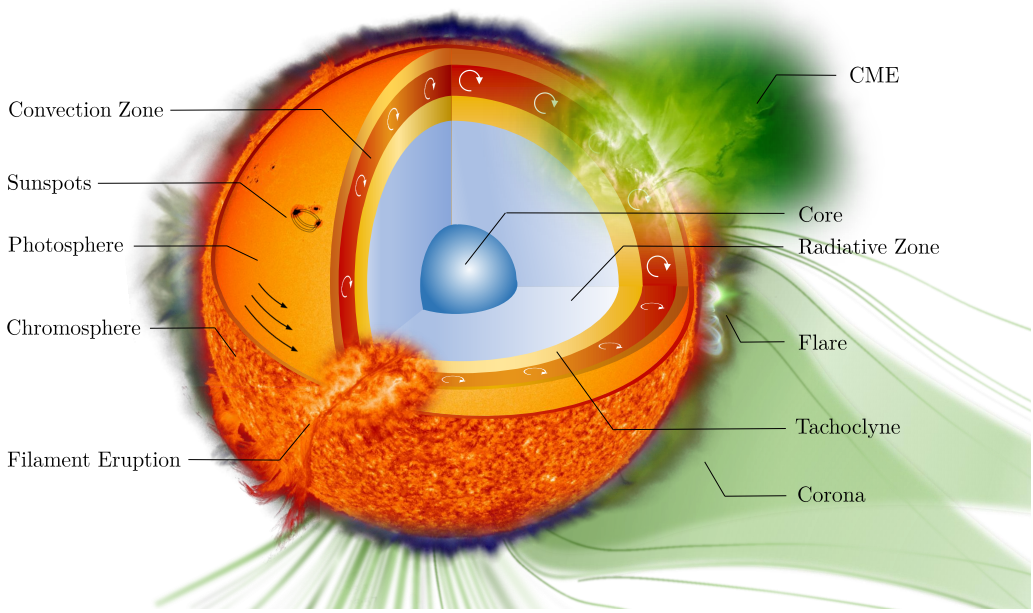

Figure (2.3) Schematic view of the structure of the Sun. Differential rotation is shown by black curved arrows, and convection is indicated by white circular arrows. Core and radiation zone are colored in blue, while tachocylne and convection zone are in yellow and orange. In the atmospheric layers, different activity phenomena like sunspots, filament eruptions, flares and CMEs can be seen. The layers of the atmosphere used in this figure are observations of the *Atmospheric Imaging Assembly* (AIA, Lemen *et al.* 2012) onboard of the SDO spacecraft (see Section 4.1)[1](see also Chapter 4).

[1]https://sdo.gsfc.nasa.gov/ (13.12.19)

2.1.3 The Solar Activity

Since the first solar observations with an astronomical telescope, over time the picture of the Sun as a static gaseous sphere was shown to be outdated. Dark regions on the solar surface, that appeared, disappeared and moved, were discovered. These sunspots appear usually in groups and consist of a dark umbra surrounded by a brighter penumbra as shown in Figure 2.4. Using different filters in the EUV at higher altitudes above the photosphere, they appear as bright areas called *active regions* (AR) (see although Section 3.1.1), which are accompanied by large loops and complex structures anchored around the spots. Systematic white light records of sunspots were made by the German astronomer Samuel Heinrich Schwabe. He discovered a regular pattern in this fluctuations and found the *Schwabe cycle* with a period around 11 years (Schwabe, 1844). Wolf (1856) defined for systematic records the relative sunspot number SSN (today the *International Sunspot Number*, S_n) including in its original form the number of sunspots n_s, the number of sunspot groups n_g and the scaling coefficient k:

$$SSN = 10k \cdot (n_s + n_g). \tag{2.1}$$

The k factor relies on the observation conditions, telescope aperture and the observers experience. The latter introduces a subjective valuation. Together with flaws and bias in the measurements, like the Waldmeier weighting bias (Hathaway, 2015), it was necessary to apply corrections to the recorded sunspot number (Clette *et al.* 2014). Although, the sunspot number is the most prominent activity index, selected radiation observables proved to track the Sun's activity, too. The *total solar irradiance, EUV emissions* and *10.7 cm Radio flux* have the advantage over the sunspot number in that they are disk integrated. By measuring the intensity of the green corona at the FeXIV 530.3 nm line, the *coronal index* presents the activity at higher altitudes (Rybanský, Rušin, and Minarovjech, 2001). Most of the solar activity indicators follows Poisson statistics (Hathaway, 2015). Figure 2.5 shows the corrected 13-month smoothed monthly total sunspot number starting from 1900 to July 2018, showing solar cycle 14 to 24. The beginning of a new cycle can be seen by the appearance of a high latitude sunspot having an opposite polarity with respect to the preceding sunspots. Solar cycle are recorded since the beginning of extensive recording of sunspots in 1755 (Kane, 2002). Long term variations in the duration and maximum of the solar cycle indicate overlaying periods from additional cycles. The Gleissberg cycle with a 80 to 90 year period can also be seen in Figure 2.5 through the variation in the amplitudes of the 11 year cycle (Gleissberg, 1939). Another cycle in the solar activity with a period of 210 years, the Suess cycle, was found by reconstructing cosmic ray modulation leaving its chemical footprints in tree rings and ice cores by variation in the concentration of ^{14}C and ^{10}B (Suess, 1980).

In the early 20^{th} century, George Ellery Hale measured the magnetic field of sunspots using spectroscopy, and linked the magnetic activity of the Sun with the solar cycle for the first time (Hale, 1908). He showed that sunspots are cooler than the surrounding photosphere, which is an effect of the inhibited convection in a spot by the magnetic field. In his following work, Hale *et al.* (1919) found a general behaviour in the latitudinal appearance as well as in the polarity of the magnetic field in sunspots (see Figure 2.4). This fundamental observational characteristics are summarised in *Spörer's law*, *Joy's law* and *Hale's Polarity laws*:

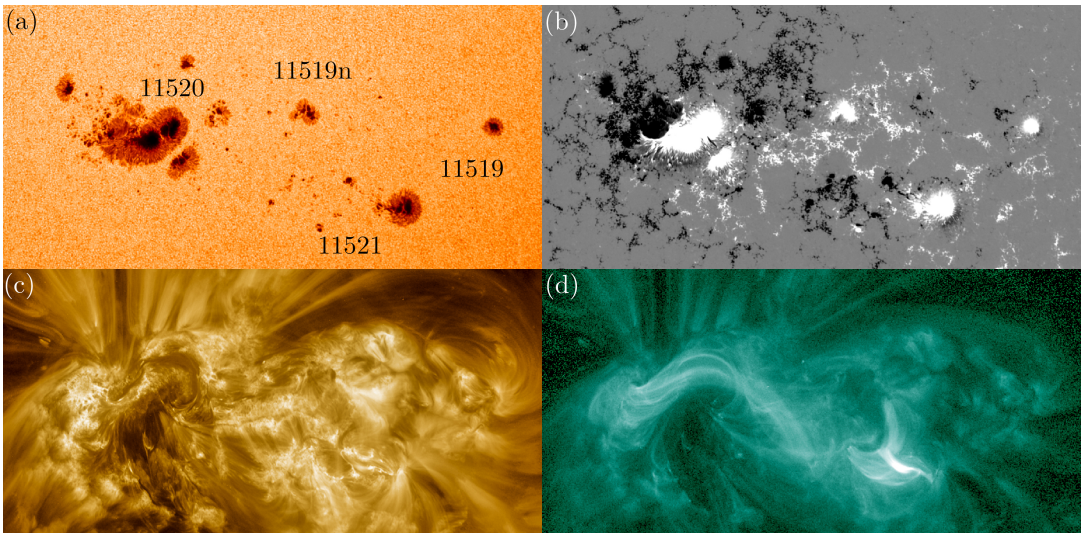

Figure (2.4) Example of sunspot groups and active regions observed on July 12, 2012 15:00 UT with SDO HMI continuum (a), HMI magnetogram (b), AIA 193 (c) and AIA 94 (d) (see Section 4.1). Granules of the photosphere are visible around the sunspots consisting of dark umbra and surrounding penumbra. From left to right the active regions 11520, 11519n, 11521 and 11519 are shown.

- Preceding spots appear at lower latitudes and the inclination axis of a sunspot group with respect to the solar equator is proportional to its latitude.
- The polarity of bipolar groups switches from the preceding/following group.
- Corresponding groups in different hemispheres have opposite polarities.
- Spots of preceding/following cycles switch the polarity sign, too.

By observing the overall polar magnetic field of the Sun, Babcock (1959) noted that it reverses polarity during the activity maximum, and that its strength is in antiphase with respect to the sunspot number. Solar activity is therefore an effect of the over time changing local and especially global solar magnetic field. By reproducing successfully the general behaviour of the solar cycle, it is widley accepted that the solar magnetic field is generated by a hydromagnetic dynamo. The basic idea of the *solar dynamo* is, that an additional magnetic field is generated by the motion of a conducting fluid in the presence of an initial magnetic field (Babcock, 1961). As long as the magnetic diffusion by the energy loss of the plasma resistance is smaller than the induction effect, the dynamo successfully amplifies the magnetic energy. Dynamo theory is in detail highly complex but the underlying process to drive a regenerative dynamo cycle is the transformation from a *poloidal* magnetic field B_p into a *toroidal* magnetic field B_t and, very important, vice versa. There are two main effects responsible for this conversions driving the solar dynamo, which are explained below in detail and illustrated in Figure 2.6:

The Ω-Effect:

The initial magnetic field in a highly conducting plasma is preserved, which is called *flux-freezing*. This leads to a shearing of field lines when the plasma is moving. As

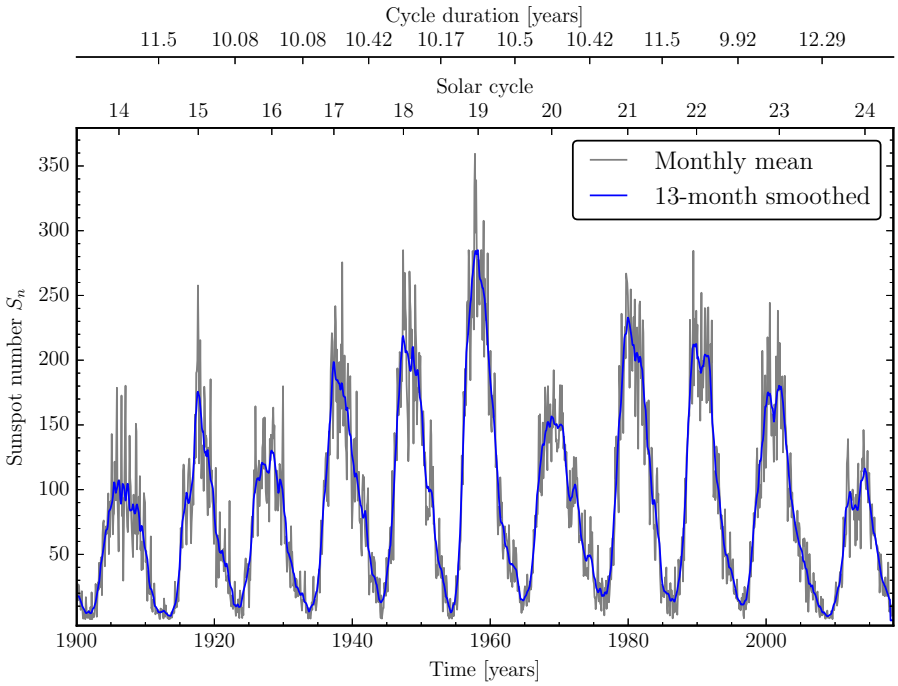

Figure (2.5) Plot of the international total sunspot number S_n from 1900 until July 2018 showing solar cycles 14 to 24. The monthly mean values are represented in grey and the corresponding 13 month smoothed data in blue. The Version 2 data set was plotted. It contains corrections of past inhomogeneities reported by Clette *et al.* (2014); Clette and Lefèvre (2016), and is provided by the WDC-SILSO, Royal Observatory of Belgium, Brussels.[2]

a consequence, over time, a poloidal field, lying in the Sun's meridional plane, is winded up at the equator around the solar rotation axis by differential rotation (see Fig. 2.6 a-c). It was found by helioseismology that the Ω-*effect* mainly takes place at the base of the convection zone in the tachocline (Howe *et al.*, 2000). The converted toroidal field is twisted by turbulent convection and builds up intense magnetic *flux ropes* which rise to the photosphere by the increase of magnetic pressure. Their footpoints on the surface hinder convection causing a cooling of the plasma and creating sunspots at higher latitudes.

The α-Effect:

In order to convert B_t back to B_p, Parker (1955) suggested to consider the small-scale motions of convection cells. The turbulent motion of the solar plasma combined with the differential rotation results in a helical motion and a poloidal field component, which has an inverted polarity with respect to the initial one. On a large-scale the sum of these small-scale meridional fields acts as a large poloidal field (see Fig. 2.6d to f).

[2] http://sidc.be/silso/datafiles (13.12.19)

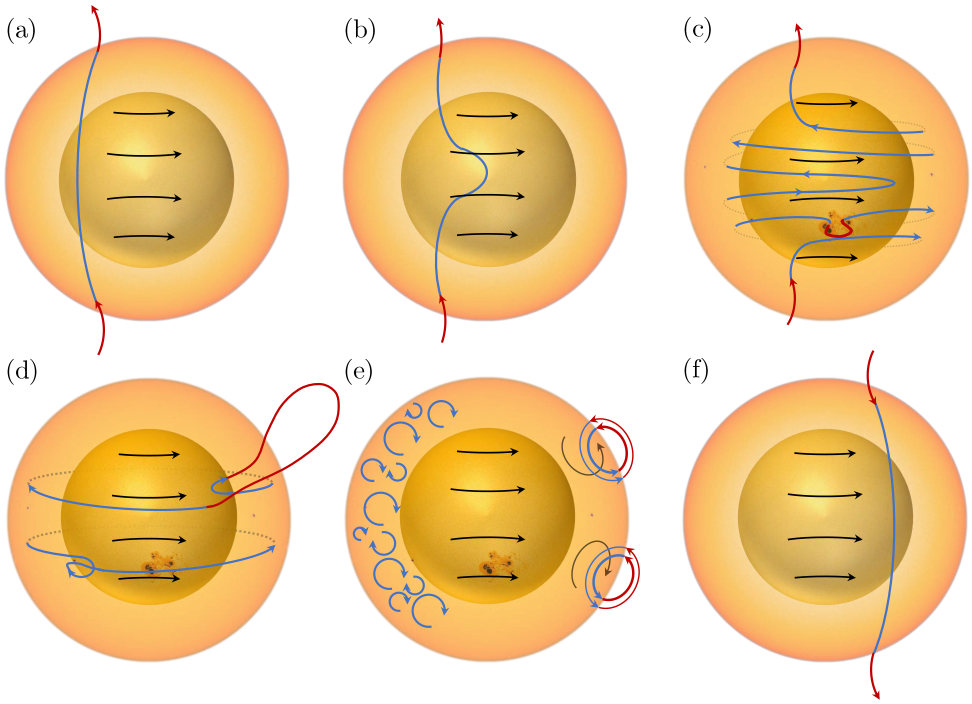

Figure (2.6) Concept of the solar dynamo models. Internal fields are represented in blue, while fields over the photosphere are in red. (a) to (c) showing the Ω-effect. The initial configuration in (a) is a primary poloidal field in the minimum of the solar cycle. Differential rotation drags the frozen in magnetic field and winds it up (b and c). (c) Buoyant loops break through the photosphere by increasing magnetic field density and sunspots are formed. (d) The combination of differential rotation and convection twists the toroidal field into a helical shape. α-effect and BL-mechanism differ in the scale of the loops. On the left side of (e), the small scale poloidal fields merging to a global field (α-effect) are shown. On the right side, the BL-mechanism is shown. The meridonal flow (black circular arrows) transports the field from spots and active region poleward causing the overall field to reverse (f). Adapted from Dikpati and Gilman (2007).

An alternative to Parker's mean-field α-effect is the empiricaly proved *Babcock-Leighton* (BL) *mechanism*.

The BL mechanism:

As the up winding by the Ω-effect continues, additional flux rises and spreads over the surface by magnetic diffusion and reconfiguration. More sunspots appear at lower latitudes with stronger twisting and denser magnetic fields until the solar maximum is reached. The meridional flow transports the magnetic field poleward causing the overall polar field to reverse (Babcock, 1961; Leighton, 1969).

If this process is completed, the 11 year activity cycle has ended and after another activity cycle the magnetic field is back to its original configuration. The magnetic cycle lasts therefore ∼22 years and is called *Hale cycle*. Although the solar dynamo theory reproduces

the overall behaviour of the magnetic cycle, it does not include the fine details of small-scale observations like ephemeral active regions (small bipolar regions with a maximum total flux of 10^{20} Mx that generally do not produce sunspots (Harvey and Martin, 1973)) besides active regions. To solve the entire problem, considering the full MHD equations connected with a complete knowledge of the depth and latitude depending velocity field of the differential rotation, is required. Furthermore the connection with the heating of the solar atmosphere, which is believed to be also a problem of magnetic nature, has to be understood and included. For this reason more effort in figuring out the basic nature of the involved physical processes is needed, rather than to develop complex computational intensive models (Bushby and Mason, 2004).

Solar activity takes place on a large range of temporal and spatial scales: starting with the emitted irradiance of the Sun, including the small structures and sunspots on the photosphere, up to effects and phenomena based on ejected plasma, which propagates through the solar system. Latter phenomena are of special interest in the field of space weather and are presented in the next section.

2.2 Solar Phenomena and the Heliosphere Connection

As a result of solar activity, magnetic energy is transformed in other forms of energy, which drive solar phenomena. The latter can be observed as the strong impulsive releases of radiation, movements of solar plasma and acceleration of particles to relativistic speeds. Since solar phenomena, correlated in occurrence and strength with the Sun's activity, were linked to disturbances of Earth's electromagnetic environment, it was necessary to invest efforts into uncovering the full Sun-Earth connection. The entire scope of the danger originating from major disturbances of Earth's magnetosphere, which are called geomagnetic storms, became clear with the Carrington event 1859, when telegraphs were destroyed and aurora were seen over London (Carrington, 1859). At the latest by the discovery of the non-empty interplanetary space in the beginning of the spacecraft and satellite era, these effects were summarised in the term of *Space Weather*, which defines all cosmic and solar influences affecting the interplanetary medium, and in particular the Earth. In the following, the different solar activity phenomena, which represent the different energy transport forms going out from the Sun, their physical properties and how they influence the Earth as well as the near-Earth space are explained in more detail.

2.2.1 Solar Flares

Flares are observed as explosive, spatial and temporal limited emission of light in a wide range of the electromagnetic spectrum, spanning from radio wavelengths to γ-rays for the strongest flares. An example of a flare observation in different EUV wavelengths can be seen in Figure 2.7. The first observation of a flare was made by Carrington (1859), who noticed two bright patches within a sunspot group while observing the Sun. This sudden energy breakout is triggered by the reconnection of a magnetic field and happens frequently in active regions. The stored magnetic energy is released in the form of radiation, plasma heating as well as particle acceleration and can exceed 10^{25} J in the case of a major event (Bothmer and Daglis 2007, p. 362). Flares are best observed in EUV and X-ray wavelenghts because of the high contrast to the dark photosphere and the heating

Table (2.2) List of flare types and GOES classification of X-ray flares with some basic parameters (Aschwanden *et al.*, 2000).

Type	**Class**	**Peak Flux** [W m^{-2}]	**Spectral regime**	**Energy** [J]	**Length** [Mm]
Nanoflare			EUV	10^{17}-10^{20}	2-20
Microflare			EUV, SXR	10^{20}-10^{23}	5-50
(Milli)Flare	**A**	$< 10^{-7}$	EUV, SXR, HXR	10^{23}-10^{26}	10-100
	B	10^{-7}-10^{-6}			
	C	10^{-6}-10^{-5}			
	M	10^{-5}-10^{-4}			
	X	$> 10^{-4}$			

of the atmospheric solar plasma by reconnection, as it can be seen in the Figures 2.3 and 2.4.
Because flare properties cover several orders of magnitude their dynamic range is categorised first by the observable spectral regime and energy dividing them into nano- (EUV), micro- (Soft X-rays, SXR) and milliflares (or simply flares, Hard X-rays, HXR), while nano- and microflares can also be observed outside of active regions. Details about the different types are listed in Table 2.2. Since the high temperature of the corona became aware, a great debate was started about the heating mechanisms acting in it. Since Parker (1983) introduced them, nanoflares are contentious discussed as part of the puzzle (Aschwanden *et al.*, 2000; Bingert and Peter, 2013; Kirichenko and Bogachev, 2017). However, their low intensity compared to the background makes detailed analysis challenging. A more precise classification system, which is based on the peak flux from 1 to 8 Å measurements by the *Geostationary Operational Environmental Satellite* (GOES, Baker and Savides 1975) system near Earth, is used for flares. The categories, listed in Table 2.2, are scaled logarithmically and can be subdivided into 9 linear subclasses.

In contrast to other activity related phenomena, the flare occurrence does not follow Poisson statistics, which is pointed out by considering only the more energetic events that fluctuate stronger and differ from the sunspot number (Temmer, 2010). High energetic hard X-ray flares seem to appear with a lag of several years according to the solar maximum, and show a variation period of 22 years indicating a close connection to dynamo processes in the solar interior (Cowling, 1945; Hudson, 2007; Temmer, 2010). The deviation from the Schwabe cycle allows the conclusion of a nonlinear response between flare occurrence and free magnetic energy (Aschwanden, 2005).

There are several models describing the flare process, which distinguish in principle only in the nature of the driving mechanism and its geometry leading to the magnetic reconnection. Possible drivers are prominences, filaments or plasmoids *above* the reconnection site or changes in the magnetic configuration *under* the reconnection site like photospheric emergence (Aschwanden 2005, p.449). Different models are explained more detailed in Section 2.2.3. All models preceed in three phases. After the magnetic structure was long

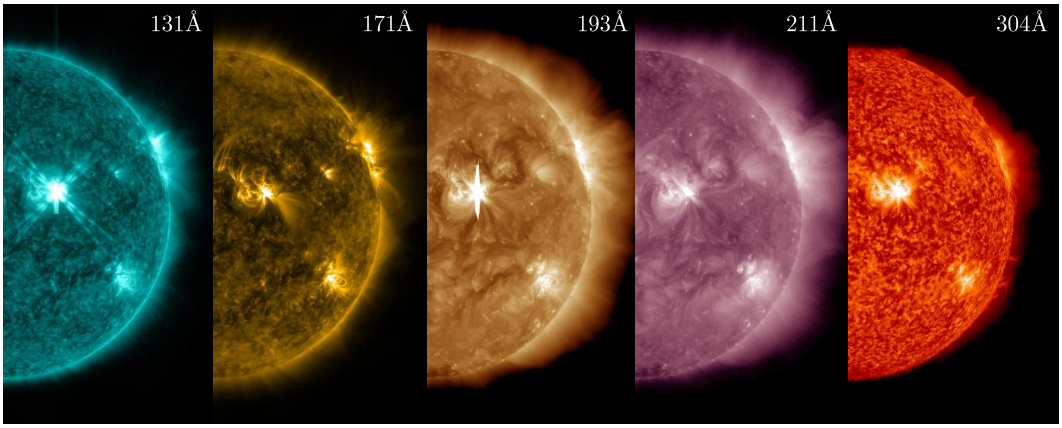

Figure (2.7) Example of a flare observation from SDO/AIA in different EUV wavelengths on September 6, 2011 22:26 UT. The individual channels, which indicate the central wavelength of the used filter in units of Ångström, are annotated in the image.

enough stable building up a significant amount of magnetic energy, in the *preflare phase*, the driver moves the system slowly out of equilibrium by a weak instability. The streched and sheared field starts to reconnect in the following *onset phase*. Energy is released impulsively speeding up the driving process. Continuous reconnection releases more and more energy creating at their footpoints along the field lines hot X-ray loops. Finally, the field closes down until the magnetic energy is decomposed and a new equilibrium is reached. The HXR and SXR emissions in the flare-time-profile peak shifted to each other with a delay of the SXR maximum to the HXR maximum constituted in the different physical processes the radiation is emitted. While in the impulsive HXR phase, the radiation is emitted by electrons accelerated to high energies up to $\sim$ 1MeV, in the gradual SXR phase, the photons are emitted by thermal bremsstrahlung.

Strong X-ray flares can cause high-frequency radio blackouts lasting for minutes to hours. Because of their ionising radiation they produce disturbances in the total electron content (TEC) altering the Earth's *ionosphere*. High frequency signal transmissions with satellites, or the utilisation of reflections from the ionosphere are affected, and can be disrupted leading, in the worst case, to the loss of a satellite. A recently prominent event was the 4^{th} of November 2015 radio flare. It reached more than 50000 SFU at GHz frequencies, and led to a blackout of about two hours of the majority of southern swedish aviation radar systems (Opgenoorth *et al.*, 2016). No warnings by safety systems were made because the unusall strong radio emission came from an intermediate M3.7 flare. This event demonstrates not only the vulnerability of technology by space weather effects, but even the gaps in our understanding of it. Radio communication, navigation and radar systems become parts of the infrastructure that modern society is highly depending on. For this reason the German project *OPTIMAP (Operational Tool for Ionosphere Mapping and Prediction)* was founded by the German Space Situation Awarenes Centre to develop a service providing maps and forecasts of the ionosphere corrected by solar effects. Within this project we were able to lay the foundations not only to forecast ionospheric disturbances but also to take them into account for corrections.

2.2.2 The Solar Wind

Even before the launch of the first satellites equipped with instruments able to measure the enviromental conditions of space, the *solar wind* nature was predicted in the work of Biermann (1951) and Parker (1959), denoting it *corpuscular*. As a continuous stream of ionised particles, mainly hydrogen and helium, the solar wind carries solar mass into space with a rate of $10^9\,\mathrm{kg\,s^{-1}}$, which is four times smaller than the one by nuclear fusion (Lang 2009, p. 67). Biermann noted by observing comets, that their ion tails point always radially away from the Sun, indicating like giant interplanetary weather vanes the direction of the solar wind. In fact, Nisticò *et al.* (2018) showed recently, that the oscillations of cometary tails can be explained by vortex shedding similar to vanes making it possible to determine local plasma properties of the ambient solar wind. The solar wind quantities can be measured in composition, velocity, magnetic field strength and direction, density and temperature by *in-situ* instruments. Furthermore, the solar wind maintains pressure versus the interstellar medium and builds up a bubble, the so-called heliosphere, which defines the region of space dominated by the Sun. It turned out, that there are two types of solar winds, mainly distinct by their speeds. The *slow* wind has a typical speed under $450\,\mathrm{km\,s^{-1}}$, and the question about its origin is still not completely solved (Bothmer and Daglis 2007, p. 39). Nevertheless, several authors suggested about possible source regions. Open magnetic field lines near the boundaries of CHs (Wang and Sheeley, 1990), transient plasma blobs ejected from helmet streamers (Wang *et al.*, 1998), outflows around active regions (Vanninathan *et al.*, 2015) or jets created by coronal bright points (Subramanian, Madjarska, and Doyle, 2010). However, the strong variability of the slow solar wind does not allow to determine the effective source region (Kilpua *et al.*, 2016).

In the case of the fast solar wind, moving with speeds over $450\,\mathrm{km\,s^{-1}}$ up to $\sim 800\,\mathrm{km\,s^{-1}}$ (Bothmer and Daglis 2007, p. 39), the situation is different. In-situ measurements over multiple Carrington rotations reveal a systematic change in the solar wind speeds repeating every $\sim$ 27 days. Combined with X-ray imaging of the Sun, the origin of the fast wind was identified to be in CHs extending to the central meridian rotating with the Sun. In general, the ions in the solar atmosphere have to be take up additional kinetic energy to be ejected as solar wind, because the escape velocity of $617\,\mathrm{km\,s^{-1}}$ (Lang 2009, p. 63) exceeds the thermal velocity of the particles ($222\,\mathrm{km\,s^{-1}}$ for a hydrogen atom at a temperature of $2 \cdot 10^6\,\mathrm{K}$, Lang 2009, p. 64). Thus the solar wind speed depends highly on the expansion factor of open magnetic field lines. Besides the speed, the two states of the solar wind differ slightly in abundance and temperatures, while the proton density differs by a factor of ~ 3.6 (Schwenn and Marsch, 1990). The slow solar wind is more dense, but compared to the fast one, the proton flux is nearly the same in both. Recent results from Eduardo *et al.* reveal evidence for a possible third component, a very slow solar wind with speeds $< 300\,\mathrm{km\,s^{-1}}$ coming from polar CHs. To clarify this indication, further studies are necessary. The averaged values of the bimodal solar wind are summarised in Tab. 2.3.

On its way to the outer edge of the solar system, the solar wind carries the magnetic field of the Sun with it through flux freezing and builds up the interplanetary medium (IPM) with its interplanetary magnetic field (IMF). Since the Sun rotates, the IMF shapes a structure not in radial lines away from the Sun, but reminiscent of an Archimedian spiral, namely the *Parker spiral* illustrated in Figure 2.8. Between the two magnetic hemispheres the *heliospheric current sheet* (HCM) lies as a magnetic neutral layer enclosed by the open

magnetic field lines in the solar wind and directed in- and outward of the Sun. The Sun's dipole axis is tilted with respect to the rotation axis of about $\sim 12°$ leading to an up and down wobbling of the HCM while the Sun rotates, which is called the *ballerina model*, according to the skirt of a spinning ballerina.

The Ulysses spacecraft took in-situ measurements nearly orthogonal to the ecliptic plane

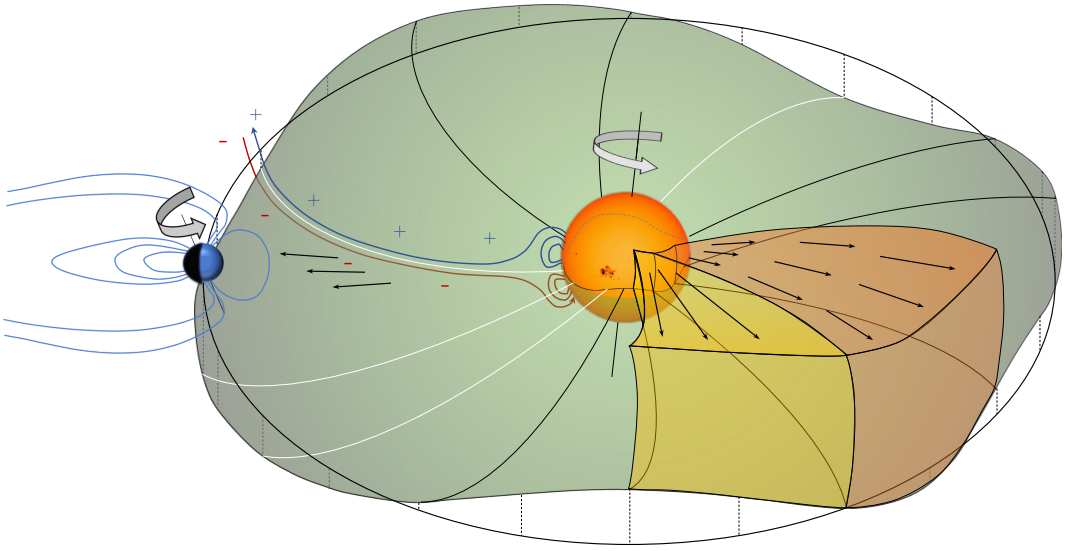

Figure (2.8) Schematic view of the Sun-Earth interactions through the solar wind. The Sun's magnetic field is carried out by open magnetic field lines in the bimodal solar wind having a fast (yellow region) and slow (orange region) components. Since the Sun is rotating the fieldlines shape in the so-called Parker spiral. The HCM (green) divides positive (dark blue) and negative (red) polarities of the IMF. By the continous particle stream of the solar wind, the Earth's magnetosphere (light blue) is compressed on the dayside and pulled apart on the nightside. After Bothmer and Daglis (2007).

and showed that the distribution and variation of the solar wind follows the Schwabe cycle (McComas *et al.*, 1998b). During solar minimum, the slow solar wind is concentrated in a belt $\pm 20°$ in latitude around the heliographic equator, while the fast solar wind dominates the heliosphere and is measured at intermediate heliolatitudes up to the regions of the solar poles (Bothmer and Daglis 2007, p. 40). The IMF represents at this time the solar dipole field having almost exclusively one polarity prevailing per hemisphere. More complex magnetic fields evolve in the solar atmosphere with the cycle going to the maximum and no predominance in the individual hemispheres regarding the polarity can be observed any more. Furthermore, the structure of the velocity distribution becomes more and more disordered.

In order to determine the radial dependency of the solar wind velocity, density and magnetic field, several investigations were made showing discrepancies between theory and measurements. Scintillations in extragalactic radio source observations, generated by the moving inhomogeneous solar wind, like the interference in Earth's atmosphere by convecting air bubbles, causing the stars to twinkle, gave not only the first hints of

the bimodal nature of the solar wind but made also velocity measurements of the solar wind outside of the ecliptic plane possible (Rickett and Coles, 1980, 1991). Direct in-situ observations were made with the two *Helios* spacecrafts, whose heliocentric distance ranged from 0.31 to 0.98 AU for Helios 1, and 0.29 to 0.98 AU for Helios 2, respectively (Rosenbauer *et al.*, 1977). Sheeley *et al.* (1997) derived the solar wind speed in a range of 2-30 $R_\odot$ with coronagraph white-light observations of prominent features during solar minimum. By neglecting projection effects and fitting only in the plane of sky they found the wind speed $w(r)$ to be:

$$w^{\mathrm{She}}(r) = \sqrt{v_a^2 \left(1 - e^{-(r-r_1)/r_a}\right)}, \tag{2.2}$$

in the case of an asymptotic speed $v_a = 418.7\,\mathrm{km\,s^{-1}}$ when $r - r_1 >> r_a$ with $r_1 = 4.5\,R_\odot$ and $r_a = 15.2\,R_\odot$. Analysing 11 type III radio bursts (see Sec. 2.2.3) observed with the radio experiment WAVES onboard the WIND satellite in the declining phase of solar cycle 22, Leblanc, Dulk, and Bougeret (1998) were able to determine a distance dependent model on the number density of free electrons starting at heights of $1.8\,R_\odot$ in the corona up to 1 AU. By assuming that proton and electron densities are essentially equal in the solar wind and adding a normalisation factor, ensuring that the model matches the averaged number density measured near Earth in times of the solar minimum ($7.2\,\mathrm{cm^{-3}}$), the model is given by

$$n_w^{\mathrm{Leb}}(r) = \frac{n(r = 1\,\mathrm{AU})}{7.2} \left(\frac{k_1}{r^2} + \frac{k_2}{r^4} + \frac{k_3}{r^6}\right) [\mathrm{cm^{-3}}]. \tag{2.3}$$

Equation 2.3 represents the average proton number density of the solar wind $n_w(r)$ with the coefficients $k_1 = 3.3 \cdot 10^5$, $k_2 = 4.1 \cdot 10^6$, $k_3 = 8 \cdot 10^7$ and r is in $R_\odot$. By assuming flux conservation, the solar wind speed can be expressed with:

$$w^{\mathrm{Leb}}(r) = w(r = 1\,\mathrm{AU}) \left(1 + \frac{k_4}{k_2 r^2} + \frac{k_6}{k_2 r^4}\right)^{-1}, \tag{2.4}$$

in which the simplification of $w(r = \infty) = \lim_{r\to\infty} w(r) = \mathrm{const.} = w(r = 1\,\mathrm{AU})$ for the asymptotic solar wind speed $w(r = \infty)$ was used. Future and ongoing missions, like the NASA's latest addition to the heliosphysics space fleet, *Parker Solar Prope* (PSP) (Fox *et al.*, 2016) (launched on the 12^{th} of August 2018), which will reach in its closest perihelion a minimum distance of $9.86\,R_\odot$ being the satellite flying closer to the Sun than ever before, and ESA's *Solar Orbiter* (Müller *et al.*, 2013) with an orbit inclination between 25° and 36° (depending on the exact launch date) will provide the next generation of in-situ measurements. In order to predict the solar wind characteristics at PSP's perihelia, Venzmer and Bothmer (2018) determined an empirical model for the inner heliosphere including solar activity based on the OMNI2 dataset (King and Papitashvili, 2005), which is a combination of near Earth in-situ measurements of different satellite missions since 1963. Furthermore, the calculated frequency distributions distinguish between the fast and slow states of the solar wind. The extrapolation down to the low distances of the PSP perihelion in the corona is performed by the use of Helios data, and the obtained power laws for number density and velocity are

$$n_w^{\mathrm{Ven}}(r) = n(r = 1\,\mathrm{AU}) \cdot r^{2.093}, \tag{2.5}$$

$$w^{\mathrm{Ven}}(r) = w(r = 1\,\mathrm{AU}) \cdot r^{0.058}. \tag{2.6}$$

Table (2.3) List of basic solar wind parameters measured with the Helios 1 and 2 spacecraft (Rosenbauer *et al.*, 1977). The proton flow speed v_p is given as range while density n_p, total magnetic field strength $|B|$ proton and electron temperature T_p and T_e are given as averaged and normalised values at a distance of 1 AU using a $1/r^2$ law (Schwenn and Marsch 1990 and Bothmer and Daglis 2007, p.39).

Type	v_p in [km/s]	n_p in [1/cm³]	$\|B\|$ in [nT]	T_p, $T_{\mathbf{He}}$, T_e in [10^4K]	**Abundance** H, He, Metals
slow	>300 to ∼450	8.3	∼4	3.4, 17, 13	∼94%,∼4%, ∼2%
fast	>450 to ∼800	2.7	∼5	23, 73, 10	∼95%,∼5%, <1%

Also the distribution of magnitude and orientation of the magnetic field transported by the solar wind, as well as its electric field, are of great interest. Since our planet generates a magnetic field too, the interaction between this three fields is known as *goemagnetic activity*. The IPM drives a complex system of currents in Earth's iono- and magnetosphere, whose main components are the *polar auroral electrojets* and the *equatorial magnetospheric ring current*. While the electrojet currents consist mainly of free electrons moving in the auroral oval along the magnetic field lines with $\sim 10^6$ A into the ionosphere, the ring current is formed by trapped ions coming from injections of the ionosphere and the solar wind (Daglis *et al.*; Bothmer and Daglis 2007, p. 40-42). Variations in the particle flux of the solar wind cause the magnetosphere to respond, the currents move up and down until flow pressure and magnetic pressure are balanced again. This process happens frequently due to the high variability of the solar wind and ensures, that by the never off breaking particle flux, a constant compression on the dayside magnetosphere, while the night-side shapes a long tail. If IMF and Earth's magnetosphere are orientated antiparallel, reconnection happens not ony in the dayside, but also in the night-side magnetosphere accelerating trapped ions and electrons from the tail to the poles. Strong events with high velocities or strong antiparallel magnetic field ($-B_z$) induce the electric field $E = v \times B_z$ and drive *geomagnetic storms*. The induced currents act in the whole magnetosphere down to the ground, and interact with every long artificial conductor like power grids, pipelines and rails. Especially in power grids, the additional high voltage induced from a geomagnetic storm can lead to an overloading of transformers. The most prominent example for such an event was the storm in March 1989 causing the *Quebec blackout* in Canada (Lang 2009, p.339-340).

2.2.3

2.2.3 Coronal Mass Ejections

Solar flares are often, but not always, accompanied by the ejection of coronal plasma bound in large magnetic structures, the so-called *coronal mass ejections*. Containing masses around $10^{11} - 10^{13}$ kg (Vourlidas *et al.*, 2010) and propagating with speeds from a few tens to more than 2500 km s^{-1} (Webb and Howard, 2012) into the heliosphere, CMEs show enormous lateral expansions. While most of the ejected solar plasma originates from the low corona, cooler and denser material coming from prominences having their seeds in the photosphere and chromosphere were also observed (Burlaga *et al.*, 1998). Often they come along with filament eruptions (FEs, see Section 3.1.2), post eruptive arcades (PEAs, see Section 3.1.1), shocks or particle events (see below) implying relations in the deeper physical processes (Webb and Hundhausen, 1987). Observations of the two STEREO spacecrafts of CMEs from different viewpoint are shown in Figure 2.9. The structure of CME 1 includes a bright filament, while CME 2 appears diffuse. The averaged CME frequency varies like other activity related phenomena in amplitude and phase with the solar cycle from 1 d^{-1} in solar minimum to 5 d^{-1} at solar maximum, and shows the same two maxima developments as the sunspot number (Gopalswamy *et al.*, 2005, 2006). Like the solar flare occurance, the CME frequency is shifted compared to the solar cycle but only by months and not years.

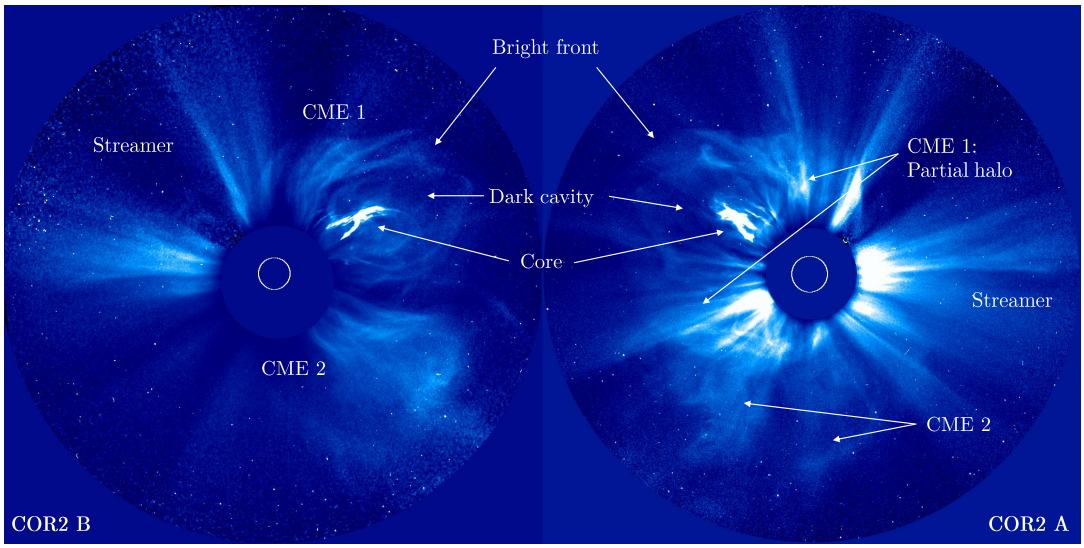

Figure (2.9) Observations of the SECCHI/COR2 coronagraphs onbord the STEREO A (right) and B (left) spacecraft. The images were taken on November 9, 2011 14:54 UT, and show two CMEs. Data provided by NASA and processed with IDL Solarsoft (see Chapter 4.2.2).

Earth-directed CMEs are the most geoeffective solar phenomena (Bothmer and Zhukov, 2007; Baker *et al.*, 2008). Based on their high speeds combined with strong magnetic fields, which they transport with them, they are leading to distortions in Earth's magnetosphere as already discussed in Section 2.2.2. CMEs do not emit radiation by themselves but are visible through Thomson scattering (see Section 3.4.1) of sunlight by free electrons as it is also the case for coronal material. Using *coronagraphs* (further explained in Chapter 4.1.4) blocking the light of the photosphere and applying background substraction techniques

Table 2.4. Comparsion of different CME catalogues. Widths in the COR2 and KINCAT catalogues are the GCS angular widths ω_{FO} (see Sec. 3.4.2). The Multi-viewpoint Coronal Mass Ejection Catalog (MVC) is divided into events observed with the STEREO spacecrafts A and B (see Sec. 4.1.1). It is important to note, that the large differences between the LASCO and the KINCAT catalogues originate from the different selection criteria. While the LASCO data are means of every in C2 or C3 detected CME, the KINCAT events were selected to be the brightest and best analysable events of the COR2 catalogue.

Catalogue	**LASCO**[a]	**COR2**[b]	**KINCAT**[c]	**MVC-A**[d]	**MVC-B**[d]
# of Events	>10000	243	122	1101	646
Speed [km/s]	489	553	629	427	496
Width [°]	47	89	93	50	47
Mass [10^{15} g]	1.3		13		
kin. Energy [10^{23} J]	2.0		69		

[a] Speed: Webb and Howard (2012), mass and kin. energy: Vourlidas *et al.* (2010, 2011).
[b] Bosman *et al.* (2012)
[c] Pluta *et al.* (2018)
[d] Vourlidas *et al.* (2017)

in order to remove the bright scatterd light of the corona, the much fainter CMEs are detectable in white-light images. Owning to the fact of their faint coronal signatures and the appropriated high technical effort necessary to observe them, CMEs were discovered lately compared to other solar phenomena. The first observations of CMEs were made with space borne coronagraphs onboard the OSO-7 and Skylab covering solar heights of $2.8 - 10\,\mathrm{R}_\odot$ (Koomen *et al.*, 1975) and $1.5 - 6\,\mathrm{R}_\odot$ (MacQueen *et al.*, 1980) in the early 1970s (Tousey, 1973; Tousey, Howard, and Koomen, 1974; Gosling *et al.*, 1974).

Enhanced space borne and ground based instruments were developed over time to measure the basic characteristics of CMEs. Analogue to star surveys, event catalogues of identified and measured CMEs were produced (e.g. the HELCATS catalogues[3], for more details see Chapter 4). In Table 2.4 some example catalogues, differing in the usage of viewpoints as well as selection and identification criteria, with their averaged CME properties are listed. For a long time, coronagraphs were positioned along the Sun-Earth connection line, more precise in an Earth orbit or in L1, allowing only observations from one perspective and analysis in the *plane of sky* (POS), which represents the image plane orthogonal to the observer line. As consequence one important parameter for characterisation is the CMEs angular width in the POS, also sometimes referred as position angle range Δpa. CMEs spanning a wide angular range around the solar disk appear larger by perspective because their component along the observer line is larger. These events are called *partial halo* CMEs if they have a $\Delta pa > 120°$ (e.g. in Figure 2.9) and *full halo* (or simply *halo*) events if they envelope the full solar disk.

[3] https://www.helcats-fp7.eu/products.html (13.12.19)

The determined kinematic quantities and masses span a range over 2-3 orders of magnitudes while the angular widths of the ejection can exceed by factors between 3 and 10 the width of the corresponding active region on the solar disk (Vourlidas *et al.*, 2002; Yashiro *et al.*, 2004). The general morphology of a CME is described by the classical "three-part" structure, visible in Figure 2.9 (Low, 1996; Cremades and Bothmer, 2004). It is formed of a bright leading front curved in a loop, whose footpoints are anchored at the solar surface, followed by a dark cavity, which encloses a bright core containing prominence material (Fisher and Poland, 1981; Illing and Hundhausen, 1985). This structure is explained in terms of a magnetic FR, sketched in Figure 2.10, depending on the SR polarity orientation, as well as the hemispheric helicity (Bothmer and Schwenn, 1998). Since Riley *et al.* (2008) showed in MHD simulations the belonging of the FR to the dark cavity, the bright front is interpreted as mass compression of the ambient material ahead of the FR. This picture was further confirmed by the findings of Vourlidas *et al.* (2013) and Vourlidas (2014). Despite the majority of CMEs having a FR structure, there are some exceptions observed with much more complex and distorted geometries. Deforming and disturbing factors are for example: pre-existing coronal streamers at lower heights or coronal holes, and, at larger distances, the interaction with the ambient solar wind. Furthermore, Bothmer and Mrotzek (2017) showed that the overall 3D configuration depends on the geometry and complexity of the corresponding active region, whose substructures expand with the CME as well.

Single viewpoint observations are strongly affected by projection effects in the POS of the imaging instrument, having significant influence on the CME appearance in a coronagraph and, on a account of this, on the determined kinematics (Cremades and Bothmer, 2004). This uncertainty due to a single perspective led to misconceived results in past studies, which was reduced only after multi-viewpoint observations have been made available (see Chapter 4). CMEs observed in the heliosphere with solar distances of $\gtrsim 50\,\mathrm{R}_\odot$ are called *interplanetary coronal mass ejections* (ICMEs) for historical reason. By their passage of satellites having in-situ instruments onboard, important ICME parameters complementaring white-light observations can be measured. An ICME in-situ signature, as illustrated in Figure 2.10, contains, if it is super sonic, an interplanetary shock in front of a sheath region followed by a *magnetic cloud* (MC) (Burlaga *et al.*, 1981; Goldstein, 1983). MC measured at 1 AU have been identified as the CME's FR (Bothmer, 2003) and are identified in in-situ data by the following criteria:

- The direction of the magnetic field rotates by a large angle in a time range of one day parallel to a plane.
- The average magnetic field in the time range of the rotation is stronger than the average field of the solar wind.
- The average temperature in the time range of the rotation is lower than the average temperature of the solar wind.

Shock and sheath region can be separated from the solar wind by the abrupt rise in density, velocity and absolute strength of the magnetic field followed by strong fluctuations of B representing the compressed plasma. The clarity of the magnetic FR topology may depends on the track of the instrument through the expanded ICME moving past it. In a perfect hit close to the ICME's core as can be seen by the trajectory of spacecraft $\mathrm{S/C}_1$ in Figure 2.10, the magnetic field will rotate according to the helical nature of the FR

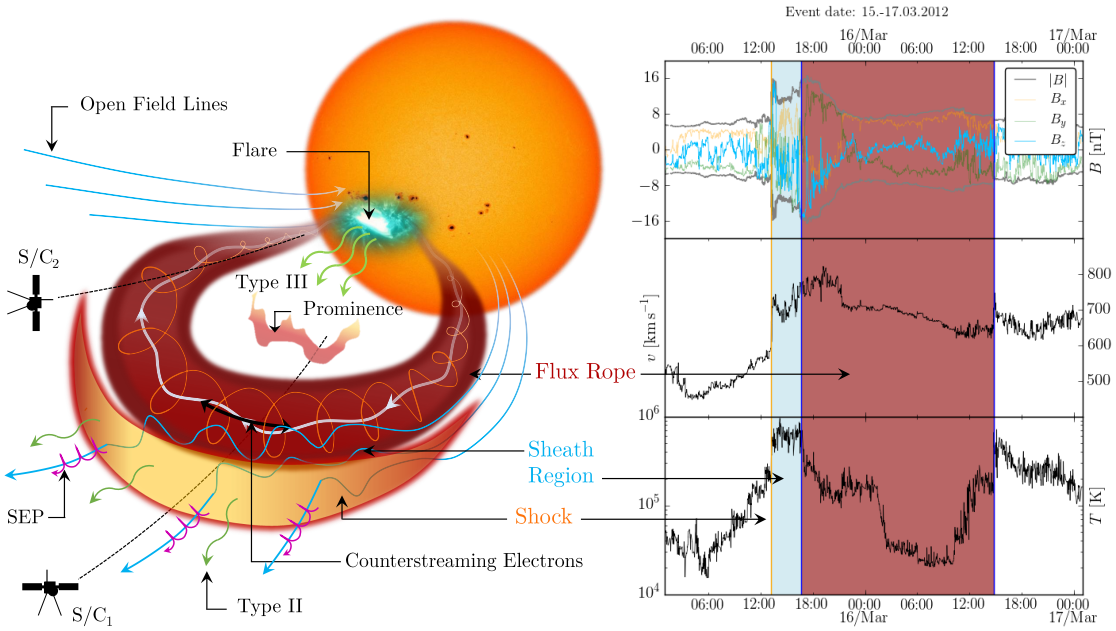

Figure (2.10) Schematic view of the structure of an ICME. On the right, a FR-ICME with shock and prominence is illustrated. On the left, the corresponding in-situ measurements (OMNI 1min data provided by Goddard Space Flight Center[4]of an Earth-directed event in March 2012 were taken) containing the magnetic field components, speed and temperature are plotted. Two spacecraft trajectories, S/C_1 and S/C_2, are marked by the black solid lines. The plotted in-situ measurements corresponds to the trajectory of S/C_2. Other possible occurring space weather effects associated with CMEs are included. After Zurbuchen and Richardson (2006).

while at the same time the flow speed constantly decreases. A hit at the flanks or legs (S/C_2) is followed by a long lasting detection of a more constant magnetic field (Marubashi *et al.*, 2015). However, other plasma parameters are used to indicate the measurement of an ICME. In general, enhanced abundances of metals and helium compared to the solar wind as well as low proton and electron temperatures are observed in-situ with some ICMEs (Richardson and Cane, 2010). As a consequence of the FR configuration, counter streaming electron beams measured parallel and anti-parallel to the magnetic field of an ICME, flow along the closed field lines connected with the Sun (see Figure 2.10).
White-light observations as well as in-situ measurements confirm the FR nature of CMEs (Vourlidas *et al.*, 2013). Therefore it is logical to assume also a eruption model including magnetic FRs. However, the connection between solar source regions, which provides the magnetic field, and the CME kinematics is a problem, that disadvantages by the lack of observations in the early stages of CMEs in which the magnetic energy is transformed. Nevertheless different trigger mechanisms were developed over time. They are discussed together with the solar source region properties of CMEs and their kinematics in more detail in Chapter 3.

[4]https://cdaweb.sci.gsfc.nasa.gov/index.html/ (13.12.19)

2.2.4 Solar Energetic Particles

Besides cosmic rays, the Sun is also a source of high energetic particles, which are related with CME and flare events. While cosmic rays rain isotropically down to Earth, *solar energetic particles* (SEPs) travel along the field lines of the IMF. SEPs are in general not as energetic as their cosmic counterparts, but their flux is several orders of magnitude larger. The composition of SEPs reflects that of the solar wind, an consists mainly of protons, electrons, helium and few heavy ions up to iron, but in contrast they move with near-relativistic speeds responsible for their high energies. Depending on the nature of the accelerating process, protons and electrons can reach energies of up to 20 GeV respectively 100 MeV (Lang 2009, p. 345-346). SEP events are categorised by their temporal energy profile, based on their acceleration sites and basic composition, into *gradual* and *impulsive* events. Their basic characteristics are compiled in Table 2.5.
Impulsive SEP events are associated with short lasting impulsive flares on the scale of minutes, while gradual events follow long duration soft X-ray emissions and are, in the majority of cases, accompanied by fast CMEs. Both classes are linked with different types of radio bursts, which are characterised by the drift frequency of radio emissions (see Wild, Smerd, and Weiss 1963). Type III radio bursts, created by electron beams with energies of $1 - 100$ keV (Howard, 2011) propagate from reconnection sites of flares rapidly along open magnetic field lines into the slower electrons ahead of the IPM (Wild, 1950). They are short-lived phenomena spanning a frequency range of 10 kHz to 1 GHz, and are linked to impulsive events (Reid and Ratcliffe, 2014). Gradual events are accelerated by shockwaves, and occur with Type II bursts emitted near the electron plasma frequency by accelerated electrons driving Langmuir waves (Cairns *et al.*, 2003). Main source for shockwaves near the Sun are super-Alfvénic CMEs propagating faster than the ambient solar wind. During solar maxima impulsive events occur with a rate of $\sim 1000\,\mathrm{a}^{-1}$, and are thus 10 times more frequently than gradual events (Bothmer and Daglis 2007, p. 144). SEPs have not necessarily to originate directly from the solar atmosphere but it is also possible

Table (2.5) Observational properties of impulsive and gradual SEP events. Adapted from Gosling (1993) and Reames, Kahler, and Ng (1997).

		Impulsive events	**Gradual events**
Acceleration site		Flares	Shocks
X-Ray Observations		Hard	Soft
X-Ray duration		Minutes	Hours
Radio bursts		Type III (V)	Type II (IV)
Events linked with CMEs			96%
Rate [a^{-1}]		1000	100
Duration of SEP event		Hours	Days
Abundance	Particles	Electron-rich	Proton-rich
	He/He	~ 1	~ 0.0005
	Fe/O	~ 1	~ 0.1
	H/He	~ 10	~ 100

that particles of the IPM can be accelerated by the electric field generated between fast and slow solar wind streams in *co-rotating interaction regions* (CIRs) (Aschwanden 2005, p. 736). Further outward in the heliosphere, shocks driven by CIRs can also accelerate particles (Barnes and Simpson, 1976).

SEPs pose to be a major threat to humans. In unprotected environments, outside the terrestrial magnetosphere, the radiation dose of a strong event exceeds limiting values, not only causing serious health hazards but also, in the worst case, beeing deadly. In a space exploration age in which manned missions to Mars, or even further away, are becoming of interest to the society, SEPs are of increasingly relevance. Even if the magnetosphere is protecting us, high energy protons with > 1 GeV are able to spiral down the magnetosphere and to produce secondary particles, which are able to reach ground level. Lower energy protons penetrate the atmosphere in polar regions down to altitudes of air routes and increase the radiation received by airplane crews and passengers (Lang 2009, p.364). Also scientific imagers in space are affected by particle showers making them blind for hours if SEPs hit the detectors and over-saturate the pixels.

2.3 Summary

This chapter has presented in parts which role the Sun played in our history. Understanding the mechanisms driving the solar activity is not only important to satisfy our curiosity, but also for better knowledge about the Sun-Earth connection. In more than 400 years of telescope-based observations, a lot of discoveries were made, and the Sun lost some of its myths. The different space weather phenomena interact on a wide range with Earth's environment, affecting space missions and life on Earth. While the discussed phenomena and their connections to each other are summarised in Figure 2.10, Table 2.6 concludes their impacts and transit times (TT) from the Sun to a distance of 1 AU. Since the TT of solar flares and SEPs are in the range of minutes, they do already arrive at Earth when they are detected. Therefore, forecasting and warning of them is very difficult, or nearly impossible. Dealing with non-relativistic speeds and consequently TT within days, allow for a different treatment of CMEs and solar wind observations.

Table (2.6) Comparison of the properties and transit times to Earth's orbit for different activity phenomena and their space weather impacts.

	v [km s^{-1}]	**Frequency**	**TT**	**Impact**
Solar Wind	300-800	continuous	3-5 d	Interaction with Earth's Magnetosphere. Geomagnetic storms.
Flares	c	1-20 d^{-1}	5-8 min	Ionising radiation and radio blackouts.
CMEs	20-2500	1-5 d^{-1}	12 h-4 d	Geomagnetic storms.
SEPs	~ 0.8c	100-1000 a^{-1}	20-30 min	Radiation hazard. Damage on electronics.

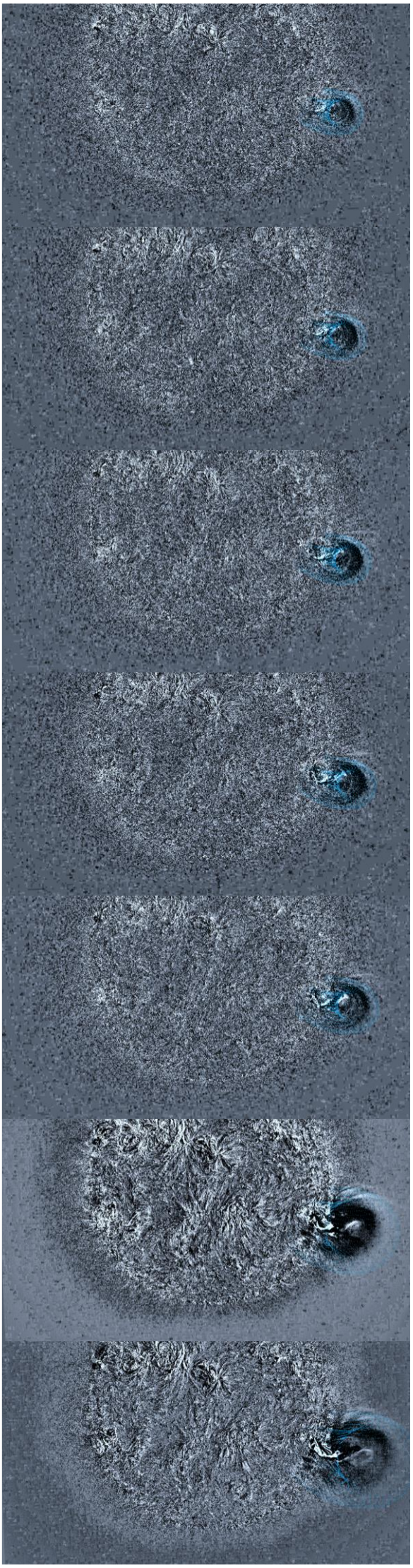

Chapter 3

Theories and Observations of the CME Evolution

"My young friend, I wish that science would intoxicate you as much as our good Göttingen beer."

Carl F. Gauss

In order to analyse the kinematic properties of a CME, the knowledge about its source, the driving forces and the influences of the ambient medium, where the CME propagates through, is fundamental. In this chapter, the connection between the CME source region and the CME parameters describing its kinematics, are pointed out. Beginning with the characteristics of active regions and activity phenomena accompanying a CME event, the early stages of a CME including the theoretical triggering mechanisms are introduced and explained in more detail. The discussion focuses on the theoretical background needed for the data analysis of this work. This includes CME SR properties, propagation models, namely the torus instability model and the aerodynamic drag model that describe the CME trajectory close to the Sun and throughout the heliosphere. Finally, the theoretical basics, needed for the observation of CMEs and to measure their characteristics are described.

Cover Figure: Time series of STEREO SECCHI/EUVI 195 B observations at a wavelength of 195 Å of event #1 (see Table 4.2. The modelled GCS fit is shown by the blue grid.

3.1 CME Source Regions

By observing CMEs with coronagraphs, whose occulters cover the lower solar atmospheres, its initiation and the exact location of the solar source region can not be identified with them. However, according to the observed CME orientation in space and its projection onto the solar surface, it is generally believed that CMEs originate from bipolar and also more complex magentic configuration onto the photosphere. Locating the exact photospheric source regions of CMEs is a non-trivial problem for several reasons. First of all, it is a problem of temporal-, spatial- and spectral scales. While the photospheric magnetic field changes on timescales of several hours, the CME's initial acceleration phase takes place over a timescale of minutes up to $\sim 1\,\mathrm{h}$ (Subramanian and Dere, 2001). For the majority of CMEs, the acceleration phase occurs within the first $2\,\mathrm{R}_\odot$ (Webb and Howard, 2012). The impulsive release of the magnetic energy results in a fast expansion of the atmospheric structures, requiring observations at high temporal cadence and covering a large *field of view* (FOV), which is from the practical and technical part hard to realise. In order to trace the whole process, from the formation of the CME's FR to its eruption, observations in several EUV wavelengths have to be compared with coronagraphic white-light images to identify same features of the erupting structure. Often this is not possible, mainly because of the faint CME features compared to the Sun's bright atmosphere. Although, the exact 3D shape and orientation of a CME is often not unambiguously determinable. If multi-viewpoint observations are available, the separation angle of the observers has to be large enough to get additional 3D information and to minimise projection effects. Furthermore, the observed heliospheric coordinates of the CME's apex are not strictly constant during its propagation within the FOV of the coronagraph. Deflection of a CME can already start within the first solar radii leading to a false projection in longitude and latitude back onto the solar surface.

The CME onset must include a runaway process moving the magnetic structure, that will become the CME, out of equilibrium with the overlying and surrounding field. In most theoretical models this is done by magnetic reconnection, which releases 10^{32} ergs (Forbes *et al.*, 2006). As mentioned in the previous chapter, CME eruptions are accompanied by other forms of solar activity able to remove the free magnetic energy out of the system. The predominant energy release is of mechanical nature caused by the acceleration of the CME and a probably expanding filament. Around half of the energy release by reconnection is transformed into kinetic energy (Forbes *et al.*, 2006). Other forms are electromagnetic emission in a broad wavelength range by flares or the acceleration of SEPs, as well as the reconfiguration of the magnetic field visible through PEAs. All these effects are closely linked with the CMEs and provide additional information about the source regions and the magnetic processes driving the eruption. Several studies, which differ in the number of analysed events and phase in the solar cycle, associated CMEs with other activity phenomena to determine their corresponding solar source regions. Munro *et al.* (1979) used Skylab observations from 1973-1974 close to solar minimum, and reported that 40% of the observed CMEs are related to flares while 70% are associated with FE. Near solar maximum in 1980, 68% of the CMEs analysed by Webb and Hundhausen (1987) were observed with FE, 47% with X-ray flares and 37% with Hα flares. Another study by Subramanian and Dere (2001) using mainly SOHO data from 1996-1998 (from solar minimum to the rising phase) showed that 41% of their CME set belongs to AR,

44% to FEs embedded in ARs and 15% to FEs outside of ARs. Within the HELCATS (see Chapter 4) project, an automated back-propagation algorithm has been applied on the HICAT CME catalogue containing $\sim$ 2000 events to identify the associated source regions. Nearly 45% of the CME events were related to flares (Murray *et al.*, 2018). In the following sections, the main characteristics of this features are presented.

3.1.1 Active Regions

The definition of active regions evolved in time thanks to the availability of observational windows complementary to the visible wavelength regime. Since a long time, ARs are clearly identified with the presence of sunspots, which is still the criterion for the National Oceanic and Atmospheric Administration (NOAA) to assign a number to an AR. However, Kiepenheuer (1968) defined an AR as:

> The totality of all observable phenomena preceding, accompanying and following the birth of sunspots including radio-, X-, EUV- and particle emission.

In this definition *sunspots* is nowadays associated with *magnetic fields* due to the knowledge obtained within the last decades. However, the classification system introduced by Hale *et al.* (1919) (formally known as the *Mount Wilson classification system*) allocates the observable appearance of sunspots to the overall magnetic configuration of magnetic flux and sunspots in an AR. The great advantage of the Hale classes over more complex systems is, even though it depends highly on the subjective perception of symmetry of the observer, that it is adequately universal to describe nearly every appearing AR. The classes are divided into the three main classes: (α), (β) and (γ). (α) is referred to single sunspots or a sunspot group in which only one polarity is present (the corresponding opposite polarity is not concentrated enough to form a sunspot). Bipolar ARs with a simple separation are of type (β). If an AR contains negative and positive polarities irregularly distributed in a way that classification as a bipolar group is not possible, it is of class (γ). Also the combined class of (β-γ) is possible. It is a bipolar group, sufficient disordered in polarity that no single line between the centres of polarity can be drawn. Künzel (1965) introduced the appendix of the (δ)-class, which is assigned to ARs containing umbrae that are separated by $< 2^\circ \sim 24\,\mathrm{Mm}$ with at least one penumbra having opposite polarity. It can be added as enhanced scheme describing more complex regions; (β-δ), (β-γ-δ) and (γ-δ). Jaeggli and Norton (2016) studied the appearance of the different classes for a time interval of nearly one Hale-cycle (1992-2015) concluded that the total (α) and total (β) ARs, including the (γ) and (δ) appendix, make up 20% respectively 80% of all occurring ARs over almost the whole solar cycle, except a short period during the solar minimum, with 35% and 65%.

By observing the hot plasma over sunspot groups in EUV or X-ray wavelengths, ARs appear as bright islands in the chromosphere and lower corona. In magnetograms the full photospheric extension of ARs becomes visible and the total flux of one region can reach more than $10^{20}\,\mathrm{Mx}$ (van Driel-Gesztelyi and Green, 2015). The concentrated magnetic field in ARs can be seen by plasma upflows, which are a consequence of heating in the chromosphere, following the field lines and acting in this way as a tracer. Numerous hot and dense plasma loops, the so called *coronal loops*, form and are much brighter than the background corona. Coronal loops are build up as a consequence of the much less than

unity ratio between thermal pressure $p_{\rm th}$ and the magnetic pressure $p_{\rm B}$, which is defined as the *plasma-*β, implying the inhibition of plasma movements perpendicular to the magnetic field. Their photospheric footpoints are sunspots usually of bipolar - in active times also of more complex multi-polar - nature resulting into primarily closed field lines in ARs. Most of the solar activity happens in ARs and the chromospheric upflows provide $\sim 80\%$ of the thermal energy necessary for the coronal heating (Aschwanden, 2001). Today, it is commonly accepted that bipolar ARs are formed by buoyant FRs breaking through the photosphere. As discussed in Section 2.1.3, these FRs are believed to be generated by the dynamo processes in the tachoclyne and stay anchored in it during the emergence phase, which is why they are also called Ω-loops (Zwaan, 1987). Being parts of the toroids, which are produced by the transformation of a poloidal into a toroidal field, the loops form at every penetration point two flux regions of different polarity building one AR. In this way several ARs can be formed by a single toroid (Rust, 1994), while every buoyant FR is influenced by the Coriolis force, magnetic tension, plasma vortices, hydrodynamic as well as MHD drag and large-scale convective motions (van Driel-Gesztelyi and Green, 2015).

As discovered by Hale *et al.* (1919), the bipolar axis of ARs shows systematic tilt angles with respect to the solar equator, a property of Joy's law (see Section 2.1.3). The exact physical processes of this fundamental observation is controversially discussed since it was first published. There are two basic effects that could be responsible for it. Already Babcock (1961) has argued that the generated toroidal field by the Ω-effect of the solar dynamo would not be perfectly toroidal and a poloidal component would remain. Consequently a small angle to the pole would retain in a toroid. He proposed also that the convective motion of uprising plasma around an AR is additional affected by the Coriolis force, which introduces a tilt angle as well. In contrast, Wang and Sheeley (1991) suggested that the buoyant FR itself is affected by the Coriolis force, while Leighton (1969) considered deformed kinks of the twisted FRs responsible for the observed tilt. McClintock and Norton (2013) considered in their study the possibility of a combination of both effects. The dependency of an AR's tilt angle $\Gamma_{\rm AR}$ to the latitude θ of the AR was found by Wang and Sheeley (1989, 1991) to be:

$$\sin(\Gamma_{\rm AR}) = 0.48\cos(\theta) + 0.03. \tag{3.1}$$

Furthermore, they noted that lower-total-flux ARs show larger tilt angles and their averaged values scatter wider compared to the tilt angles of stronger ARs. Other quantities contributing to the general scatter in the tilt angle could be identified to be the age, size, length of the neutral line (also referred as polarity inversion line (PIL) or magnetic inversion line), distance to centre of the butterfly diagram and the magnetic twist of the AR (Harvey, 1993; Fisher, Fan, and Howard, 1995; Holder *et al.*, 2004). For example, the bipolar axis is at first randomly orientated and becomes organised within the first days.

Another characteristic quantity of an AR is the separation of the polarities. Analysing 2700 bipolar ARs of cycle 21 (1976-1986), Wang and Sheeley (1989) found the connection between the magnetic flux f of leading spot and the polarity separation $L_{\rm BSP}$ to be:

$$f(L_{\rm BSP}) = 4 \cdot 10^{20}\,{\rm Mx}\;\; L_{\rm BSP}^{1.3}, \tag{3.2}$$

where f is in Maxwell and $L_{\rm BSP}$ in units of heliographic degrees. In good agreement with these results, the correlation determined by Tian, Liu, and Wang (2003) between magnetic flux in 10^{20} Mx and and the polarity separation in Mm is $f_{20} \sim L_{\rm BSP}^{1.15}$. The evolution of

the polarity separation over time is a relatively poorly analysed process, but nevertheless, there is a lag between the peak time of the magnetic flux and the peak separation distance (van Driel-Gesztelyi and Green, 2015).
There are several proxies for the free magnetic energy of an AR. Falconer, Moore, and Gary (2008) introduced the weighted integral over the length of the strong-gradient main neutral line WL_{SG} that is defined as:

$$WL_{\mathrm{SG}} = \int |\nabla B_z| dl, \tag{3.3}$$

in which $|\nabla B_z|$ represents the horizontal gradient of the AR's vertical magnetic field (Tiwari *et al.*, 2015). To calculate WL_{SG}, Equation 3.3 is integrated over all PILs within an AR, which separate opposite polarities with a cutoff of 20 G in the moderate field strength and 150 G in the horizontal potential field (Falconer, Moore, and Gary, 2008; Tiwari *et al.*, 2015). Another proxy is the Schrijver R value, which is a measure of the amount of flux close to the PIL (Schrijver, 2007). It is calculated with strong-gradient-neutral-line pixel maps from magnetogram data that are convolved with a 15 Mm Gaussian to get the unsigned flux of this area. For more details, see Schrijver (2007).

Newly emerging ARs are born into an environment, in which older ARs are already present. They emerge twisted and transport magnetic helicity as well as free magnetic energy from the solar interior outside (Leka *et al.*, 1996). Therefore the interaction between new emerging flux and pre-existing flux plays an important role in the evolution of an AR affecting significantly their lifetime. AR CMEs are often attributed to changes in the magnetic field configuration over timescales of several hours. These are in general caused by the emergence or cancellation of magnetic flux due to process in or under the AR (or even under the photosphere), but also by the interaction between neighboring ARs or growing parasitic polarity fields (Subramanian and Dere, 2001).

Flux cancellation

Flux cancellation is the disappearance of magnetic fields with different polarities along the PIL and provides another mechanism to form a FR. The process of flux cancellation is outlined in Figure 3.1 and is interpreted as the submerging, annihilation or the expelling into higher regions of magnetic flux through reconnection. Like its emergence, the cancellation of flux might occur not only in ARs but anywhere where fields of opposite polarity are pushed together: at PILs separating an AR from opposite polarity regions, outside of ARs in ephemeral regions or at filament sides, too (Livi, Wang, and Martin, 1985; Martin, Livi, and Wang, 1985; Wang, 2001). As the AR evolves, convective flows and the effect of differential rotation lead to a fragmentation and spatial extent of the magnetic flux. Opposite magnetic polarities "collide" along the PIL and disappear in LOS magnetograms. The reconnection between two magnetic field lines in the lower atmospheric layers removes magnetic flux from the photosphere and creates new field lines crossing the PIL, one long loop nearly parallel to the PIL and one shorter loop perpendicular to it (Figure 3.1d red and blue lines), but with new footpoints. Depending on the height in which the initial reconnection happens, the smaller loop could submerge or the longer one could rise. As flux cancellation continues, more and more sheared magnetic field concentrates above the PIL and a FR is formed which is the basic structure allowing cooler and denser material to form a filament. Potential fields are transformed by the process of flux

cancellation into non-potential fields providing the energy for the activity in a decaying AR (van Driel-Gesztelyi and Green, 2015). In MHD simulations it is shown that flux cancellation can lead to the formation of a FR (van Ballegooijen and Martens, 1989) and, as long as the cancellation process of a background field continues, a FR will be pushed higher, finally resulting in the loss of its equilibrium and the formation of a current sheet (Forbes, Priest, and Isenberg, 1994; Lin *et al.*, 1998). The aspect ratio of a current sheet is 1:100000 (e.g. a book page aspect ratio is $\sim 1:2000$) implying that this surface current has nearly no thickness. MHD 3D simulations by Linker *et al.* (2003) shows, that an erupting FR released through flux cancellation would reproduce white light observations made with coronagraphs. Indeed, several studies were able to connect the cancellation of magnetic flux directly to the eruption of CMEs (Lin, Raymond, and van Ballegooijen, 2004; Bothmer and Tripathi, 2007) or to the occurrence of flares (Livi *et al.*, 1989).

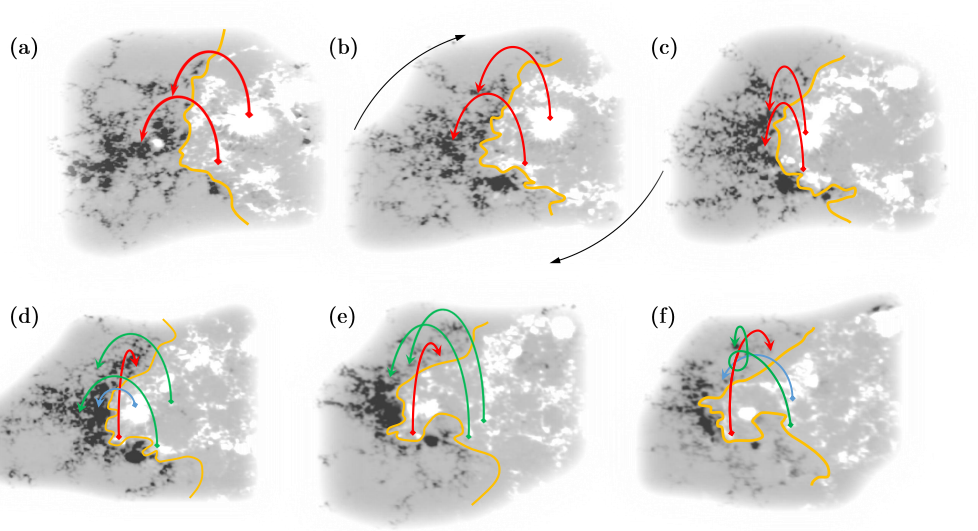

Figure (3.1) Pattern of the process of flux cancellation. From (a) to (c) magnetic field lines (red) of a bipolar active region are sheared by photospheric flows or/and the action of differential rotation (black arrows). Through magnetic reconnection (d) a long loop (red) nearly parallel to the PIL and a small one (blue) are formed. The process is repeated by overlying loops (green) in (d) to (f). As the region evolves and flows along the PIL (orange) continue, more and more field lines are pushed to the PIL. Further reconnection creates a FR winding up along the initial sheared field formed in (d).

Sigmoids

A special field configuration of ARs is a *sigmoid* structure, a S-shaped field geometry which is a result of the shearing of a dipole field. An example of a sigmoidal structure is illustrated in Figure 5.15. Because of the differential rotation, being fastest at the solar equator, the direction of a sigmoid's curvature depends on the hemisphere where the AR is located. The normal S-shape occurs at the southern solar hemisphere while the reverse S-shape is only observable at the northern hemisphere. The formation of sigmoids takes place in three phases (van Ballegooijen and Martens, 1989). In phase one, after the emergence of the AR, flux diffusion and cancellation cause an increase of shear. Due to the

build-up of flux flowing parallel to the PIL in combination with remaining, not cancelled in phase one, flux , two "J's" on both sides of the polarities are formed, marking phase two. In the last phase, the continuously flux cancellation generates twisted field lines along the PIL having a poloidal field component and giving the AR the S-shape. Therefore, it is possible to determine the magnetic helicity of the AR with the shape of the sigmoid. While the S-shape is a sign for positive helicity (right-handed), the inverse stands for negative helicity (left-handed) (Palmerio *et al.*, 2017). Sigmoids provide free magnetic energy for a flare or an eruption because their non-potential magnetic fields have larger excess energies than the potential field configuration (Aschwanden 2005, p.12). Canfield, Hudson, and McKenzie (1999) compared AR morphology and size showing that the S-shaped (also inverse S-shaped) ARs have a larger tendency to erupt than non-sigmoidal ARs and that there is a correlation to the AR size.

Post Eruptive Arcades

In the aftermath of a CME eruption, PEAs are frequently observed in EUV and soft X-ray wavelengths at the CMEs SR. They are a consequence of the magnetic reconfiguration and appear as newly forming post-flare loops. These loops rise slowly to higher altitudes with the reconnection side and along the PIL into the direction of the borders of the AR as it is shown in Figure 3.2. Not every CME eruption is accompanied by a PEA and sometimes they are connected with two ribbon flares. According to CME triggering models (Section 3.2.1), it is believed that PEAs are formed by the underside reconnection process which is followed by the CME eruption (Howard, 2011). Although PEAs are not part of CMEs, they are aligned similarly to the CME's FR because of their common origin, which was shown by Tripathi, Bothmer, and Cremades (2004a). The decay of ARs exhibits the decrease of magnetic flux density as well as the plasma temperature, emission and pressure (van Driel-Gesztelyi and Green, 2015). In this phase, filaments and flux ropes are formed through flux cancellation and the evolution of the AR, which favours the eruption of CMEs and/or filaments while the flare occurrence is rapidly decreasing with the magnetic flux density.

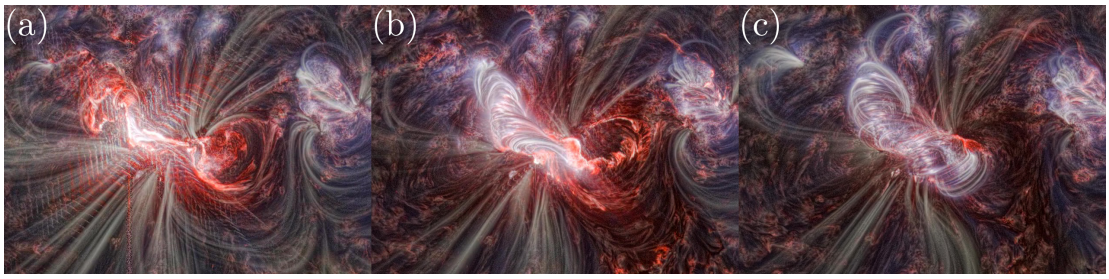

Figure (3.2) Example of a PEA observed with SDO AIA in March 7, 2012. The images are composites of AIA 171 Å, 211 Å and 304 Å and are processed with the PM-NAFE algorithm (Druckmüller, 2013). (a) X 5.4 flare emerging from AR 11429 at 00:17 UT. (b) and (c) PEA at the same region at 01:19 UT respectively 03:49 UT. Courtesy of Miloslav Druckmüller.

3.1.2

3.1.2 Filament Eruptions

A filament can be observed as dark variable line absorbing photospheric light. Also prominences are filaments but in difference they are observed as plasma outflows at the solar limb that emit light. As seen in the previous section, filaments can be formed by the magnetic evolution in ARs. However, the presence of a FR provides the *filament channel* which is filled by cooler and denser plasma. Hence, filaments can also form outside of ARs, for example in ephemeral regions or between ARs resulting in a strong variability on the length of filaments from a few thousand kilometres up to more than a solar radius (Rust and Kumar, 1994). The sudden disappearance of a filament by the eruption of the magnetic structure is called *filament eruption* (FE). There are three basic concepts how a filament's material is accumulated: *coronal condensation*, *footpoint injection* and *footpoint heating*. Condensation of coronal material occurs when radiative cooling is more efficient than thermal conduction and allows cool plasma to condensate in the filament channel. Since filaments have a mass of about $10^{13} - 10^{14}$ kg, coronal sources alone, without mass support from the chromosphere, would absorb with a few FE the corona and therefore pose an insufficient mass source. If a pressure gradient is present, cooler chromospheric material is injected through the footpoints by siphon flows into the filament channel. A siphon flow can also be established by an asymmetric heating at the footpoints. Tiny differences in the heating rate between the footpoints drive condensation at the looptop and cause the required pressure gradient. Because the magnetic field in filaments is mostly horizontally aligned, the measurement of its strength is, at least on the solar disk, not possible by using the Zeeman effect. In prominences at the limb, strengths around 10 G where measured (Athay *et al.*, 1983). A filaments magnetic configuration can be determined with relatively simple observational methods. Assuming that the filament channel, lying nearly parallel over the PIL, is covered by a loop arcade (e.g. between the different polarities of an AR) and using LOS magnetograms to identify the sign of the polarities, the direction of the filament axis and with it the current direction can be derived. Furthermore, by applying additionally the hemispheric helicity rule from Rust and Kumar (1994), stating that the chirality[1] of filaments is preferentially left-handed (right-handed) on the northern (southern) solar hemisphere, the complete overall magnetic topology of a filament is known.

Depending on the changes in the magnetic field configuration as well as the equilibrium between heating and cooling, filaments can be short-lived or remain stable for months, if magnetic fields prevents them from sinking down into the chromosphere by the gravitational pull (Priest, 1989). Thermal energy to unbalance a filament is transferred by absorption of UV radiation, dissipation of MHD waves or thermal conduction from the surrounding coronal material, whilst UV absorption provides the most efficient penetration depth for threaded filaments (Heinzel and Anzer, 2003). The sudden disappearance (also shortened DB for *disparition brusque* from french) marks the last stage of a filament when it erupts into the heliosphere. FE are strongly associated with CMEs and flares as shown by Feynman and Martin (1995), who correlated FE with emerging photospheric

[1] It should be noted that the magnetic chirality and helicity are representing both the topological structure of helical magnetic field. While the chirality gives a qualitative description of the handedness, the helicity is the volume integral of the magnetic field and is in this way a quantitative property. When analysing filaments it is also common to call left-handed filaments *dextral* and right-handed ones *sinistral* if they are seen by an hypothetical observer in the chromosphere.

flux and CMEs. As already discussed in Section 2.2.3, they are included in the bright core of the typical "three-part" structure observed in white-light images of CMEs. By analysing the MCs of ICMEs, it was shown by Bothmer and Schwenn (1998) that the FR magnetic helicities of erupting filaments associated with CMEs are for the overwhelming majority of cases identical to the corresponding in-situ measured MC. In their study they have clearly confirmed the FR nature of CMEs and developed a classification system in which the polarity and orientation of the FR reflects that of the SR filament and MC of the corresponding CME/ICME structure. According to this system, assuming the FR axis is lying in the ecliptic plane (*low-inclination* FR) and perpendicular to the line connecting the Sun and the spacecraft, FR are categorised in four basic types summarised in Figure 3.3. First of all, they are divided into left- and right-handed (LH, RH) FRs and second into the two possible directions of the axial field. The two LH possibilities are measured if the magnetic field vector rotates, pointing first south (S) (north, N), then east (E) (west, W) along the FR axis and finally N (S). In this case the FR are of type SEN and NWS respectively. The rotation of RH FRs starts with a magnetic field vector pointing first S (N), W (E) on the FRs axis and then N (S). Using the angles of the magnetic field vector with respect to the ecliptic plane measured in-situ, SN-FRs show $\Delta\theta > 0°$ (NS-FRs $\Delta\theta < 0°$) with $180° < \phi < 0°$ for SEN and NES, respectively, $360° < \phi < 180°$ for SWN and NWS. Mulligan, Russell, and Luhmann (1998) adapted the Bothmer and Schwenn (1998) scheme and added for FRs that axis is orientated perpendicular to the ecliptic plane (*high-inclination* FR) the four FR types ESW (equal to NES), ENW (NWS), WSE (SEN) and SWN (WNE), which are equal in chirality to the four types in the ecliptic plane simply rotated counter clockwise by 90°.

In the recent works of Palmerio *et al.* (2017) and Palmerio *et al.* (2018), by comparing in-situ measurements with X-ray, EUV, VIS and magnetogram observations of ICME SRs, it was shown, that the FR morphology and orientations of an ICME can be relatively easy determined (forecasted) by using intrinsic proxies. These proxies might be the above discussed SR characteristics like sigmoids (X-ray and EUV), sheared arcades, the twist of coronal arcades, flare ribbons, PEA and filament details. They provide information about the axis inclination of SRs mirroring the magnetic configuration of the corresponding CME/ICME very well as long as it propagates radial and expands in a self-similar manner, which is not necessarily the case and it is the subject of the kinematic part of this chapter.

3.2 The Early CME Stages

In order to explain the physical processes driving a CME, triggering models have to explain the CME's early evolution and the accompanying phenomena discussed above. For this reason, a classification into the individual phases a CME evolves to connect the observations with the models is important. The kinematics of CMEs can be divided into three phases:

- the acceleration phase ($< 5\,R_\odot$),
- an inner heliosphere phase ($< 50\,R_\odot$),
- an outer heliosphere phase ($\geq 50\,R_\odot$).

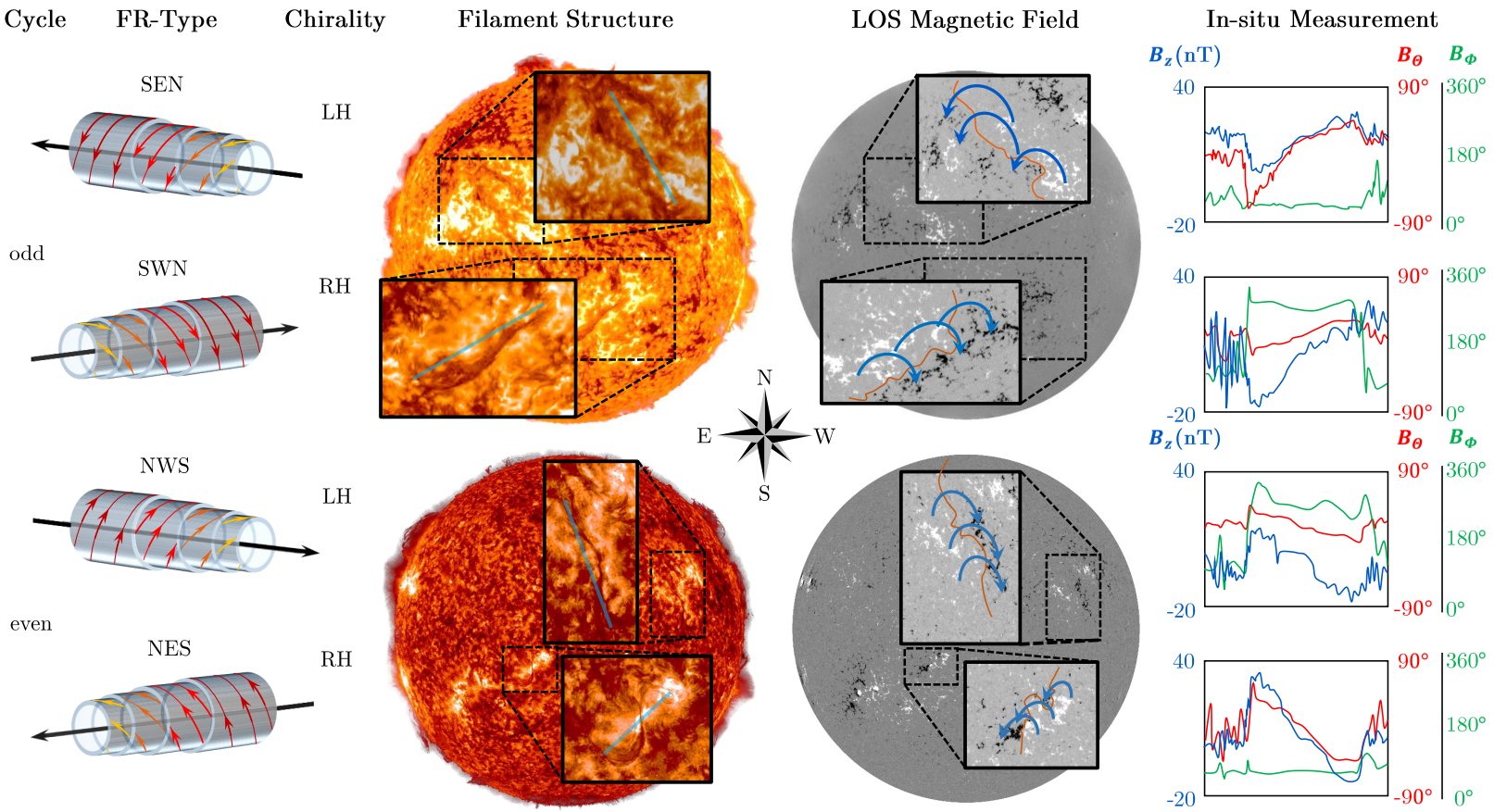

Figure (3.3) The FR scheme of Bothmer and Schwenn (1998) showing the connection between FR orientation and the magnetic configuration of associated filaments on the Sun. *Left panel*: Possible FR types and their chirality according to odd and even solar cycles. *Left middle panel*: Example of observations of filaments with respect to the FR types. *Right middle panel*: Corresponding LOS magnetograms with outlined magnetic loops and PIL. *Right panel*: Example of corresponding in-situ measurements of the B_z component (blue) in GSE and angles of the magnetic field vector B_θ (red) and B_ϕ (green) with respect to the eclipic plane. Adapted from Bothmer and Schwenn (1998).

Observations reveal that the acceleration process for most CMEs finishes within the first two solar radii (Webb and Howard, 2012). Consequently, the CME triggering mechanisms must involve an efficient energy supply transforming magnetic into kinetic and thermal energy on a relatively short timescale compared to the formation timescales of ARs. In the initial acceleration phase, in which the CME erupts, its evolution in the helionsphere is determined by its momentum, direction and mass. However, through the influence of the ambient solar wind, the CME's trajectory could be strongly affected in the second phase as will be discussed in Section 3.3. Finally, in the last phase, the CME equalises gradually to the speed of the solar wind.
Because of the low altitudes in which the initiation takes place, coronagraphs, with FOVs usually starting at a distance $> 2\,R_\odot$, are not suited to observe the CME launch and formation. This observational gap is filled by the use of imagers and spectrographs measuring in short wavelength regimes, primary in EUV. Using these instruments, pre-CME structures, also known as CME precursors (i.e., sigmoids and filaments) are observed. By analysing them, CMEs eruptions can be predicted and triggering mechanisms identified. These mechanisms are reviewed as follows.

3.2.1 CME triggering models

According to the above discussed observations in ARs, the listed CME precursors and the theoretical understanding of the magnetic process acting in the solar atmosphere, several triggering models have been developed explaining in detail the CME formation, initiation and the related near-solar surface phenomena like flares and filament eruptions.
The existing models can be divided into two general classes. In the first one magnetic energy is directly transformed into thermal and kinetic energy. The second class are storage models in which the magnetic energy is slowly build-up until the equilibrium is distorted and the energy is released. Storage models encounter the challenge of a paradox resulting from the CME eruption itself. The question is: How the net amount of build-up energy can be decreased if the stretching of the magnetic field during the eruption increases the magnetic energy? The exact nature of the violation causing the instability between the involved forces differs from model to model, but all of them depend on some type of reconnection during the runaway process of the eruption.

The 2D Standard Flare-CME Model

The 2D magnetic reconnection model, also known as *CSHKP model*, developed over decades and named after the five main Authors (Carmichael, 1964; Sturrock, 1966; Hirayama, 1974; Kopp and Pneuman, 1976), has become a standard model describing the process of a CME/filament eruption accompanied by a flare event. Upgraded versions, including the observations with enhanced instruments were published by several Authors (e.g. Tsuneta, 1996, 1997). Driven by a rising filament the null point is stretched and deforms into a current sheet above the PIL in direction of the filament. This initiates a Sweet-Parker or Petschek magnetic reconnection, which differ basically in the length of the diffusion region, respectively (see Aschwanden 2005, pp. 409). An electric current parallel to the PIL causes the collapse of the magnetic fields on both sides of the current sheet driving plasma inflows followed by an X-type reconnection. As a result of the reconnection and the inflows, plasma outflows will go out from the diffusion region, which becomes the source of possible slow and fast shocks. The impulsive dissipation of magnetic energy heats

the coronal plasma and accelerates particles (see Section 2.2.4) at the X-point region. By thermal conduction and precipitating particles, the thermal energy is transported downward into the chromosphere to the footpoints of the newly reconnected magnetic loops under the X-point region. There, the hot temperatures lead to the evaporation of plasma filling the loops with overheated and dense material emitting SXR. While the loops cool down from $T_e \sim 40\,\mathrm{MK}$ to $T_e \sim 10^4\,\mathrm{K}$, they can be also observed in EUV and H_α wavelengths. Fast shocks in the plasma outflows from the X-point collide with the magnetic field of the filled loops which produce HXR sources on the looptops. The Lorentz force along the upward reconnection accelerates the FR. Since the acceleration depends on the value of the plasma-β, the eruption becomes faster as the plasma-β decreases.
Above the initial X-point, the filament continuously rises dragging a X- or Y-point reconnection, that leads in turn to a rise of the loops and an increase in the footpoint separation. In order to extend this 2D model, it can be repeated along the third dimension to reproduce double ribbons or loop arcade observations. Although the CSHKP model may fit a lot of observations, it is inadequate to explain more complex quadrupolar flare loops or 3D nullpoint topologies (Aschwanden 2005, p.439). Therefore, a further development of the 2D Standard Model, the *2D quadrupolar Flare-CME model* was proposed (Uchida *et al.*, 1998, 1999). Starting with two parallel arcades and a filament lying in between them, the initial magnetic configuration resembles that one observed in neighbouring ARs or ephemeral regions. The two magnetic regions are pushed together by a flow pattern converting the filament channel into a current sheet, which becomes through stronger shear unstable. While the reconnection above the X-point drives the expansion of the FR structure, implying the acceleration of the filament above the escape velocity and the eruption of a CME, the reconnection of the field lines below the X-point drive the formation of a PEA.

Emerging Flux Model

New *emerging flux* is a key process in the dynamics of ARs. Furthermore, if its polarity is inverse to the ambient flux favouring magnetic reconnection, it triggers an instability in a pre-existing FR and can cause a eruption in its subsequent magnetic evolution as pointed out by Heyvaerts, Priest, and Rust (1977). In its original formulation, the model considers only emerging magnetic flux under a filament channel leading to a flare, which proceeds in three phases: in the preflare phase, the emerging flux reconnects with preexisting flux and heats in this way the current sheet between them. As the current sheet loses equilibrium and expands, the impulsive phase starts and accelerated particles lead to chromospheric evaporation. Finally, in the main phase, a new steady state is reached and reconnection happens only marginally. Because the current sheet formation and reconnection is very short lived, it is believed that the model is only applicable to explain small flare events (Forbes and Priest, 1984; Forbes, 2000).
In order to explain associations between emerging flux and CME eruptions, Chen and Shibata (2000) adapted the model to fit it as CME triggering mechanisms as depicted in Figure 3.5. If the flux emerges beneath the pre-existing FR, it reduces the magnetic pressure by annihilation with the old magnetic loops directly over the PIL, which drives the whole magnetic structure to contract and to move the plasma from both sides inward to the PIL. A current sheet forms and the consequentially the FR rises. In another scenario, flux is emerging outside of the filament channel reconnecting with large loops over the FR and decreasing the magnetic tension on the FR. It is moved up and also in direction to

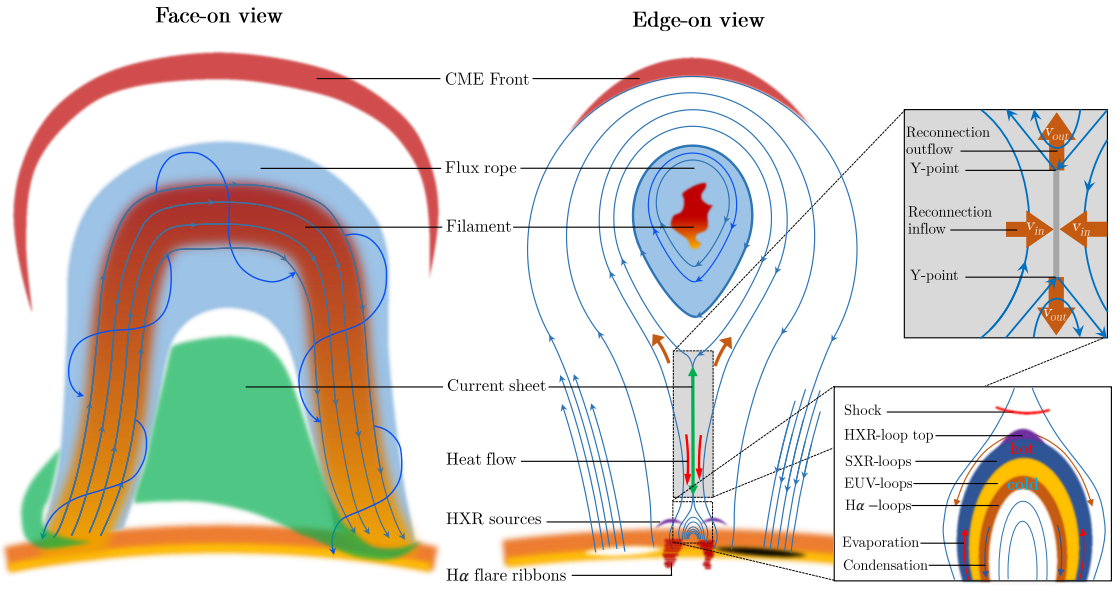

Figure (3.4) Schematic diagram of the 2D Standard Flare-CME model formally known as CSHKP model. *Left*: Face on view of a FR configuration with embedded filament and current sheet. *Right*: Edge-on view of the complete magnetic structure with magnifications of the reconnection diffusion region and the flare loop structure. Adapted from Chen (2017).

the reconnection side. The current sheet forms in this case from the collapsing X-type null point. Both scenarios provide the required magnetic configuration necessary for the CSHKP model.

The Equilibrium Loss Model

A fully analytical CME triggering model was developed by Forbes and Priest (1995), in which a magnetic FR structure evolves through a bunch of subsequent equilibria, the so-called *equilibrium loss model*. The starting point is a pre-existing potential magnetic FR configuration described by the *Grad-Shafranov* equation. The initially stationary height decreases gradually by convergence flows reducing the separation distance between the FR's footpoints and leads the system to evolve through a sequence of stable solutions until a critical footpoint separation is reached. From this point on, the FR loses the equilibrium and undergoes a sudden expansion which forms a current sheet. The smallest reconnection rate, triggered by some resistivity or external motion, would be sufficient enough at this point to accelerate the CME over the escape velocity and release the entire stored magnetic energy of the system.

The Magnetic Breakout Model

Differently from the above discussed models but similar to the second scenario of the emerging flux model, the reconnection triggering the eruption is localised externally to the filament channel in the *magnetic breakout model* (Antiochos, DeVore, and Klimchuk, 1999; Aulanier *et al.*, 2000). Magnetic breakout is the process of reconnection and opening

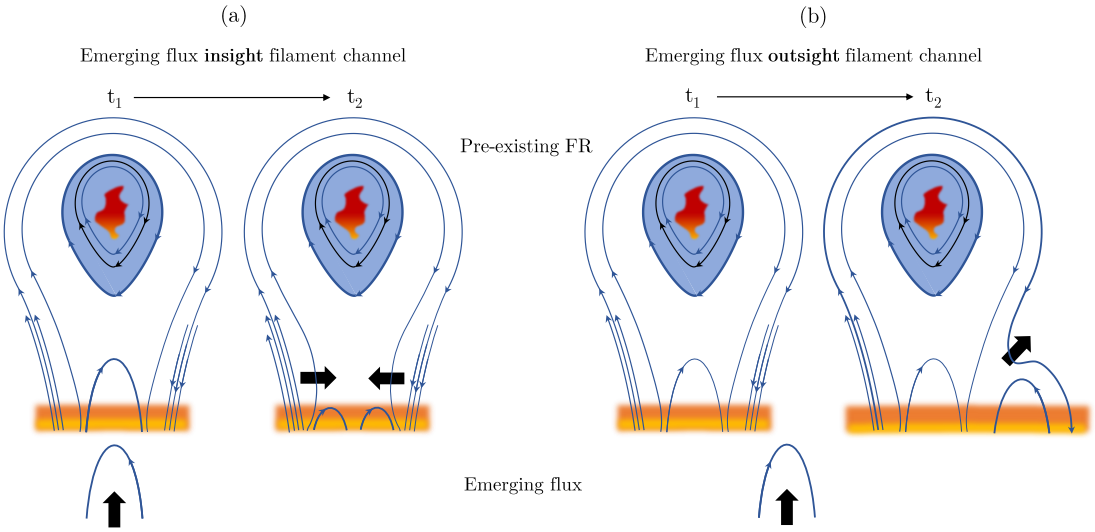

Figure (3.5) Depiction of the two possibilities of the emerging flux triggering mechanism for CMEs. If flux of opposite polarity to a pre-existing FR configuration emerges inside the filament channel (a), reconnection will cancel the low lying loops and reduce the magnetic pressure. The magnetic field is dragged by plasma inflows and a current sheet is formed. In the other scenario of emerging flux outside of the filament channel (b), reconnection with the large overlying loop moves the magnetic structure up and a current sheet is formed near the null point. Adapted from Chen and Shibata (2000).

of low-lying sheared magnetic fields. The initial configuration of the model, which is illustrated in the first panel of Figure 3.6, consists of four photospheric polarity regions that are separated by three PILs and are expelled as flux systems into the solar atmosphere with a nullpoint placed in the corona. A filament channel evolves by shear motions, flux emergence or flux cancellation in one of the two ARs. As long as the magnetic pressure increases, the overlying potential fields and the low-lying FR configuration rise and increase the downward directed magnetic tension. If a new steady-state is reached, magnetic energy is built-up by continuously asymmetric evolution of the overall magnetic structure, which decreases the width of the current sheet to a critical value and drives reconnection between the neighbouring flux systems. This starts an exponential increase in the expansion rate of the FR because the reconnection decreases the magnetic tension by removing the above flux, which drives faster outward expansion of the field and, in turn, causes reconnection below the FR that becomes gradually faster and increasing the upward directed Lorentz force. While the above reconnection distinguishes from the one below the FR, the latter is explained by the CSHKP model and can be the source of flares or PEAs. The magnetic breakout model explains well the interaction between multi-flux systems frequently observed (e.g. Bothmer and Mrotzek 2017) and can be combined with many possible 3D reconnection scenarios (Aschwanden 2005, p.447).

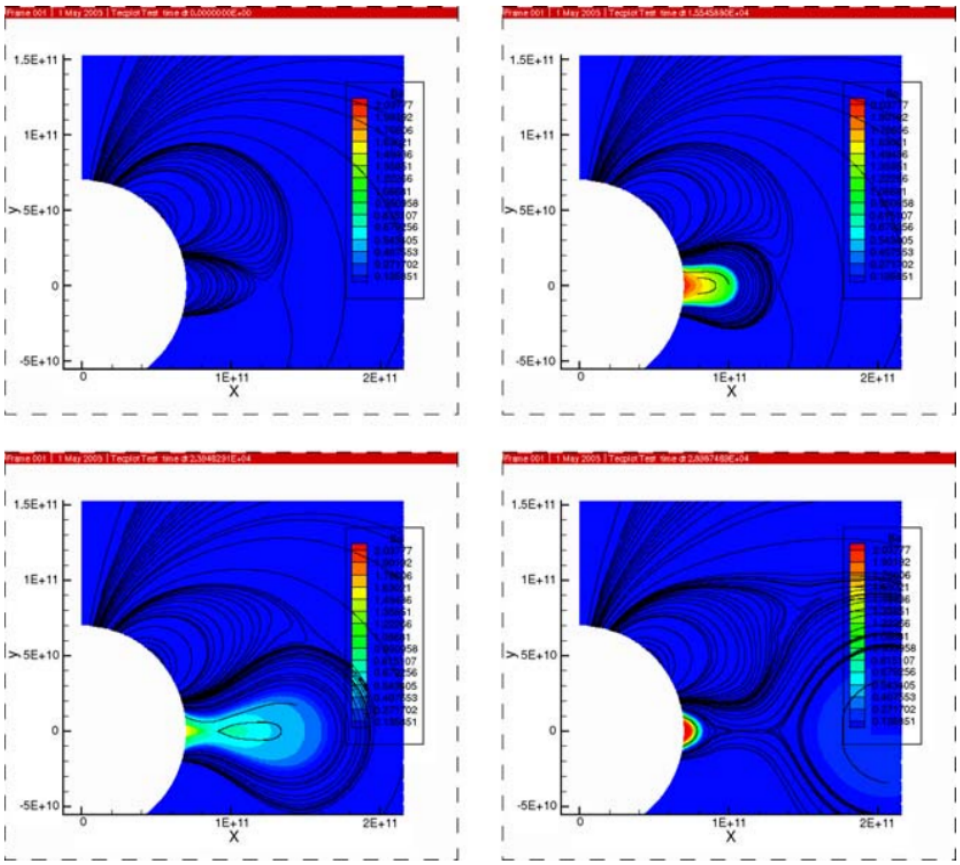

Figure (3.6) Axisymmetric simulation of a magnetic breakout scenario at four different times. Left to right and top to bottom the times are $t = 0$, 4.3, 6.6 and 8.1 h (From Forbes *et al.* 2006.)

Instability and Catastrophe Models

Since all CME triggering models deal with the problem of the balance between upward and downward directed forces and rely on a specific (external) effect disturbing this balance, the idea behind the class of *instability/catastrophe models* is to launch an eruption by an instability caused by the magnetic structure itself.
Priest and Forbes (1990) developed a CME model in which a magnetic system containing a FR evolves into a catastrophic collapse by a line current in a filament. If the magnetic energy in such a system exceeds a critical value, a force imbalance between magnetic tension and pressure results into the loss of equilibrium (instability) followed by an eruption, as shown in ideal MHD simulations (Forbes and Isenberg, 1991). The difference of the *catastrophe model* to the previous mentioned models is that magnetic reconnection, although it takes place as well, it is not a triggering process in this model but the consequence of a catastrophic eruption of the pre-existing FR. Another possible cause of an instability lies in the geometry of the magnetic structure. Omnipresent perturbations in the highly complex and continuously evolving solar atmosphere leave a FR rarely to be unaffected. Hence, *kink instabilities* have been considered as the canonical source for magnetic instabilities. Already small perturbations acting on a kink, containing FR, result in an exponential

growth of the kink and destabilise the whole helical structure. Sakurai (1976) argued that simulations of kink instabilities fit well the observed height-time profiles of erupting filaments. In other studies the influence of photospheric line-tying on kink instabilities in twisted FR was investigated and a critical twist of the FR in between 2 and 6π was found (Hood and Priest, 1979).

Following the work on laboratory plasmas for tokamak fusion devices, the *torus instability* (TI) CME model was developed by Kliem and Török (2006). They consider a CME as a partial current ring which is anchored at the solar photosphere and expanding into the corona driven by a Lorentz self force (hoop force). In order to drive successfully a fusion device, the plasma's torus shape in the reactor must be preserved and the TI suppressed by employing external poloidal magnetic fields. In nature and especially in a low-β plasma like in stellar atmospheres, poloidal fields are complex and inhomogeneous making the appearance of TIs in the solar photosphere and corona plausible. The TI can be treated as a homogeneously distributed kink instability over the entire torus. However, in contrast to the kink instability model, it is not possible to stabilise the FR by a toroidal magnetic field component, since the Lorentz force is pointing radially away from the torus. The TI model involves magnetic reconnection to reduce the force of the overlying magnetic fields restraining the eruption by the instability. If reconnection sets in at the rear side of the expanding ring, this let the instability "slide" through the external poloidal field (Török and Kliem, 2005). Furthermore, the reconnection process causes dynamic effects affecting also the magnetic field of the ejected FR, which were neglected by Kliem and Török (2006). The partially conversion of overlying magnetic fields into poloidal flux joining the FR would induce an additional current and amplify the hoop force leading to a stronger acceleration of the CME torus (Welsch, 2018). Nevertheless, even if the TI model does not provide an analytical correlation between CME speed and ribbon flux or between CME speed and mass, it has the advantage with respect to other triggering models that the initial Lorentz force can be determined from the geometry of the CME, linking its quantities with those of the CME SR.

3.2.2 TI Driven Lorentz Force Model

The theoretical description of the equilibrium in a torus current configuration was established by Shafranov (1966) involving an external magnetic field, which is necessary to balance the radial outward pointing forces of the plasma pressure gradient and the Lorentz force. In general the thermal pressure gradient can be neglected due to the conditions in the solar atmosphere holding a low-β plasma (Gary, 2001; Wiegelmann and Sakurai, 2012; Wiegelmann *et al.*, 2015). This reduces the problem to a balance between two Lorentz forces $\mathbf{F}_\mathrm{L} = \mathbf{J} \times \mathbf{B}$ with currents $\mathbf{J}$ and magnetic fields $\mathbf{B}$, which are generated by the external poloidal magnetic field $\mathbf{B}_\mathrm{ext}$ holding the FR down and the Lorentz hoop force of the current in the FR. The hoop force F_FR by the torus current, is given in cgs units and per unit length by (Shafranov, 1966; Chen, 1989):

$$F_\mathrm{FR}(r) = \frac{I^2}{rc^2}\left[\ln\left(\frac{8r}{b(r)}\right) - \frac{3}{2} + \frac{l_i}{2}\right], \tag{3.4}$$

with the FR height r, the electric toroidal current I, the CME's minor radius b (which is the torus minor radius) and the internal inductance l_i which is for a uniform current density $l_i = 1/2$ (Kliem and Török, 2006). An external poloidal magnetic field inhibits the

CME ejection with the force $F_{\rm ext}$ which is:

$$\mathbf{F}_{\rm ext}(r) = \frac{1}{c}\mathbf{J} \times \mathbf{B}_{\rm ext}(r) = \frac{1}{c}\int Id\mathbf{l} \times \mathbf{B}_{\rm ext}(r),$$
$$F_{\rm ext}(r) = \frac{1}{c}IB_{\rm ext}(r) \qquad \text{per unit length.} \tag{3.5}$$

Combining equations 3.4 and 3.5, the force balance equation for the Lorentz force per unit length $F_{\rm l}$ and for the total Lorentz force $F_{\rm L}$ acting on the CME's FR are:

$$F_{\rm L}(r) = \pi r F_{\rm l}(r) \quad \text{and}$$
$$F_{\rm L}(r) = \frac{\pi I^2}{c^2}\left[\ln\left(\frac{8r}{b(r)}\right) - \frac{3}{2} + \frac{l_i}{2}\right] - \frac{\pi r}{c}IB_{\rm ext}(r). \tag{3.6}$$

The hoop force, the force generated by external field and the resulting total Lorentz force are plotted in Figure 3.7 (top panel) for typical CME values of $B_{\rm ext} = 0.013\,{\rm G}, b/r = 0.3$ and $n = 2.5$ (Kliem and Török, 2006). In order to get $F_{\rm L}$, the current along the CME's FR axis and the external magnetic field have to be calculated, since they can not be provided by observations. The external poloidal field is represented by

$$B_{\rm ext}(r) = B_{\rm eq} \cdot \left(\frac{r}{r_{\rm eq}}\right)^{-n} \quad \text{for} \quad r \geqslant r_{\rm eq}. \tag{3.7}$$

$B_{\rm eq}$ is the external field strength at $r_{\rm eq}$, which is the height of the flux rope at the force balance point. For heights $r \leqslant r_{\rm eq}$ a finite external field can be assumed. In this ansatz the decay index n plays a major role. As mentioned above, TI will occur only, if the external magnetic field decays sufficiently fast in direction of the major torus radius. This means that, since the hoop force is decreasing with height r, $B_{\rm ext}(r)$ must decrease faster. Bateman (1978) derived a critical value for n to be $n_{\rm cr} = -rd\,ln(B_{\rm ext}/dr) \geqslant 3/2$ and, as will be shown, $n \neq 2$ is a necessary condition. The current can be determined by the assumption of the conservation of the total magnetic flux $f_{\rm tot}(r_1) = f_{\rm tot}(r_2)$ (Bateman, 1978), which includes the flux in the FR $f_{\rm FR}$ as well as that of the external flux $f_{\rm ext}$, it is expressed as (see Kliem and Török 2006):

$$f_{\rm tot} = f_{\rm FR} + f_{\rm ext} = c \cdot L \cdot I - 2\pi\int_0^R B_{\rm ext}(r)dr. \tag{3.8}$$

While the inductance P in the torus ring is described by Chen (1989):

$$P = \frac{4\pi r}{c^2}\left[\ln\left(\frac{8r}{b(r)}\right) - 2 + \frac{l_i}{2}\right], \tag{3.9}$$

it has to be assumed, that the configuration of the external magnetic field is not changing through the process of the eruption. By equating the total flux $\phi_{\rm tot}(r_{\rm eq})$ at the height in which both forces are in balance with the total flux $f_{\rm tot}(r)$ at any given height and substituting equation 3.9 in equation 3.8, the current carried by the FR at a given height and with the quantities in the equilibrium state of the FR ($I_{\rm eq}$,$r_{\rm eq}$ and $c'_{\rm eq}$) is:

$$I(r) = \frac{c'_{\rm eq} r_{\rm eq} I_{\rm eq}}{c'\ r}\left(1 + \frac{c'_{\rm eq} + \frac{1}{2}}{2c'_{\rm eq}}\frac{1}{2-n}\left[\left(\frac{r}{r_{\rm eq}}\right)^{2-n} - 1\right]\right) \quad \text{with} \tag{3.10}$$
$$c'(r) = \ln\left(\frac{8r}{b(r)}\right) - 2 + \frac{l_i}{2} \quad \text{and} \quad c'_{\rm eq} = c'(r = r_{\rm eq}).$$

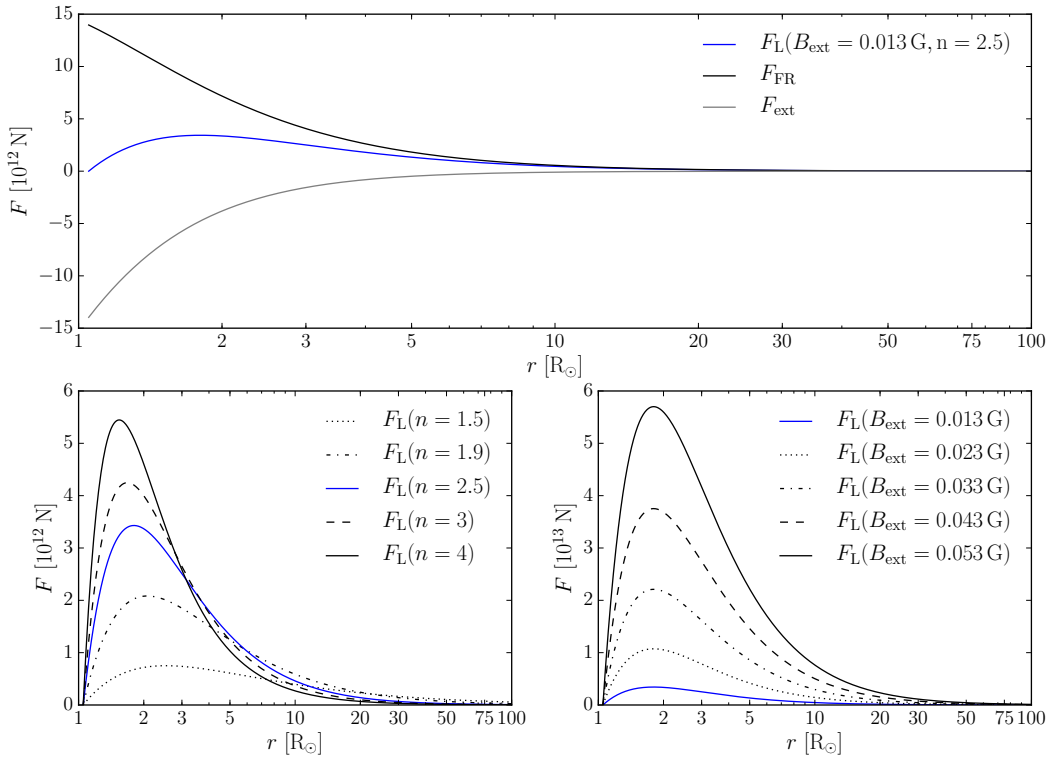

Figure (3.7) *Top*: Hoop, external and resulting total Lorentz forces for typical CME values. *Bottom left*: $F_{\rm L}$ for variable values of n with fixed values of the external magnetic field strength of $B_{\rm ext} = 0.013\,{\rm G}$ and aspect ratio of $b/r = 0.3$. *Bottom right:* $F_{\rm L}$ for variable values of $B_{\rm ext}$ with fixed value of $n = 2.5$ and aspect ratio $b/r = 0.3$.

The equilibrium torus current I_{eq} is determined by evaluating the force balance at r_{eq}:

$$\begin{aligned} F_{\rm ext}(r) &= F_{\rm FR}(r) \\ \frac{\pi r_{\rm eq}}{c} I_{\rm eq} B_{\rm ext}(r_{\rm eq}) &= \frac{\pi I_{\rm eq}^2}{c^2}\left[\ln\left(\frac{8 r_{\rm eq}}{b(r_{\rm eq})}\right) - \frac{3}{2} + \frac{l_i}{2}\right] \\ \Rightarrow I_{\rm eq} &= \frac{B_{\rm ext}(r_{\rm eq}) h_{\rm eq} c}{c'_{\rm eq} + \frac{1}{2}}. \end{aligned} \tag{3.11}$$

From equation 3.10 it can be seen that $n \neq 2$. By estimating the critical decay index, two different scenarios of CME eruptions can be considered. The first one is a freely expanding ring and the second one an expanding ring with a constant total current, which describes the initial acceleration phase of a CME, whose footpoints are anchored on the Sun. While Titov and Démoulin (1999) concluded for the latter a threshold of $n \geqslant 2$, in the case of the freely expanding ring the critical decay index is $n_{\rm cr} = 3/2 - 1/4\, c'_{\rm eq}$. During the eruption, the line tying of magnetic field maintains the initial current at the footpoints to stay constant. Even if it is unclear how much of this current is transported up into the corona, $I(r) = I_{\rm eq}$ can be taken as an assumption of maximal acceleration in case of a major event, since $I(r)$ decreases with r. The resulting critical decay index is $n_{\rm cr} = 3/2 - 1/(2\, c'_{\rm eq} + 1)$. An additional consequence of a constant ring current would be the increase of the FR

aspect ratio through the eruption. This supports also the observations, that stronger and faster events show much larger expansions than slower ones (e.g. Pluta *et al.* 2018).

3.3 Propagation in the Inner Heliosphere

While the Lorentz force given by the TI model decreases fast after peaking around $2\,R_\odot$, as illustrated in Figure 3.7, the interaction between CME and the ambient solar wind dominates the further propagation in the inner heliosphere. It is commonly accepted that this interaction via collisionless transfer of momentum by MHD waves at the CME's front equalises its speed to the one of the surrounding medium and is described by the *drag-based model* (DBM) (Cargill *et al.*, 1996; Cargill, 2004). It is the magnetohydrodynamic analogue of the aerodynamic drag, which is why it is also called *aerodynamic drag model*. The total force equation of a CME consists of the total Lorentz force, the gravitational influence of the Sun decelerating the CME, the gas pressure pointing radial outward and the drag force. Since the plasma-β is under unity in the most parts of the solar atmosphere and the effect of gravity onto CME dynamics is sufficiently small (Chen and Krall, 2003) compared to the net Lorentz force, the gas pressure and gravitational pull can be neglected. Hence, an equation of motion for CMEs is defined by the sum of the Lorentz and the drag force F_D:

$$F(r) = m_\mathrm{CME} \cdot \ddot{r} = F_\mathrm{L}(r) + F_\mathrm{D}(r). \tag{3.12}$$

Observations of CMEs faster than the ambient solar wind reveal a gradual deceleration, while slower CMEs are dragged up and are accelerated to the solar wind speed (Maloney, Gallagher, and McAteer, 2009; Gopalswamy, 2013). The deceleration of fast CMEs can also provide an explanation for the discrepancy between fast CMEs observed remotely and the in-situ measurements at 1 AU of the corresponding ICMEs, being only a few hundreds of kilometres per second faster than the solar wind and significantly slower than the extrapolated speeds. By treating a CME as a coherent body moving through a fluid with a high Reynolds number, which indicates turbulent flows in fluid and which is the ratio of inertial and viscous forces, the CME is equivalent to a rigid body in a hydrodynamic flow (Landau and Lifshitz, 1987). This is a valid assumption, since the eruptive mass is connected by a FR. The drag force is than determined by the difference in speeds of the CME $v(r)$ and the ambient solar wind $w(r)$ and the often used drag parameter $\gamma(r)$:

$$F_\mathrm{D}(r) = \gamma(r)\,[v(r) - w(r)]\,|v(r) - w(r)|. \tag{3.13}$$

The drag parameter includes the dimensionless drag coefficient $C_\mathrm{D}(r)$ (Batchelor, 2000) depending on the shape of the engulfed body given by the cross section of the CME $A_\mathrm{CME}(r)$ and the solar wind density $\rho_w(r)$:

$$\gamma(r) = C_\mathrm{D}(r) A(r) \rho_w(r). \tag{3.14}$$

As the hydrodynamic processes of the coupling are summarised by the drag coefficient, its value reflects the strength of the momentum transfer. For this reason an evaluation of C_D is a crucial task in the determination of the drag force. In previous works (Batchelor, 2000; Vršnak *et al.*, 2010; Carley, McAteer, and Gallagher, 2012), a drag coefficients of order unity without a distance dependency is often used for simplification and it is argued, that other uncertainties, e.g., the inhomogeneity of the solar wind, play a superior role. Cargill (2004) used 2.5D MHD simulations of a set of slow and fast, as well as heavy

and tenuous CMEs to derive C_{D} empirically. The results show a dependency of the drag coefficient on the density ratio between CME and ambient solar wind leading to larger values than unity. In general the drag coefficient depends on the Reynolds number Re, which is an dimensionless number for the ratio between inertial and viscous forces. In order to derive an analytical microphysical prescription of C_{D}, Subramanian, Lara, and Borgazzi (2012) considered experimentally derived data for high Reynolds numbers from Achenbach (1972) and obtained $C_{\mathrm{D}}(Re)$ for the drag on a static sphere to be:

$$C_{\mathrm{D}}(Re) = 0.1478 - 42834Re^{-1} + 9.8 \cdot 10^{-9}Re. \tag{3.15}$$

It should be noted, that Equation 3.15 is only valid under the assumption of a not deforming rigid body in an subsonic flow with a high Re. However, since the sound speed in the solar wind is at its maximum in the solar corona $\sim 147\,\mathrm{km\,s^{-1}}$ (Aschwanden 2005, p. 317) and is decreasing with larger distance from the Sun (at 1 AU it has a value of $\sim 60\,\mathrm{km\,s^{-1}}$, (Bruno and Carbone, 2013)), the propagation of a CME in the ambient solar wind is not subsonic but supersonic. Because of the nearly locally incompressibility of the turbulent fluctuations in the solar wind (Bruno and Carbone, 2013; Zank *et al.*, 2016), this circumstance is solved by applying the general accepted Morkovin hypothesis (Bradshaw, 1977). This hypothesis states that, in almost constant density flows, the turbulent structures in boundary layers and wakes around a body are closely the same for sub- and supersonic flows. The total pressure profile along the symmetry axis of a CME measured in-situ shows an increases at the boundaries of the MC, signature of an overpressured region, that is not deforming under tangential forces (Russell, Shinde, and Jian, 2005; Jian *et al.*, 2006). Following Sachdeva *et al.* (2015), the Reynolds number of a CME with the solar wind viscosity ν_w is:

$$Re(r) = \frac{|v(r) - w(r)|\, b(r)}{\nu_w(r)}. \tag{3.16}$$

In a collisionless plasma with large mean-free path lengths, like in the case of the solar wind, momentum transfer by proton-proton collisions does not occur. Viscosity in the solar wind arises by magnetic kinks in the solar wind encountering its particles. More precise, by the interaction of Alfvénic waves with the solar wind protons. Using the rms thermal speed of a proton in the solar wind:

$$v_p^{\mathrm{rms}} = \sqrt{\frac{3k_{\mathrm{b}}T}{m_p}}, \tag{3.17}$$

with a typical temperature of $T = 10^5\,\mathrm{K}$ (Subramanian, Lara, and Borgazzi, 2012), the solar wind viscosity is:

$$\nu_w = \frac{2\sqrt{6}}{15} v_p^{\mathrm{rms}} \lambda_w, \tag{3.18}$$

with λ_w the mean-free path length of a proton in the solar wind. After Sachdeva *et al.* (2015, 2017), the ion inertial length (Bruno and Trenchi, 2014) can be taken as a characteristic scale:

$$\lambda_w = \frac{v_a}{\Omega_i} = \frac{c}{\omega_p} \sim \frac{228}{\sqrt{n_w}}\,[\mathrm{km}], \tag{3.19}$$

with v_a being the Alfvén speed, Ω_i the ion cyclotron plasma frequency and ω_p the ion plasma frequency. Representative cases with different initial values, considering slow, moderate and fast CMEs in a slow and a fast ambient solar wind stream, are compared

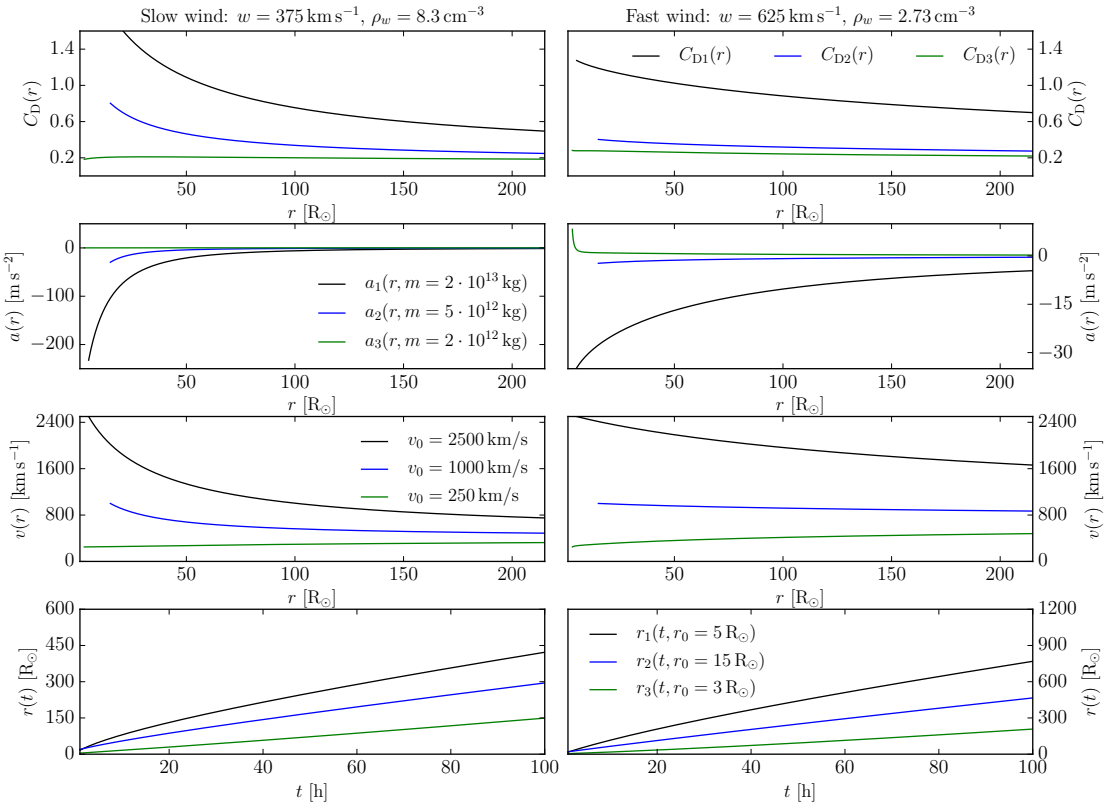

Figure (3.8) Representative examples of the dynamics of three CMEs in a slow and in a fast solar wind described by the DBM with different initial and ambient conditions. *Left*: CME dynamics in a slow solar wind stream with the averaged values at a distance of 1 AU as in Table 2.3. *Right*: Same dynamics like in the left column but in a fast solar wind stream. *From top to bottom*: The drag coefficient $C_{\mathrm{D}}(r)$ as presented in Equation 3.15, CME acceleration $a(r)$, CME velocity $v(r)$ and heliospheric distance of the CME apex to the Sun over time $r(t)$. The colours indicate CME dynamics with the same initial speed v_0, height r_0 and mass.

in Figure 3.8. The central role of the drag force by the ambient medium on the CME (ICME) affecting its propagation is commonly accepted. Another question arises in terms of space weather and predicting arrival times, but also in the understanding of the correct form of C_{D} and the strength of the momentum coupling: What is the heliospheric distance range where the drag force is the dominating force? Additionally, where does the drag force prevail over the Lorentz force and where is the CMEs speed completely equalised to the one of the ambient solar wind? Whereas both ranges were investigated by several authors, there is no unambiguous consensus on these questions. Zhang and Dere (2006) and Webb and Howard (2012) state that the CME initial acceleration phase dominated by the Lorentz force takes place at distances $\leqslant 2\,\mathrm{R_\odot}$, but Vršnak (2006) suggested a decrease of the Lorentz force with $\propto r^{-2}$ within the first $30\,\mathrm{R_\odot}$. In a case study, Carley, McAteer, and Gallagher (2012) reported an force magnitude peaking with $3.4 \cdot 10^{14}\,\mathrm{N}$ at $\sim 3\,\mathrm{R_\odot}$ and settling to an average value of $3.8 \cdot 10^{13}\,\mathrm{N}$ above $\sim 7\,\mathrm{R_\odot}$, which is in good agreement

with the results of Byrne *et al.* (2010), who found that above $7\,R_\odot$ the CME dynamics are dominated by the drag force. By analysing remote observations of a representative set of 38 slow and fast CMEs with a TI Lorentz force and a drag based model, Sachdeva *et al.* (2017) defined the ranges more precisely. The Lorentz force peak of all CMEs of the set is reached between 1.65 and $2.45\,R_\odot$, while for the fast CMEs (reaching a speed $> 900\,km\,s^{-1}$ near the Sun) the drag becomes the dominating force between 3.5 and $4\,R_\odot$, and between 12 and $50\,R_\odot$ in the case of slow events ($< 900\,km\,s^{-1}$). On the other hand, most ICMEs are decelerated to the ambient solar wind speed within heliospheric distances up to half an AU as argued by Temmer *et al.* (2011); Vršnak *et al.* (2013) and Rollett *et al.* (2016). As shown in Figure 3.8, this is confirmed by theory for most of the CMEs in a slow ambient solar wind, but not for speeds as in the case of an intermediate Carrington event ($v_0 = 2500\,km\,s^{-1}$) in a fast solar wind stream.

By combining equation 3.13 to 3.19 the distance dependent drag force model is depending only on the observables $v(r), A(r)$ and m_{CME} as well as on the solar wind quantities $n_w(r)$ and $w(r)$, which depend on the heliocentric distance r. Since the solar wind is highly variable and the first in-situ measurements in the direct neighbourhood of the Sun are taken by the PSP mission at the time of writing, the usage of solar wind models as discussed in section 2.2.2 provides currently the best procedure to include the 1D distance dependency of the solar wind. In contrast, using advanced geometric modelling methods, it is possible to derive these three CME observables from a series of coronagraph white light images, which will be described in the next sections and in Section 4.2.4.

3.4 Three Dimensional CME Modelling

CMEs are optically thin structures that are visible through scattered light. In the following the theoretical concept of Thomson scattering is outlined, which is the basis for 3D modelling of CMEs using white-light observations. Furthermore, the *Graduated Cylindrical Shell* (GCS) model (Thernisien, Howard, and Vourlidas, 2006) to describe the 3D shape of CMEs based on a FR configuration is introduced. Using the theory of Thomson scattering in combination with this model, basic CME characteristics such as its mass can be determined from white-light observations.

3.4.1 Thomson Scattering

Since CMEs and coronal structures are visible in white-light by the photospheric light scattered by free electrons, the knowledge about the underlying scattering theory is an important part in the understanding of coronagraphic and heliospheric observations. The inelastic scattering on free or quasi-free charged particles is described in general by *Compton scattering*. In the case of visible light, in which kinetic energy of the electron and frequency of the photon are preserved during the collision, the low-energy limit of Compton scattering is reached and the collision is elastic. This special case is known as *Thomson scattering* (Jackson, 1975) and can be applied under following conditions (Howard and Tappin, 2009):

- The separation of the scattering particles has to be large compared to the coherence length of the radiated light.

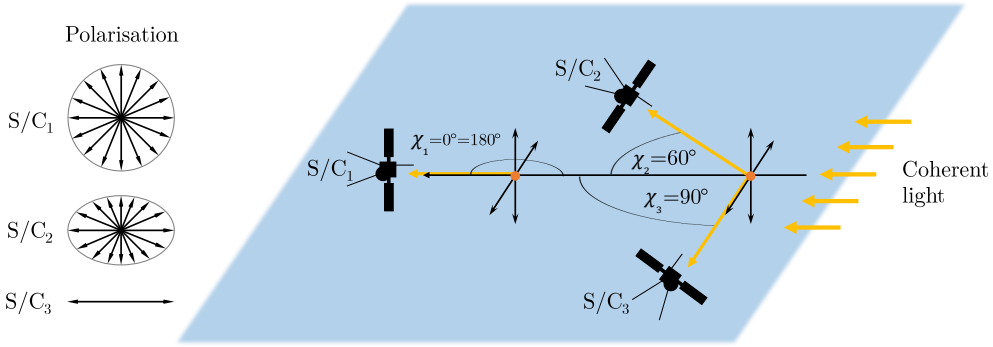

Figure (3.9) Illustration of the influence of the scatter angle χ on the polarisation of the scattered wave on a single electron. The three observers S/C$_1$, S/C$_2$ and S/C$_3$ will measure unpolarised, partially polarised and linear polarised light since they will see a different, projected, oscillations behaviour of the electron depending on their viewpoint. After Howard and Tappin (2009).

- The rest mass energy of the scattering particle must be significantly high compared to the photon energy.

In the corona and in the case of the solar wind in the heliosphere, both conditions are valid. In the following, the principle of Thomson scattering is outlined for the reason of simplification under the assumption of a single electron (or small volume of electrons) scattering light going out from a point source. The electric field of an unpolarised monochrome wave going out from the photosphere accelerates a free electron in the corona. Because the electron is forced by the electric field to oscillate in its direction, it will re-emit dipole radiation of the same wavelength as the incident wave. The polarisation of the re-radiated wave that appears to an observer depends on the scatter angle χ, which is the angle between the incident wave and the LOS to the electron. This observational behaviour is depicted in Figure 3.9 for the three cases $\chi = 0$ or $\chi = \pi$, $0 < \chi < \pi/2$ and $\chi = \pi/2$. Under an angle of $\chi = 0$ or $\chi = \pi$, there is no observational difference in the polarisation between incident and scattered wave since the electron displacement is seen equally distributed in all directions. As the scatter angle increases to $\chi = \pi/2$, the oscillation amplitude in the plane defined by an observer and the incident wave, and thereby the observed electric field in this plane will decrease resulting in a partially polarised wave. If the LOS lies perpendicular to the direction of the incident wave, the scatter angle is $\chi = \pi/2$ and the oscillation along the LOS is not detected. Only a motion of the electron perpendicular to the LOS-incident-wave-plane remains for the observer and a linear polarisation with the maximum electric field amplitude is detected. The intensity of the component perpendicular to the incident wave remains isotropic, but, the one parallel to the projected incident wave varies with $\cos^2$ of the scatter angle. The total scattering cross section σ_T of an electron is determined by integration of the differential cross section $d\sigma/d\zeta$ over all solid

angles, while $d\zeta$ is an element of χ (Jackson, 1975):

$$\frac{d\sigma}{d\zeta} = \frac{1}{2}(1+\cos^2\chi)\left(\frac{e^2}{4\pi\epsilon_0 m_e c^2}\right)^2, \tag{3.20}$$

$$\sigma_T = \frac{8\pi}{3}\left(\frac{e^2}{4\pi\epsilon_0 m_e c^2}\right)^2 = 6.65\cdot 10^{-29}\,\mathrm{m}^2. \tag{3.21}$$

Complementary, the Thomson cross section σ_e (Billings, 1966), being the differential cross section for perpendicular scattering, is:

$$\sigma_e = \left(\frac{e^2}{4\pi\epsilon_0 m_e c^2}\right)^2 = 7.95\cdot 10^{-30}\,\mathrm{m}^2\,\mathrm{sr}^{-1}. \tag{3.22}$$

In reality, the Sun is not a point source and the incoming light is integrated over the full visible photosphere coming from different angles. Therefore, the effect of limb-darkening has to be considered, which was studied by Minnaert (1930). By applying a suitable coordinate system expressing the different polarisation components in terms of an angular segment of the photosphere, transverse and radial scattered intensities can be calculated. A full explanation of the coordinate system, the used algebra and the derivation of the intensities can be found in Howard and Tappin (2009), whose treatment follows the one from Minnaert (1930) and Billings (1966). Including the limb-darkening coefficient u the emitted intensity of the photosphere Φ is:

$$\Phi = \Phi_0\left(1-u+\frac{u\sqrt{\cos^2\zeta-\cos^2\Omega}}{\sin\Omega}\right), \tag{3.23}$$

with I_0 as the intensity of the Sun (power per unit area per unit solid angle), ζ as an angle between a point C on the Sun and the vector $\mathbf{SQ}$ from the solar centre S to the scattering point Q and Ω being the angle between the tangent crossing the Sun and going through Q. By using Equation 3.23 the tangential, radial and polarisation intensities, Φ_T Φ_R and Φ_P, are:

$$\Phi_\mathrm{T} = \zeta[(1-u)C_\mathrm{H} + uD_\mathrm{H}], \tag{3.24}$$

$$\Phi_\mathrm{P} = \zeta\sin^2\chi[(1-u)A_\mathrm{H} + uB_\mathrm{H}], \tag{3.25}$$

$$\Phi_\mathrm{R} = \Phi_\mathrm{T} - \Phi_\mathrm{P}, \tag{3.26}$$

using $\zeta = I_0(\pi\sigma_e)/2z^2$, where z is the distance from Q to the observer. A_H,B_H,C_H and D_H are the so called van de Hulst coefficients, which are calculated from the solar surface to a distance of 0.1 AU in Figure 3.10, van de Hulst (1950) summarising some trigonometrical functions and generally used for simplification. While the distance between Sun and scattering electron increases, Ω becomes more and more negligible and the Sun light becomes stronger collimated. Finally, the total intensity scattered off an electron near the Sun as an extended light source is:

$$\Phi_{tot} = (\Phi_\mathrm{T} + \Phi_\mathrm{R}) = 2\Phi_\mathrm{T} - \Phi_\mathrm{P}. \tag{3.27}$$

The total and single intensity components are plotted for an electron distance of $3\,\mathrm{R}_\odot$ from the photosphere over the scatter angle χ in Figure 3.10. Since the intensity is direct

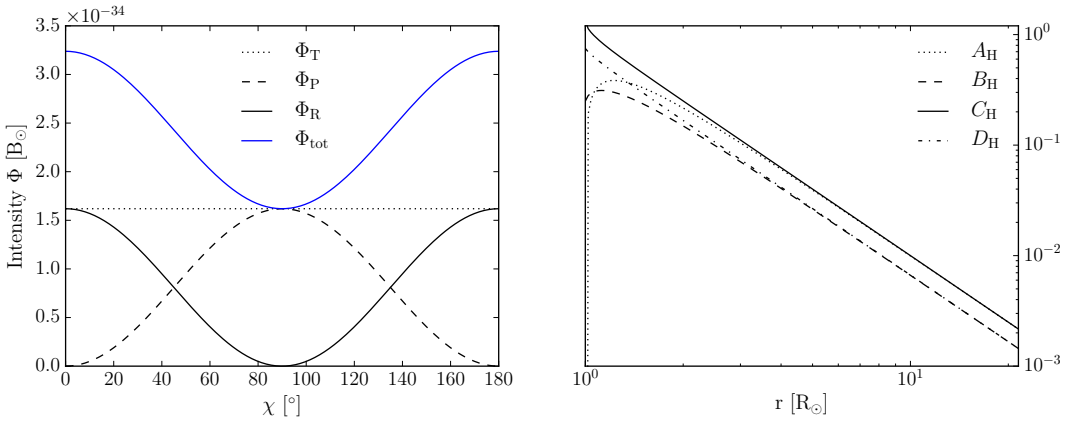

Figure (3.10) *Left*: Intensity components (power per unit solid angle) scattered by a single electron at a position of $3\,R_\odot$ from the solar surface. *Right*: Calculated van de Hulst coefficients. For more details see Howard and Tappin (2009).

proportional to the amount of electrons scattering light at a certain point under the angle χ to an observer, the number of electrons can be calculated from the measured intensity. In this way, a CME's mass can be measured by the scattered intensity and the knowledge of it's particle composition (see Section 3.4.4) From Figure 3.10, it is obvious that the scattering efficiency reaches a minimum with a scatter angle of $\chi = \pi/2$ because Φ_T stays is independent of χ and Φ_R is 0 at $\chi = \pi/2$. On the other hand, the intensity of the Sun light as well as the electron density decreases with increasing distance (see Section 2.2.2). Hence, the incident intensity and the number of electrons is maximised at the point along the LOS at which it has the shortest distance to the Sun. This is true if the LOS lies orthogonal to **SQ** and $\chi = \pi/2$. Taking all three effects into account, the distance (angular) dependency of the incident intensity and the number of scattering electrons predominate the angular dependency of scattering efficiency. Going one step further, considering every point in space in which a certain LOS going out from a observer is $\perp$ to **SQ**, the so called *Thomson Sphere*, being the surface with maximal scattered Intensity, can be constructed (Vourlidas and Howard, 2006). The Thomson spheres of two spacecraft observing the same heliospheric volume under different scattering angles are illustrated in Figure 3.11. As highlighted in Howard and Tappin (2009), the Thomson sphere is not a criterion for the detectability of a CME or coronal structure, but it holds some important conclusions for the interpretation of the observed CME structures that are all projected onto the POS. CMEs, as extended structures, are not located in one plane. Certainly, the intensity of the different CME parts varies with χ. This becomes more important as a CME propagates further into the heliosphere and its volume expands (see Figure 3.14 for the distance dependent increase of the CME widths). Therefore, the projection effects of Thomson scattering have are a crucial impact on the geometrical modelling and, more basic, in the identification of CME structures.

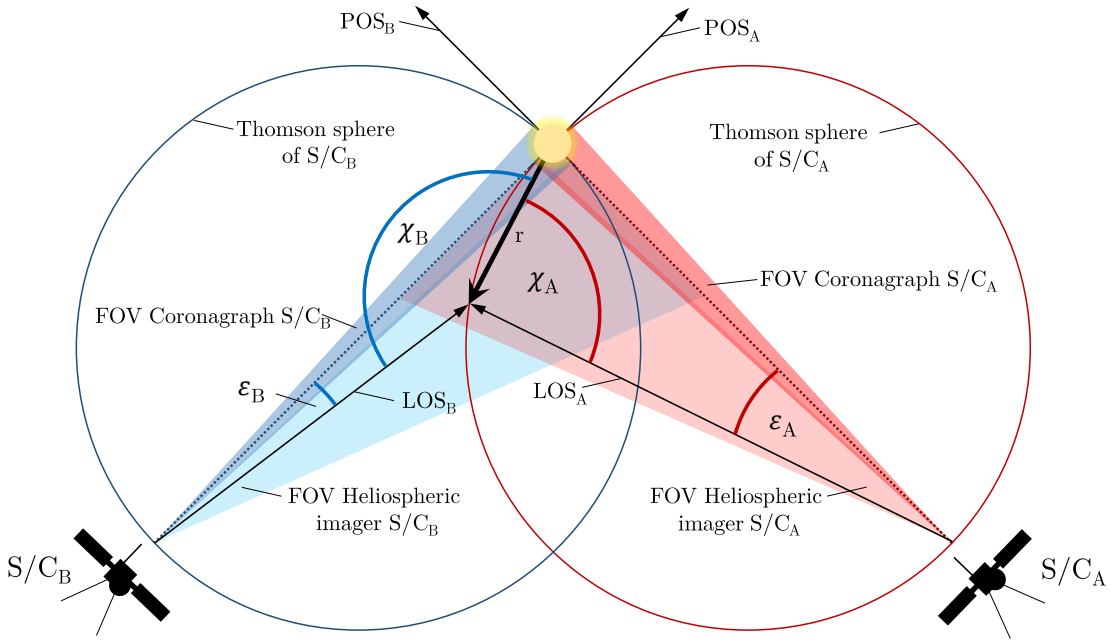

Figure (3.11) The concept of the Thomson sphere as can be seen from the example of two STEREO spacecrafts S/C$_A$ and S/C$_B$ with a separation angle of $\Delta\phi = \pi/2$. While S/C$_A$ observes the scattering volume with a heliospheric imager under a scatter angle of $\chi_A = \pi/2$, for SC$_B$ the scatter angle is $\chi_B > \chi_A$ and the scattering volume lies not on the spacecraft's Thomson sphere. The angles ϵ_A and ϵ_B are the elongation angles under which the observed volume appears in the POS$_A$ and POS$_B$ of the instruments of the two spacecraft.

3.4.2

3.4.2 The GCS Model

In order to reproduce the geometry of the large scale FR nature of CMEs, Thernisien, Howard, and Vourlidas (2006) developed the GCS model based on the findings of Cremades and Bothmer (2004). The shape of the GCS geometry is reminiscent of a popular french breakfast pastry, which is why it is sometimes called as the croissant model. While the main body of the FR is represented by a tubular section, the CME legs are formed by two cones anchored in the solar centre. Face-on and edge-on views of the geometry are depicted in the Figures 3.12 and 3.13. It can be seen that the largest diameter of the FR b is at the symmetry line (y) dividing the FR in two equal parts and marking also the position of the CME apex, whose height coincides with the one of the leading edge. The geometry of the GCS model and its location in space is fully described by six parameters shown in Figure 3.12 and listed below:

- *Position*: To determine the corresponding SR and the direction, the CME is moving to, the Carrington longitude ϕ_{CME} and heliographic latitude θ_{CME} of the apex

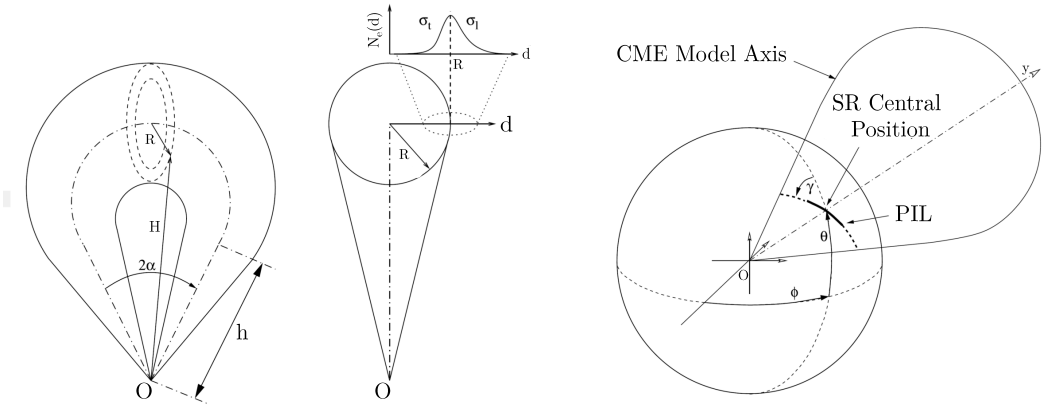

Figure (3.12) Scheme of the GCS geometry. *Left*: Face-on and edge-on view of the GCS FR structure. The cones, separated by 2α, are anchored in the origin O with the height h. A vector **H** is pointing to a point on the GCS surface and the radius at the thickest section of the tube is labelled with R. In the edge-on view, the density profile along the axis d of the cross section is with σ_{leading} and $\sigma_{\text{trainling}}$ shown. *Right*: Scheme of the position and orientation parameters of the GCS model. Adapted from Thernisien, Howard, and Vourlidas (2006).

projected onto the solar surface are used .

- *Orientation*: The orientation of the FR symmetry axis (dashed-dotted line in Figure 3.12) is given by the tilt angle Γ_{CME}, being the angle between the FR axis and the solar meridian at ϕ_{CME}.

- *Structure*: Two structural parameters the separation of the legs and the FR's size are adjusted. While the dimensionless aspect ratio of the FR κ is defined by $\sin(\delta)$, in which δ represents the cone half angle (see Figure 3.13), the separation of the legs is given by the half angle α between the cone axis and symmetry line y.

- *Height*: The height of the leading edge r is a function of the two structural parameters and the height h of the legs at which the cones are attached to the tubular section (Thernisien, Howard, and Vourlidas, 2006):

$$r = h\frac{(1+\kappa)(1+\sin(\alpha))}{(1-\kappa^2)(\cos(\alpha))}. \tag{3.28}$$

While the construction of the cones is straightforward, the deviation of the tubular section is more sophisticated. However, it can be derived with some geometrical considerations and the use of r, κ and α as shown in Thernisien (2011). To simulate synthetic white light coronagraph images, a density profile is added to the GCS geometry. An asymmetric Gaussian profile perpendicular to the symmetry axis was found to fit best the white light observations of Cremades and Bothmer (2004). The density profile peaks at the outer shell surface of the model and decreases to both sides with different widths σ_s to ensure that the brightest region of the model is located at the GCS surface. Using $\sigma_s = \sigma_{\text{trainling}}$

inside the GCS-FR volume ($d < R$ in Figure 3.12) and $\sigma_s = \sigma_{\text{leading}}$ outside the GCS-FR volume ($d > R$ in Figure 3.12), the density profile is (Thernisien, Howard, and Vourlidas, 2006):

$$N_e(d) = N_e e^{-\left(\frac{d-a}{\sigma_s}\right)^2}. \tag{3.29}$$

Another common geometrical model to describe shape and height of a CME is the *cone model* as described by Zhao, Plunkett, and Liu (2002) and later, fully analytically, by Xie, Ofman, and Lawrence (2004). In this model a CME is treated as a cone with circular cross section whose tip is anchored in the solar centre and expanding self similar with a constant angular width radial away from the Sun. Originally, this model was developed to forecast arrival times and fit deprojected velocities of halo CMEs using LASCO C2/C3 observations. Within the work of Millward *et al.* (2013), in which the software tool *CME Analysis Tool* (CAT) was developed at the *Space Weather Prediction Centre* (SWPC) to provide CME input parameter for the 2.5 D MHD *WSA-Enlil* model, this simple cone geometry was replaced by a more realistic curved polygon. The form of this polygon is derived from the lemniscate of Bernouli (Lawrence, 1972), which is extended into 3 D to achieve a geometry, that is reminiscent to a "teardrop" having a circular cross section. Although the "teardrop" shape fits the overall visual appearance of a large set of CMEs observed in white light coronagraph images, there is no physical justification or background in the usage of this form. But, since the CAT software was developed to provide initial speed, direction and extension of a CME in order to improve the forecast, it was foreseen to work with beacon or level 0 data (see Chapter 4). This near-real time (NRT) data are available with the shortest available cadence but are, compared to reduced science data, of reduced quality. For this reason, the GCS model presents a more advanced model including a larger set of free adjustable parameters and reproduces the physical nature of the FR shape of a CME. In addition, with the possibility to fit the axis of the FR with Γ, it links and provides a comparison between SR and coronagraph observations (see Cremades and Bothmer 2004).

3.4.3 CME Cross Section

As seen in Section 3.3 in the formulation of the drag parameter $\gamma(r)$, the CME's cross section $A(r)$, is a crucial impact factor in the DBM model, affecting significantly the drag parameter. By fitting the GCS model to CME observations $A(r)$ can be estimated. In a first approximation, the cross section at a given time of a GCS FR can be expressed by an ellipse. The ellipse major and minor axes are the edge-on and face-on widths of the FR, as illustrated in Figure 3.13 and labelled with W_{fo} and W_{eo}. While the edge-on width is $W_{\text{eo}} = 2R(\beta = \pi/2)$, the face-on width can not be determined analytically. By using the fitted GCS parameter r, κ and α, W_{fo} is computed numerically by finding the angle β, for which the x-component of the vector $\boldsymbol{BP}$, which is the vector starting in B (see Figure 3.13) and ending on the outer tubular surface in the x-y-plane, is at its maximum. The elliptical CME cross section is then:

$$A(r) = \pi \frac{W_{\text{eo}}}{2} \frac{W_{\text{fo}}}{2} = \pi\, R(\beta = \pi/2)\, \frac{BP_x(\beta_{max})}{2}. \tag{3.30}$$

A detailed explanation of the formulas defining the GCS dimensions and the used algebra is pointed out in Thernisien (2011). Using Equation 3.30 the CME cross sections for different input values of α and κ are shown in Figure 3.14, in which in the bottom left

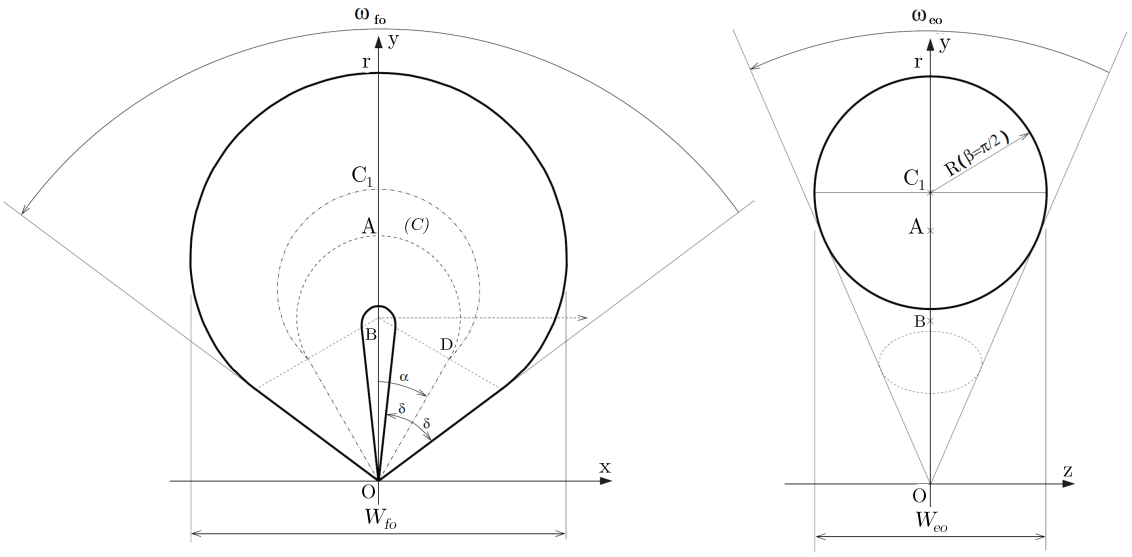

Figure (3.13) The GCS geometry with important dimensions that can be derived from h, κ and α. Only solid lines are in the image plane. *Left*: Face-on view of a cut along the x-y plane. The z-axis points orthogonal out of the image plane. *Right*: Edge-on view of a cut along the z-y-plane. This cut represents the thickest part of the FR. Adapted from Thernisien (2011).

panel the half angle and in the bottom right panel the aspect ratio is varied. In the top panel, major and minor axis of the ellipse are plotted over the heliospheric distance. All functions in this figure are derived under the ideal assumption of a self similar expansion of the CME without distance dependencies in the half angle and aspect ratio.

3.4.4 Mass determination

3.4.4

The detected light in white-light coronagraph observations is not emitted directly from the coronal material, but, it originates from the photosphere and is scattered in the corona off free electrons (see Section 3.4.1). Therefore, coronagraph images are also indirect density measurements of the coronal electron content. A CME, as denser structure with respect to the ambient background corona, appears for this reason as brightness enhancement in white-light images. The exact determination of CME masses from this observations is a highly non-trivial task requiring precise image calibration and reduction to exclude background signatures and projection effects Colaninno and Vourlidas (2009). In a first step, the images have to be calibrated to units of mean solar brightness $H/H_{\odot}$ (MSB). After the usual data reduction, a carefully selected pre-event image, as a base difference image, has to be chosen and to be subtracted from the image sequence containing the CME. Typically this is an image recorded as close in time as possible before the CME eruption to avoid variation due to the solar rotation or changes in the (background) coronal configuration (Stewart *et al.*, 1974; Poland *et al.*, 1981; Howard *et al.*, 1985; Hundhausen, Stanger, and

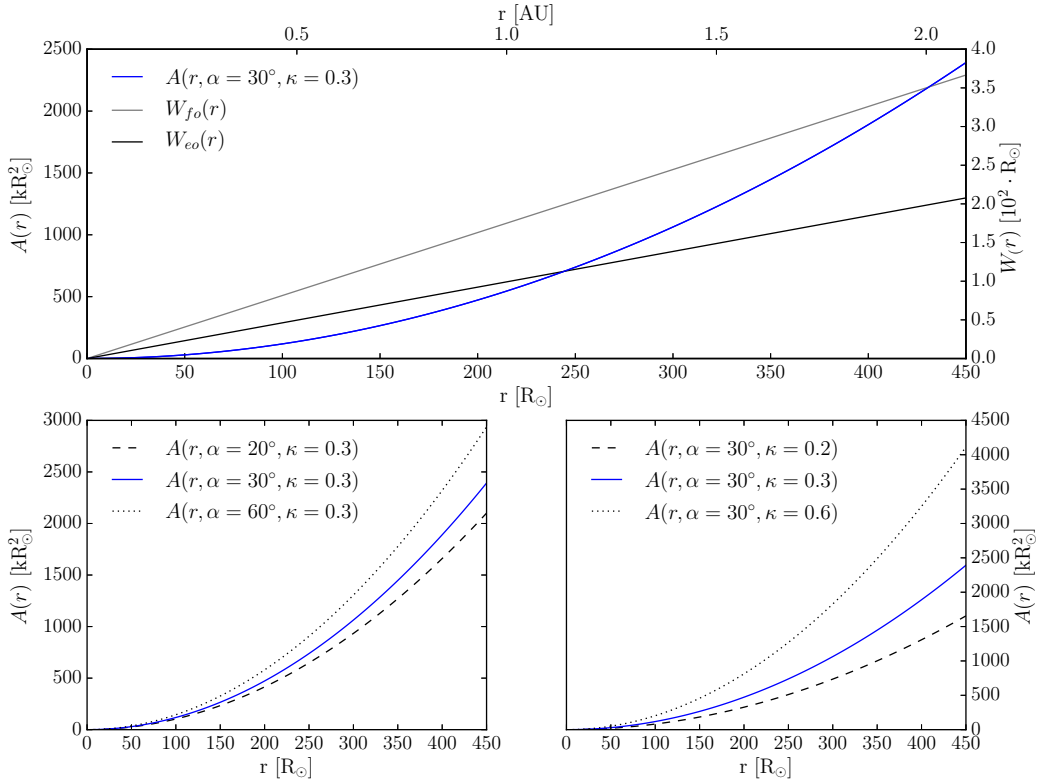

Figure (3.14) Examples of the CME cross section computed with Equation 3.30 using different input parameters. *Top*: CME cross section $A(r)$, face-on width W_{fo} and edge-on width W_{eo} for $\alpha = 30°$ and $\kappa = 0.3$ *Bottom left*: CME cross section for different values of α and $\kappa = 0.3$ *Bottom right*: CME cross section for different values of κ and $\alpha = 30°$.

Serbicki, 1994), since the F-corona becomes increasingly the main signal contributor at heights of $> 3\,\mathrm{R}_\odot$. The resulting difference images are corrected by the influence of the background F- and K-corona as well as static structures (e.g. streamers), which would otherwise contaminate the observations and contribute to the measured density warping the CME mass. After this, the images are in units of excess MSB. Hence the observed brightness is integrated over the LOS and the electron distribution along it remains unknown, it is assumed that all electrons, contributing to the scattered brightness, are located in one plane. There are two different assumptions according to the orientation of this plane. The first one is that this 2D plane has the longitudinal shift ϕ to the POS, which is the longitudinal propagation direction of the CME (the "directional mass determination", see Pluta *et al.* 2018). In another approximation, the plane is projected onto the POS, the so called $\phi = 0°$ approximation. In a next step, not depending on which plane-assumption was chosen, the region of interest (ROI) containing the CME structure must be defined for every image in the sequence. This can be done by defining the ROI manually (Subramanian and Vourlidas, 2007) or through the sector method (Vourlidas *et al.*, 2010), in which the sector in the coronagraph images containing the CME is determined by the occulter height, the height of the CME front as well as the central and edge PAs of the CME.

Applying the theory of Thomson scattering (see Section 3.4.1), the excess brightness in the ROI is converted into the number of excess electrons (Billings, 1966), that would be necessary to scatter the measured excess brightness per pixel:

$$m = \frac{H_{obs}}{H_e(\phi)} \cdot 1.97 \cdot 10^{-24} \quad [\mathrm{g}]. \tag{3.31}$$

In Equation 3.31 m is the mass per pixel, H_{obs} the observed brightness and $H_e(\phi)$ the brightness of a single electron with an angular separation of ϕ to the POS. Integration over the ROI together with the usage of an assumed CME composition lead to the calculated projected CME mass. A common assumption for the CME composition is a mixture of completely ionised H and He (90% and 10%) (Hildner *et al.*, 1975).

Since the CME (mass) is initially covered by the occulter of a coronagraph and is moving in and out of the instruments FOV over the recorded image sequence, the misleading term "mass evolution" is often attributed to the over time increasing measured CME mass. Indeed, by the magnetic connection to the Sun, plasma can flow up into the CME structure and also mass down-flows are possible in the process of the CME initiation. However, the real CME evolution seems to be mainly finished in the FOV of coronagraphs ($\sim 2 - 15\,\mathrm{R}_\odot$) and observations showed no mass down-flow in this regime. Furthermore, CME masses and energies tend to reach a constant plateau above a height of $\sim 10\,\mathrm{R}_\odot$, which was excluded to be an instrumental effect since this behaviour was observed in the overwhelmingly majority of CME events observed in various instruments on-board of different satellites (Vourlidas *et al.*, 2000; Colaninno and Vourlidas, 2009; Pluta *et al.*, 2018). The asymptotic CME mass is determined using the analytical function given by Colaninno and Vourlidas (2009):

$$m(r) = m_{obs}(1 - e^{-r/X}), \tag{3.32}$$

where $m(r)$ is the measured mass at a certain height of the CME's apex, m_{obs} the asymptotic final (observed) CME mass and X the fitted normalisation height.

The calculated CME mass is affected by the uncertainties of assumptions additional to the actual measurement errors. Concentrating on the effects of Thomson scattering analysing the consequences of the $\phi = 0°$-assumption, Vourlidas *et al.* (2000) showed, that using this method, determined masses may be underestimated by a factor up to ~ 2 depending on the CME width, which was supplied by the MHD simulations of Lugaz, Manchester, and Gombosi (2005). On the other hand, Vourlidas *et al.* (2010) found in a numerical study considering the effects of the approximation of the "directional mass determination" an exponentially growing mass overestimation if $\phi > 60°$ to the POS. Under this angle the "directional mass determination" seems to be more accurate than the $\phi = 0°$-assumption. Other errors in the mass measurement are related to brightness contributors not substracted by the base difference image and being in the ROI. Planets do frequently enter the FOV of coronagraphs and cause effects like blooming on the camera sensors. While CMEs are ejected, they, or their shocks, can interact with streamers resulting in a deflection or the change of their brightness. This effects are difficult to reject with a base difference image. Prominences can affect mass determination due to strong Hα emission occurring from a larger fraction of neutral hydrogen at its cooler temperature (see Figure 2.9). Since the passband of some coronagraphs is centred at the

Hα-line this could produce a local maximum in the mass-height profile (Carley, McAteer, and Gallagher, 2012).

3.4.5 The Effect of Virtual Mass

The concept of *virtual* or *added mass* describes in fluid dynamics the additional inertia occurring in a system, in which a moving body is interacting with its ambient medium. The accelerated or decelerated body displaces and accelerates through momentum coupling some volume of the ambient fluid. As discussed in Section 3.3, a CME moving in the ambient solar wind may be treated as a rigid body in a hydrodynamic flow. In this case, the effect of virtual mass must be included in the force consideration and the total CME mass m_{CME} is the sum of the true observed mass m_{obs} and the virtual mass m_v. The virtual mass of a sphere moving in a fluid is approximately half of the mass of the displaced fluid (Landau and Lifshitz, 1987; Cargill *et al.*, 1996). By expressing this formulation with the volume of a CME V_{CME} and the solar wind density ρ_w, the total mass of a moving CME is:

$$m_{CME} = m_{obs} + m_v = m_{obs} + \frac{\rho_w(r) V_{CME}}{2}. \tag{3.33}$$

Cargill (2004) investigated the effect of virtual mass on the dynamics of CMEs in MHD simulations. He showed, that as closer the ratio between CME and ambient solar wind densities becomes unity, virtual mass plays an increasingly important role in the value of the drag coefficient and so for the CME dynamics.

3.5 Summary

Summarising the keynotes of CME kinematics and the properties of their corresponding solar source regions, it is important to note that the forest of developed CME triggering mechanisms is dense, interwoven and in some parts very dark. The role of magnetic reconnection is in the meanwhile general accepted, but since it is difficult to observe a CME's initiation in detail, the evaluation of triggering mechanisms relies on more extended studies. MHD simulations provide a good opportunity to test models and compare the results with magnetograms, observations of the lower corona and the evolved CME structures in coronagraph images. In a number of cases this was realised successfully. However, they are computationally expensive. Also observations are affected by projection effects and uncertainties making comparisons sometimes challenging. In order to analyse the initial Lorentz force accelerating a CME, the TI model provides a fully analytical model considering the observed FR nature and geometry of CMEs. After the initial phase of the CME acceleration is finished, the aerodynamic drag force dominates the further evolution of the CME propagation and dynamics in the heliosphere. Even if the presented DBM-model is a simple 1D model, its success in the adequate description of the interaction between CME and ambient solar wind as well as the accurate extrapolation of CME quantities, validated through in-situ measurements, was shown in several studies.

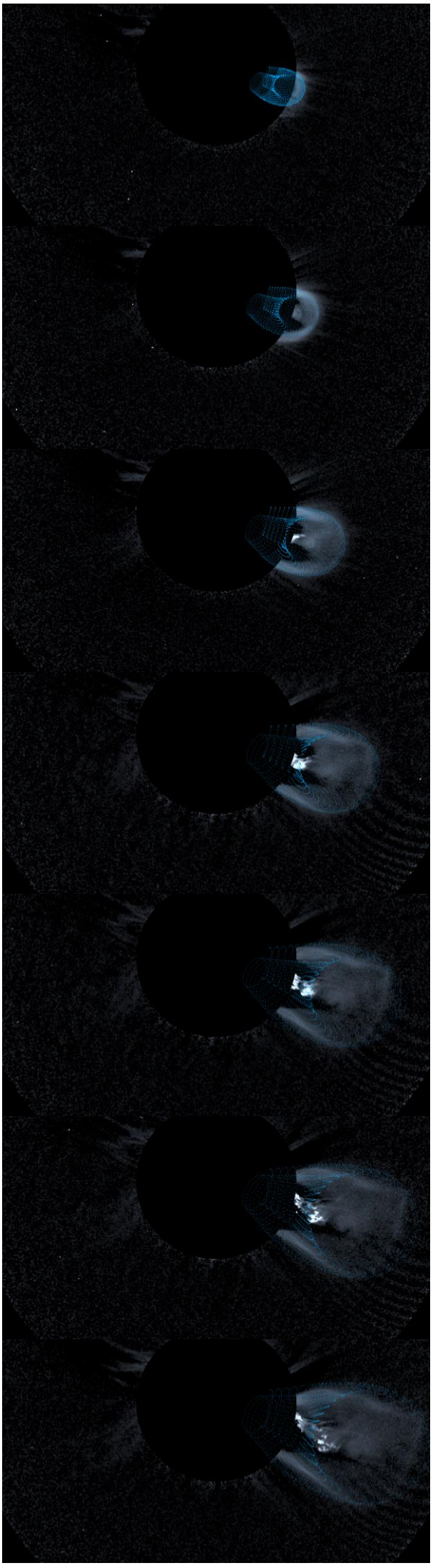

Chapter 4

Missions, Data and Methods

"It is hard to describe the exact route to scientific achievement, but a good scientist doesn't get lost as he travels on it."

Isaac Asimov

Monitoring a CME from its birthplace on the Sun up to its passage near Earth requires a set of imagers observing in different parts of the electromagnetic spectrum, as well as in-situ instruments measuring the plasma properties. While magnetic imagers measure the photospheric magnetic conditions of a CME's SR, the initial acceleration phase of a CME can be observed using EUV observations under certain conditions. In the inner heliosphere, remote white light observations from coronagraphs and heliospheric imagers are the main data set used to analyse a CME's trajectory and dynamics. Finally, the arrival near Earth, at the Lagrange point L1, and the changes to the ICME kinematics by the interaction with the ambient solar wind can be measured by in-situ plasma instruments. In order to explain a CME's trajectory under the influence of the ambient solar wind and its real 3D kinematics, events for which multi-viewpoint observations taken from different satellites exist, are selected using specific criteria. The CME height-time-profiles achieved from this remote sensing instruments are analysed with a TI Lorentz force and a dynamic drag based model. For this purpose, the CME geometry, its mass and its propagation direction is taken into account.

Cover Figure: Time series of SECCHI/COR1 B observations of event #1. For more details see Table 4.2. The GCS fit is shown by the blue grid.

4.1 Remote Sensing and In-situ Instruments

In order to study the CME kinematics and the magnetic properties of their corresponding SR, adequate analysis methods have to be chosen. This includes a careful selection and inspection of the necessary data sets required for the methods of choice. Since CME observations depend on space borne instruments, in the coronal and heliospheric case, data from ongoing satellite missions were taken for analysis. In the following, an overview of ongoing heliospheric spacecraft missions and their instruments, with special emphasis on the instruments recording the data used in this work, is given. Afterwards, the criteria to reduce the available data to a relevant selection are explained. In the final part, the applied analysis methods to obtain a CME's SR, kinematic and geometric properties are outlined.

4.1.1 Ongoing Satellite Missions

The Solar and Heliospheric Observatory

One of the success stories in ESA's and NASA's instrumentation history, and still the flagship of the fleet, is the SOHO mission launched in December 1995. The satellite is placed in a halo orbit around L1 and its continued operation is extended up to at least 2020.[1] An extension until 2022 is expected, but extrapolation of the degradation process of SOHOs solar cells indicate a critical power loss around this time.
The instruments building SOHOs payload are organised into three groups: Helioseismology with three instruments, solar atmosphere remote sensing with six instruments (see Section 4.1.4 and 4.1.3) and solar wind in-situ measurements with three instruments. This combination of experiments showed the complex magnetic connections between the single solar atmospheric layers and the Sun's interior, since they could be observed in parallel for the first time. This led to new insights into the Sun's structure and its rotational behaviour (Fleck 2005 and references therein), the first observations of a flare-triggered "solar quake" (Kosovichev and Zharkova, 1998) and, despite the fact that CMEs were already discovered during the time of the OSO-7 and Skylab ATM coronagraphs, it were the SOHO observations boosting our understanding of CMEs to the current state. Moreover, space weather forecasts for Earth's magnetic environment were made possible by the continuous monitoring of the corona and inner heliosphere. Using single-viewpoint data doesn't allow for deprojection of the POS-observations, and because CMEs are optically thin, the exact 3D nature of CMEs is hard to determine. Because of that, the mission concept of the following solar observatory (see below) was quite different.

The Solar Terrestrial Relations Observatory

Launched in October 2006, STEREO is NASA's third Solar Terestrial Probe (STP) mission consisting of the two nearly identical spacecrafts STEREO A (Ahead) and B (Behind), which were carried into Earth-like orbits around the Sun. While STEREO A's orbit is a little bit closer to the Sun compared to Earth's orbit, the orbit of STEREO B is a little bit further away. In this way, the angular separation of the satellites changes continuously by about 44-45°a^{-1} (Kaiser *et al.*, 2008) providing the first stereoscopic observations of

[1] http://sci.esa.int/director-desk/59839-green-light-for-continued-operations-of-esa-science-missions/ (13.12.19)

the Sun and its energy as well as matter flow from different vantage point. The scientific objectives of the STEREO mission are (Kaiser *et al.*, 2008):

- Understand the causes and mechanisms of CME initiation.
- Characterise the propagation of CMEs through the heliosphere.
- Discover the mechanisms and site of energetic particle acceleration in the low corona and interplanetary medium.
- Develop a 3-D time-dependent model of the magnetic topology, temperature, density and velocity of the ambient solar wind.

To achieve these objectives, both STEREO spacecrafts contain four complementary instrument suits to reach a better understanding of CMEs, SEPs and the solar wind. The SECCHI package comprises four imaging instruments to track solar transients and CMEs from their ejection region in the low corona up to Earth distance at 1 AU (see a detailed explanation in Sections 4.1.4, 4.1.5 and 4.1.3) which was first observed and analysed by DeForest, Howard, and McComas (2013) and a great step forward in terms of space weather prediction. In order to track radio bursts generated by stream of energetic electrons and shockwaves of CMEs in the solar wind (see Section 2.2.1), the *S/WAVES* (STEREO/WAVES, Bougeret *et al.* 2008) instrument was developed. The antenna system is capable to perform 3D localisation of radio emissions with the three mutually orthogonal monopole stacer antenna of six meter length, which cover a frequency regime from below 1 Hz up to 16 MHz and with a narrow frequency channel at 30 MHz. In-situ measurements are performed by two instrument suites. The first is the *In-situ Measurements of Particles and CME Transients* (IMPACT, Luhmann *et al.* 2008) suite consisting of seven instruments, that measure the 3D distribution of the solar wind, superthermal electrons, the IMF and SEPs. The fourth suite, the *PLAsma and SupraThermal Ion Composition* (PLASTIC, Galvin *et al.* 2008) investigation complements the solar wind measurements of IMPACT by providing the in-situ plasma mass and charge state of protons, alpha particles and heavy ions.
The STEREO spacecrafts were launched in October 2006 and reached opposition in 2011. After a planned reset to test solar conjunction commands, the contact with STEREO B was lost in October 2014. During the superior solar conjunction in March 2015, STEREO A was operating in a safe mode to protect the high gain antennas from damage by solar radiation. After the conjunction, when a larger angular separation to the Sun was reached, STEREO A started sending data again in July 2015. Using NASA's Deep Space Network (DSN) the contact to STEREO B was reestablished in August 2016. It was found that because of an anomaly in the guidance and control system the satellite lost its orientation and started uncontrolled spinning.[2]

The Solar Dynamics Observatory

The first mission launched as part of NASA's *Living with a Star* (LWS) program is the SDO. It provides nearly continuous observations of the Sun in different wavelengths and

[2]News of the STEREO mission: https://stereo.gsfc.nasa.gov/news/news.shtml (13.12.19)

high spacial resolution with a rapid cadence. The data of SDO are of unprecedented quality and reveal the details of the highly dynamic nature of the solar corona, e.g. coronal rain (Mason, Antiochos, and Viall, 2019). Three scientific experiments, to investigate the deeper processes of the solar activity, are mounted on the spacecraft. AIA (see Section 4.1.3) is an imager linking the solar surface with the higher atmospheric layers. The variability of the solar EUV radiation affecting Earth's ionosphere is measured with the *EUV Variability Experiment* (EVE, Woods *et al.* 2012). An evolution of SOHO's *Michelson Doppler Imager* (MDI) instrument is the Helioseismic and Magnetic Imager (HMI, Schou *et al.* 2012) taking full-disk higher spatial resolution magnetograms with new vector magnetogram capabilities (see Section 4.1.2). Since the high resolution and the rapid cadence require a downlink rate of more than 100 Mbps, SDO was placed in an inclined geosynchronous orbit around Earth.

The Advanced Composition Explorer and Wind

In order to measure the characteristics and composition of the solar wind, SEPs and cosmic rays, the *Advanced Composition Explorer* (ACE, Stone *et al.* 1998) and the *Wind* (Ogilvie and Desch, 1997) spacecraft were placed outside of Earth's magnetosphere at the Lagrange point L1. Both satellites complement each other with their different spectrometer charge analysers and magnetometers to measure the IMF parameters, the ionic charge states and the energies and masses of different ions, protons and electrons. Using Wind data, Kasper *et al.* (2013) showed that ion cyclotron resonance is a possible explanation for the heating and acceleration of the solar wind.

4.1.2

4.1.2 Magnetographs

Since Hale (1908) linked the magnetic field of sunspots with the solar activity, the need to study the solar magnetic field and the magnetic activity cycle arose. The magnetic field in the Sun's plasma can be determined using the Zeeman effect, which describes the splitting of spectral lines in the the presence of a magnetic field. Space-borne instruments to measure the entire photospheric magnetic field are currently the magnetographs onboard SOHO and SDO.
The HMI instrument is part of the SDO payload and is an advanced version of MDI onboard of SOHO especially in terms of temporal and spatial scales. For this reason, the magnetorgrams taken with HMI are used for the SR analysis in this work. Both instruments are so called filtergraphs, taking sequences of filtergrams in different polarisation states at different wavelengths around a spectral line with a large Landé factor (MDI: 676.8 nm Scherrer *et al.* 1995; HMI: Fe I 617.3 nm Schou *et al.* 2012). From these raw-filtergrams, the Stokes parameter are calculated and continuum intensity images, longitudinal and vector magnetograms as well as Dopplergrams are generated (Scherrer *et al.*, 2012). Line of sight (LOS) magnetograms are produced with a cadence of 45 s, and also a 12 min average of the longitudinal magnetic field is generated to track the evolution of the photospheric magnetic field. HMI uses two 4k x 4k CCDs and reaches a resolution of 0.5 ”/px, which is more than twice as good as the resolution of MDI.

4.1.3 EUV Imagers

The chromosphere, the transition region and the lower corona are typically observed in emission lines of highly ionised iron species, helium and carbon in the extreme ultraviolet. Since their emission characteristics depend on the temperature, which is the predominant parameter defining the different layers of the solar atmosphere, the height at which the corresponding emission line is formed can be associated (Lemen *et al.*, 2012). In this work, data of the EUVI instrument of the STEREO/SECCHI suite and the AIA EUV-imager on SDO were analysed.

The EUVI instrument of STEREO is based on the successful concept of the EIT instrument onboard of SOHO. It is a Ritchey-Chrétien telescope whose entrance aperture is divided into quadrants/channels and covered by thin narrow-band metal filters blocking most of the UV, visible as well as IR light. The single quadrants/channels take images at the wavelengths 17.1 (Fe IX), 19.5 (Fe XII), 28.4 (Fe XV) and 30.4 nm (He II) with a cadence of 5 min (Howard *et al.*, 2008). By using a 2k x 2k backside illuminated CCD, a FOV of $\pm 1.7\,R_{\odot}$ (POS) centered on the Sun and a plate scale of 1.6 ”/px is covered (Howard *et al.*, 2008).

AIA onboard of SDO consists of four Cassegrain telescopes observing ten wavelengths in the EUV-, UV- and visible regime between 9.4 and 450 nm. A detailed instrument descriptions is given by Lemen *et al.* (2012). All four telescopes have their own guide telescope and image-stabilization systems, which ensures a highly precise coalignement and the elimination of jitter by the spacecraft to under 0.24 arcsec in each axis. The baseline-cadence for one EUV and one UV or visible-light image is 12 s with a full-frame resolution of 4k x 4k, corresponding to a plate scale of 0.6 ”/px and a FOV of 41 arcmin circular diameter (Lemen *et al.*, 2012). Together with the HMI instrument, ARs can be mapped from their photospheric source up to the lower corona and at the high cadence of AIA the evolution can be tracked in very high detail.

4.1.4 Coronagraphs

A coronagraph is a special type of telescope optimised to observe the faint solar corona by blocking the light of the visible solar disk (Lyot, 1939). For this purpose, an optical element called occulter, which is comparable with the moon during a total solar eclipse, is used. Since the scattered sunlight by the Earths atmosphere is too bright to observe coronal structures around the Sun, space-borne coronagraphs are much more effective in terms of usable FOV, data quality and available observation time than ground based instruments. Active coronagraphs are the LASCO/C2 and LASCO/C3 instruments onboard SOHO and the SECCHI/COR1 and SECCHI/COR2 instruments onboard the STEREO spacecrafts. The key-data used in this work were recorded with the COR1 and COR2 instruments and the C2 and C3 coronagraphs, which are described in the following. Their main characteristics are summarised in Table 4.1.

LASCO/C2 and LASCO/C3 are externally occulted coronagraphs using the principles described by Evans (1948). However, the faint coronal signal is still covered by the internal stray light of the instrument. But, the instruments stray light is unpolarized while the ob-

served light is highly polarized by the nature of Thompson scattering (see Section 3.4.1). By observing in three different linear polarization states and calculating the polarized brightness (see Billings 1966), the scattered light of the instrument can be nearly eliminated. For this reason, every image acquisition sequence contains three images taken with different polarizers in C2 and C3. Besides the three polarizers, C2 and C3 are equipped with a combination of 7 broad- and narrow-band filters for the spectral range of 400 to 1050 nm. Both coronagraphs are equipped with 1k x 1k CCDs and together they cover a FOV of 1.5 up to 30 $R_\odot$ in the POS, with a resolutions of 11.4 and 56 ”/px, respectively (Brueckner *et al.*, 1995).

The first space-borne internally occulting refractive coronagraph, SECCHI/COR1, covers a FOV of 1.3 to 4 $R_\odot$ (POS). Together with the high cadence of 5 min, this allows the observation of the early CME evolution. The internal occulting design was chosen, since it provides better spatial resolution in the inner FOV (Howard *et al.*, 2008). Like the LASCO coronagraphs, the SECCHI coronagraphs take a sequence of three images with polarizations 0° and ±60°. To avoid smearing of the changing coronal structures, the image sequence is taken within a time range of 11 s. COR1 observations are not made in the full white light spectral regime like other coronagraphs but with a 22.5 nm wide bandpass filter centred around the H_α-line. The CCD of COR1 is of 1k x 1k size, leading to a plate scale of 3.75 ”/px.

The SECCHI/COR2 coronagraphs are inspired by the successful design of the SOHO LASCO/C2 and LASCO/C3 instruments and are externally occulted, ensuring a lower level of stray light compared to SECCHI/COR1, which allows CME observations at greater elongations. Because of the requirement to finish the whole polarized image sequence within 15 s to avoid smearing of fast CMEs, the optical design has a higher light gathering power than the LASCO coronagraphs. This was achieved by increasing the entrance aperture, using a 2k x 2k CCD (for a spatial resolution comparable to the one of C2) with 80% quantum efficiency and changing the polarizer material to better match the solar spectral peak (Howard *et al.*, 2008). The FOV of SECCHI/COR2 is 2 to 15 $R_\odot$ (POS), with a resolution of 15 ”/px and a cadence of 15 min. Additionally, SECCHI/COR2 has a multi exposure observation mode that takes images at polarisation angles of 0° and 90°. The resulting image corresponds to a total brightness image, saving telemetry costs and increasing the cadence. Low resolution total brightness images of SECCHI/COR2, calculated onboard with a polarized image sequences, are transmitted continuously via the beacon channel, which is useful for space weather purposes.

The LASCO as well as the SECCHI coronagraphs are designed to have an overlap between the different FOVs allowing a gapless observation of CMEs, which is shown in Figure 4.1 by some example observations from the SECCHI instruments. Although the STEREO A and B instruments are nearly identical, there are differences in the data quality because of the slightly different orbits, but also for technical reasons like thermal bending of the SECCHI/COR 1 occulter stem or a slight change in the SECCHI/COR2 B instrument pointing.

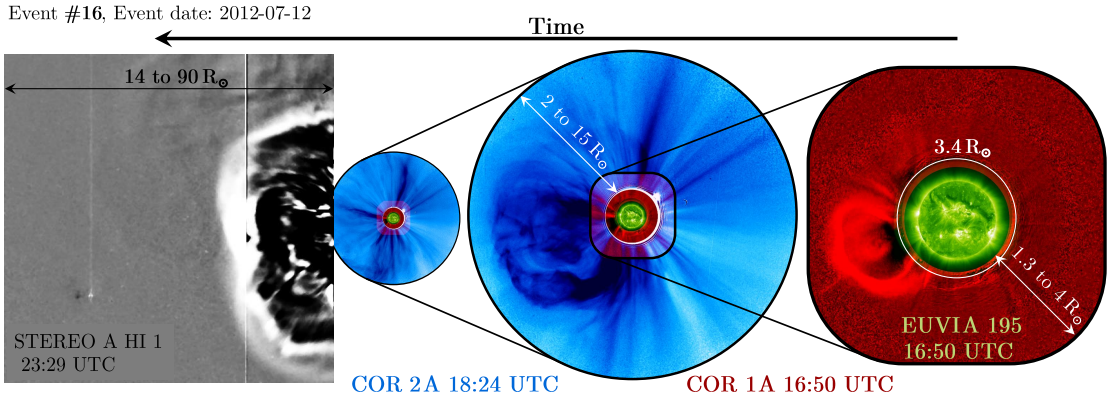

Figure (4.1) STEREO A/SECCHI observations of event #16 (see Table 4.2) on July 12, 2012. From left to right images from HI1, COR2, COR1 and EUVI 195. Images were processed with the program ESA JHelioviewer[3]and illustrate the different FOV to observe the individual evolution stages of the CME.

4.1.5 Heliospheric Imagers

4.1.5

A heliospheric imager is a wide-angle white-light camera that is off-pointed from the Sun to observe the solar wind as well as CMEs propagating through the heliosphere. Observing the faint scattered light of CMEs in the outer corona and inner heliosphere sets enormous requirements onto the optical specifications of such an instrument. Since the CME signal in this range is about two orders of magnitude fainter compared to the summed intensity of the background K and F corona (Socker *et al.*, 2000), the instrument stray-light should be at least an order of magnitude below the coronal intensity to exclude a significant contribution to the statistical error of the required long time exposures. Considering elongation angles from the Sun up to about 90°, the stray-light level has to be in a range of 10^{-13} to 10^{-14} $B_\odot$ (Eyles *et al.*, 2009).
As the first instruments of their kind, the heliospheric imagers HI1 and HI2 are part of the STEREO/SECCHI suite. A complex multi-baffle system blocks direct sunlight and ensures that stray-light of the spacecraft components can not enter the optical systems. The two wide-angle cameras of HI1 and HI2 cover elongation angles of 4° - 24° and 18.7° - 88.7°, respectively (Eyles *et al.*, 2009). The CCDs have a size of 2k x 2k, but a 2 x 2 binning is used. Taking the observation criteria mentioned above into account, exposure times of 20 min and more than 1 h are needed to reach the required signal to noise ratio for HI1 and HI2. The HI instruments on both STEREO spacecraft made it possible to track CMEs to heliospheric distances of Earth's orbit and beyond for the first time, but also to stereoscopically measure the 3D properties of CMEs at this distance.

4.2 Data Analysis

4.2

The data analysis requires a clearly defined data selection procedure, which is based on selection criteria, in advance to the individual analysis steps. After the data selection, the data have to be corrected from instrumental effects and to remove the background corona.

[3]https://www.jhelioviewer.org/index.html (13.12.19)

Table 4.1. List of satellites and their instruments whose data are used in this work. The FOV is given from solar centre to detector edge. Remote sensing instruments are indicated by RS and in-situ instruments by IS.

Satellite Suite	**Instrument**	**Type**	**Observation**	**FOV** [$R_\odot$, °]	**Resolution** [”/px]	**Cadence** [min]	**Analysis**
SDO [a]	AIA[b]	RS EUV Imager	CME precursors SR and CME	0.3, 1.5	0.6	1/5	SR: Geometric and magnetic properites
	HMI[c]	RS Magnetic Imager	Photospheric LOS mag. field	0.55, 0.29	0.91	12	
SOHO[d] LASCO[e]	C2	RS White light coronagraph	CME structure and POS height	1.5-6 , 0.4-1.6	11.4	12	CME geometry and kinematics
	C3			3.7-30 , 1.0-8.1	56	12	
STEREO[f] SECCHI[g]	EUVI 195	RS EUV Imagerr	CME precursors SR and CME	1.7, 0.4	1.6	5	CME geometry and kinematics
	COR1	RS White light coronagraph	CME structure and POS height	1.3-4.0, 0.3-1.0	3.75	5	
	COR2			2-15, 0.5-4.0	15	15	
	HI1	RS Heliospheric Imager	CME POS height	14-90 , 20	70	40	CME kinematics
ACE[h]	MAG[i]	IS Magnetometer	In-situ mag. field			1	L1 CME kinematics
	SWEPAM[j]	IS Particle Monitor	Plasma properties				

[a] Pesnell, Thompson, and Chamberlin (2012), [b] Lemen *et al.* (2012), [c] Schou *et al.* (2012).
[d] Domingo, Fleck, and Poland (1995), [e] Brueckner *et al.* (1995).
[f] Davila *et al.* (1996), [g] Howard *et al.* (2008).
[h] Stone *et al.* (1998), [i] Smith *et al.* (1998), [j] McComas *et al.* (1998a).

Since the data are corrected, the individual analysis steps to determine SR and CME kinematic characteristics, which are explained in more detail afterwards, can be applied.

4.2.1 Data Selection Criteria and Procedure

In the first step for a systematic study to answer the question about the relationship between a CME's SR and it's kinematic behaviour, the requirements on the event selection, data and methods for analysis have to be defined. The starting point is to consider, which model is used to describe the CME kinematics and which CME quantities are necessary for this purpose. In this work the dynamic drag model described in Section 3.3 is chosen to study the outer trajectories of CMEs, which means that CME height-time (r-t) profiles, with a wide range and low uncertainties beginning at the early stages close to the Sun and extending far into the heliosphere, are needed. In order to avoid projection effects and to get the real 3D CME propagation, the GCS model (see Section 3.4.2) is applied to data from the EUV-imagers, coronagraphs and helioshperic imagers of the SOHO and STEREO spacecrafts. To validate the extrapolated drag model of the CME trajectories and the solar wind properties, only events with in-situ measurements from L1 are selected. The second that has to be considered in the selection of events, is the availability of SR parameters. Magnetograms are taken continuously by SOHO and SDO. Both satellites have the same perspective and observe the part of the solar photosphere facing Earth. However, SDO has a higher telemetry compared to SOHO since it is placed in an Earth orbit. Because of that the magnetograms of HMI and images of AIA are of higher spatial resolution and higher cadence making time resolved magnetic and EUV observations of CME SR possible. Bringing both considerations together we obtain following data selection criteria:

- The events have to lie within in a time interval of 22 months after the opposition of the STEREO spacecrafts, which was reached at February, 6 2011. Due to the separation angle of the three satellites to each other between 90° and 130° (see Figure 4.2 a and b), most different perspectives are available favouring 3D modelling.
- Only Earth directed events for which in-situ as well as magnetogram and EUV images are available, allowing drag model comparison and SR analysis, are selected.
- To minimise projection effects, only events with simultaneous coronagraph observations from both STEREO and SOHO spacecrafts are chosen. This criteria excludes observation with large data gaps from one of three viewpoints ($\Delta t > 60\,\mathrm{min}$).
- The events have to be visible in COR1 and HI1 to extend the r-t profile down to the SR ($r < 2\,\mathrm{R}_\odot$) and further outward into the heliosphere ($r \sim 80 - 100\,\mathrm{R}_\odot$). Data from HI2 are excluded since GCS modelling within its FOV is a highly difficult task and the results would not be a benefit through the reduced fit-quality.
- The white light appearance of CME features in the images has to be bright and clear enough to allow GCS fitting with high precision and small uncertainties. In other words, the CMEs should show a clear morphology (see Bosman *et al.* 2012).

By applying the above set selection criteria, events were selected by the following procedure:

1. In order to find Earth-directed CMEs, the *SOHO LASCO CME Catalogue* provided by the *Coordinated Data Analysis Workshops* (CDAW) Data Center of NASA [4] was searched for partial and full halo CMEs within the time range of 22 months after the opposition of the STEREO spacecrafts. Partial or full halo CMEs propagate along the observers LOS since they cover the solar disk.

2. To exclude backside events and to fulfil the criteria of simultaneous coronagraph observations from different viewpoints, the CME candidates were identified in STEREO A and B data. By combining the CME propagation direction as seen in the STEREO observations with the information of the SOHO LOS, the Earth-directed events were identified. Additionally, only events clearly visible in both STEREO spacecrafts were selected.

3. All events selected so far were inspected to be visible in EUVI 195, COR1, COR2 and HI1 without showing large data gaps of more than a few minuets, ensuring the continuity of the CME trajectory. The compiled video sequences of the STEREO Science Center were used for this purpose.

4. For all events, SDO/AIA and HMI data were checked with the IDL tool of the *Virtual Solar Observatory*[5] for availability within ±8 hours around the first EUVI 195 or COR1 observations of the selected events.

5. In the final step, in-situ data of ACE and Wind are surveyed for ICME signatures within eight days after the first appearance of the CME in COR1.

The basis of the second step of this procedure is the *Kinematic Database Catalogue* (KINCAT)[6] of the EU FP-7 project *Heliospheric Cataloguing, Analysis and Techniques Service* (HELCATS)[7], which was created at the Institut für Astrophysik in Göttingen by me and Adam Pluta under the lead of Volker Bothmer. The objectives of the HELCATS project were the systematic exploration and cataloguing of the STEREO observations, in particular SECCHI COR2, HI 1 and HI 2 data. The KINCAT catalogue contains the averaged geometries, the linear speeds and masses of 122 CMEs observed between May 2007 and October 2013. All events were modelled with the GCS model, which was applied to SECCHI/COR2 coronagraph observations of both STEREO spacecrafts. Detailed explanation of the applied techniques and catalogue data of the HELCATS project can be found in Harrison *et al.* (2018); Pluta *et al.* (2018); Murray *et al.* (2018) and Barnes *et al.* (2019).

According to the selection criteria and procedure, 21 events in the time range between July 8, 2011 and November 21, 2012 were selected for analysis. Their basic observational characteristics are listed in Table 4.2. The positions of the STEREO spacecrafts at the times of the first and last events as well as the time interval of the data set in the solar cycle are represented in Figure 4.2. Except for five events, EUVI images are available for all selected CMEs to analyse their very early kinematics and geometry.

[4] https://cdaw.gsfc.nasa.gov/ (13.12.19)
[5] https://docs.virtualsolar.org/wiki/VsoIDL (13.12.19)
[6] http://www.affects-fp7.eu/helcats-database/database.php (13.12.19)
[7] https://www.helcats-fp7.eu/index.html (13.12.19)

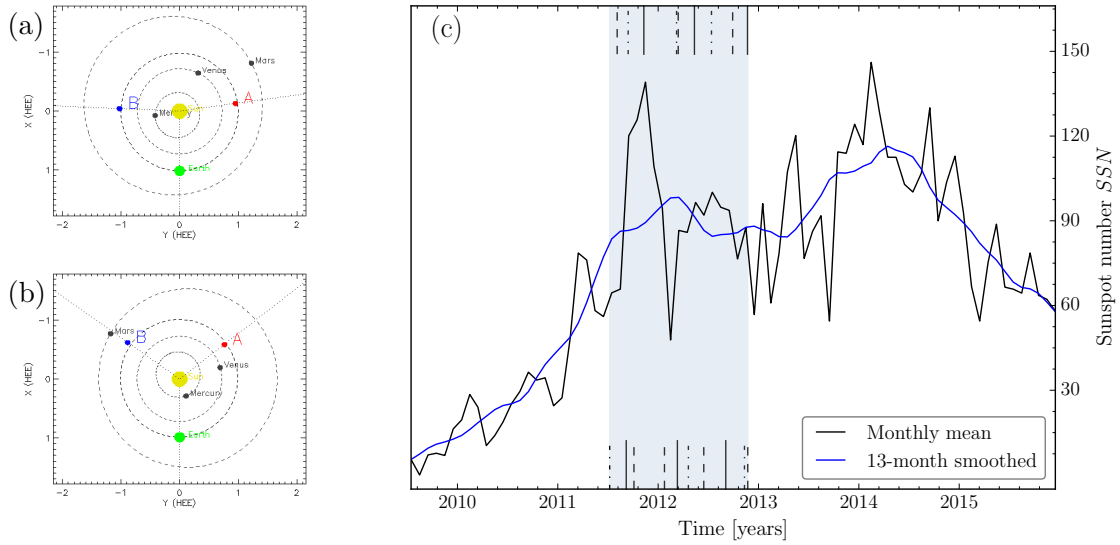

Figure (4.2) (a) and (b) Positions of the spacecrafts at the time of event #1 and #21 generated with the STEREO Orbit Tool[8]. (c) Monthly mean (black) and 13-month smoothed (blue) Sunspot number of solar cycle 24. The light blue area represents the time range of the analysed ensemble and vertical solid, dashed and dot-dashed lines show the times of the single events.

4.2.2 Data reduction and Processing

4.2.2

Before images from STEREO, SOHO and SDO can be used for analysis, they have to be reduced and corrected from optical effects like vignetting and electrical characteristics like image sensor bias. The individual processing steps are done with IDL Solarsoft (Ware) (SSW) system, a software environment written in IDL containing data bases and libraries to analyse solar physics data from space borne missions.

STEREO/SECCHI uncompressed 16-bit fits images are available in Level-0.5 from several sources (e. g. NASA Stereo Science Center[9] or UK Solar System Data Centre[10]). The top of the images is already aligned to the ecliptic north and the header contain telemetry as well as auxiliary data. By using the routine `secchi_prep.pro`, the images were processed to Level-1.0, which contains a normalisation by the exposure time, a conversion to the physical units of MSB and the correction of vignetting and other optical distortions, flat-field frame, bias-frame as well as the correction of image processing done onboard of the satellites (Howard *et al.*, 2008). While COR1 Level-1.0 data are processed from a sequence of the three polarized images to one total brightness, COR2 Level-0.5 images are already available as total brightness images. The data processing of SECCHI/HI images requires some additional steps to those mentioned above for the reason of the different instrument design. The HI cameras have no shutter leading to a vertical smearing during the CCD clearing prior to an exposure and the read out of the CCD. By using a ma-

[9]https://stereo-ssc.nascom.nasa.gov/pub/ (13.12.19)
[10]https://www.ukssdc.ac.uk/solar/stereo/data.html (13.12.19)

trix multiplication algorithm, the images are de-smeared. While this correction was done with `secchi_prep.pro`, the onboard software already performs some pre-processing steps differing from the other SECCHI instruments. One correction is a consequence of the shutterless camera design and the long exposure time of HI, causing that bright objects in the FOV, like planets or bright stars, can lead to the saturation of CCD columns. Generally these columns can not be recovered and have to be removed. Since the intensity of the scattered light decreases with radial distance to the Sun, more integration time to reach the required signal-to-noise ratio is necessary in the FOV of HI compared to the inner coronagraphs. To avoid the build up of saturated pixels by cosmic ray hits, the total integration time is split into a number of short 40 second exposure images which are summed up after they are scrubbed from cosmic ray events (Eyles *et al.*, 2009).

SOHO/LASCO coronagraph Level-0.5 images are provided by the U.S. Naval Research Laboratory (NRL)[11] and were processed in a similar way like the STEREO/SECCHI images with the SSW procedure `reduce_level_1.pro`, containing all necessary routines for the single calibration and reduction steps. The processing procedure for LASCO/C2 and LASCO/C3 data is explained in detail by Llebaria, Lamy, and Bout (2004) and Morrill *et al.* (2006)

In coronagraph (also HI) images, the background corona has to be removed using a base-difference subtraction. In general, the image taken directly prior to the sequence of interest, the "pre-event" image, is subtracted from the sequence to avoid variations due to the solar rotation or changes in the coronal configuration. By using this technique, variable or quasi-static structures like coronal streamers and also other CMEs remain in the sequence, which is why it is in some cases more suitable to select an earlier pre-event image (Vourlidas *et al.*, 2010).
In a final processing step, the images are prepared for mass determination by using the `make_mass_fits.pro` which translates from units of MSB to grams per pixel (gpp) and applies the approximations described in Section 3.4.4 (Savani *et al.*, 2013).

The science data of SDO/AIA and SDO/HMI are provided by the Joint Science Operations Center (JSOC) Science Data Processing (SDP)[12]. While the lowest available data Level of AIA images starts at Level-1.0 (in all wavelengths) HMI data are already at Level-1.5. This means all necessary reduction and calibration steps to reach science data quality are already performed. However, for multi-wavelength analysis with the various wavelength channels of AIA, the data have to be processed to Level-1.5 because of the slightly different orientations and plate scales between the different wavelengths. A co-alignment to the common pointing, rescaling to the same plate-scale and derotation was done with the SSW procedure `aia_prep.pro`. The resulting Level-1.5 data are interpolated to a plate-scale of 0.6" per pixel, aligned to the solar centre and rotated to have the north-south solar axes in the vertical image axes and the east-west axes in the horizontal image axes.

[11] https://lasco-www.nrl.navy.mil/lz/level_05/151228/c3/ (13.12.19)
[12] http://jsoc.stanford.edu/ (13.12.19)

Table 4.2. List of selected events for analysis after applying the selection criteria. Column 1 shows the event number used in the following for simplicity. Columns 2 and 3 show date, time and time range of the events while the columns 4 to 7 show the number of images taken by the different instruments on board of STEREO and SOHO. The SR type in the Hale classification scheme can be seen in the last column.

#	Date	Time obs.	# of GCS frames				SR
		First contact + [h]	EUVI	COR1/2	C2/C3	HI1	
1	08.07.11	23:40 + 13.8	15	12/9	11/21	22	β
2	04.08.11	01:55 + 14.3	1	3/4	5/26	18	β-γ
3	06.09.11	01:50 + 17.6	2	14/19	12/33	6	β-γ
4	06.09.11	22:15 + 26.5	4	10/13	8/50	33	β-γ-δ
5	13.09.11	21:55 + 31.5	3	27/15	16/45	38	β
6	04.10.11	16:10 + 38.0	-	48/25	24/29	44	H_α-plages
7	26.10.11	09:35 + 55.3	-	26/13	20/52	38	β-γ
8	09.11.11	13:06 + 13.0	5	9/9	5/31	15	β
9	23.01.12	01:15 + 18.3	18	18/5	6/17	18	β
10	07.03.12	00:20 + 17.8	2	3/2	1/23	24	β-γ-δ
11	10.03.12	17:20 + 15.2	6	8/7	3/23	18	β-γ-δ
12	13.03.12	17:20 + 20.3	2	12/11	9/21	22	β-γ
13	19.04.12	14:45 + 37.1	-	22/14	18/41	51	β
14	11.05.12	23:05 + 23.0	5	10/10	4/33	29	α
15	14.06.12	12:40 + 16.5	15	9/6	4/25	19	β-γ-δ
16	12.07.12	15:45 + 18.0	9	8/6	3/-	21	β-γ-δ
17	02.09.12	01:56 + 32.0	3	29/14	14/16	21	β-γ
18	27.09.12	23:15 + 28.3	9	10/9	4/30	37	β
19	09.11.12	14:15 + 36.4	-	14/15	9/30	45	α
20	20.11.12	11:10 + 27.6	-	22/15	9/37	34	β
21	21.11.12	15:26 + 26.0	5	9/12	9/37	30	β-γ

4.2.3 Source Region Analysis

The corresponding SRs of the selected CMEs were identified in a two-step process. In the first, existing catalogues were inspected for CME precursors and for activity phenomena associated with CMEs like solar flares, filament eruptions and PEAs. A wide time window of 8 hours prior to the first coronagraph observation was set for this purpose and results of the *Low Coronal Event Catalogue* (LOWCAT), the *Linked Catalogue of Solar, Heliospheric and In Situ CME Observations* (LINKCAT) and the KINCAT catalogue were used. These catalogues are the results of the HELCATS working packages WP 2, 3 and

4, in which ICMEs/CMEs were traced back to their solar SR.
Other catalogues used are the *GOES Soft X-ray Flare List*[13] and the SOHO LASCO CME Catalogue.
In the second step, SDO AIA data of several wavelengths, SDO HMI magnetograms and SHARP data (Bobra *et al.*, 2014) were inspected to identify the exact active regions as well as the coordinates of the CME precursors and associated phenomena found in the first step.

To obtain the magnetic field properties of the identified ARs, HMI data were processed within the collaboration of the HELCATs project by S. Murray from the Trinity Collage Dublin with the *Solar Magnetic Feature Detection and Tracking for Space Weather Monitoring* (SMART) algorithm developed by Higgins *et al.* (2011). The SMART code detects ARs by finding concentrated magnetic flux based on the growing of magnetic regions. The quiet magnetic background and transient small scale features on the photosphere are rejected by image differencing of LOS magnetogram sequences allowing the tracking of ARs and the study of their evolution over time. Standard magnetic properties as flux, field strength or area, but also more sophisticated parameter like the Schrijver R value (Schrijver, 2007) and the Falconer weighted integral over the length of the strong-gradient main neutral line WL_{SG} (Falconer, Moore, and Gary, 2008) are computed for every AR in every magnetogram for the sequence (for more details see Higgins *et al.* 2011 and Murray *et al.* 2018). A time range of ± 6 h around the eruption times with 12 min-averaged LOS magnetograms was analysed for the corresponding ARs of the dataset. At the CME eruption time, the PIL angle with respect to the solar equator was calculated with independent routines originally written by D. Jaster in the course of his Bachelor thesis at the Institut für Astrophysik, Göttingen. Also these routines make use of a region-growing-algorithm and de-projected HMI LOS magnetograms.

4.2.4 Forward Modelling

In order to record the trajectory, geometry and orientation of the individual events, the GCS model described in Section 3.4.2 was applied to processed Level-1.0 data of the SECCHI and LASCO instruments listed in Table 4.1. Initially, the time range in which the event was observed was identified for this instruments on the three spacecrafts. In the next step, the pre-event for the single sequences was chosen with particular attention to other events in the specific time ranges. Slow and faint CMEs have extended time intervals over which changes in the coronal background lead to a poor background subtraction. In these cases it can be advisable to use another later base-difference image within the time interval. To reduce the subjective influence of the modeller to a minimum, a procedure to fit the GCS model was developed based on the experiences gained in the HELCATS project. Therefore the following order was strictly respected:

1. Check the entire sequence for outstanding features (i.e. filament material) and shocks in the white-light appearance of the CME. By tracking these features over the image sequence, the overall CME evolution can be estimated.

2. Fit all concurrent observations in the three perspectives of the spacecrafts to model the orientation in space (ϕ_{CME}, θ_{CME} and Γ_{CME}) of the CME. The maximal tolerable

[13] ftp://ftp.ngdc.noaa.gov/STP/ (13.12.19)

time gap between the images from different perspectives is $\Delta t = 2\,\mathrm{min}$ to declare them as concurrent.

3. Fit times at which the CME is visible in overlapping FOVs of different cameras. This excludes the loss of tracking of the leading front of the CME since it can appear brighter or fainter through the different instrument sensitivities especially at the overlap of COR2 and HI1.

4. Fit all other available images in between the already fitted concurrent and overlapping FOV observations.

All steps should be performed in chronological order of the observation, since the shape of the CME could evolve and is affected by the surrounding medium. Every time is modelled dynamically. Therefore, all six GCS parameters are free variables and were fitted independently. This is different to the HELCATs project or other studies that use the assumption of a complete self-similar expansion, where the apex height is fitted as free parameter while the other parameters are fitted once and kept fixed for the complete image sequence.

Using the r-t-profiles obtained in this way, the basic kinematic characteristics as velocity-, and acceleration profiles were determined. The CME masses were measured by converting the Level-1.0 data to mass-images as described in the Sections 3.4.4 and 4.2.2 by using the fitted GCS geometries and orientations.

4.2.5 Solving the Equation of Motion

The equation of motion of a CME is given in Equation 3.12 including the Lorentz force and the MHD drag force. This differential equation can not be solved analytically and a numerical solution deals with a large set of unknown variables. For this reason, the problem was split into two parts. To analyse the CME kinematics in the inner heliosphere, the recorded r-t-profiles were analysed with the DBM introduced in Section 3.3. The model inputs are the GCS r-t-, α-r- and κ-r-profiles as well as the calculated CME mass M_{CME} obtained from GCS fitting. Since all variables in this drag-only approach of a DBM depend on the distance to the Sun, the model can be considered as completely dynamical. Žic, Vršnak, and Temmer (2015) suggested a possible method to determine the free parameters of the model by minimising the residuals. The model presented here works in a similar way, where the ordinary differential equation given in Equation 3.13 is successively solved with an alternating set of input parameters. For every solution, the coefficient of determination (R^2), which is:

$$R^2 = 1 - \frac{\sum_{n=0}^{N}(r(t_n) - r_{\mathrm{D}}(t_n))}{\sum_{n=0}^{N}(r(t_n) - \bar{r})}\,, \tag{4.1}$$

is computed and maximised by minimising the residuals between all CME height measurements $r(t_n)$ and the computed DBM solution $r_D(t_n)$. Free parameters of the model are the solar wind speed at 1 AU $w_{1\,\mathrm{AU}}$, the solar wind proton density at 1 AU $n_{1\,\mathrm{AU}}$ as well as the height r_0 and velocity v_0 at which the drag becomes the dominating force. The fitting routines, written in *python*[14], include the calculation of the CME cross sec-

[14] https://www.python.org/ (13.12.19)

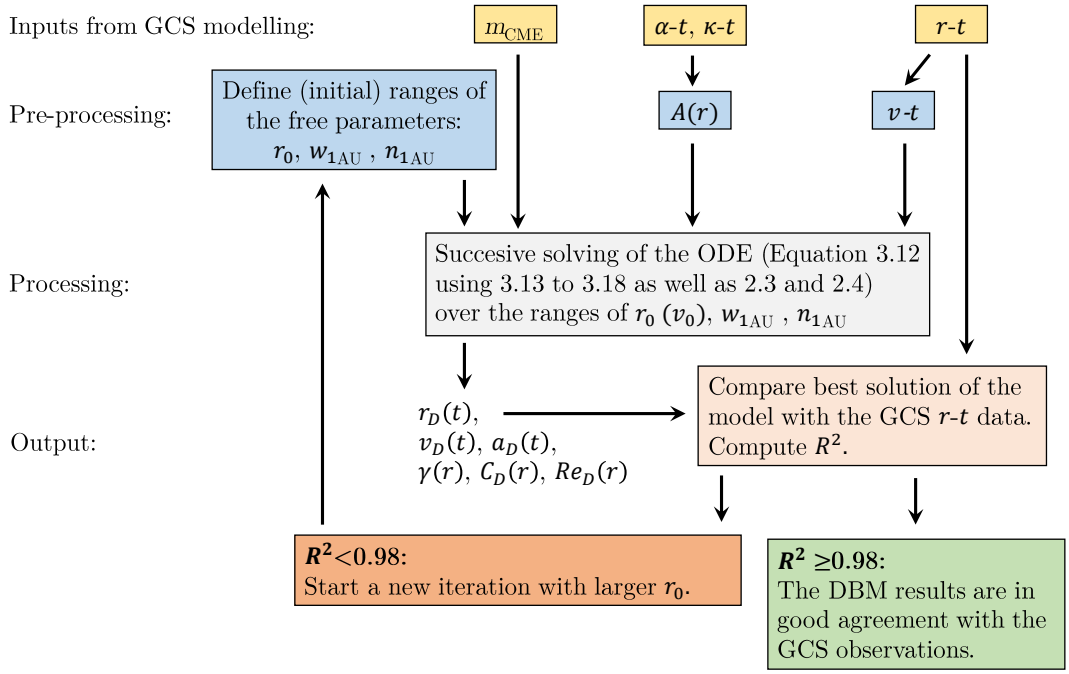

Figure (4.3) Scheme of the developed drag-only algorithm, solving the DBM introduced in Section3.3.

tion and determination of v_0 from the r-t-profile to find automatically the best matching input-parameter set. A scheme of the algorithm is shown in Figure 4.3.

To analyse the kinematics in the inner heliosphere and to verify the fitted parameter, the code was executed with two data-sets differing in direction of motion: Once in the direction of the fitted GCS apex and again with the CME component directed to L1 and the Earth that was calculated by the transformation of the r-t-profile. The model parameters, obtained from the corrected height-time profiles in Earth direction (r_E-t-profile), and the extrapolated CME drag-trajectory was finally compared with the in-situ ICME signature and the measured solar wind parameters in front of the ICME.

In the second part, the kinematics close to the Sun were analysed with TI-model presented in Section 3.2.2. Inputs for the computation are r_0 as well as the α-r- and κ-r-profiles derived from GCS fitting. The *python*-procedures calculate the Lorentz-acceleration by finding the minimal decay index n for which the Lorentz-profile for heights above r_0 is below the absolute drag force, since r_0 defines the point of force balance. This defines the minimal physical solution of the Lorentz-force. In order to find a proxy for the upper limit, n is altered until the Lorentz acceleration matches the observed maximum acceleration derived from the r-t-profiles.

4.3 Concluding Summary

- There are several active science and space weather missions whose observations and measurements of the Sun, the corona and the heliosphere can be combined to track CMEs from their origin to heliospheric distances of 1 AU and beyond.
- The analysed data-sets used in this thesis where recorded by the EUVI, COR1, COR2 and HI1 instruments onboard the STEREO spacecrafts, the C2 and C3 coronagraphs onboard SOHO and the AIA EUV imager and HMI filtergraph on SDO.
- A set of 21 CMEs was selected because of favourable spacecraft positions for 3D GCS modelling as well as available SR and in situ data.
- All data were calibrated and processed to ensure science level data quality.
- Magnetic and geometric SR properties were computed by using the SMART code.
- State of the art fully dynamical 3D multi-viewpoint GCS modelling was performed to measure the CME trajectories, masses and to derive their basic kinematics as well as CME geometries.
- The kinematics were analysed with physical models including the interaction with the ambient solar wind and initial acceleration phase by magnetic Lorentz forces.

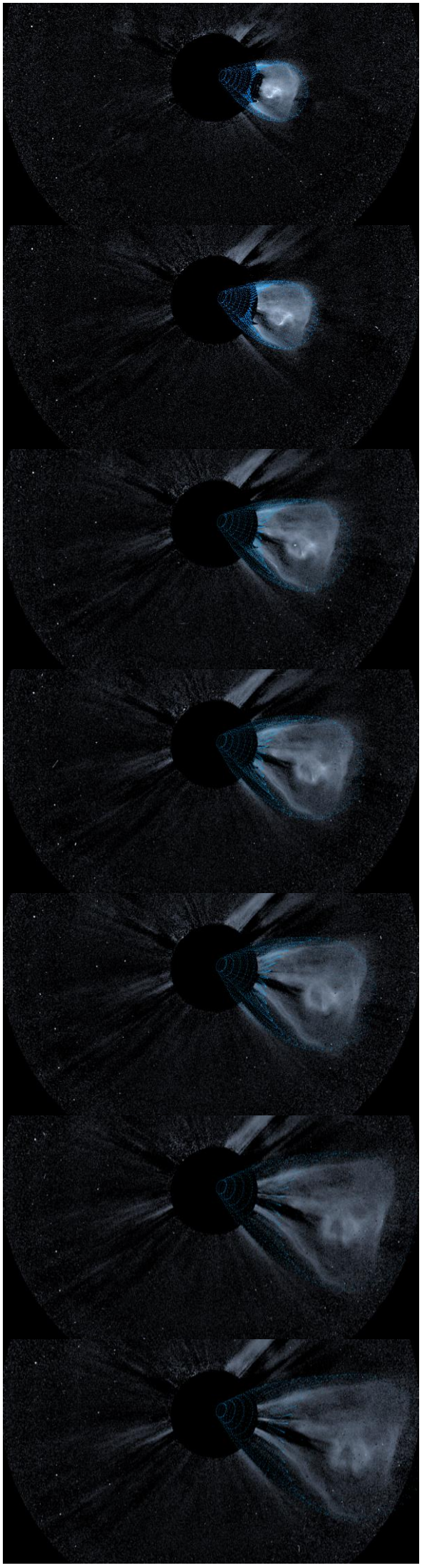

Chapter 5

Results and Discussion

"When found, make a note of."

Charles Dickens

In this chapter, I present the results of the methods and models that were presented in the preceding chapters and applied to the selected events. The presentation of the results is organised in four parts. In the first part, the GCS modelling results are discussed since they are the input data to the following analysis steps. The GCS modelling results obtain the geometrical and kinematic evolution of the CMEs in the inner heliosphere. Furthermore, using the theory of Thomson scattering, the CME masses were determined with the GCS geometry. The second part contains the results of the SR investigation. All ARs, identified as the corresponding SR of the selected events, were analysed on their geometry, flare characteristics and magnetic properties. In order to describe the CME/ICME kinematics, taking the interaction with the ambient medium into account, a dynamic drag model was used. The model results are discussed and compared with in-situ measurements of the ICMEs taken at L1 in the third part. By using the DBM results, the TI Lorentz force model was used to evaluate the initial acceleration of the CMEs. The findings of this analysis are presented and compared with the SR results in the final part.

Cover Figure: Time series of SECCHI/COR2 B observations of event #1. The GCS fit is shown by the blue grid.

5.1 Geometrical Modelling with the GCS Model

The GCS model was applied to all available observations of the STEREO A and B instruments EUVI 195, COR1, COR2 and HI1 as well as SOHO C2 and C3 observations. Selected difference images of each instrument of the 21 events together with the overlayed GCS grid are merged in the mosaics of Figures 5.1 and 5.2 and in the appendix A.1 to A.19. In a few cases, observations of single instruments were not available, which is why some mosaics contain blank spaces. It shall be noted that the single viewpoints are not always concurrent and the images were selected for the reason of best visibility of CME white-light features.

5.1.1 Geometrical Results

The ranges of the fitted GCS parameters defining position, orientation and shape are summarised in Table 5.2 for all events. Both position angles are measured in the Carrington coordinate system and the tilt angle Γ is measured $\pm 90°$ from the solar equator, which has $\Gamma = 0°$, while positive angles are rotated counterclockwise starting from the equator. It should be noted that this orientation is different to the original formulation of the model presented in Thernisien, Howard, and Vourlidas (2006), which was later changed in the work of Thernisien, Vourlidas, and Howard (2009) to the one explained above. For all events the GCS parameters and calculated face-on- as well as edge-on-angular widths, W_{fo} and W_{eo}, are plotted versus the solar distance of the apex in Figures 5.4 and A.20 to A.29. As an example, the GCS grid of event #1 is shown in the in a HEEQ coordinate system for the first and last observation time including the Earth-component, which is highlighted in green, in Figures 5.5. Modelling uncertainties of the single GCS parameters are described in the sensitivity analysis of Thernisien, Vourlidas, and Howard (2009), but their work includes only the two viewpoints of the two STEREO spacecrafts. In order to estimate an error range of the GCS parameters ϕ, θ, Γ, κ and α when using three viewpoints, the uncertainties found by Thernisien, Vourlidas, and Howard (2009) were linearly scaled with the number of viewpoints. Since the height error depends also on the instruments plate scale and Thernisien, Vourlidas, and Howard (2009) focused in their study on COR2 data, the height error was, in addition to the number of viewpoints, scaled with the plate scale ratios of the single instruments with respect to the plate scale of COR2. The resulting errors of the single model parameters are summarised in Table 5.1 and are in good agreement with the works of Mishra, Srivastava, and Singh (2015), who used multi-fit attempts.

Nearly all events show a lateral expansion indicated by the increase of κ and α, which is described in the following with the differences of the last and first observation $\Delta\kappa = \kappa(t = t_{\text{last}}) - \kappa(t = t_0)$ and $\Delta\alpha = \alpha(t = t_{\text{last}}) - \alpha(t = t_0)$. Event #12 shows the largest expansion of the data set of $\Delta\kappa = 0.8$ and $\Delta\alpha = 75.7°$, which is equivalent to an increase of 900%

Table 5.1. Estimated uncertainties of the single GCS model parameters.

σ_r [$R_\odot$]						σ_ϕ [°]	σ_θ [°]	σ_Γ [°]	σ_α [°]	$\sigma\kappa$
σ_r^{EUVI}	σ_r^{COR1}	σ_r^{COR2}	σ_r^{HI1}	σ_r^{C2}	σ_r^{C3}					
± 0.04	± 0.07	± 0.33	± 1.88	± 0.11	± 0.67	± 2.8	± 1.2	± 14.5	$^{+8.6}_{-4.6}$	$^{+0.05}_{-0.03}$

Table 5.2. Results of GCS modelling for all 21 events.

#	ϕ [°]	θ [°]	Γ [°]	α [°]	κ
1	260.5 – 275.9	-20.1 – -12.3	22.4 – 7.8	5.6 – 40.5	0.11 – 0.51
2	326.5 – 317.2	18.4 – 20.1	-62.0 – -75.5	11.5 – 39.4	0.17 – 0.50
3	229.2 – 236.0	20.7 – 30.7	-39.1 – 2.8	10.6 – 72.1	0.15 – 0.59
4	230.3 – 230.3	21.8 – 29.6	39.1 – 36.9	12.0 – 31.0	0.13 – 0.28
5	128.6 – 131.9	21.8 – 20.1	-20.1 – 3.9	15.4 – 38.0	0.45 – 0.52
6	242.6 – 241.4	-20.0 – -1.5	-10.6 – -8.9	26.0 – 31.0	0.27 – 0.47
7	303.0 – 292.7	19.0 – 14.5	-70.6 – -65.4	28.8 – 31.0	0.39 – 0.39
8	61.5 – 67.1	27.4 – 24.6	-29.6 – -26.3	4.5 – 42.8	0.06 – 0.58
9	213.5 – 201.2	26.8 – 35.8	-43.0 – -88.9	19.6 – 85.0	0.26 – 0.79
10	296.3 – 311.6	22.4 – 25.2	-50.9 – -69.7	19.0 – 79.9	0.21 – 0.46
11	294.0 – 293.7	15.1 – 12.3	-41.9 – -57.0	18.2 – 46.7	0.16 – 0.38
12	291.4 – 271.3	20.1 – 14.0	-62.0 – -39.7	10.1 – 85.8	0.10 – 0.90
13	53.7 – 85.0	-26.8 – -28.5	48.1 – 3.9	10.9 – 84.4	0.11 – 0.71
14	161.0 – 138.6	-12.9 – -11.7	24.0 – 36.3	20.7 – 44.7	0.11 – 0.58
15	83.8 – 92.8	-23.0 – -23.5	6.7 – 8.4	43.3 – 85.2	0.28 – 0.85
16	86.1 – 74.9	-14.7 – -15.1	7.3 – 15.1	5.6 – 43.3	0.20 – 0.66
17	120.1 – 96.1	6.1 – 17.3	-1.1 – -7.3	43.3 – 54.5	0.41 – 0.47
18	162.1 – 157.6	11.2 – 7.3	-51.4 – -86.1	35.2 – 75.7	0.32 – 0.78
19	298.5 – 296.7	-22.4 – -17.9	32.5 – 21.2	18.2 – 37.2	0.26 – 0.43
20	172.3 – 173.3	15.6 – 11.2	-72.7 – -58.1	33.8 – 35.8	0.46 – 0.46
21	129.7 – 120.7	3.9 – 11.7	24.6 – 19.6	12.9 – 75.2	0.09 – 0.58

and 850%, respectively. By regarding the mean values of the ensemble, the events erupt with $\kappa(t = t_0) = 0.22$ and $\alpha(t = t_0) = 19.3°$, expand by $\overline{\Delta\kappa} = 0.34$ and $\overline{\Delta\alpha} = 36°$ and show a maximum of $\kappa(t = t_{\text{last}}) = 0.57$ and $\alpha(t = t_{\text{last}}) = 55.2°$ on average. There exists a clear correlation between the aspect ratio and half angle, which is plotted in Figure 5.3. A fit of $\Delta\kappa$ versus $\Delta\alpha$ yields the linear relationship of:

$$\Delta\alpha = (86.4 \pm 13.9) \cdot \Delta\kappa + 6.4 \pm 5.6\,, \tag{5.1}$$

with a coefficient of determination of 0.67. Even if the correlation is weaker ($R^2 = 0.5$ and $R^2 = 0.58$), the values of κ and α at t_0 and t_{last} follow this general trend.

CME deflections, a change in the apex longitude and latitude, could be observed for all events. On average, the maximum deflection in the longitude and latitude from the first to the last observation of an events is $\overline{\Delta\phi} = 10.2°$ and $\overline{\Delta\theta} = 5.3°$, while the maximum change in ϕ and θ is about 31.3° and 18.5°, respectively.

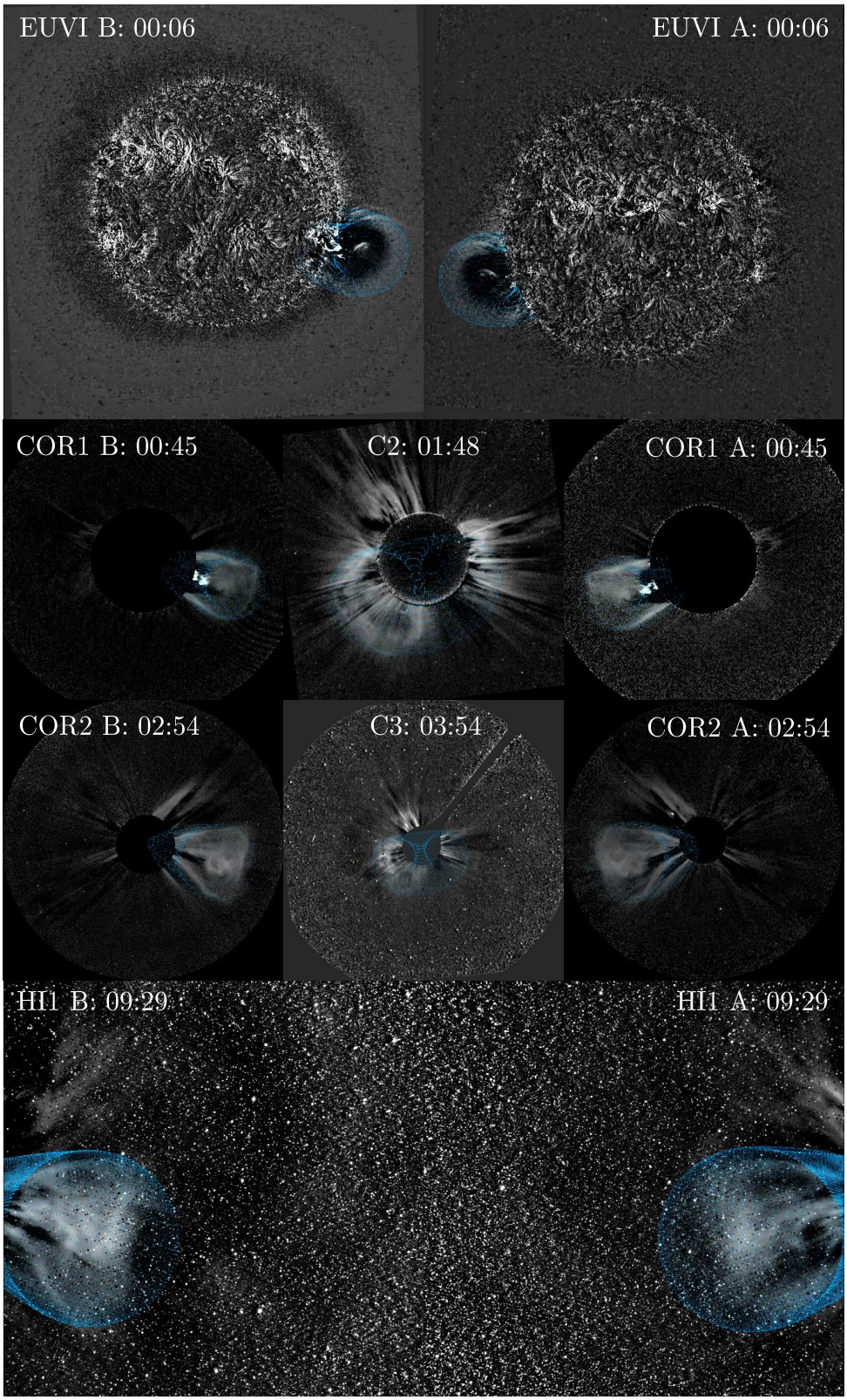

Figure (5.1) Selected observations of event #1 on July 8, 2011 from all available remote-sensing instruments with overplotted GCS grid (light blue). The images are running difference images processed as described in Section 4.2.2.

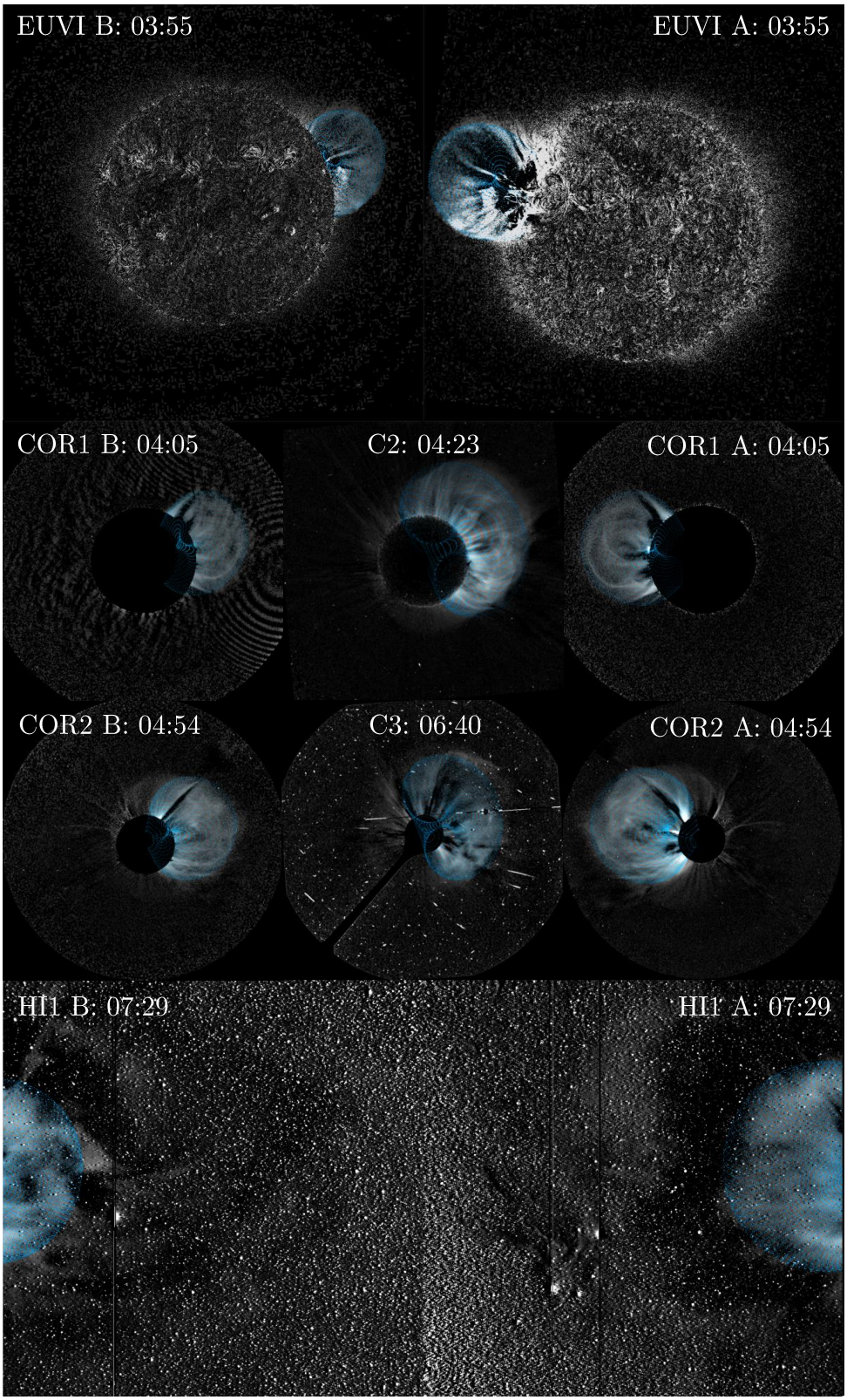

Figure (5.2) Same as Figure 5.1 for Event #2 on August 8, 2011.

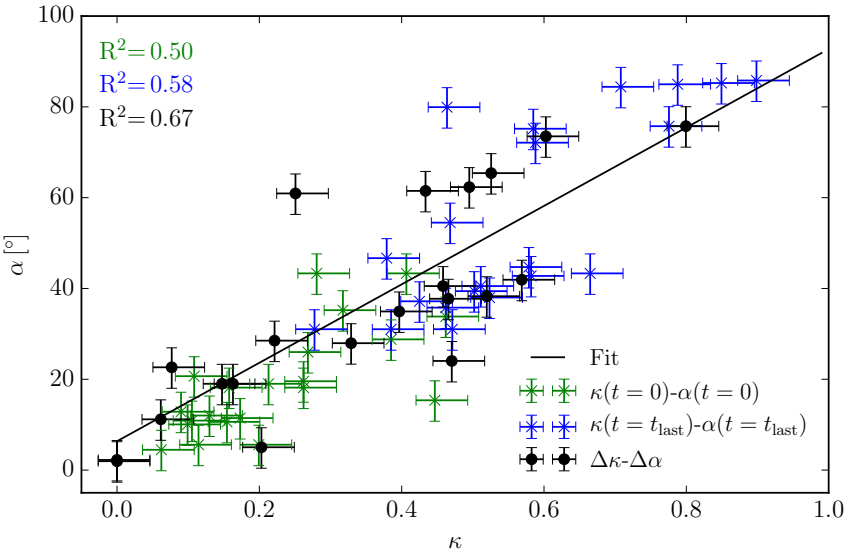

Figure (5.3) Relationship between κ and α. The fitted GCS aspect ratio are plotted against the half angle for the first and last observation of an event in green and blue, respectively. The differences between these values are plotted in black and fitted using a linear regression. The coefficients of determination are given in the corresponding colours.

While the majority of events (85%) show no further deflection above $30\,R_\odot$, a strictly radial propagation without further deflection above $20\,R_\odot$ was observed in 57% of the events.

All 21 events show a rotation around the symmetry axis indicated by the changing tilt angle $\Delta\Gamma = \Gamma_{max} - \Gamma_{min}$ during the individual observation sequences. The average rotation is $\overline{\Delta\Gamma} = 16.5°$ while event #9 has the largest rotation of 45.8° of the data set. It should be noted that the tilt angle has the largest relative uncertainty of all GCS model parameters. According to the error range of ±14.5°, a definite rotation can be seen in ten events of the ensemble. For 58% of the events, the rotation ends within a height of $15\,R_\odot$ and, for 81%, Γ stays constant above heights $> 20\,R_\odot$, which, in the most cases is in the FOV of COR2, and for all events in the FOV of C3.

A self-similar expansion of the CME starts at the height r^{SSE} from which on W_{fo} and W_{eo} stay constant. The angular widths can be calculated by (Thernisien, 2011):

$$W_{fo} = 2(\alpha + \delta) = 2(\alpha + \arcsin(\kappa)) \quad \text{and}$$
$$W_{eo} = 2\delta = 2\arcsin(\kappa).$$

They depend only on the half angle and the aspect ratio of the GCS geometry. Therefore, the criteria for a self similar expansion is reached if $\alpha(r)$ =const. as well as $\kappa(r)$ =const., at which point $r = r^{SSE}$. This height is reached for all events within the first $50\,R_\odot$ and for 85% of the events within $30\,R_\odot$.
The results are in good agreement with the findings of Isavnin, Vourlidas, and Kilpua (2014), who observed deflections and rotations over distances starting close to the Sun up to 1 AU. They found that 60% of the total geometrical evolution takes place in the first

$30\,R_\odot$. The maximum longitudinal and latitudinal deflection observed in their study are $\Delta\phi = 29°$ and $\Delta\theta = 49°$, while the observed rotations ranges from 4° to 164°.
CME deflections and rotations are a frequently discussed topic (e.g. Möstl *et al.* 2015; Owens, Lockwood, and Barnard 2017; Wang, Hoeksema, and Liu 2019). Sources that deflect CMEs during their propagation may be the ambient coronal medium and interactions with different solar wind streams (Wang *et al.*, 2004). It was shown in several studies that CMEs deflect away from CH (Cremades and Bothmer, 2004; Gopalswamy *et al.*, 2009). Also the interaction of multiple events was shown to be a possible mechanism for deflections (Lugaz *et al.*, 2012).
Non-self-similar expansions of the FR shape within the early evolution could be observed in nearly all events by the increase of κ and α. A strong correlation, presented in Figure 5.3, could be found. These results suggest that the expansion of the angular width and the FR diameter, which are described by the GCS face-on and edge-on widths, are not independent to each other. The found relationship between κ and α is different compared to our results derived from the analysis of the KINCAT data (Pluta *et al.*, 2018). Indeed, in this work the GCS model was applied fully dynamical in contrast to the events of the KINCAT, which were fitted with GCS parameters averaged over the COR2 image sequence.
A self similar expansion was observed for the majority of events above heights of $30\,R_\odot$, which is supported by the findings of Kuzmenko and Grechnev (2017), and for all events at heights above $50\,R_\odot$. However, this result has to be taken with caution since at these heights the accuracy of the 3D modelling becomes less meaningful by different factors. First of all the CME white light signature is at larger heliospheric distances poorly visible by the decreasing Thomson scattering. Furthermore, the full CME structure exceeds the FOV of HI1 and is often not completely observable. Finally, the number of observations and viewpoints is lower for these distances. For these reasons, a further expansion cannot be eliminated at larger distances.

5.1.2 CME Kinematics from GCS Modelling

The kinematic analysis of the data is based on the height-time-profiles of the GCS apex, which represents the leading edge of the CME and are derived by the GCS modelling of the image sequences taken with the EUV imagers, coronagraphs and heliospheric imagers. Almost every data point of the *r*-*t*-profiles is a measurement of a multi-viewpoint analysis of simultaneous observations of at least two spacecrafts. In the following, the process of the kinematic analysis is described in more detail.

In past studies and CME catalogues, linear and low degree polynomials were often fitted to observed POS height-time-profiles and the CME velocities and accelerations were determined by numerical differentiation (i.e. like in the SOHO LASCO catalogue or in the HELCATS KINCAT catalogue). The measured *r*-*t*-profiles of this work are of much more detail since multi-viewpoint and multi-instrument data were used, which is not possible in a large catalogue study. A least square spline fitting method was used to fit the measured *r*-*t*-profiles of the 21 events. This method provides a way to fit data with an unknown underlying physical process to high accuracy as it was done in several CME case studies (Temmer, 2010; Bein *et al.*, 2011). Spline fits depend on the smoothing regulated by the degree of the used polynomials and by the number and positions of the internal nodes.

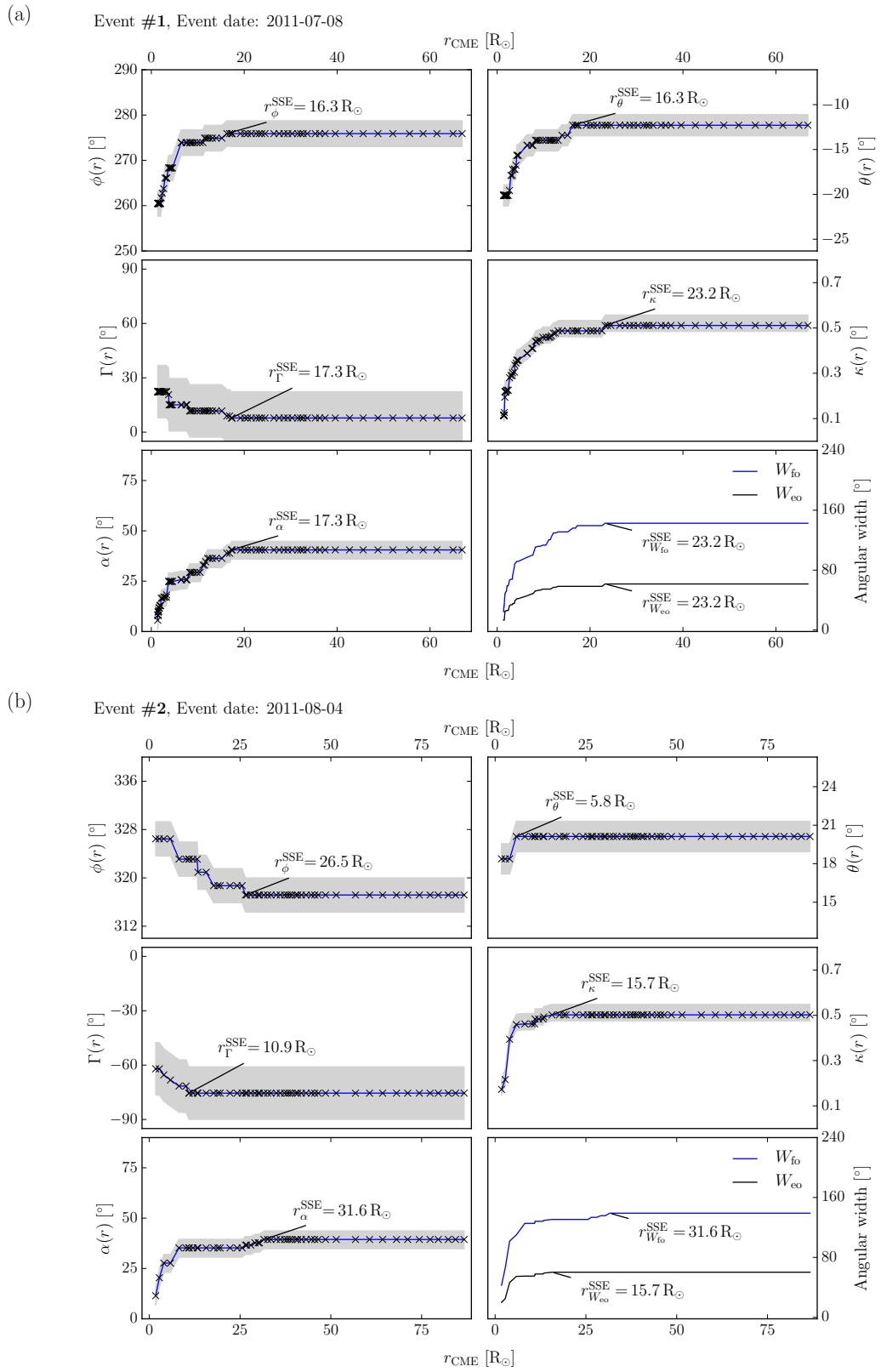

Figure (5.4) Geometrical results of the events #1 (a) and #2 (b). All GCS parameters were plotted versus the solar distance r of the observation. The error ranges are shown by the grey areas.

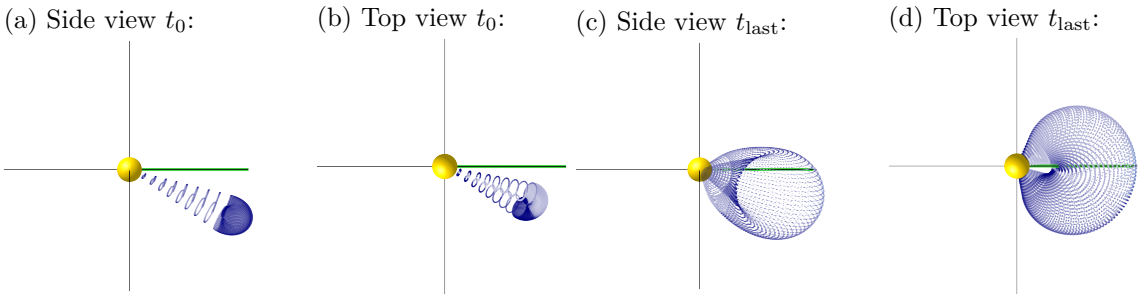

Figure (5.5) GCS Model (blue grid) of event #1. (a) and (b) show the fitted GCS model of the first observation, (c) and (d) show the one of the last observation. (a) and (c) show the side view, while (b) and (d) show the top view in a HEEQ coordinate system with the Sun in the centre (yellow sphere) and the direction to Earth on the right side (marked by the green line).

When using to many nodes, the resulting fit is strongly affected by the statistical scattering of the data leading to an overfitted model. On the other hand, an undersized number of nodes causes a large smoothing and poor fit accuracy. In order to balance both effects, the polynomial degree d was confined to a range of $d = 3$ to $d = 6$ and the number of nodes was limited to a maximum of $m/5$ and a minimum of $m/15$, where m is the number of data points of the height-time-profile. By dividing the spline segments into equal parts of the total amount of data points, the smoothing is stronger at larger solar distances and hence at a height where the measurement uncertainties are large. An automatic procedure was written that iterates over the number of nodes and the polynomial degree to minimise the residuals. By computing the central differences of the height-time data, the velocity-time- v-t and acceleration time a-t-profiles are obtained. The spline method was applied to the three point moving average of theses profiles to minimise the multiplicative errors by differentiating and to fit the CME speed $v(t)$ as well as CME acceleration $a(t)$.

All data and derived kinematic profiles are plotted in Figure 5.8 and the Figures A.30 to A.39 in the Appendix. The error-bars of the first part of the r-t data might be to small to recognise due to the large height range. For further comparison, the maximum CME speed derived from the spline fit of the smoothed v-t profile $v_{\text{max}}^{\text{fit}}$ and the maximum speed $v_{\text{max}}^{\text{der}}$ of the numerical derivative of the spline fit of the r-t-profile, $\dot{r}(t)$, as well as the speeds at $r = 12\,\text{R}_\odot$, v_{12} and $r = 50\,\text{R}_\odot$ are annotaed in the plots. Same was done with the a-t-profiles for the CME acceleration. Additionally, a spline interpolation was used to fit the 3 point moving average of the a-t-profile. The errorbars of the r-t-profile are listed in Table 5.1 for the different instruments. Spline fits are plotted in blue, derivatives in dotted black and spline interpolated data in light blue. The grey error ranges indicate the standard derivatives of the spline fits. The fitted maxima of the CME speeds and accelerations are listed in Table 5.3. It can be seen that the differences of the numerical deviations to the spline fits lie within the error range of the standard deviation. In Figure 5.6, the distributions of v_{max}, v_{12} and a_{max} are shown together with the velocity distribution of the HELCATS KINCAT catalogue. As described in Pluta *et al.* (2018), the CME speed at a distance of $12\,\text{R}_\odot$ turned out to be an important kinematic parameter. This

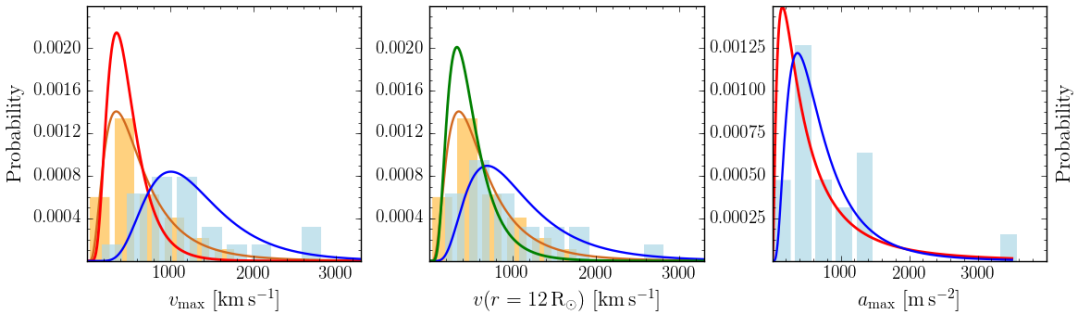

Figure (5.6) Distribution of the maximum CME speed, the speed at 12 $R_\odot$ and the maximum acceleration. The histograms of the kinematic results are shown by the light blue bars and the fitted log-normal distributions are plotted in blue solid lines. Furthermore the data of the KINCAT catalogue (orange) including their log-normal distributions (dark orange), the results of Bein *et al.* (2011) (red) as well as the CME speed distribution (green) of LASCO observations from 1996 to 2001 (see Yurchyshyn *et al.* 2005), are shown.

could be reasoned in the force balance at this height. Since v_{12} describes the kinematics at a height above the typical maximum accelerations of the Lorentz force and below heights at which the drag force decelerated the CME by significant amounts, it is a good quantity to compare individual CMEs (Bothmer and Mrotzek, 2017). In the data set of this work, v_{max} and v_{12} vary between 404±60 and 2801±149 km s^{-1}, respectively. While the maximum speeds of all events vary between 530±55 and 2874±162 km s^{-1}, the maximum CME accelerations range from 114±102 to 3575±379 m s^{-2}. Lognormal functions were fitted to the data since the CME speeds are independent and randomly distributed. The lognormal fit of the KINCAT data peaks at 351 km s^{-1}, which is in good agreement with the results of Yurchyshyn *et al.* (2005) who analysed all CMEs observed with LASCO from 1996 to 2001. In contrast to this results the lognormal fits of the selected 21 events peak for v_{max}, v_{12} and a_{max} at 1008 km s^{-1}, 692 km s^{-1} and 369 m s^{-2}, respectively. Also the average values, which are 629 km s^{-1} (KINCAT), 1374 km s^{-1} (v_{max}), 1125 km s^{-1} (v_{12}) and 822 m s^{-2} (a_{max}), are higher for the 21 selected events. The height at which the acceleration is maximal $r_{a_{max}}$ lies below 3 $R_\odot$ for 71% of the events and varies from 1.4 to 10.5 $R_\odot$. Comparing the distribution of the kinematic results with that of other studies (e.g. the HELCATS and LASCO catalogues), the data set presented in this thesis is with $v_{max} > 1000$ km s^{-1} for 71% of the events more representative for fast CMEs than for slower ones. This is not surprising since the CME brightness is correlated with its speed (Wang *et al.*, 2011) and one of the selection criteria was that only bright CMEs with clear white light structures should be analysed. Furthermore, the time interval of the selected events lies within the first peak of the solar maximum as can be seen from Figure 4.2.
All kinematic characteristics are plotted and compared in Figure 5.7. The maximum observed CME speed and the CME mass are represented by the marker colour and size, respectively. A relationship between the height of the maximum acceleration and the height of the first observation r_0^{obs} was found to be:

$$r_0^{obs} = 10^{(-0.09\pm0.07)} \cdot r_{a_{max}}^{(0.91\pm0.13)}. \tag{5.2}$$

While $r_{a_{max}}$ and r_0^{obs} show a high correlation of $R^2 = 0.71$, this is different ($R^2 = 0.22$) in

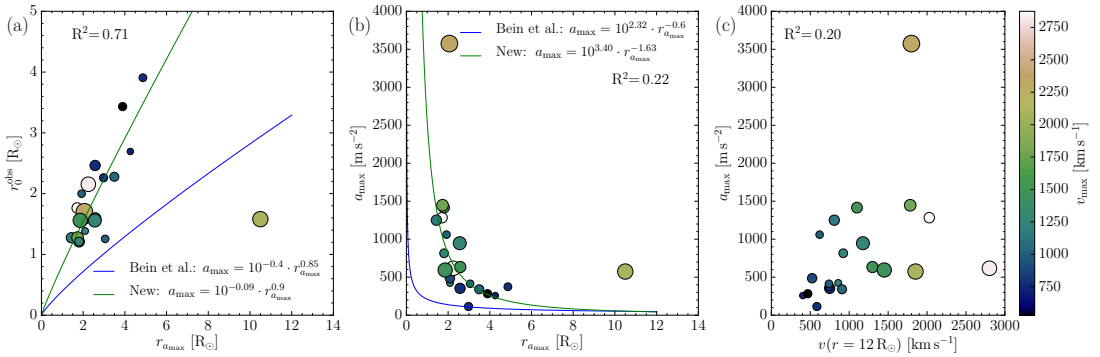

Figure (5.7) Comparison of the kinematic characteristics of the 21 selected CMEs. Marker size and colour represent the maximum CME speed and the CME mass, respectively. While the result of Bein *et al.* (2011) are shown in blue, fits of the data of this work are shown in green.

the case of $r_{a_{max}}$ and a_{max}. Also if the majority of events follows the fitted law of:

$$a_{max} = 10^{(3.40 \pm 0.15)} \cdot r_{a_{max}}^{(-1.6 \pm 0.5)}. \tag{5.3}$$

There are two outliers. One of these is event #9, having an unusually long acceleration phase up until $\sim 10\,R_\odot$ with several peaks. Since the source of this multiple acceleration processes is unclear, the event was rejected from the fits. The second outlier is event #12, which sticks out, compared to the other events, by the presence of a bright diffuse shock in the white-light structure of the CME. This could have introduced a larger uncertainty in the height. However, since a clear explanation was not found, it was not excluded from the fits. As can be seen from Figure 5.7, this result differs strongly from the result of Bein *et al.* (2011). In their study, they used a data set of 95 events observed with the STEREO SECCHI instruments. In contrast to this work, the CME kinematics were analysed in the POS and the *r*-*t* profiles were recorded using the leading edge of the white light CME structure. Despite this work contains less events than the data set of Bein *et al.* (2011), the average acceleration of both works are close to each other with 822 and $752\,m\,s^{-2}$, respectively. Since in this work the 3D CME characteristics are used, the uncertainty is reduced. Nevertheless, it has to be noted, as mentioned above, that this data set is more representative for faster CMEs.

Also visible, even through the smoothing of the 3 point average, are evidences of oscillations in the kinematic profiles, best visible in the *v*-*t*- and *a*-*t*-profiles, that can not be fully explained by multiplicative errors of the differentiation or statistical scatter. This behaviour can be seen particularly in the profiles of the events #1, 5, 7, 8, 9, 11, 13, 15, 19, 20 and 21. A Fourier transform analysis was performed on the interpolated *a*-*t*-profile to determine the periods of the oscillations.

This analysis was limited to the data of the first $25\,R_\odot$ since a damping of the oscillations can be seen and the number of data points at low solar distances is higher, reducing the uncertainty. The periods vary between 29 and 93 min while for 76% of all events the period is below 60 min. The found periods of the CME oscillations support the results of Lee, Moon, and Nakariakov (2015) and Lee *et al.* (2018), who reported periods between

24 and 48 min. These oscillations are damped which is probably the reason of the drag force. The polarisation of the oscillations found by Lee *et al.* (2018) were also detected by Kim, Nakariakov, and Cho (2014) as vertical oscillation of a rising FR at lower scales in the corona. Because the uncertainties to larger heliospheric distances in the outer FOV of C3 and HI1 increase largely and the acceleration or deceleration by the drag superimposes the kinematic profiles, it is difficult to observe this behaviour at these distances. Following the estimates of Lee *et al.* (2018) and the MHD simulations of Cargill, Chen, and Garren (1994) possible sources for the oscillation could be the Lorentz forces acting on the FR. According to the observed expansion in the angular widths of the CMEs, a feed-back of the expanding toroidal magnetic field in the FR are reasonable to drive oscillations. However, further analysis and observational investigations are needed to clarify the question about the existence and the possible source of CME oscillations.

5.2 CME Mass Determination

The CME masses were determined using SECCHI COR1 and COR2 as well as LASCO C2 and C3 data since these instruments provide a wide FOV around the Sun to ensure sufficient observations also for fast CMEs. It was shown by Colaninno and Vourlidas (2009), that the CME masses determined separately with LASCO and SECCHI data are in good agreement and can be compared without further calibration. Even if the occulters of the COR1 and C2 instruments cover large parts of the early evolution of a CME, the mass derived from their data can be used by applying equation 3.32 in combination with the larger FOV of the COR2 and C3 coronagraphs. By using the GCS modelling results of the fitted CME orientations with respect to the POS of the coronagrapgh observations, the mass-images were generated as described in Section 3.4.4 and 4.2.2 to convert from MSB units into gpp.

All masses measured from the calibrated mass-images of the individual events are shown in Figures A.40 to 5.12, including the final CME masses determined by the regression of Equation 3.32 of the measurements of the individual satellites. The errors of the mass measurements cumulate from different uncertainties in the mass-image conversion, geometrical uncertainties of the integration and necessary assumptions in the mass calculation theory. In their study, Vourlidas *et al.* (2010) did a comprehensive analysis of all uncertainties in the determination of CME masses from LASCO observations, beginning with the data calibration process and including all steps through the mass integration. They found an uncertainty of 5.5% in the conversion from digital numbers to MSB, and an additional 4% by the conversion from MSB to excess MSB by image differencing. Conservative models assume a CME composition with a proportion of 90% hydrogen and 10% helium, which corresponds to $1.94 \cdot 10^{-24}$ g per electron that is involved in the light scattering structure (Hildner *et al.*, 1975). A more recent in-situ analysis of ICMEs by Reinard (2008) showed a slightly lower helium proportion of only 6%. As in the work of Vourlidas *et al.* (2010), an 6% uncertainty to the total mass error is added to include the differences in the composition. Since the fitted GCS FR model defines the area in which the mass per pixel is integrated, the errors of the single GCS parameters play a role for the total mass error, too. By adding all uncertainties listed in Table 5.1 to the modelled GCS FR of selected bright

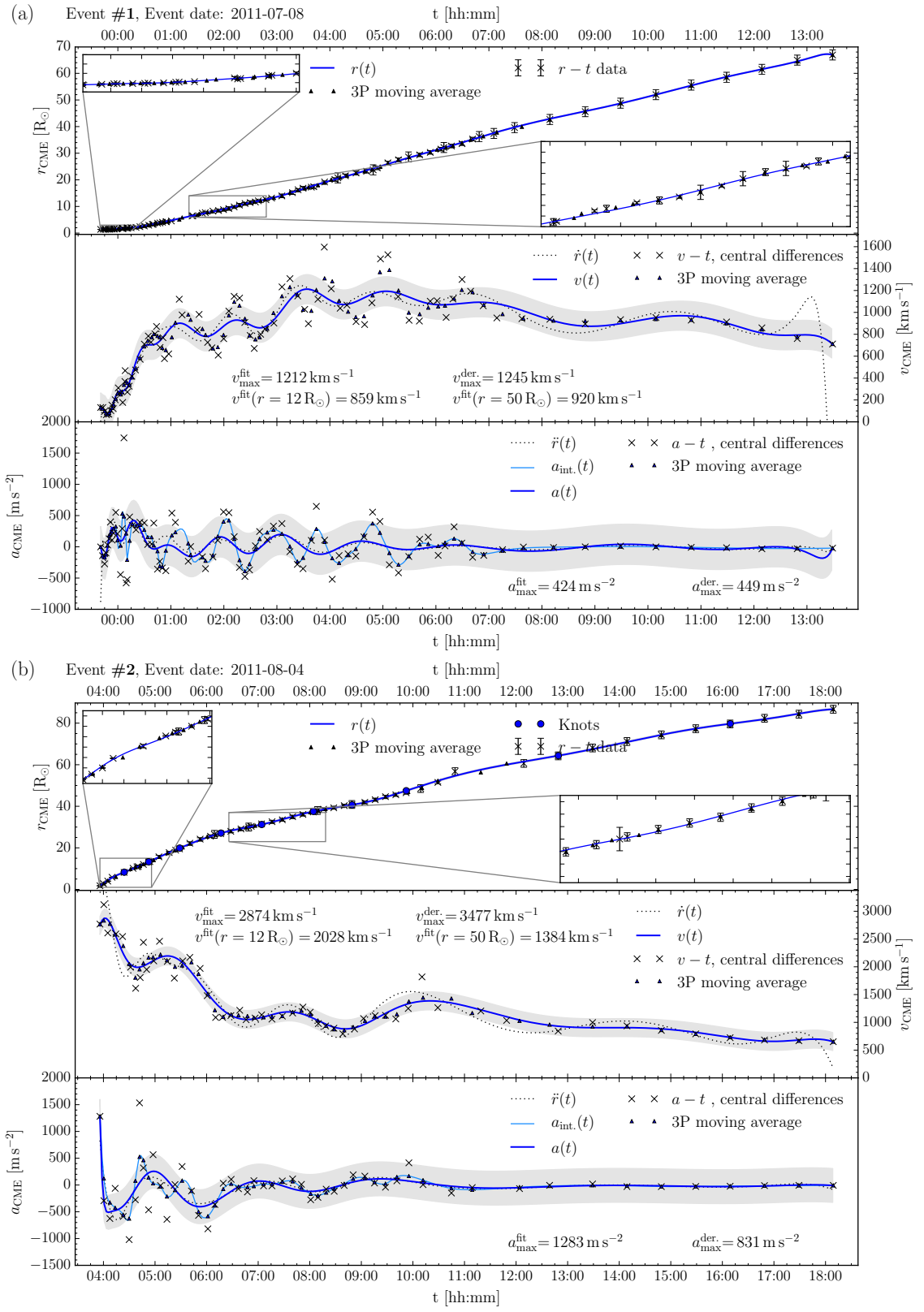

Figure (5.8) Kinematic results of the events #1 (a) and #2 (b). A detailed explanation is given in Section 5.1.2. *Top row*: r-t-profile and excerpts of the early CME states. *Middle row*: v-t-profile. *Bottom row*: a-t-profile. The 3 point moving averages of all profiles were fitted with splines (blue). Spline derivatives are represented by the black dotted lines.

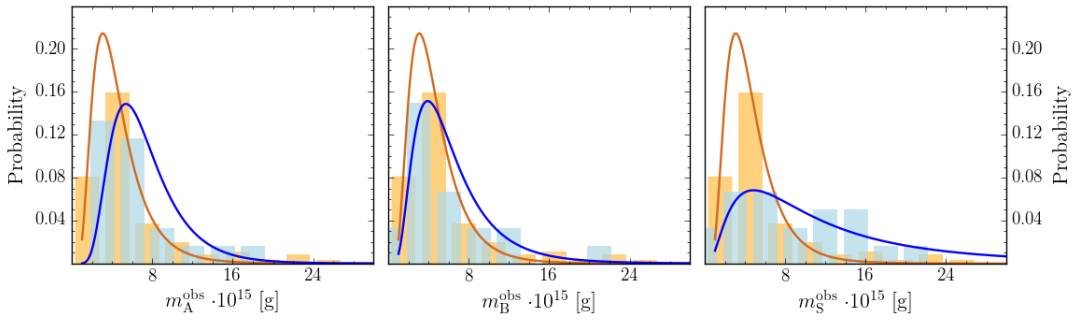

Figure (5.9) Distribution of the CME masses measured from the different viewpoints of STEREO A, STEREO B and SOHO. The histograms of the mass determination results are plotted in light blue bars and the fitted log-normal distributions are shown by blue solid lines. Furthermore the data of the KINCAT catalogue (orange) including their log-normal distributions (dark orange) are shown.

events of the data set, the maximum error of the integration area of 4.5% was estimated. Since the "directional mass determination" (Pluta *et al.*, 2018) method is used, projection effects can be neglected. The accumulation of all uncertainties results in a total error for a single mass measurement of 20%.
The data and fits are colour-coded according to the satellites the data were recorded with as follows: SOHO in green, STEREO A in red and STEREO B in blue. STEREO A, STEREO B and SOHO data were fitted individually while applying the fitting function to COR2 or C3 measurements led for the majority of events to the convergence within $35\,R_\odot$ of the CME mass. In the case of fast CMEs with a few observations in COR2 or C3, COR1 and C2 mass images were included to ensure the fit converging.

Masses, which are calculated from observations of partial or full halo CMEs are marked with (pH) (partial Halo) and (fH) (full Halo), and their fits are indicated by dashed lines. In one case (event #17, labeld with (S)), a streamer within the GCS integration grid could not be removed by the techniques explained in Section 4.2.2, and its brightness enhancement by the interaction with the CME affected the mass measurements. The evaluation of the individual converging fits at a distance of $30\,R_\odot$ gives the determined CME masses as measured from the different viewpoints. All determined masses, together with the average mass for every event, are listed in Table 5.3. In order to minimise mass overestimation according to full halo events in single perspectives (see Pluta *et al.* (2018)), masses calculated from halo events were excluded for the calculation of the average mass. If a CME appears in all perspectives as halo event, the masses of all viewpoint were used. In general the masses determined using STEREO A and B observations are in good agreement to each other, indicating accurate fitting of the CME longitude and latitude. For 10 events, the masses determined using LASCO data are much larger than the STEREO masses. The mass distributions are shown in Figure 5.9 for the individual results of the three spacecrafts and are compared with the histogram of the mass determination results of the KINCAT catalogue. It can be seen that the events of this work are more massive than the events of the KINCAT catalogue. In other words, low mass CMEs are underrepresented in the data set. Lognormal fits to all distributions give peak positions of 3.08 (KINCAT), 5.36 (STEREO A), 3.91 (STEREO B) and 4.84 (SOHO) in units of 10^{15} grams. The mean

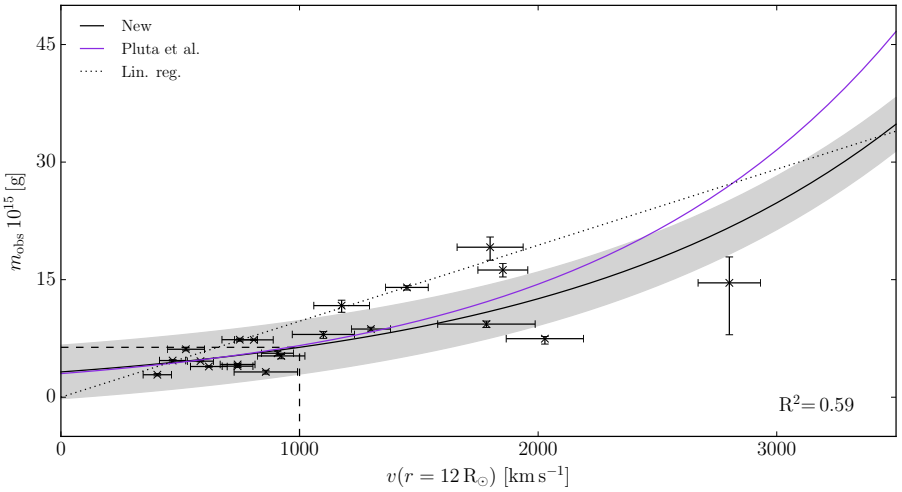

Figure (5.10) Correlation between the average CME mass derived from the mass measurements of the single viewpoints and the CME speed at $12\,{\rm R}_\odot$. A linear regression was performed with the $\log(m_{\rm av})$ values and is represented by the black curve while the grey area represents the uncertainty derived from the standard deviation. The fitting parameter of the regression can be seen in Equation 5.7. Furthermore, the correlation we derived from the KINCAT data (Pluta *et al.*, 2018) (blue) and a linear regression of $m_{\rm av}$ is shown by the dotted line for comparison.

values, in units of 10^{15} grams, are 12.6, 8.89, 8.32 and 8.32, respectively.

The masses determined from STEREO A, STEREO B and SOHO data were correlated with the CME kinematics. In Figure 5.11, the CME masses of the individual viewpoints are plotted versus the maximum velocity, the velocity at $12\,{\rm R}_\odot$, the velocity at $50\,{\rm R}_\odot$ and the maximum acceleration. The fitting function already introduced in Pluta *et al.* (2018) equation (8) was used to fit the data. For a better comparison, the fitting results of the KINCAT catalogue and a linear regression are overplotted. The highest correlations were found between the velocity at $12\,{\rm R}_\odot$ and the STEREO A and STEREO B masses with $R^2 = 0.74$ and $R^2 = 0.66$, respectively. To determine the uncertainty, the standard deviation was calculated and is represented by the grey area in the plots. The same was done for the average mass and v_{12}, which correlates with $R^2 = 0.59$ and is plotted in Figure 5.10. The derived fitting results are:

$$\log(m_{\rm obs,A}) = (3.5 \pm 0.5) \cdot 10^{-4}\, v_{12} + 15.47 \pm 0.06, \tag{5.4}$$

$$\log(m_{\rm obs,B}) = (3.7 \pm 0.6) \cdot 10^{-4}\, v_{12} + 15.41 \pm 0.08, \tag{5.5}$$

$$\log(m_{\rm obs,S}) = (2.9 \pm 0.9) \cdot 10^{-4}\, v_{12} + 15.61 \pm 0.12 \quad \text{and} \tag{5.6}$$

$$\log(m_{\rm obs,av}) = (2.95 \pm 0.6) \cdot 10^{-4}\, v_{12} + 15.55 \pm 0.07, \tag{5.7}$$

which differs, in the cases of the mass measurements of STEREO A, STEREO B and specifically the average masses, only slightly from our results presented in (Pluta *et al.*, 2018). In contrast, the correlation between the maximum CME acceleration and the observed mass is low with a maximum of $R^2 = 0.42$ for the STEREO B masses. In

general, the results of the determined CME masses agree well with our analysis of the more comprehensive KINCAT catalogue within the HELCATS project (Pluta *et al.*, 2018) and lie within the range of other studies (Vourlidas *et al.*, 2000, 2010, 2011). They underpin the conclusion that the CME speed at $r = 12\,\mathrm{R}_\odot$ is a good indicator for the CME mass. Especially for $v < 1800\,\mathrm{km\,s^{-1}}$ the results are very similar, which increasingly differ to faster CMEs. Since the CME masses could be determined for the individual events with more detailed data than it was possible in the larger catalogue study of the KINCAT, the CME masses of this work show smaller uncertainties.

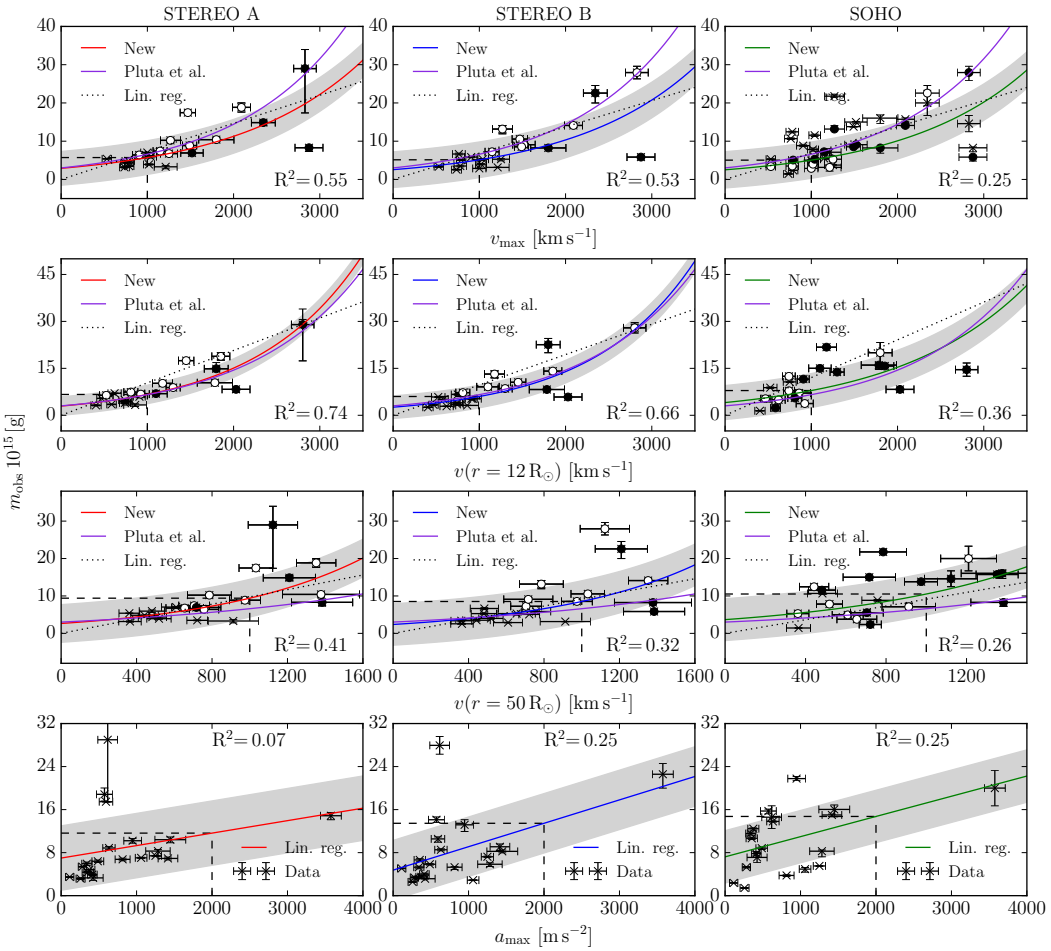

Figure (5.11) Correlation between the CME masses measured from different viewpoints with the individual spacecraft instruments and kinematic parameters. *Left row*: CME masses measured with STEREO A SECCHI/COR1 and SECCHI/COR2. *Middle row*: CME masses measured with STEREO B SECCHI/COR1 and SECCHI/COR2. *Right row*: CME masses measured with SOHO LASCO/C2 and LASCO/C3. Filled circles represent full halo CMEs while partial halos are represented by non-filled circles. The fit function found in Pluta *et al.* (2018) (by analysing the the HELCATS catalogue) (light blue) and a linear regression (dotted line) are included for reference. Red, blue and green curves show the new fitted functions to the data. For a better comparison, the corresponding CME mass of a CME speed of 1000 km s^{-1} and an acceleration of 2000 m s^{-1} are marked by the dashed lines.

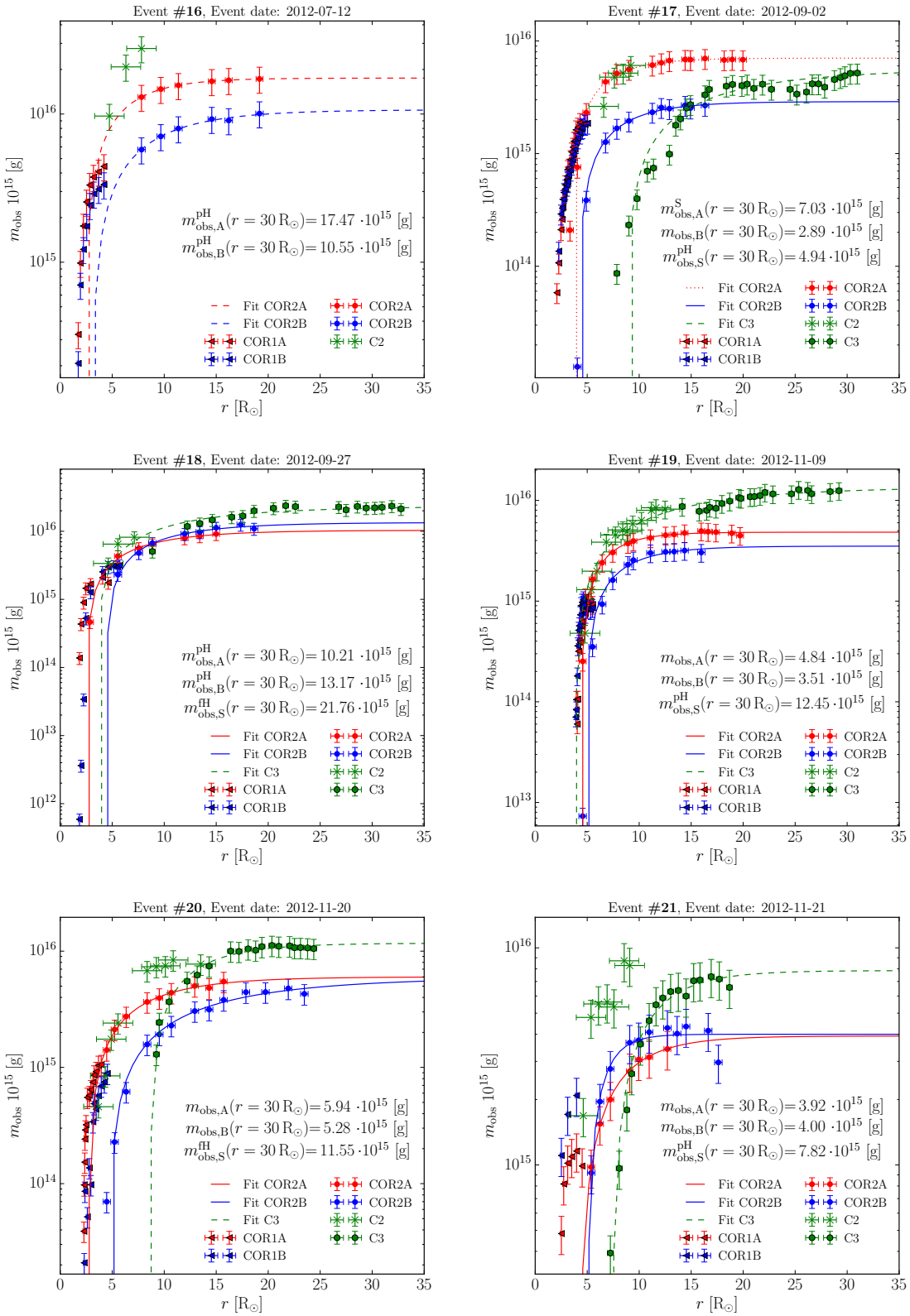

Figure (5.12) Results of the mass determination of the events #16 to #21. The colours red, blue and green indicate data of STEREO A, B and SOHO, respectively. Mass fits of CME signature observed as partial halo (pH) or full halos (fH) are plotted with dashed lines, in the case of the presence of streamers with dotted lines.

Table 5.3. Kinematic results of all 21 events.

#	$v_{\max}$ [km s^{-1}]	v_{12} [km s^{-1}]	$a_{\max}$ [m s^{-2}]	$m_{\mathrm{obs,A}}$ 10^{15} [g]	$m_{\mathrm{obs,B}}$ 10^{15} [g]	$m_{\mathrm{obs,S}}$ 10^{15} [g]	$m_{\mathrm{obs,av}}$ 10^{15} [g]	E_{kin} 10^{24} [J]
1	1212±133	859±133	424±322	3.3 ± 0.4	3.2±0.1	7.1±0.9	3.2± 0.4	2.4±0.6
2	2874±162	2028±162	1283±316	8.3 ± 0.3	5.8±0.3	8.3±0.2	7.5± 0.3	30.9±4.4
3	905±78	524±78	486±263	6.4 ± 0.2	5.8±0.2	8.8±0.2	6.1± 0.2	2.5±0.4
4	1148±81	808±81	1250±208	7.4 ± 0.1	7.2±0.1	5.5±0.1	7.3± 0.1	4.8±0.7
5	789±55	585±55	114±102	3.5 ± 0.1	5.1±0.1	2.4±0.1	4.6± 0.1	1.4±0.2
6	735±60	404±60	258±106	3.2 ± 0.2	2.6±0.1	1.4±0.1	2.9± 0.2	0.8±0.2
7	530±55	468±55	282±92	5.4 ± 0.1	3.4±0.2	5.3±0.1	4.7± 0.1	0.7±0.2
8	1517±130	1100±130	1416±361	6.9 ± 0.3	9.1±0.5	15.0±0.2	8.0± 0.3	9.2±1.6
9	2091±105	1852±105	574±247	18.8 ± 1.2	14.1±0.5	15.7±0.4	16.2± 1.2	35.5±4.4
10	2828±149	2801±149	617±211	29.0 ± 5.0	28.0±1.6	14.6±2.1	28.5± 5.0	135.4±41.5
11	1800±204	1783±204	1447±474	10.4 ± 0.5	8.2±0.3	16.0±0.8	9.3± 0.5	15.1±3.5
12	2345±138	1799±138	3575±379	14.9 ± 0.6	22.6±2.0	20.0±3.3	19.1± 0.6	52.6±6.5
13	762±75	750±75	353±199	4.4 ± 0.1	6.7±0.2	10.7±0.2	7.3± 0.1	2.1±0.4
14	1251±99	923±99	815±193	6.8 ± 0.2	5.3±0.2	3.7±0.1	5.3± 0.2	4.1±0.7
15	1490±82	1299±82	634±149	8.9 ± 0.3	8.5±0.2	13.8±0.1	8.7± 0.3	9.7±1.1
16	1470±89	1450±89	594±210	17.5 ± 0.1	10.6±0.4		14.01± 0.1	15.1±1.8
17	1000±77	620±77	1060±184	7.0 ± 0.1	2.9±0.1	4.9±0.3	3.9± 0.1	2.0±0.3
18	1268±117	1176±117	947±283	10.2 ± 0.4	13.2±0.9	21.8±0.4	11.7± 0.4	9.4±1.8
19	779±73	740±73	374±175	4.8 ± 0.1	3.5±0.2	12.5±0.2	4.2± 0.1	1.3±0.2
20	1039±67	908±67	341±150	5.9 ± 0.3	5.3±0.2	11.6±0.3	5.6± 0.3	3.0±0.4
21	1019±64	740±64	413±154	3.9 ± 0.2	4.0±0.2	7.8±0.4	4.0± 0.2	2.0±0.3

5.3 Analysis of CME SRs

In the following the results of the identification of SRs to their corresponding CMEs, the analysis of their magnetic properties as well as the relationships to the CME kinematic characteristics are presented.

5.3.1 SR Identification

In a first step to identify the SRs of the selected CMEs, catalogues of CME-accompanying phenomena like, SXR and HXR Flares, PEAs, flare ribbons and filament eruptions, all merged in the *Heliophysics Events Knowledgebase*[1], were inspected within a time window of ±8 hours to the first COR1 or EUVI observations. The positions of matching phenomena were compared to the GCS longitude and latitude to check if they belong to the CME. Phenomena differing by more than ±25 degrees in longitude and ±10 degree in latitude were not rejected. The same was done for ARs in HMI data by checking the *NOAA/USAF Active Region Summary* and *HMI Active Region Patch* (Bobra *et al.*, 2014). At least one AR could be identified as CME SR for every event of the data set. The identified SRs of the first three events can be seen in Figure 5.13 and for the events #4 to #21 in the Figures A.43 to A.48 in the appendix. All figures contain a full Sun AIA composite of the channels 304, 171 and 211, processed by M. Druckmüller with the PM-NAFE algorithm[2] (Druckmüller, 2013) as well as a concurrent HMI magnetogram, processed with the SMART code by S. Murray. Both images were scaled to compensate the different FOV and to match the same width of the Sun. By using the NAFE algorithm, fine coronal features in AIA images are enhanced with a noise adaptive fuzzy equalisation method without decreasing dynamic range and producing artifacts, as methods based on Fourier transformation or convolution do.
All NOAA, HARP and SMART IDs as well as the position of flux weighted SR centre, computed with SMART, and accompaning activity phenomena for the individual events are listed in Table 5.4. In the case of the events #8, #18 and #20, no single NOAA region could not be assigned to the CME. The SRs of the events #8 and #18 lie in between two NOAA regions while the SR of event #20 is on the right side of two NOAA regions. The AR identified as SR of events#1is not listed in the HARP. Same is true for event #14 but for the NOAA AR Summary. Smart IDs are always a running number of detected SRs in the actual HMI observations, which is why the IDs of the actual observation time of the presented Figures are listed in Table 5.4. The corresponding hale classes are listed in Table 4.2. According to the study of Jaeggli and Norton (2016), the majority (86%) of SR are (β)-class ARs. Except for one event (#6), all events are accompanied by other activity phenomena. Out of a total of 21 events, 16 FEs (76%), 15 FLs (71%) and 13 PEAs (62%) could be associated.

5.3.2 Comparison of Geometrical Properties

The CME longitude (in the carrington coordinate system), latitude (Stonyhurst coordinates) and its orientation with respect to the solar equator, obtained from GCS modelling of the first appearance in EUVI or COR1, are compared in Figure 5.14 to the determined

[1] https://www.lmsal.com/hek/ (13.12.19)
[2] http://www.zam.fme.vutbr.cz/druck/Sdo/Pm-nafe/Algorithm/0-info.htm (13.12.19)

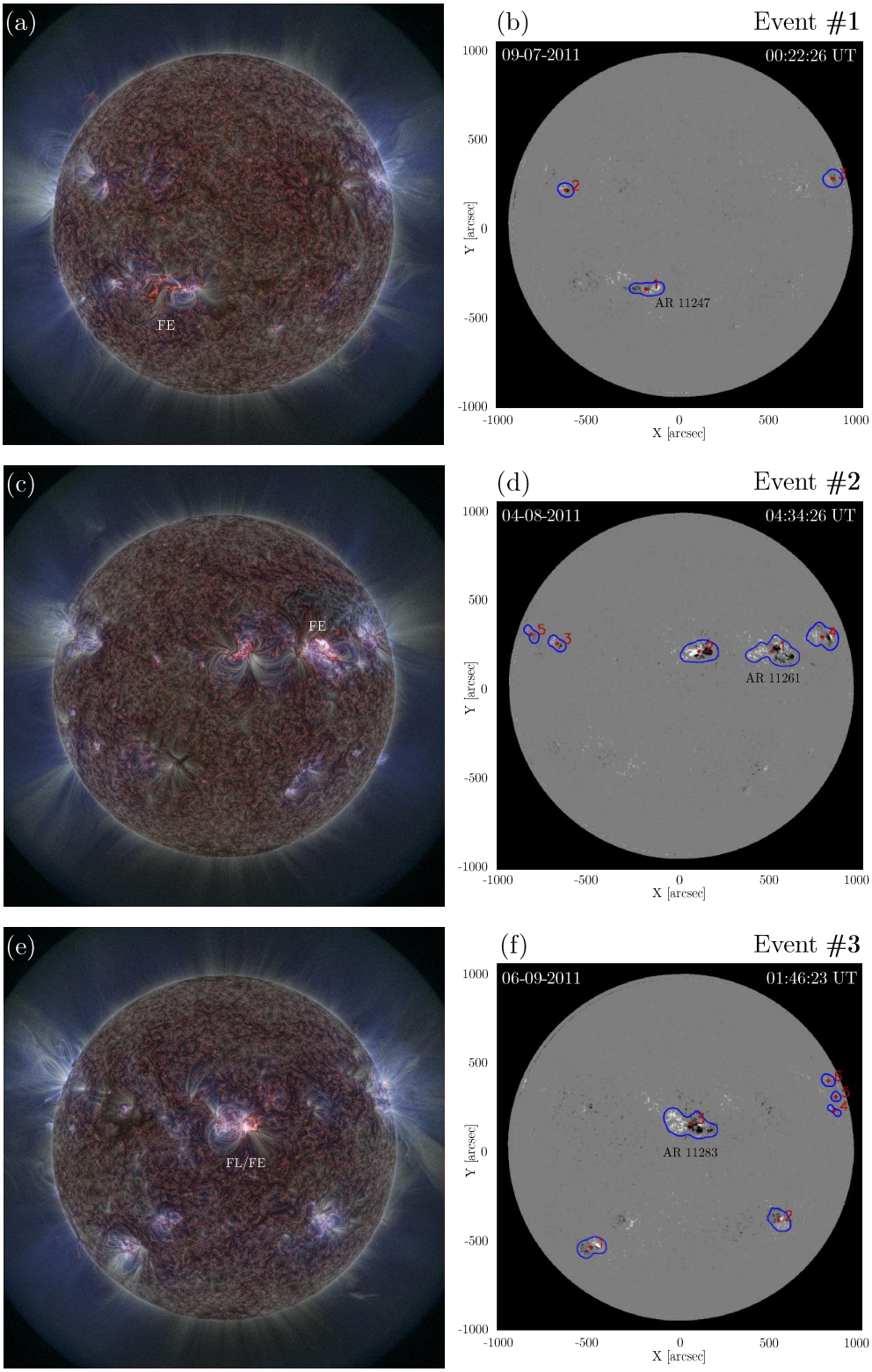

Figure (5.13) Identified CME SRs of the events #1 to #3. (a), (c) and (e) are AIA composites of the channels 304,171 and 211 processed with the PM-Nafe algorithm by M. Druckmüeller. (b), (d) and (f) are HMI 12 min average magentograms processed with SMART code by S. Murray. Activity phenomena as well as NOAA and HARP AR numbers are labelled for the identified CME SRs.

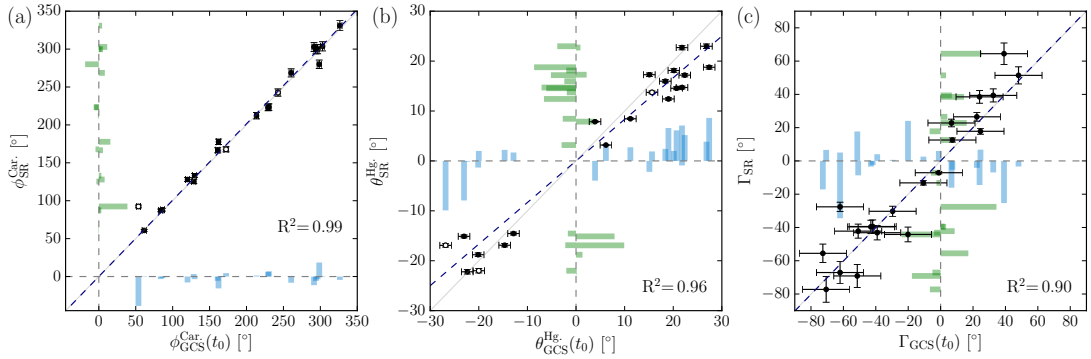

Figure (5.14) Direct comparison of CME and SR longitudes (a), latitudes (b) and tilt angles (c) obtained by GCS modelling and analysis of magnetograms. While ϕ_{SR} and θ_{SR} were determined by the weighted magnetic flux centre with the SMART code, Γ_{SR} was computed independently as described in Section 5.3.2. Longitudes are given in the Carrington coordinate system and latitudes in Stonyhurst coordinates.

flux weighted centre of the corresponding SRs. While for the majority of events the longitudes of SRs and CMEs match within the error range (see Table 5.1) and show in general only slight differences with an $R^2 = 0.99$, a systematic offset to lower SR latitudes can be seen in the comparison of SR and CME latitudes. A linear regression reveals a relationship of:

$$\theta_{\mathrm{SR}} = (0.83 \pm 0.04) \cdot \theta_{\mathrm{CME}}. \tag{5.8}$$

The majority of identified SRs concentrates at latitudes between 10 and 25° with three outliers that are close to the solar equator. Independently to the analysis with the SMART code (see below), the PILs of all identified CME SRs and their tilt angles to the solar equator γ_{SR} were determined using a region-growing-algorithm originally written by D. Jaster in the course of his Bachelor thesis at the Institut für Astrophysik, Göttingen. EUVI 304 and HMI 12 min averaged LOS magnetograms taken as close as possible in time to the CME eruptions were used for this purpose. After a PIL was found by the region-growing-algorithm, the general shape is split into segments that are modelled with linear regression. In the majority of events, one single segment describes the PIL sufficiently accurate. However, in some cases the AR is strongly sheered and quite complex so that more segments are more accurate. The determined SR tilt angles range between -80° and +70°. In order to estimate an uncertainty for these measurements, the same analysis was performed with other observation times around the first appearance of the CMEs. The resulting error of the SR tilt angle $\sigma_{\gamma_{\mathrm{SR}}}$ is of the order of 10% to the measured angle. Examples of determined PILs and fitted segments to determine γ_{SR} are shown in Figure 5.15 for the events #10 and #18 at different observation times. By plotting $\gamma_{\mathrm{GCS}(t_0)}$ versus γ_{SR} (Figure 5.14 (c)), it can be seen that the modelled GCS tilt angle of the CME at the time of the first appearance corresponds well to the SR tilt angle.

By taking the positions of the magnetic flux weighted centre of the ARs as SR positions, an overall shift in latitude in direction to the solar equatorial plane was found for the SRs compared to the corresponding CMEs. This could already be an evidence for a non radial propagation close to the Sun. In general, the tilt angles of the PILs agree well

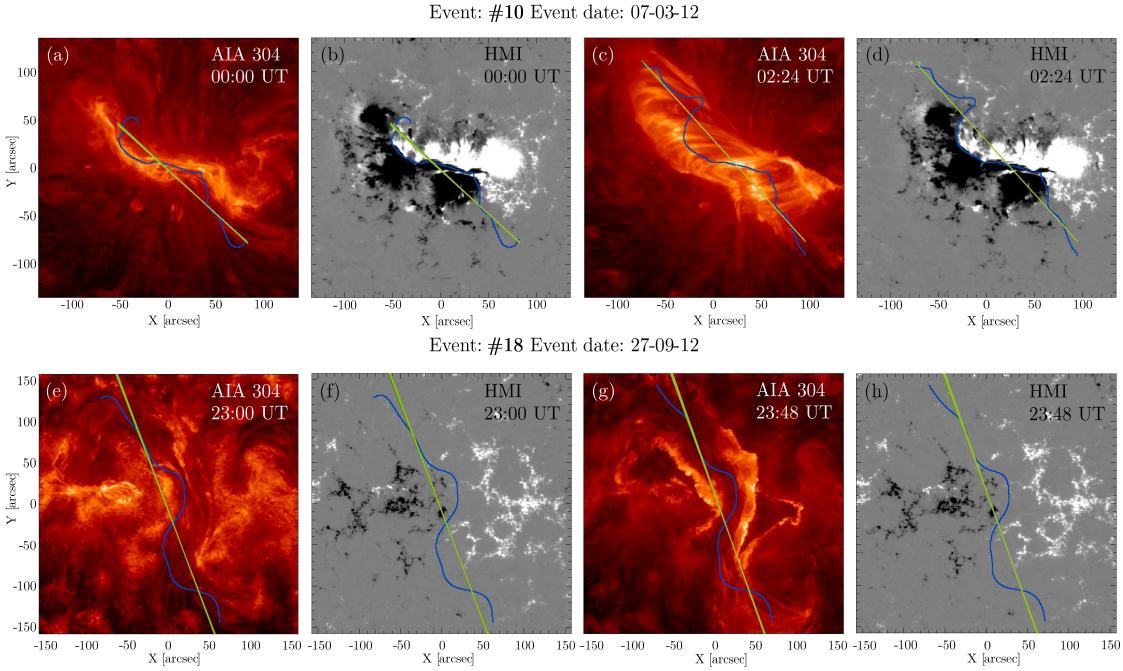

Figure (5.15) Examples of PIL and its tilt angle determination. *Top row*: EUVI 304 and HMI magnetograms of event #10 at the CME eruption time (a and b) and later in (c) and (d) with a visible PEA. *Bottom row*: Same for event #18. While in (e) an inverse sigmoidal structure can be seen, (g) shows flare ribbons at the same region after the eruption.

with the orientations of the corresponding CMEs as already shown by Cremades and Bothmer (2004) for structured CMEs observed in complementary SOHO EIT, MDI and LASCO observations. Also the orientations of structures like FE, PEAs, sigmoids or flare ribbons, as shown in Figure 5.15, agree well with the initial CME orientation supporting our results presented in a preliminary case study (Bothmer and Mrotzek, 2017) and the works of Tripathi, Bothmer, and Cremades (2004b), Palmerio *et al.* (2017) and Palmerio *et al.* (2018) exploit them as proxies for MC orientations. The small deviations can be explained by the results of our case study, in which we showed that expanding kinks of the SR are reflected in the expanding CME FR structure and differing from the global PIL orientation (Bothmer and Mrotzek, 2017).

5.3.3 CME-Flare-Relationship

Solar flares within the identified CME SRs and accompanying the eruption could be assigned in the case of 15 events. The corresponding GOES X-ray classes are listed in Table 5.4. In order to investigate the connection between the CME kinematics and the flare properties, the flare characteristics were analysed with a python library developed by J.F.P. Hinrichs within the OPTIMAP project. By applying the NOAA criteria to GOES SXR and HXR data, the beginning- and peak-times of the flares were identified. The NOAA criteria defines the flare end-time as the time at which the intensity has fallen to

half of the maximum intensity. This ensures that the background is not taken into account for further analysis in the case of weak flares, but neglects parts of the stronger flares. Because of this reason, the end-times for M- and X-class flares were identified using a threshold scaling with the intensity.
The times of the first CME appearance observed in EUVI or COR1 and the time of the maximum CME acceleration with respect to the time difference to the peak time of the flare are plotted in Figure 5.16a. A direct comparison between the time of day of the

Table 5.4. List of identified SRs and related activity phenomena of the analysed CMEs. If they were assigned, NOAA and HARP AR numbers were listed to the SRs for completeness. Since SMART IDs are running IDs of all detected ARs visible in the HMI data, the SMART IDs in column four are the IDs related to the observation times of the magnetograms shown in the Figures 5.13 and A.43 to A.48. The angular positions of the SR are given in HEEQ coordinates and are the positions of the flux weighted centre. The GOES X-ray classes can be seen for the related flares in the last column.

#	NOAA ID	HARP ID	SMART ID	ϕ [°]	θ [°]	rel. Phenomena
1	11247		1	-12.7	-18.8	FE/PEA/FL B4.7
2	11261	750	1	36.1	16.0	FE/FL M9.3
3	11283	833	3	3.3	14.6	FE/FL M5.3
4	11283	833	4	14.8	14.7	FE/PEA/FL X2.1
5	11289	847	9	9.1	22.7	PEA
6	11308	913	4	42.0	-22.0	
7	11328	976	3	27.8	12.4	FE
8	11342/11341	1041	9	-28.1	18.8	FE/FL M1.1
9	11402	1321	4	25.9	23.0	FE/PEA/FL M8.7
10	11430	1449	4	-28.7	17.2	FE/PEA/FL X5.4
11	11430	1449	3	20.0	17.3	FE/PEA/FL M8.4
12	11430	1449	1	62.7	18.1	PEA/FL M7.9
13	11459	1574	3	-21.0	-16.9	FE/PEA/FL C1.8
14		1642	2	-11.5	-14.5	FE/PEA
15	11504	1750	2	-6.8	-15.1	FE/FL M1.9
16	11520	1834	2	6.5	-16.8	PEA/FL X1.4
17	11560	1993	6	6.2	3.2	FL C2.9
18	11575/11577	2040	3	38.2	8.4	FE/PEA/FL C3.7
19	11608	2177	2	-17.8	-22.2	FE/PEA
20	11616/11619	2203	4	13.9	13.7	FE/PEA
21	11618	2220	4	-5.5	7.9	FE/FL M3.5

starting and peak times is shown in 5.16 (b). Except for the events #2 and #9, the CME and flare starting times agree well and the observation time of $v_{\max}$ lies within the flare time window. The standard deviations are $s_{\text{peak}} = 22.12\,\text{min}$ for the peak times and $s_{t_0} = 50.12\,\text{min}$ for the starting times. Furthermore, the SXR and HXR flux, $f_{\text{Fl}}^{\text{SXR}}$ and $f_{\text{Fl}}^{\text{HXR}}$, were compared with the CME kinematics. The data can be seen in Figure 5.16 (c) to (g). Because of the amount of uncertainties and scatter of the data, a linear regressions was chosen to describe the relationships. For the SXR flare flux $f_{\text{Fl}}^{\text{SXR}}$ the following results have been found:

$$
\begin{aligned}
f_{\text{Fl}}^{\text{SXR}} &= (3.1 \pm 1.2) \cdot 10^{-4} v_{\max} - 0.26 \pm 0.21 && R^2 = 0.36,\\
f_{\text{Fl}}^{\text{SXR}} &= (4.0 \pm 1.1) \cdot 10^{-4} v_{12} - 0.31 \pm 0.15 && R^2 = 0.57,\\
f_{\text{Fl}}^{\text{SXR}} &= (4.3 \pm 1.7) \cdot 10^{-2} m_{\text{av}}^{\text{obs}} - 0.19 \pm 0.18 && R^2 = 0.49,\\
f_{\text{Fl}}^{\text{SXR}} &= (1.5 \pm 0.3) \cdot 10^{-20} p_{\max} && R^2 = 0.49,\\
f_{\text{Fl}}^{\text{SXR}} &= (13.3 \pm 2.4) \cdot 10^{-27} E_{\max}^{\max} && R^2 = 0.54.
\end{aligned}
$$

The results for HXR flare flux $f_{\text{Fl}}^{\text{HXR}}$ are:

$$
\begin{aligned}
f_{\text{Fl}}^{\text{HXR}} &= (7.4 \pm 3.3) \cdot 10^{-5} v_{\max} - (7.0 \pm 5.6) \cdot 10^{-2} && R^2 = 0.31,\\
f_{\text{Fl}}^{\text{HXR}} &= (9.9 \pm 2.9) \cdot 10^{-5} v_{12} - (8.28 \pm 4.14) \cdot 10^{-2} && R^2 = 0.52,\\
f_{\text{Fl}}^{\text{HXR}} &= (9.6 \pm 4.8) \cdot 10^{-3} m_{\text{av}}^{\text{obs}} - (4.4 \pm 5.0) \cdot 10^{-2} && R^2 = 0.40,\\
f_{\text{Fl}}^{\text{HXR}} &= (3.3 \pm 0.8) \cdot 10^{-21} p_{\max} && R^2 = 0.41,\\
f_{\text{Fl}}^{\text{HXR}} &= (3.0 \pm 0.7) \cdot 10^{-27} E_{\max}^{\max} && R^2 = 0.47.
\end{aligned}
$$

In general, the SXR flux shows a stronger correlation with the CME kinematics than the HXR flux. Figure 5.16 (c) to (g) shows the most significant correlations between the SXR and HXR flux and the kinematic properties. It was found that the CME speed at $12\,\text{R}_\odot$ and the maximum kinetic Energy are strongly related to the SXR flux with coefficients of determination over 0.5, while the maximum CME speed, CME mass and maximum momentum are less correlated to the SXR flux.

5.3.4 Analysis of Magnetic Properties

The identified CME SRs were analysed with the SSW integrated SMART code as described in Section 4.2.3. For a more detailed description about the methods and algorithms implemented in the code see Higgins *et al.* (2011) as well as Murray *et al.* (2018) and studies referenced therein. SMART computes, for every AR detected in a HMI magnetogram, geometric parameters as the total, positive and negative magnetic area (A_{tot}, A_+ and A_-), the length of the PIL L_{PIL}, the bipolar separation length L_{BIP} as well as magnetic properties as the mean, maximum and minimum magnetic field strength (B_{av}, $B_{\max}$ and $B_{\min}$), the total, positive, negative, imbalance and fractional magnetic flux (f_{tot}, f_+, f_-, f_{imb} and f_{frc}), the Schrijver R value and the Falconer weighted integral over the length of the strong-gradient main neutral line WL_{SG}.
In this work, LOS 12 min average HMI magnetograms were analysed within a 12 h interval centred around the projected starting time of the CME. For the most events, this time corresponds closely to the first observation time in EUVI. In some cases the first appearance lags behind the back projected launch time of the CME. But, since the time window for

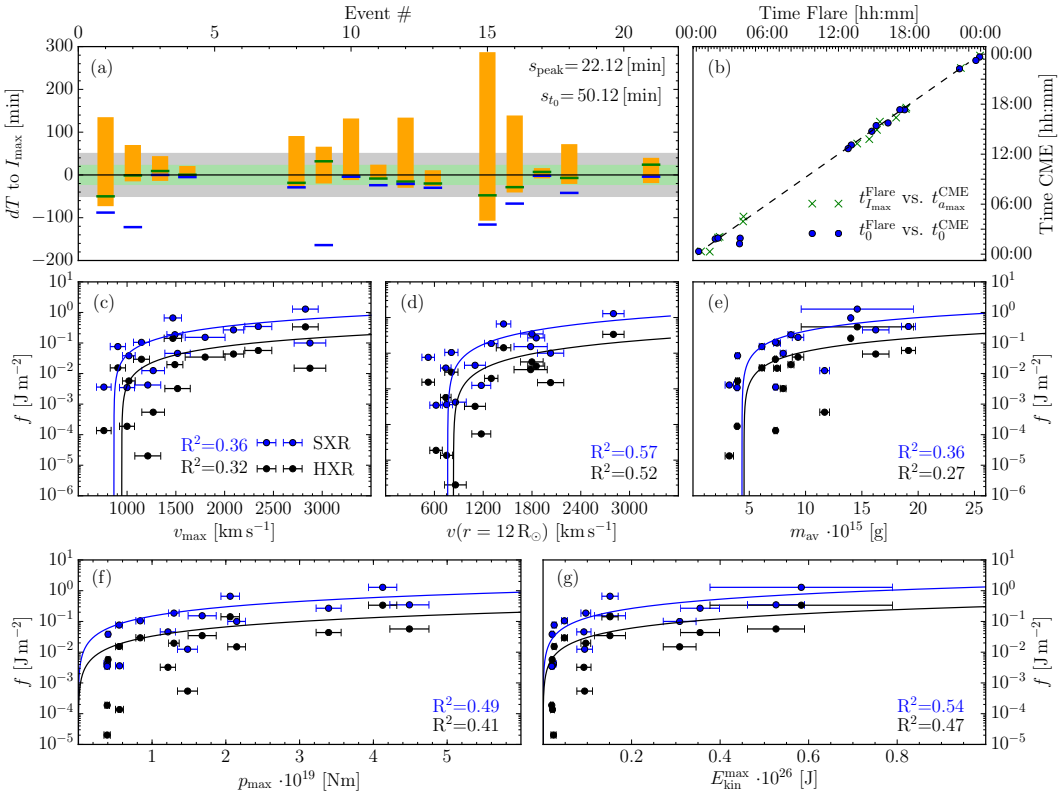

Figure (5.16) Correlation between flare and CME characteristics. Time differences dT of the observed CME start time (blue) and time of the maximum acceleration (green) to the flare peak time are shown in (a). The identified time spans of the flares are indicated by the light blue bars. Calculated standard deviations of the time differences are shown by light green (s_{peak}) and light grey area (s_{t_0}). A direct comparison is plotted in the time-of-day diagram (b). In (c) to (g), correlations of different kinematic parameters of the corresponding CMEs to the computed SXR and HXR fluxes are plotted.

analysis was chosen wide enough, a sufficient quantity of data was obtained to track the changes in the CME SRs. The 12 min average magnetograms were preferred over higher cadence HMI data products to minimise the small scale variability of magnetic properties in order to better analyse the overall evolution of the SR within the time window.

In a first step, the magnetic properties of the identified CME SRs were compared to the more comprehensive HELCATS LOWCAT catalogue. The LOWCAT catalogue contains CME observations of over 2000 events as well as 451 ARs that have been identified as CME SRs and whose magnetic properties have been analysed with the SMART code Murray *et al.* (2018). Since the LINKCAT catalogue includes no time resolved data, the mean values of the analysed SRs of this work were taken for comparison. All averaged magnetic properties of the single ARs of this work are listed in Table 5.5. Furthermore, the distributions of the averaged magnetic main characteristics of the identified SRs are plotted in light blue in Figure 5.17 together with the CME SRs of the HELCATS LOWCAT catalogue in orange. For further comparison, log-normal functions were fitted to the

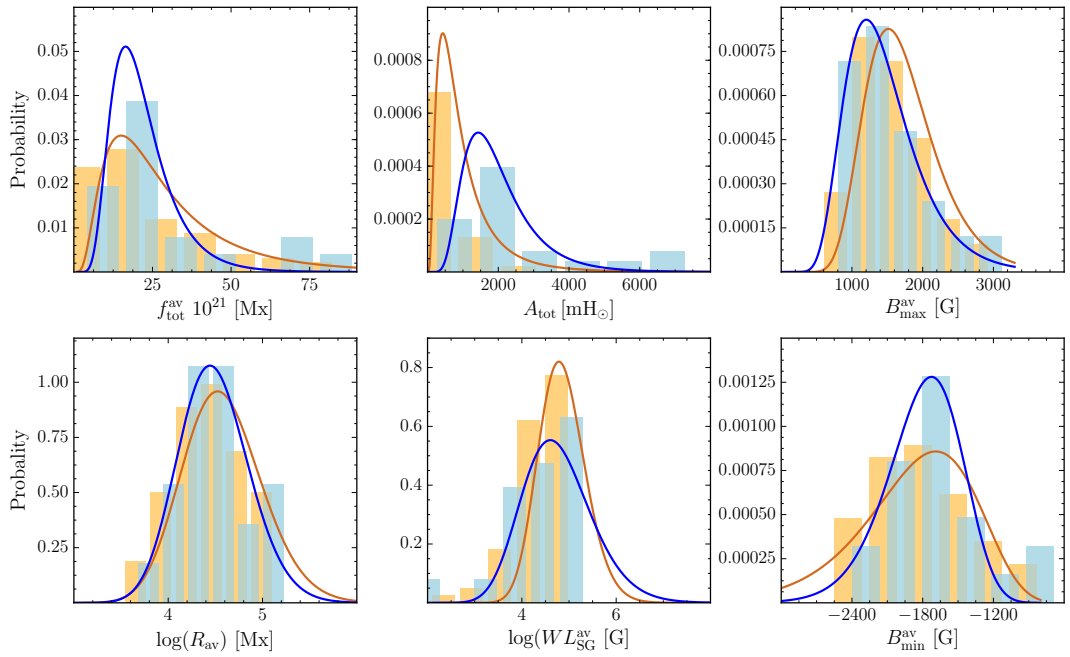

Figure (5.17) Distribution of the SR magnetic properties. The histograms of the SRs analysed in this work are shown in light blue and the fitted log-normal distributions are plotted in blue. Furthermore the data of the more comprehensive LOWCAT catalogue (orange) including their log-normal distributions (dark orange) are shown.

data. The statistical results of the comparison are listed in Table 5.6. In general, the histogram peaks and average values of the 21 selected SRs agree well with the much larger LINKCAT catalogue. Significant differences can only be seen in the total area of the ARs. While the average total area of the analysed 21 SRs is 2386 millions of solar hemispheres the average value of the LINKCAT ARs is $\sim$ 3 times smaller with 780 millions of solar hemispheres .

In the next step, the magnetic properties of the CME SRs were correlated with the geometric and kinematic properties of the corresponding CMEs, which are discussed in Section 5.1.1, 5.1.2 and 5.2. Since time resolved magnetograms were used and the evolution of the SR around the eruption time was observed, the average, maximum and minimum values of all magnetic properties were used for this analysis. Significant correlations were found with the single properties of the magnetic flux, magnetic field strength, magnetic area of the ARs, the Schrijver R value and the Falconer WL_{SG} weighted integral. These magnetic properties were correlated with the CME speeds at different heights (v_{max}, v_{12} and $v(r = 50\,\mathrm{R}_\odot)$), average CME mass from the different viewpoints m_{av}, the maximum acceleration a_{max}, the maximum momentum of the CME p_{max}, the maximum kinetic energy $E_{\mathrm{kin}}^{\mathrm{max}}$, and the CME angular widths W_{eo} and W_{fo} of the last observation beyond h_{SSE}. The results are plotted in the Figures 5.18 to 5.21. For the sake of clarity, only correlations between the single kinematic properties and the total, maximum or minimum of the magnetic property that have the largest R^2 are plotted directly versus each other in

Table 5.5. Magnetic properties of the identified SRs. All values are the average over the time changing properties within the observation window. Errors of the SMART analysis lie within 5% for all values.

#	A_{tot}	A_+	A_-	B_{av}	B_{max}	B_{min}	f_{tot}	f_+	f_-	f_{imb}	f_{frc}	L_{PIL}	R	WL_{SG}
	[sol. Hemi.]			[G]			10^{21} [Mx]					[Mm]	10^3 [Mx]	10^3 [G]
1	428.9	217.0	211.9	-4.3	1253.2	-1444.7	5.8	1.2	1.4	-0.4	-0.03	0.0	10.4	12.6
2	2031.0	654.8	1376.1	-16.1	1121.1	-1723.6	26.5	3.2	10.3	-4.2	-0.27	12.58	78.2	95.8
3	2004.1	823.1	1181.0	-10.9	1522.4	-1773.2	23.8	4.4	8.3	-2.0	-0.17	0.92	33.4	50.1
4	1800.6	710.5	1090.2	-15.3	1368.2	-1632.8	22.1	3.6	7.7	-3.1	-0.18	0.74	33.2	37.9
5	1690.1	567.2	1122.9	-16.4	937.9	-2430.6	22.9	2.6	10.6	-3.1	-0.35	0.0	20.4	25.5
6	265.5	143.9	121.6	11.2	761.7	-653.6	5.1	0.7	0.5	0.8	0.02	0.0	8.6	0.1
7	1489.5	706.1	783.4	-7.0	1201.6	-1020.9	20.5	3.6	3.9	-2.1	-0.01	0.0	18.6	5.7
8	1373.7	560.6	813.1	-15.2	969.9	-1830.5	20.8	2.7	5.9	-2.3	-0.15	0.0	18.9	9.4
9	5142.1	2511.0	2631.1	7.5	1297.5	-2076.4	66.7	13.0	19.8	2.5	-0.1	2.71	69.6	95.3
10	3815.0	1559.1	2255.9	-43.4	1885.4	-2090.9	42.3	12.8	19.6	-8.0	-0.16	48.46	179.8	221.6
11	3679.3	1513.2	2166.0	-28.4	2090.7	-1707.2	38.9	12.0	14.3	-5.4	-0.06	1.39	50.5	97.7
12	6616.0	2335.6	4280.4	-45.2	3157.1	-2324.3	76.5	21.6	29.6	-17.4	-0.1	38.35	142.5	99.9
13	2182.2	1132.0	1050.2	2.9	1703.8	-1394.7	24.9	7.2	6.7	-0.2	0.02	0.0	19.9	23.4
14	164.6	99.9	64.7	4.7	799.6	-695.1	3.2	0.5	0.3	0.2	0.06	0.0	4.5	3.2
15	3293.6	1382.7	1911.0	-17.7	2305.9	-2105.7	38.0	12.3	13.9	-4.1	-0.04	0.22	46.6	94.9
16	7375.9	3615.8	3760.1	-0.2	2396.5	-1799.6	89.5	31.4	23.0	1.2	0.09	8.49	124.9	186.3
17	1313.3	645.4	667.9	-3.3	1731.2	-1731.3	15.5	4.6	5.3	-0.4	-0.05	0.66	27.7	52.8
18	1531.0	560.6	970.3	-10.7	989.6	-2053.1	24.4	2.6	6.8	-4.1	-0.17	0.0	30.0	32.0
19	556.7	196.7	360.0	-13.8	1261.6	-1407.6	8.4	1.0	2.3	-1.7	-0.14	0.0	11.6	6.2
20	1457.3	716.1	741.3	-1.8	1422.6	-1721.6	19.9	3.8	5.2	-0.6	-0.07	0.0	22.1	9.2
21	1893.1	875.5	1017.6	-6.7	1667.2	-1940.8	22.9	5.7	8.0	-1.1	-0.1	2.62	51.3	99.9

the single subplots. The other two components of the magnetic properties are represented by the size and colour of the marker. Linear regressions were performed if the coefficient of determination is larger than 0.4 and are shown by the blue lines. Grey areas represent the range of the standard deviations.

The strongest correlations to the single properties of f were found to be with the CME mass m_{av}, a_{max}, p_{max} and $E_{\mathrm{kin}}^{\mathrm{max}}$. A linear regression yields the following results:

$$
\begin{aligned}
f^{\text{-}}_{\mathrm{max}} &= (1.65 \pm 0.19)\, m_{\mathrm{av}}[10^{15}\,\mathrm{g}] - 2.9 \pm 1.7 && R^2 = 0.80,\\
f^{\mathrm{imb}}_{\mathrm{min}} &= (6.3 \pm 0.9)\, a_{\mathrm{max}}[10^{-3}\,\mathrm{ms}^{-2}] - 1.3 \pm 1.0 && R^2 = 0.72,\\
f^{\text{-}}_{\mathrm{av}} &= (5.7 \pm 0.8)\, p_{\mathrm{max}}[10^{19}\,\mathrm{Ns}] + 2.9 \pm 1.3 && R^2 = 0.75,\\
f^{\text{-}}_{\mathrm{max}} &= (39.3.3 \pm 6.9)\, E_{\mathrm{kin}}^{\mathrm{max}}[10^{26}\,\mathrm{J}] - 5.4 \pm 1.4 && R^2 = 0.63,
\end{aligned}
$$

with the magnetic flux in units of 10^{21} Mx. From the scatter plots of Figure 5.18 it can be seen that the total f^{tot}, maximum (positive) f^{+} and minimum (negative) $f^{\text{-}}$ flux show the same general trend with respect to the single kinematic properties. Furthermore, evidence of an overall trend between the CME angular widths and the magnetic flux is visible. Since magnetic flux is the integral of the magnetic field strength over the magnetic area, a similar but less distinct behaviour can be observed for the properties of the magnetic area of the ARs. The highest coefficient of determination are reached between m_{av} and the average over time of the negative magnetic area $A^{\text{-}}_{\mathrm{av}}$. Another significant correlation was found between the CME maximum momentum and the maximum negative magnetic area $A^{\text{-}}_{\mathrm{max}}$. These relationships can be expressed by:

$$
\begin{aligned}
A^{\text{-}}_{\mathrm{av}}[10^{3}\,\mathrm{mH_{\odot}}] &= (216 \pm 26)\, m_{\mathrm{av}}[10^{15}\,\mathrm{g}] - 369 \pm 238 && R^2 = 0.79,\\
A^{\text{-}}_{\mathrm{av}}[10^{3}\,\mathrm{mH_{\odot}}] &= (774 \pm 124)\, a_{\mathrm{max}}\,[\mathrm{ms}^{-2}] - 437 \pm 224 && R^2 = 0.67.
\end{aligned}
$$

The most clear correlation with the CME kinematic parameters were found with the Schrijver R value, which is plotted in Figure 5.20. Of all AR magnetic properties considered, the maximum over the analysed time window of the R value, R_{max}, shows the most significant correlation with the CME speed. This applies especially to the CME speed at a height of $12\,\mathrm{R_{\odot}}$. Furthermore, the CME mass is well correlated with R, and in this way the same is true for the maximum CME momentum and kinetic energy. The single fitting

Table 5.6. Comparison between the statistics of the HELCATS LOWCAT catalogue and the 21 analysed CME SRs of this work. For every listed magnetic property, the peak value of the histogram (p) and the average value of all events (av.) are compared.

	f_{tot} 10^{21} [Mx]		A_{tot} 10^{-6} [sol. Hemi.]		B_{max} 10^{3} [G]		B_{min} 10^{3} [G]		R 10^{4} [Mx]		WL_{SG} 10^{4} [G]	
	p	av.	p	av.	p	av.	p	av.	p	av.	p	av.
this work	16.4	29.5	1434	2386	1.2	1.5	-1.7	-1.6	2.8	4.8	4.0	6.0
LOWCAT	15.0	30.5	433	780	1.5	1.8	-1.7	-1.8	3.3	9.6	6.1	55

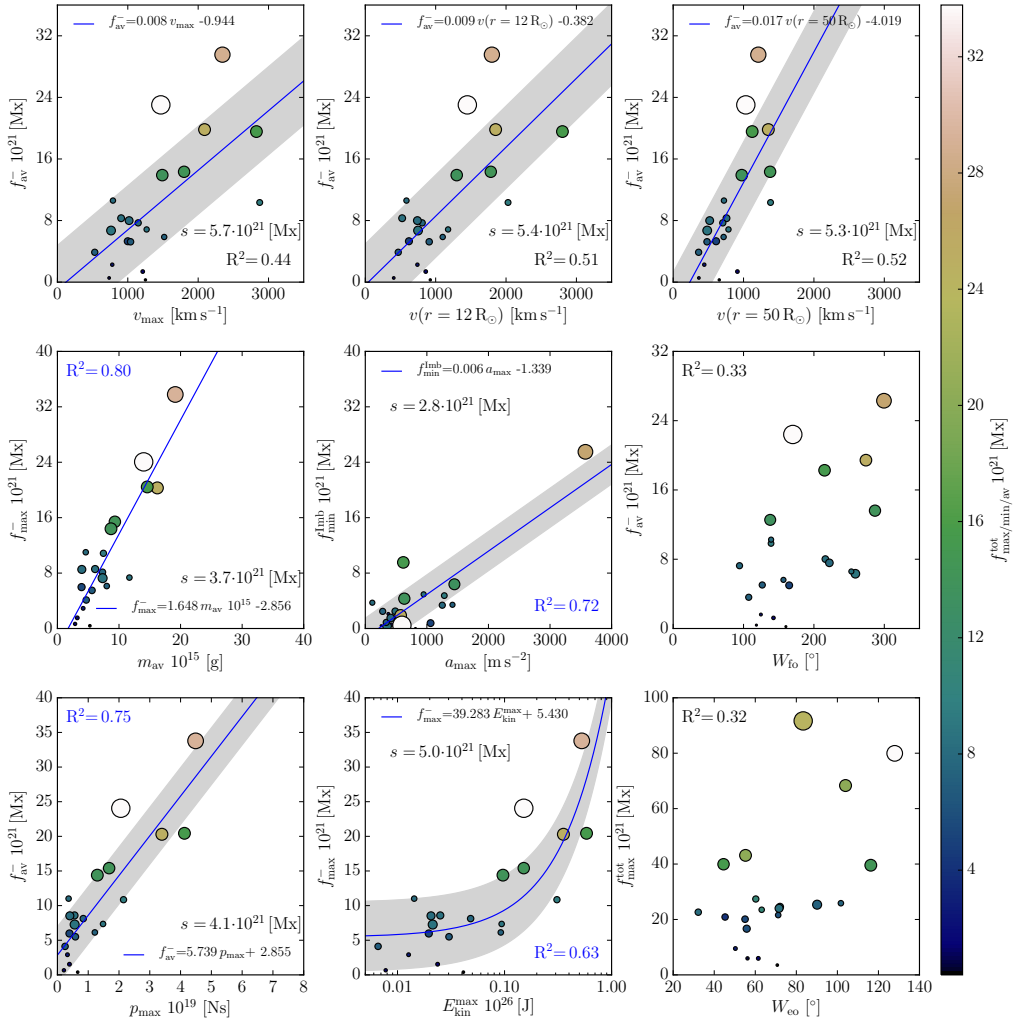

Figure (5.18) Relationship between the properties of the magnetic flux of the CME SRs and the relevant kinematic parameters. In all subplots, the marker size and colour represent the positive magnetic flux f^{+} and the total magnetic flux f^{tot} counterparts of the ordinates. The ordinate index refers to the average, maximum or minimum over time of the magnetic flux property. For correlations with $R^2 > 0.4$, linear regression was performed, whose results can be seen in the legends. The standard deviations s are indicated by the grey area.

results and corresponding coefficients of determination are summarised below:

$$
\begin{aligned}
R_{\mathrm{max}} &= (64.6 \pm 11.8)\, v_{\mathrm{max}}\,[\mathrm{kms}^{-1}] - (33.2 \pm 17.9)\, 10^3 && R^2 = 0.61,\\
R_{\mathrm{max}} &= (106.34 \pm 29.13)\, v(r = 12\,\mathrm{R}_\odot)\,[\mathrm{kms}^{-1}] - (30.3 \pm 25.4)\, 10^3 && R^2 = 0.70,\\
R_{\mathrm{min}} &= (7216 \pm 1212)\, m_{\mathrm{av}}[10^{15}\,\mathrm{g}] - (16.54 \pm 11.13)\, 10^3 && R^2 = 0.65,\\
R_{\mathrm{max}} &= (38121 \pm 4597)\, p_{\mathrm{max}} \cdot [10^{19}\,\mathrm{Ns}] - (5.9 \pm 8.3)\, 10^3 && R^2 = 0.78,\\
R_{\mathrm{max}} &= (288.3 \pm 32.6)\, E_{\mathrm{kin}}^{\mathrm{max}} \cdot [10^{26}\,\mathrm{J}] - 19.5 \pm 6.8 && R^2 = 0.80,
\end{aligned}
$$

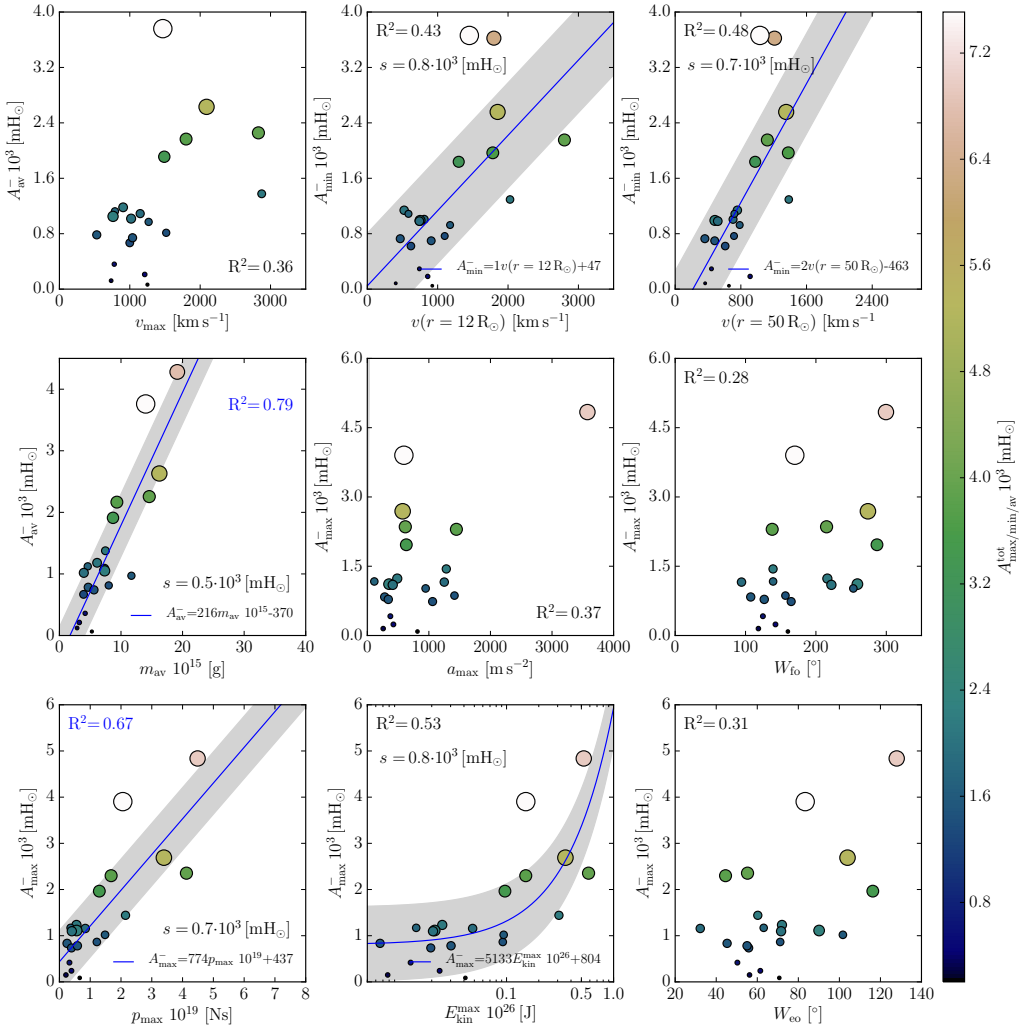

Figure (5.19) Relationship between the properties of the magnetic area of the CME SRs and the relevant kinematic parameters. In all subplots, the marker size and colour represent the positive magnetic area A^{+} and the total magnetic area A^{tot} counterparts of the ordinates. The ordinate index refers to the average, maximum or minimum over time of the magnetic area property. For correlations with $R^2 > 0.4$, linear regression was performed, whose results can be seen in the legends. The standard deviations s are indicated by the grey area.

with R in units of 10^3 Mx. As seen above in the case of the magnetic flux analysis, the correlations of the minimum as well as average values of R within the observed time window, which are presented by the marker size and colour in Figure 5.20, to the CME kinematics are also noticeable. For the majority of cases, the coefficients of determination of these properties are close to the once of the directly plotted and fitted correlations shown in the scatter plots.
By looking at the results of the correlation analysis with WL_{SG} presented in Figure 5.21, a similar but slightly weaker behaviour can be seen for the Falconer weighted integral.

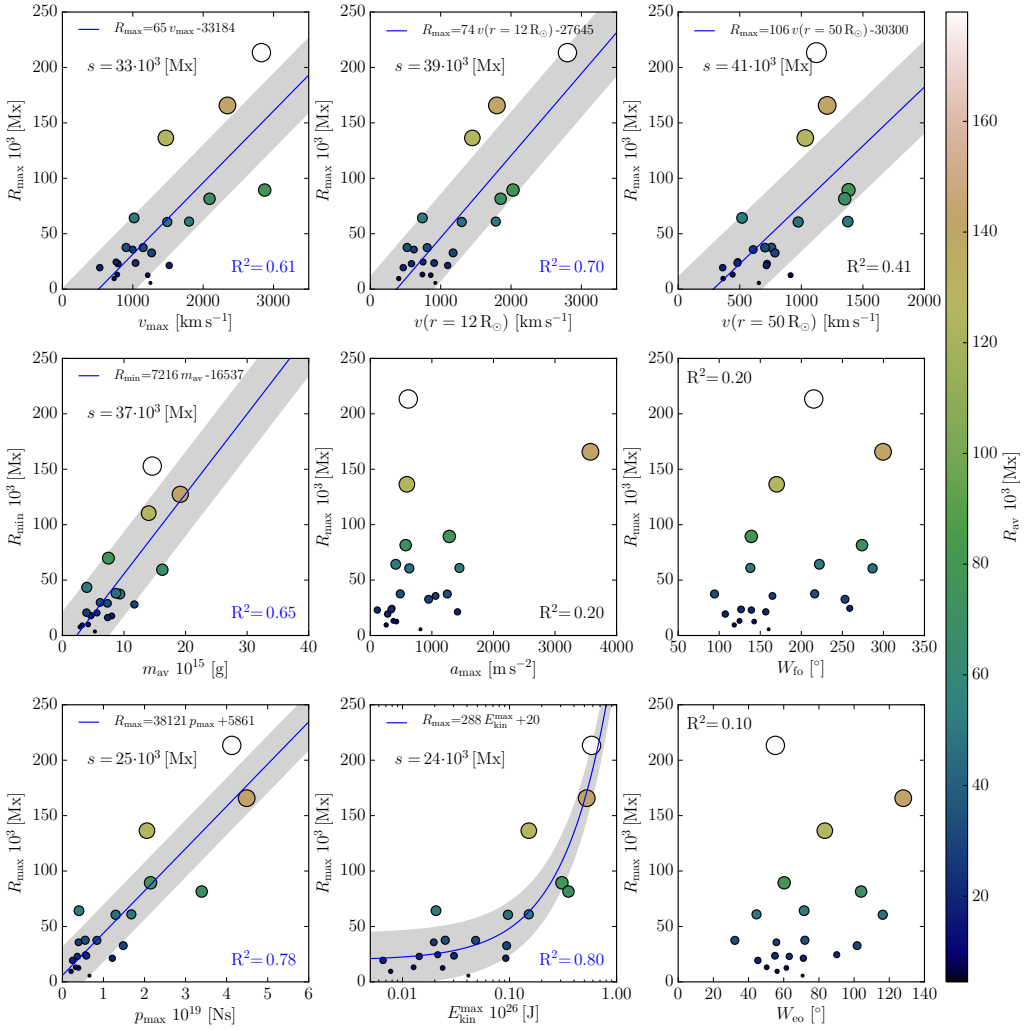

Figure (5.20) Relationship between the properties of the Schrijver R value of the CME SRs and the relevant kinematic parameters. In all subplots, the marker size and colour represent the counterparts of the ordinates and the mean Schrijver value R_{av}. The ordinate index refers to the average, maximum or minimum over time of the magnetic area property. For correlations with $R^2 > 0.4$, linear regression was performed, whose results can be seen in the legends. The standard deviations s are indicated by the grey area.

However, also the CME speed at 12 $R_\odot$, CME mass, momentum and kinetic Energy show significant correlation with WL^{SG}. The results can be summarised as follows:

$$
\begin{aligned}
WL^{\mathrm{SG}}_{\mathrm{av}}[10^3\,\mathrm{G}] &= (77.0 \pm 13.9) v_{12}\,[\mathrm{km s^{-1}}] - (26.7 \pm 17.8)\,10^3 && R^2 = 0.62,\\
WL^{\mathrm{SG}}_{\mathrm{max}}[10^3\,\mathrm{G}] &= (15.8 \pm 2.6)\,10^3\, m_{\mathrm{av}}[10^{15}\,\mathrm{g}] - (45.4 \pm 23.8)\,10^3 && R^2 = 0.66,\\
WL^{\mathrm{SG}}_{\mathrm{max}}[10^3\,\mathrm{G}] &= (60.9 \pm 7.9)\,10^3\, p_{\mathrm{max}}[10^{19}\,\mathrm{Ns}] + (2.08 \pm 11.14)\,10^3 && R^2 = 0.76,\\
WL^{\mathrm{SG}}_{\mathrm{max}}[10^3\,\mathrm{G}] &= (44.4 \pm 6.3)\,10^4\, E^{\mathrm{max}}_{\mathrm{kin}}[10^{26}\,\mathrm{J}] + (26.02 \pm 13.18)\,10^3 && R^2 = 0.72.
\end{aligned}
$$

The same analysis was performed for the maximum, minimum and average values of the

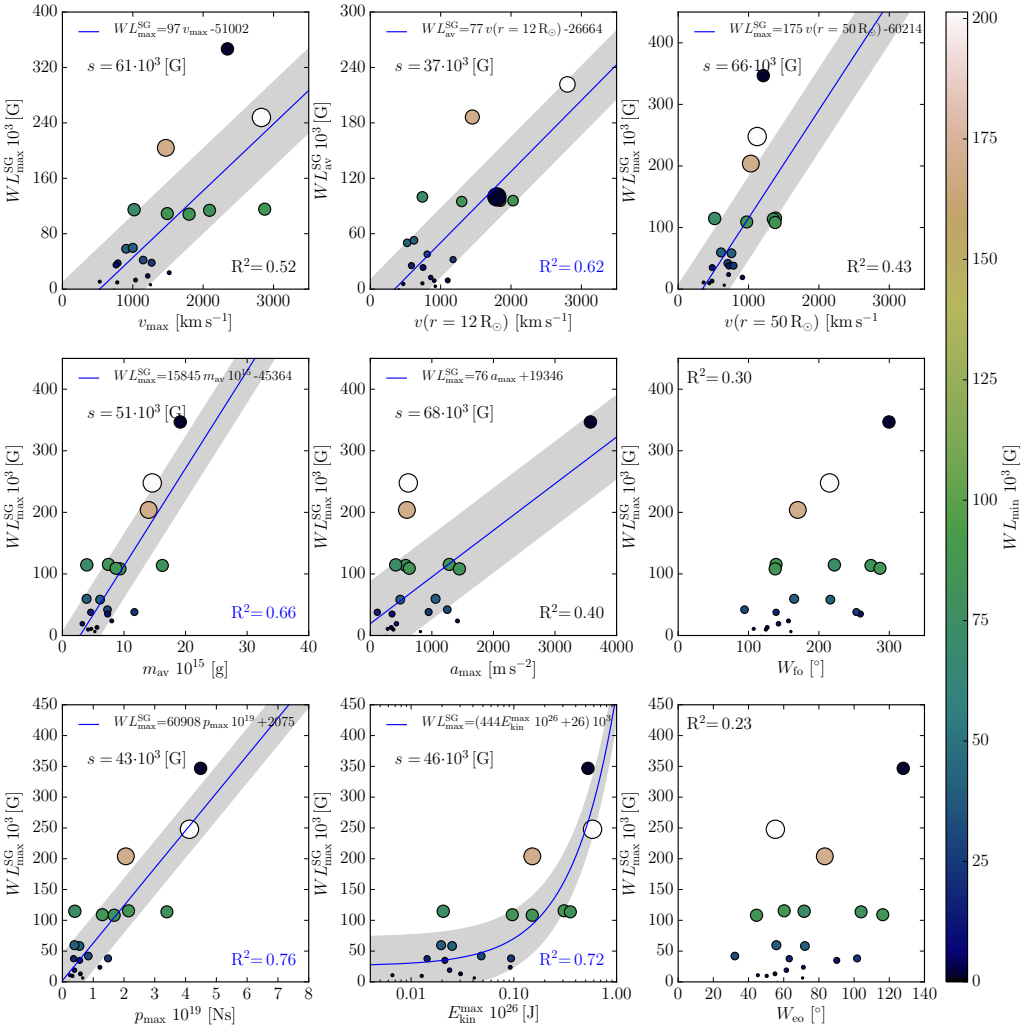

Figure (5.21) Relationship between the properties of the Falconer weighted integral R value of the CME SRs and the relevant kinematic parameters. In all subplots, the marker size represent the WL^{SG}_{av} or WL^{SG}_{max} depending on the property used as ordinate. The marker colour represents WL^{SG}_{min}. The ordinate index refers to the average, maximum or minimum over time of the magnetic area property. For correlations with $R^2 > 0.4$, linear regression was performed, whose results can be seen in the legends. The standard deviations s are indicated by the grey area.

magnetic field strength of the ARs. Essential trends between the CME kinematics and the properties of B can be seen, but no strong correlations, as for the other magnetic characteristics.

These results provide the findings of the CME mass analysis that v_{12} is an important kinematic parameter, which is connected with the CME initiation processes. The overall good correlation between R as well as WL_{SG} with the CME kinematics shows a unique dependence on the magnetic flux concentrated along the PIL. As proxies of the free magnetic energy, R and WL_{SG} have the best correlations with the CME maximum momentum

and maximum kinetic energy. This is also true for the results of the CME speed ($v_{\max}$ as well as v_{12}), which agrees well with other studies analysing AR magnetic properties and their corresponding CMEs (e.g. Venkatakrishnan and Ravindra 2003 and Tiwari *et al.* 2015). In general, it can be seen that the SR area and the magnetic flux play a major role for the early CME kinematics. However, since the magnetic properties were derived using LOS magnetograms, additional uncertainties by projection effects could not be excluded.

5.3.5 Temporally Resolved Analysis

Since temporaly resolved HMI data are used in this work, it is logical not only to analyse the extremes and average values of the individual magnetic characteristics, but also to study the evolution of the SRs before and after the CME eruption. Examples of the SR evolution are illustrated in Figure 5.22 for the magnetic properties A_{tot}, f_{tot}, B_{av}, L_{PIL}, R and WL_{SG}. The selected examples are representative for the four different types of observed evolutions in all selected ARs. The identified SR can be divided into two groups. For 11 events, emergence of new magnetic flux after the eruption could be observed, while cancellation of magnetic flux before the eruption can be seen for the other 10 events. This can be seen in Figure 5.22 by the changing magnetic area, magnetic field strength and the resulting total magnetic flux.

The two groups of events obtained this way were analysed for the total change in the magnetic properties from their extremes before or after the CME eruption time to the values at the eruption time. A significant relationship was found between the maximum CME acceleration and the change in the total flux df_{tot}. Furthermore, trends for the CME face-on and edge-on angular width as well as for the CME latitude of the first observation could be identified. Both flux groups are plotted in Figure 5.23 versus $a_{\max}$, the CME angular widths and the CME latitude. Negative values represent events with observed flux cancellation while positive values stand for events with flux emergence. In the relationship between $a_{\max}$ and df_{tot}, the two flux processes can be clearly separated. No symmetry can be seen between flux cancellation and emergence and they seem to be differently correlated with $a_{\max}$. Linear regression gives the following result for the change in case of flux cancellation $df^{\text{c}}_{\text{tot}}$ and the change in emerging flux $df^{\text{e}}_{\text{tot}}$:

$$df^{\text{c}}_{\text{tot}}[\%] = (-2 \pm 0.7) \cdot 10^{-3}\, a_{\max}\,[\text{ms}^{-2}] - (2.8 \pm 1.1) \quad R^2 = 0.47,$$
$$df^{\text{e}}_{\text{tot}}[\%] = (7.3 \pm 1.8) \cdot 10^{-3}\, a_{\max}\,[\text{ms}^{-2}] + (0.1 \pm 1.4) \quad R^2 = 0.69.$$

The majority of flux cancellation events shows large changes in the average magnetic field strengths. In contrast, only small changes of B_{av} can be seen for the flux emergence events. In the case of the CME angular widths (see Figure 5.23 (b)) no separation can be seen but an overall trend with W_{fo} and W_{eo} for df_{tot}. In general, CMEs launched at higher latitudes show smaller changes in the total flux and faster speeds at $12\,\text{R}_{\odot}$, which is indicated by the marker size in Figure 5.23. The strongest changes in B_{av} for flux cancellation and emergence are close at $\theta = 15°$. The events of the two processes seem to be symmetrical distributed around abscissa, but a unique and quantitative analysis requires a larger data set. It should be noted that two of the flux emergence events were excluded from the analysis because the flux emergence seems to happen on a larger time scale as the considered time window and the total evolution could not be analysed. In the case of event #7, a sharp peak of new emerging flux can be seen directly before the eruption. Since this event

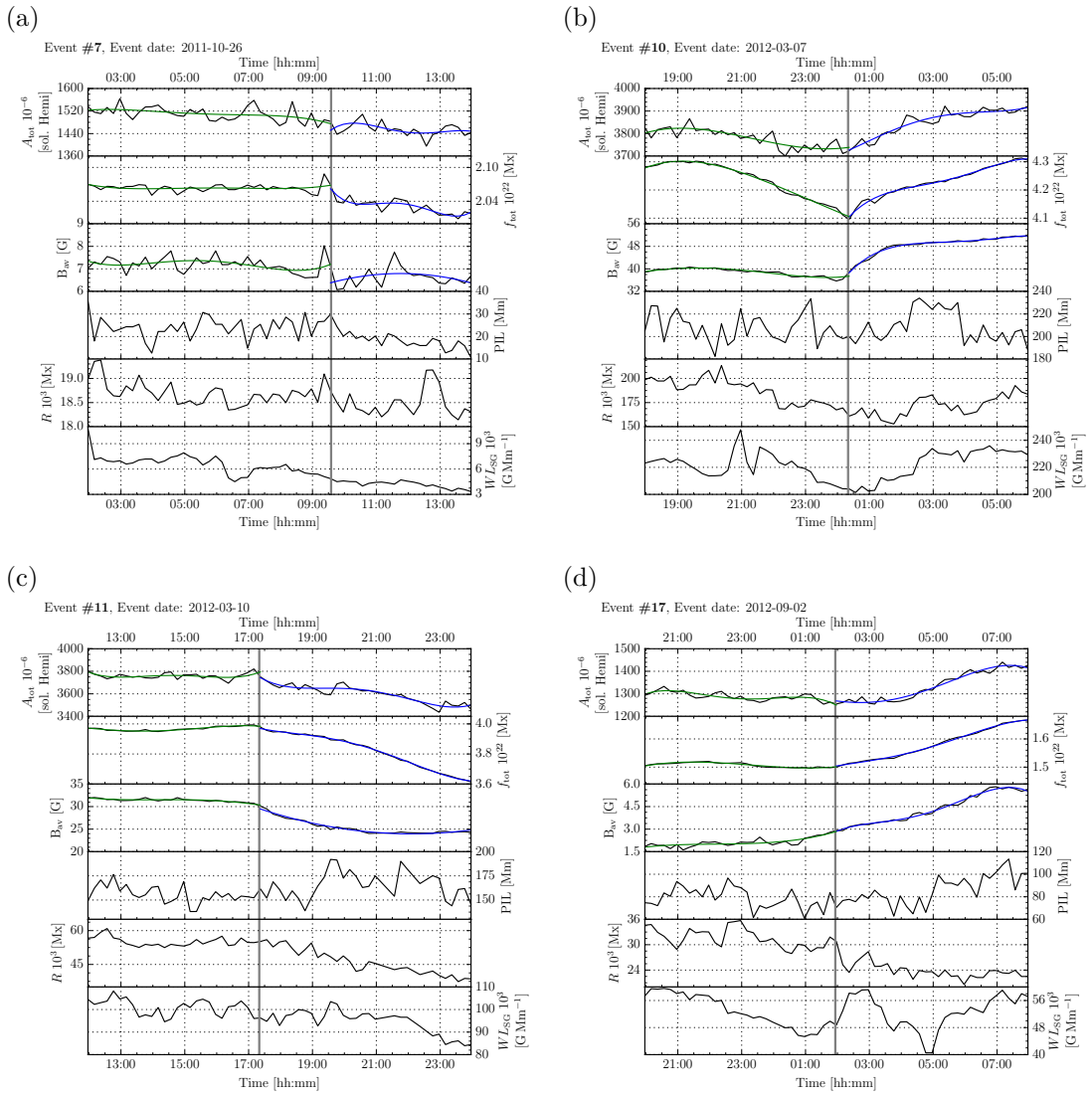

Figure (5.22) Examples of the temporal profile of SR properties. The grey line represents the time of the first CME appearance. Polynomial fits before and after the eruption are shown for the total area A_{tot}, total magnetic flux f_{tot} and average magnetic field strength B_{av} in green and blue. While the eruption time of Event #7 (a) corresponds with a short and sharp increase of f_{tot}, the events # 10, 11 and 17 ((b) to (d)) show a gradual increase or decrease of f_{tot}.

is a slow CME and no CME structure could be observed in EUVI, the eruption time must be before the first appearance in COR1. Therefore, event # 7 is counted as emerging flux event.

Flux cancellation causes the formation of a FR through the expelling of magnetic flux into higher regions while flux emergence lead to the loss of equilibrium in the case of a preexisting FR (Heyvaerts, Priest, and Rust, 1977; Linker *et al.*, 2003). Both processes are well-known to drive CMEs and flares (Livi *et al.*, 1989; Chen and Shibata, 2000; Bothmer

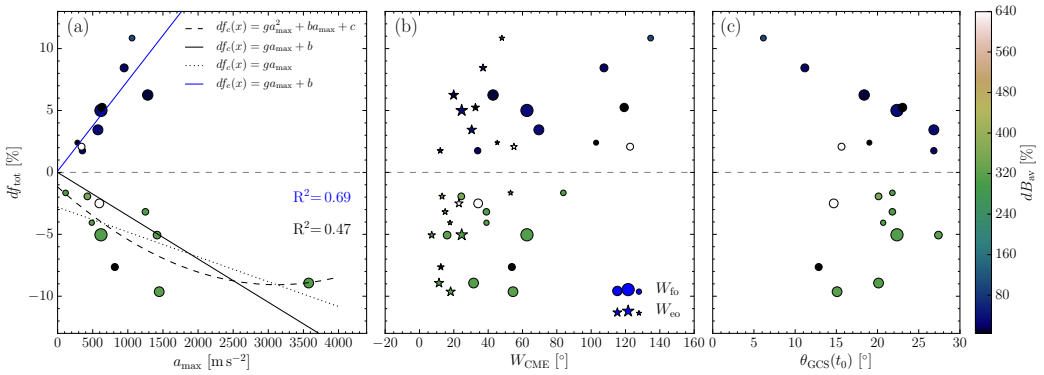

Figure (5.23) Comparison of changing magnetic flux within the SR observation window and CME properties. The y-axis presents in all three plots the changing total magnetic flux of the CME SR df_{tot} in percentage. Positive values correspond to flux emergence after the time of eruption while negative ones corresponds to flux cancellation before the CME eruption time. Marker size and colour represent CME speed at 12 $R_\odot$ and the changing average magnetic filed strength dB_{av}, respectively. (a): Correlation with the maximum observed CEM acceleration. The single curves show different fitted polynomials. (b): Correlation with the CME face-on and edge-on angular with. (c): Correlation with the CME latitude at t_0.

and Tripathi, 2007). According to the results, it looks that both processes are differently effective in accelerating the CMEs. Furthermore, the change in the average magnetic field is in general smaller for the flux emergence process than for the flux cancellation. In the case of the CME size, an overall trend with the changing magnetic flux of the corresponding AR could be observed. The latitudinal dependency to the change in magnetic flux shows that CMEs originating from higher latitudes are in general connected to smaller changes in magnetic flux. Since the differential rotation of the Sun is the main driver for both processes, this behaviour is as expected. However, by the fits for the flux cancellation, shown in Figure 5.23a, it can be seen that for a refined quantitative analysis a more comprehensive data set is necessary. The same is true for the time window in which the AR were analysed. A more extended time window covering larger parts of the AR evolution would be preferable as could be seen by the example of the two excluded events that were not analysed because neither the starting point nor the end point of the flux change could be determined. This can be seen also in the so-called "main sequence" of ARs, which gives an upper limit for the free magnetic energy build-up by an AR (Falconer *et al.*, 2009). The main sequence of the data of this work is plotted in Figure 5.24. In general, the results of Falconer *et al.* (2009) could be reproduced with the relatively small time window of observations, but, since the values of the magnetic properties close to the CME eruption time (marked by the triangles) are not close to the front edge of the individual AR data, important information are missing. However, to analyse the rate by which an AR dissipated free magnetic energy by CMEs and flares, a more extend data set with a larger time window is needed.

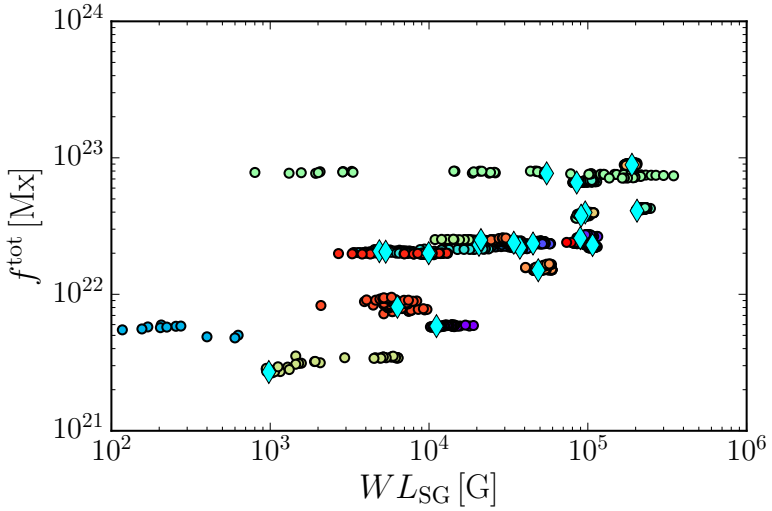

Figure (5.24) Plot of the so-called "main sequence" of ARs that are SRs of explosive solar events as CMEs and flares. The data of all ARs are plotted in different colours. The AR values that are in time nearest to the CME eruption are marked by the diamonds.

5.4 Analysis of the Interplanetary Propagation

In order to analyse the CME trajectories in the inner heliosphere including the interaction with the ambient solar wind, all r-t-profiles derived from GCS-fitting (see 5.1) were processed with the drag-only approach of a DBM introduced in Section 3.3. The algorithm used is explained in detail in Section 4.2.5. All fitted parameters and the characteristic variables, over heliospheric distances from r_0 to 1 AU, are listed in Table 5.7. The computed trajectories are shown together with the r-t-profiles of the individual events in Figure 5.27 as well as in the Figures A.50 and A.49 in the appendix. For a better comparison, linear regressions using, first, the GCS data within the FOV of COR2 (red dashed line) and, second, the data within the FOV of HI1 (orange dashed line), are shown. In general, the best fitted solutions of the single events agree well with the measured r-t-profiles derived from GCS modelling. The R^2, the coefficient of variation cv and the standard deviations s of the DBM best solutions of the single events can be found in Table A.1. While R^2 is above 0.99 for all events, cv ranges between 0.46% and 4.29%. An acceleration by the ambient solar wind can be seen only in one event of the data set (event #3) according to the DBM results. The best R^2 solutions of the remaining 20 events show a deceleration of the ICMEs. According to the result of r_0, the drag force becomes the dominating force for 62% of the events within the first 20 $\mathrm{R}_\odot$ and for all events within 40 $\mathrm{R}_\odot$.

At r_0, the initial speed v_0 ranges from 365 to 2425 $\mathrm{km\,s^{-1}}$ with an average speed of 1003 $\mathrm{km\,s^{-1}}$. The two fastest events ($v_0 > 2000\,\mathrm{km\,s^{-1}}$) of the data set are decelerated to $\sim$ 30% of v_0 at a distance of 1 AU. On average, the predicted $v_{1\mathrm{AU}}^{\mathrm{D}}$ of all events are 64% of v_0. In the case of four events, the fitted $w_{1\mathrm{AU}}$ is above 450 $\mathrm{km\,s^{-1}}$ indicating a fast solar wind ahead the CME. Ranging from 0.24 to $12.1 \cdot 10^{-8}$ $\mathrm{km\,s^{-1}}$ for all events, the drag parameter at the height r_0 is in general lower compared to the results of a static DBM as reported e.g. by Vršnak *et al.* (2013). The average drag coefficient for all events

at r_0 is 0.84 becoming smaller with larger heliospheric distances and differing significantly from unity at $r = 1\,\mathrm{AU}$ ($c_\mathrm{D} = 0.3$ on average). In Figure 5.25, the drag parameter at r_0 is plotted versus v_0 and the $c_\mathrm{D}(r = 1\,\mathrm{AU})$ versus the CME mass. Regression yields the following relationships:

$$c_\mathrm{D}(r_0) = (1.92 \pm 1.03)\,10^{-7}\,v_0^2 + (6.1 \pm 2.5)\,10^{-7}\,v_0 + 0.02 \pm 0.13,$$
$$c_\mathrm{D}(r = 1\,\mathrm{AU}) = (-2.20 \pm 6.10)\,10^{-4}\,m_\mathrm{av}^2 + (2.9 \pm 1.3)\,10^{-2}\,m_\mathrm{av} + (0.15 \pm 0.05),$$

with v_0 in units of $\mathrm{km\,s^{-1}}$ and m_av in units of $10^{15}\,\mathrm{g}$. Both correlations show a high coefficient of determination of $R^2 = 0.91$ and $R^2 = 0.83$, respectively. A positive correlation between c_D and the CME mass was already found by Cargill (2004). This result implies that the CME mass has a crucial impact on the final c_D, since the value of the drag parameter at 1 AU tends to an asymptotic value. The range of the drag coefficient agrees partially with the results of Vršnak *et al.* (2013), who found γ to lie in the range of $\sim 0.2 - 2 \cdot 10^{-8}\,\mathrm{km\,s^{-1}}$ in a static DBM ($C_D = 1$).

Figure 5.26 shows the fitted heights at which the drag becomes the dominating force for all decelerated CMEs plotted versus v_0, the latitude of the first observation of the CME and the length of the bipolar separation line of the SR. The CME mass and a_max are indicated by the marker size and colour. A clear anticorrelation between v_0 and r_0 can be seen, which is in good agreement with the results of Sachdeva *et al.* (2017). However, there are two data points that diverge from the general trend and lead to a low R^2. These events are the same outliers (#9 and #12) already seen in Figure 5.7. Furthermore, an increase of r_0 with $\theta_\mathrm{GCS}(t_0)$ and L_BSP can be observed from the data. Also in the correlation with L_BSP, events #12 is far of to the other data points. Since this is not valid for the correlation with $\theta_\mathrm{GCS}(t_0)$, this might suggest that the reason for this discrepancy is not reasoned in SR characteristics. By neglecting event #12, the coefficients of determination are $R^2 = 0.36$ for the correlations between $\theta_\mathrm{GCS}(t_0)$ and $R^2 = 0.60$ for L_BSP with r_0. The maximum observed acceleration and the CME mass, indicated by the marker colour and size, seem to have no significant effect on the height at which the drag becomes the dominant force.

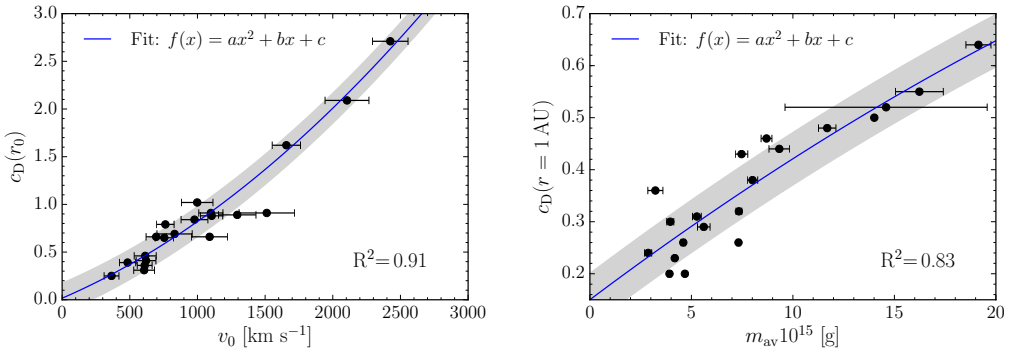

Figure (5.25) Dependencies of c_D on the initial speed v_0 at r_0 and the CME mass. Fits are shown by the blue lines and the corresponding standard deviations are represented by the grey area.

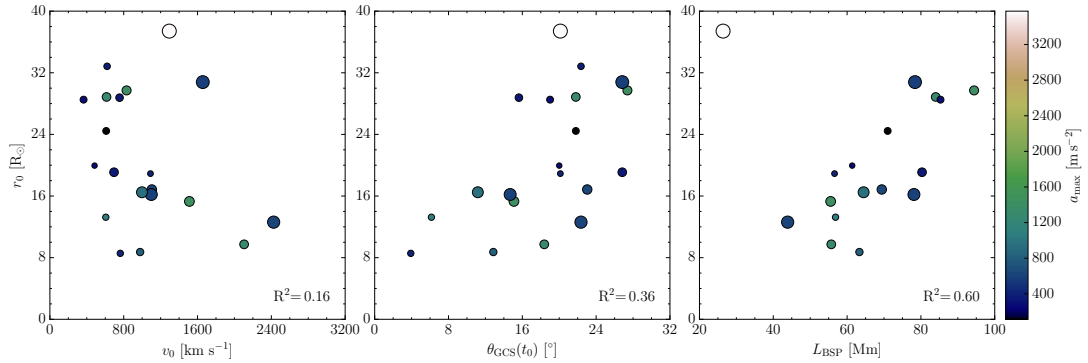

Figure (5.26) Dependencies of r_0 on CME and SR parameter. Marker colours indicate the maximum observed acceleration $a_{\max}$. The CME mass is represented by the marker size.

The results of the drag analysis reveal the importance of the solar wind for the later kinematics of CMEs and their propagation behaviour into the heliosphere. A continuous deceleration for CMEs with speeds greater than the solar wind speed and, in one case, the acceleration of a CME by the solar wind could be observed. Differing from the results of Sachdeva *et al.* (2015) and Sachdeva *et al.* (2017), the drag force becomes the dominant force within the first 40 $R_\odot$ for the events analysed in this thesis. The negative correlation of r_0 to v_0 shown by Sachdeva *et al.* (2017) was generally confirmed (see Figure 5.26), but in the form of a continuous distribution rather than the splitting into two populations of slow ($v < 900\,\mathrm{km\,s^{-1}}$) and fast CMEs ($v > 900\,\mathrm{km\,s^{-1}}$). Also a dependency of r_0 on the initial CME latitude was found. It seems that CMEs originating further away from the solar equatorial plane are later dominated by the drag.

5.4.1 Comparison of DBM Results and In-situ Measurements

5.4.1

To test the robustness and significance of the DBM-model, the obtained model trajectories were compared with the in-situ measurements taken in L1 since the selected events were all Earth-directed. For this reason, the r-t-profiles were translated from the direction of the apex into the direction to the Earth to derive the real Earth directed CME component r_E-t. In Figure 5.29 and A.51 to A.55, the results of the second run are shown. For every event, the best DBM solution is plotted similar to the apex analysis described above. Furthermore, the v_E-t-profile together with the calculated speed profile of the DBM $v_E^{\mathrm{D}}(t)$ is plotted for every event.

In addition to the best solution of the second run of the DBM model, the in-situ signatures of the corresponding ICMEs were identified in the 1 min OMNI data for comparison. In Figure 5.28, the ICME signature of event #15 is shown exemplary. The in-situ signatures of the individual ICMEs, which are described in Section 2.2.3, were identified by surveying in a time window of six days after the first CME observation for magnetic structures of shocks and MC. For every event, an ICME signature was found. By applying the scheme of Bothmer and Schwenn (1998) introduced in Section 3.1.2, the borders of the MC/FR in the ICME structure were determined. Some events were partial "hits" (sketched

by the two spacecraft trajectories in Figure 2.10), as can be seen from the GCS projection in Figures 5.5. In partial "hits", the flanks or legs of the ICME are crossed, which leads to long lasting periods of a more constant magnetic field (Marubashi *et al.*, 2015). This makes the identification of a rotation in the magnetic field difficult and the Bothmer-Schwenn-scheme could not always be used to determine clearly the beginning- and end-times of the MC. As an additional indicator, the pitch angle data of suprathermal electrons measured with ACE/SWEPAM were used to identify periods of counter-streaming electrons. To derive the properties of the solar wind in which the ICME is propagating, the average values of the solar wind speed $w_{\mathrm{av}}^{\mathrm{Pre}}$ and density $n_{\mathrm{av}}^{\mathrm{Pre}}$ over the largest undisturbed time span ahead the ICME structure were calculated. This ensures the exclusion of shocks, gradients or interaction regions. The ICME speed was fitted with polynomials within the identified time range of the MC. All model parameters of the Earth-directed runs are summarised in Table 5.8 together with the corresponding in-situ measurements computed from the OMNI 1 min data set.

A comparison between the predicted ICME and solar wind parameters at 1 AU with

Table 5.7. Results of the DBM analysis of the r-t-profiles (CME apex).

#	r_0 [$R_\odot$]	v_0 [km s^{-1}]	$v_{1\,\mathrm{AU}}^{\mathrm{D}}$ [km s^{-1}]	$w_{1\,\mathrm{AU}}^{\mathrm{D}}$ [km s^{-1}]	$n_{1\,\mathrm{AU}}^{\mathrm{D}}$ [cm^{-3}]	c_D	Re 10^7	γ 10^{-8} [km^{-1}]
1	18.91	1090	758	469	1.97	0.66-0.36	5.19-2.16	1.0-0.6
2	9.73	2105	570	278	4.04	2.09-0.43	19.83-2.88	7.2-1.4
3	3.2	468	788	898	14.58	0.35-0.18	2.0-0.4	2.8-0.4
4	28.86	614	393	250	9.36	0.46-0.26	3.17-1.16	1.7-0.9
5	24.45	610	528	370	2.96	0.36-0.26	2.21-1.22	2.4-1.8
6	19.95	484	363	250	3.94	0.39-0.24	2.46-1.03	5.1-3.2
7	28.51	365	338	275	7.88	0.25-0.2	1.09-0.57	4.6-3.5
8	29.71	831	511	250	3.84	0.69-0.38	5.53-2.36	1.66-0.93
9	30.79	1657	733	370	4.53	1.62-0.55	14.99-4.08	6.6-2.2
10	12.61	2425	583	250	7.39	2.71-0.52	26.17-3.78	6.3-1.1
11	15.3	1512	879	425	2.96	0.91-0.44	7.77-3.0	1.0-0.5
12	37.41	1294	1096	575	1.97	0.89-0.64	7.57-5.08	1.5-1.1
13	19.09	695	431	275	4.93	0.66-0.32	5.27-1.77	5.2-2.4
14	8.73	978	467	275	3.94	0.84-0.31	7.06-1.65	5.9-2.0
15	16.85	1105	667	300	1.97	0.88-0.46	7.43-3.16	2.6-1.4
16	16.2	1099	758	400	3.45	0.91-0.5	7.81-3.62	3.2-1.7
17	13.25	606	577	510	7.58	0.31-0.2	1.65-0.63	3.9-2.4
18	16.49	998	557	250	2.96	1.02-0.48	8.93-3.42	5.0-2.4
19	32.84	620	387	250	4.93	0.41-0.23	2.68-0.92	1.4-0.8
20	28.77	755	409	250	5.91	0.65-0.29	5.13-1.52	5.3-2.4
21	8.56	763	423	285	3.94	0.79-0.3	6.52-1.56	12.1-4.2

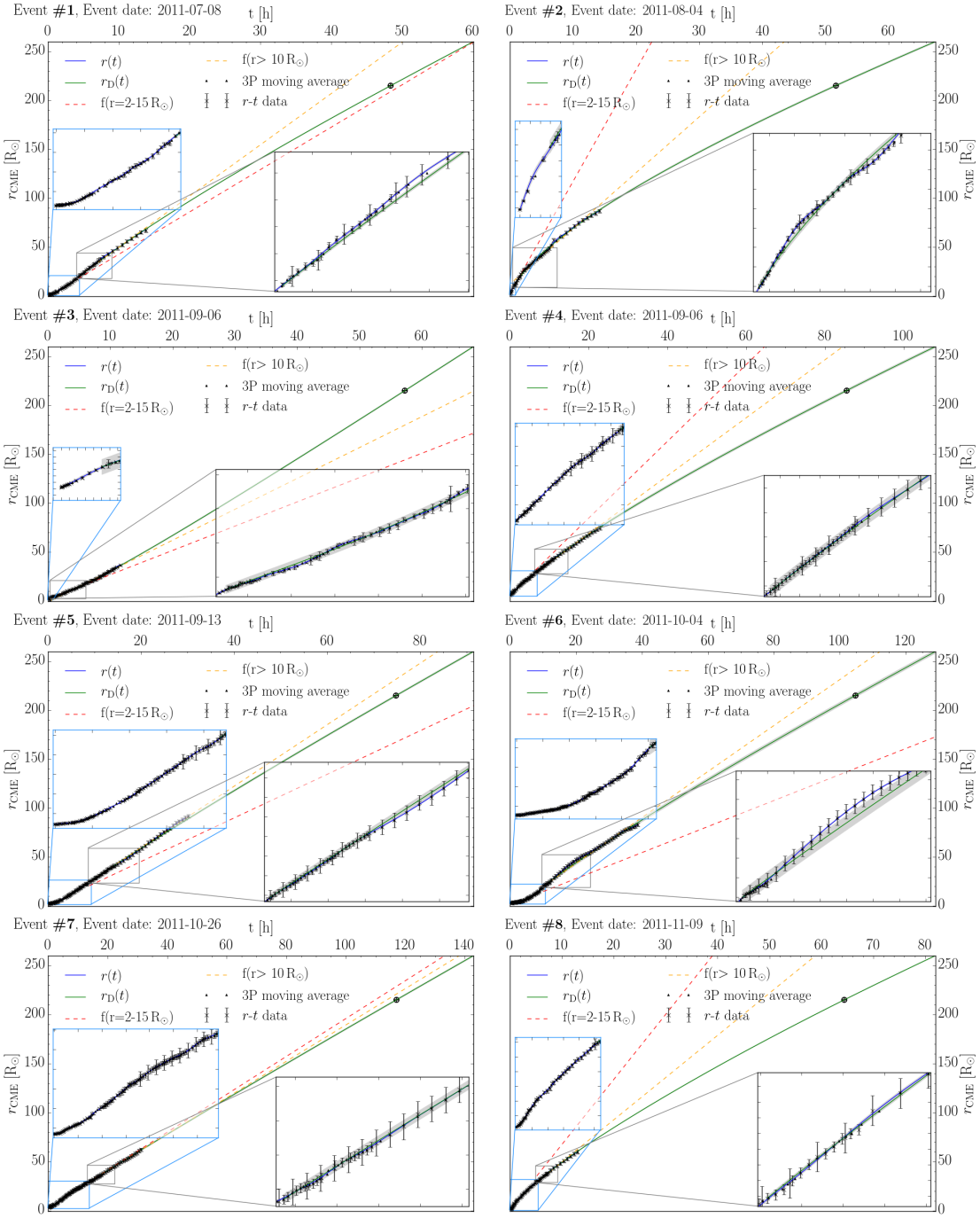

Figure (5.27) Results of the DBM analysis of the height-time-profile of the CME apex for the first eight events. The spline fit of the GCS data $r(t)$, discussed in Section 5.1.2, is shown by the blue line. Linear regressions f were performed using the data from 2-15$R_\odot$ (red dashed line) and $r > 10\,R_\odot$ (orange dashed line). The computed DBM trajectory with the largest R^2 is shown by the green line. Grey areas indicate the range of the standard deviation.

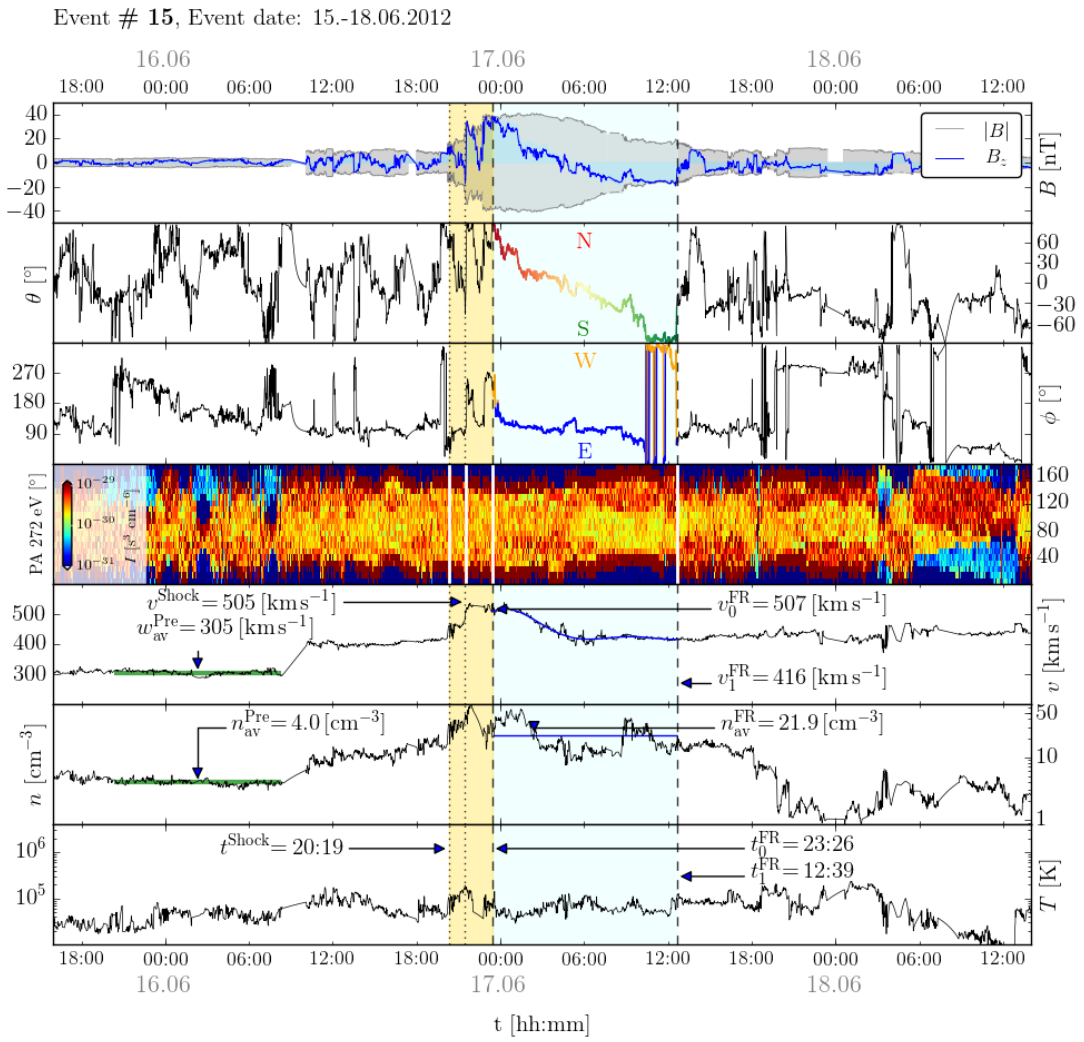

Figure (5.28) In-situ measurements from ACE of event #15. From top to bottom: Magnetic field strength with B_z-component (blue) in the GSM coordinate system, angles of the magnetic field vector θ and ϕ, intensity of the pitch angle PA of suprathermal electrons, solar wind speed v, solar wind proton density n and electron T. Shocks are marked by dotted vertical lines and the sheath region by the orange area. The beginning- and end-times of the MC are indicated by the dashed vertical lines and its duration by the light blue area. All data used for the calculation of $w^{\mathrm{Pre}}_{\mathrm{av}}$ and $n^{\mathrm{Pre}}_{\mathrm{av}}$ lie in the range of the green lines. The fitted MC speed and average density are marked by the blue lines

the measured in-situ data is illustrated in Figure 5.30. The differences between the predicted arrival times of the ICMEs of the best DBM solution and the identified arrival times of the MCs from the in-situ measurements dT_{Arr} range from -8 to +8.5 h and have a standard deviation of 4.7 h. A correlation between the CME speed and the accuracy of the model in predicting the arrival time was not found. For the fastest event at 1 AU, dT_{Arr} is +1 h and for the slowest event -1.7 h. Also multiple events, indicated by the M in Figure 5.30, seam to have no larger scatter than compared to single events. A larger scattering can be seen for the differences in predicted CME arrival speed and the real

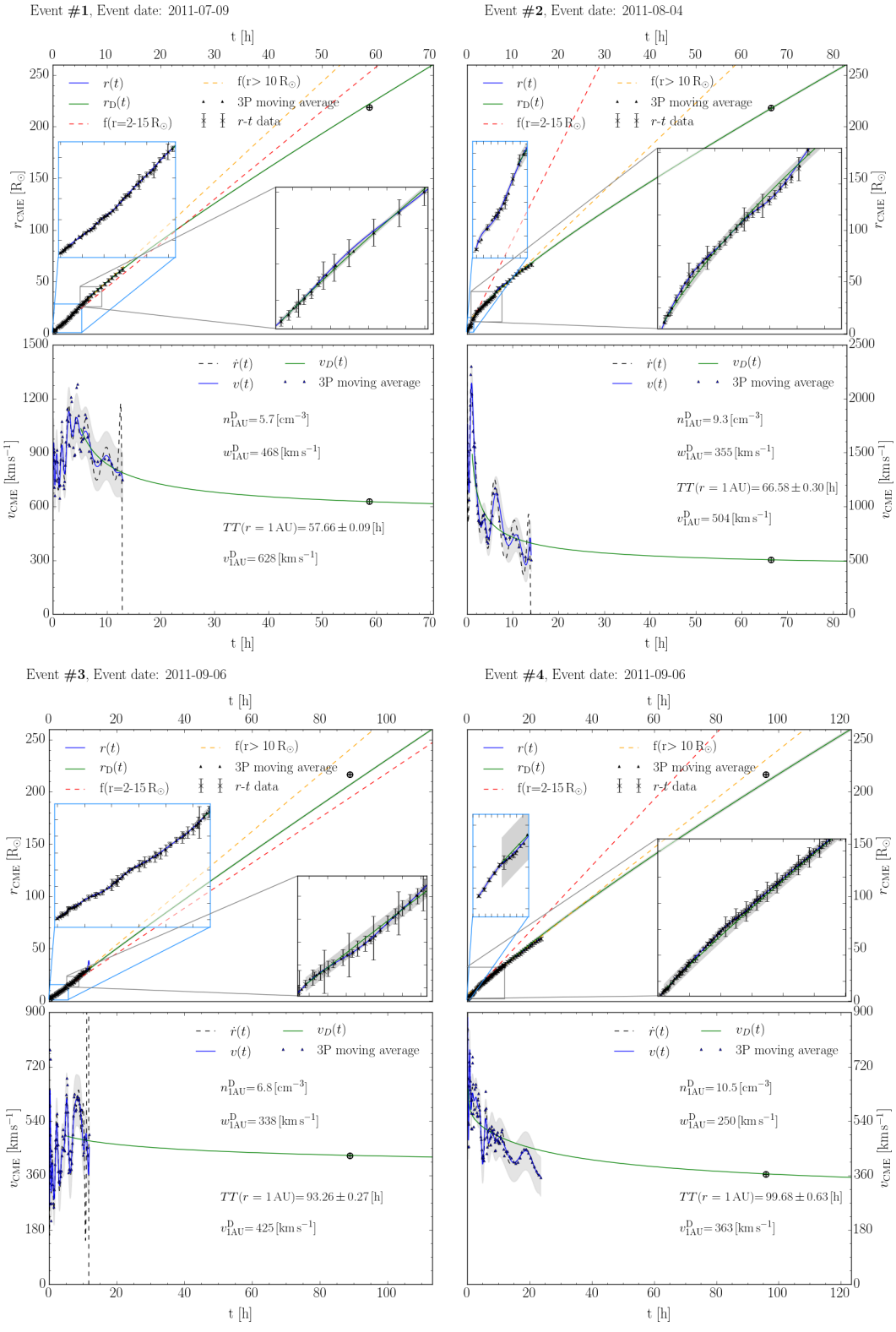

Figure (5.29) DBM results of the Earth directed component of the events #1 to #4. For every event the r_E-t- and v_E-t- profiles are shown. The Earth symbol indicates the arrival times derived from in-situ measurements.

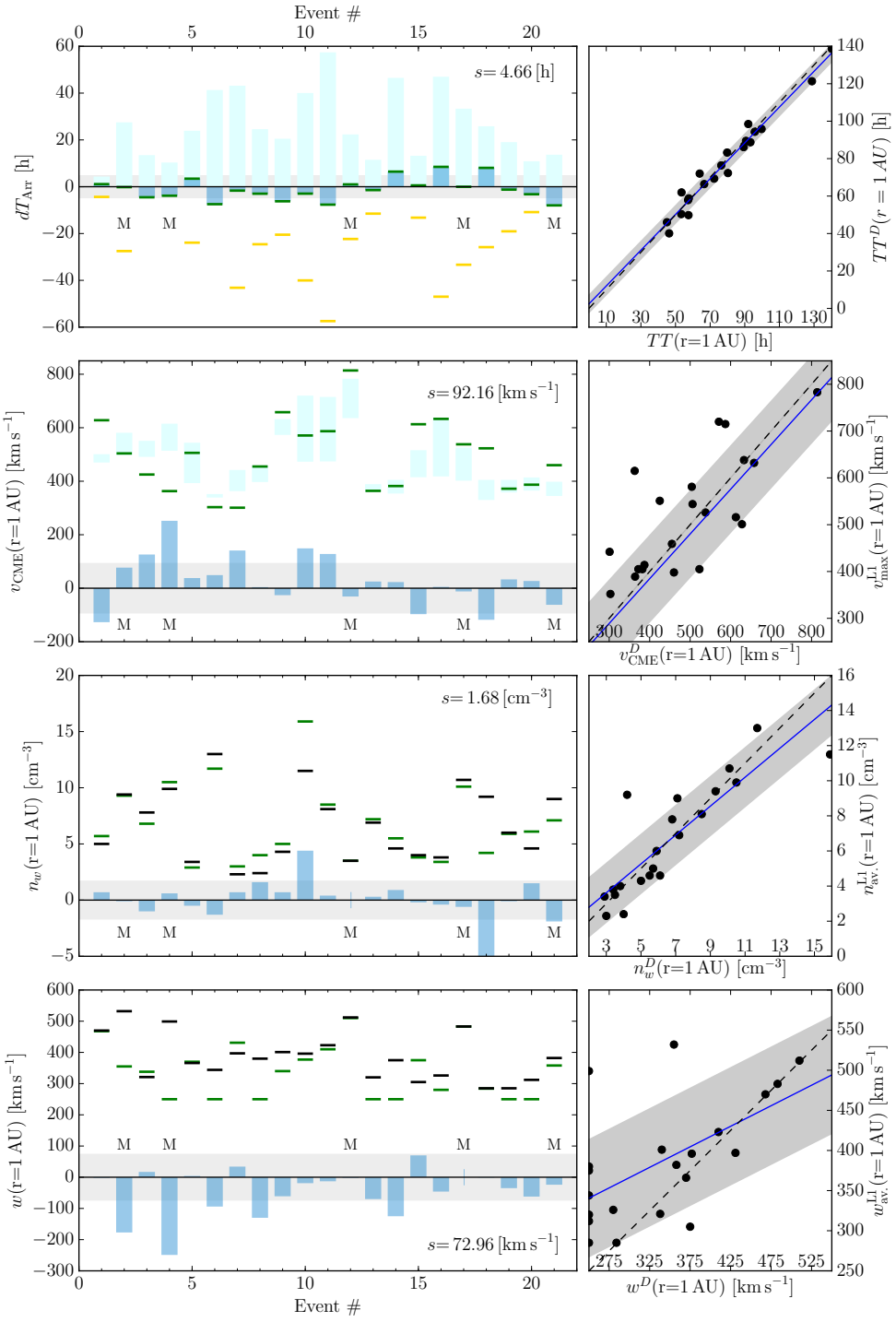

Figure (5.30) The first row shows the time differences to the identified arrival times of the MCs derived from the in-situ analysis. Green bars indicate the predicted arrival times of the best solutions of the DBM calculations and orange bars shocks. Multiple events are marked with an additional M. The duration of the MC is shown by the light blue bars. On the right, a direct comparison between the observed and predicted transit times is plotted. The following rows show the same analysis for the ICME speed, the solar wind density and the solar wind speed. In all plots, the standard deviations are shown by the grey areas and the residuals in dark blue bars.

measured once. The extremes of the residuals are -127 and +252 $\mathrm{km\,s^{-1}}$ with a standard deviation of $s = 92.16\,\mathrm{km\,s^{-1}}$. For the solar wind, the range of the differences of the predicted $n^{\mathrm{D}}_{1\mathrm{AU}}$ and $w^{\mathrm{D}}_{1\mathrm{AU}}$ of the solar wind ahead the ICME and the real in-situ measurments are between -5 to +4.4 $\mathrm{cm^{-3}}$ and -249 to +70 $\mathrm{km\,s^{-1}}$, respectively. While the results of the predicted solar wind density at 1 AU show for the majority of the events only slight deviations from the in-situ measurements in front of the ICME, the predicted solar wind speed is in general lower than the measured speeds. A possible explanation would rely on the solar wind speed model itself, which is derived from the solar wind density model of Leblanc, Dulk, and Bougeret (1998). In Figure 5.31, the solar wind speed models presented in different studies are plotted. It can be seen that the models of Venzmer and Bothmer (2018), Sheeley *et al.* (1997) and Leblanc, Dulk, and Bougeret (1998) used in this analysis, differs significantly in the range in which the DBM is fitted to the r-t-profiles.

Another source of uncertainties is the geometrical evolution of the ICME on its way through the solar wind. Cargill *et al.* (1996) showed in MHD simulations that a FR's shape

Table 5.8. Results of the DBM analysis of the r_E-t-profiles (Earth directed component).

#	$v^{\mathrm{D}}_{1\,\mathrm{AU}}$ [km s^{-1}]	$w^{\mathrm{D}}_{1\,\mathrm{AU}}$ [km s^{-1}]	$n^{\mathrm{D}}_{1\,\mathrm{AU}}$ [cm^{-3}]	TT^{D} [h]	v_{ICME} [km s^{-1}]	w^{D}_{1AU} [km s^{-1}]	n^{D}_{1AU} [cm^{-3}]	TT [h]
1	628	468	5.7	57.66	470	5.0	470-501	59.6
2	504	355	9.3	66.58	532	9.4	498-581	68.58
3	425	338	6.8	93.26	321	7.8	491-551	89.17
4	363	250	10.5	99.68	499	9.9	514-615	96.08
5	506	370	2.9	79.81	366	3.4	393-544	83.25
6	303	250	11.7	128.8	344	13	339-352	124.83
7	301	431	3.0	140.27	397	2.3	363-442	144.42
8	455	250	4.0	72.3	380	2.4	397-459	69.57
9	658	340	5.0	46.32	401	4.3	573-632	43.12
10	571	377	15.9	53.32	396	11.5	473-720	50.45
11	587	410	8.5	57.49	423	8.1	474-715	52.4
12	814	510	3.5	45.04	512	3.5	636-783	47.1
13	364	250	7.2	95.79	320	6.9	360-389	97.75
14	382	250	5.5	92.03	375	4.6	354-405	98.42
15	613	375	3.8	57.28	305	4.0	415-516	58.77
16	633	280	3.4	53.47	326	3.8	418-638	62.62
17	538	483	10.1	76.42	483	10.7	402-526	76.4
18	523	284	4.2	63.96	285	9.2	330-405	72.68
19	372	250	5.9	90.72	285	6.0	358-405	91.78
20	387	250	6.1	89.35	312	4.6	365-414	86.15
21	460	358	7.1	80.28	382	9.0	345-398	72.32

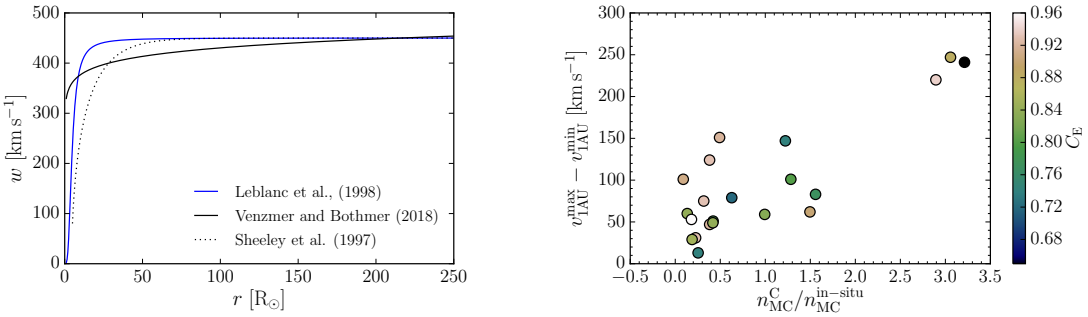

Figure (5.31) *Left*: Comparison between the solar wind speed models of Leblanc, Dulk, and Bougeret (1998), Sheeley *et al.* (1997) and Venzmer and Bothmer (2018). For more details see Section 2.2.2. *Right*: Correlation between the difference in calculated and measured MC proton densities with the expansion speed in the MC. The marker colour represents the amount of c_{E}, which measures the deviation of the height of the Earth-directed CME component with respect to the CME's apex.

is deformed by the feed back of the ambient plasma flows, which are generated by the FR motion. By analysing 400 CMEs, Owens, Lockwood, and Barnard (2017) showed that CME are indeed incoherent MHD structures, which can be deformed by inhomogenities in the solar wind. The deformation of a CME can be seen for example in the image sequences of event #1 taken from the individual SECCHI instruments, which are shown on the cover pages of the chapters 3 to 6. In a first evaluation, the difference from the ICME geometry determined by GCS modelling to the ICME geometry at 1 AU can be estimated by comparing the mean densities of the MC, calculated from in-situ measurements, with the extrapolated density of the ICME derived from the GCS geometry-profile and the CME mass. The ratio of the means between the extrapolated ICME density $n^{\mathrm{C}}_{\mathrm{MC}}$ and the measured MC density $n^{\text{in-situ}}_{\mathrm{MC}}$ in L1, is plotted versus the measured expansion speed $v^{\mathrm{max}}_{1\mathrm{AU}} - v^{\mathrm{min}}_{1\mathrm{AU}}$ within the MC derived from in-situ measurements for all events in Figure 5.31. If the ICME geometry is expanding in a self-similar manner between the heights of the remote sensing observations and L1, $n^{\mathrm{C}}_{\mathrm{MC}}/n^{\text{in-situ}}_{\mathrm{MC}}$ should be unity on the assumption that the CME mass stays constant and the in-situ measurements along the crossing line of ACE through the ICME are representative for the entire ICME. This is true for only one event and from Figure 5.31 it can be seen that for 13 events the ratio is below 0.7 while it is above unity for the rest. However, there is a trend between the ratio and the expansion speed indicating a deeper geometrical connection. An alternative explanation would be that the CME masses are underestimated for the majority of events, but since the directional mass determination method was used, this seems to be unlikely. Another point that has to be considered if CME deformations occur, is the rigid body treatment of a CME for $c_{\mathrm{D}}(Re)$ (see Section 3.3). Deriving a dynamical expression for $c_{\mathrm{D}}(Re)$ as a function of the FR shape is a non trivial task.
In Figure 5.32, the DBM runs with the height-time-profiles of the CME apex and the Earth-directed component are compared. The speed at $r = 1\,\mathrm{AU}$ for the apex run is in general faster than for the Earth-directed component and a trend is visible. In the case of the results for w^{D}_{1AU} and n^{D}_{1AU} no trend or correlation is visible. Also the CME widths and the initial CME longitude seam to be not correlated with the DBM parameter.

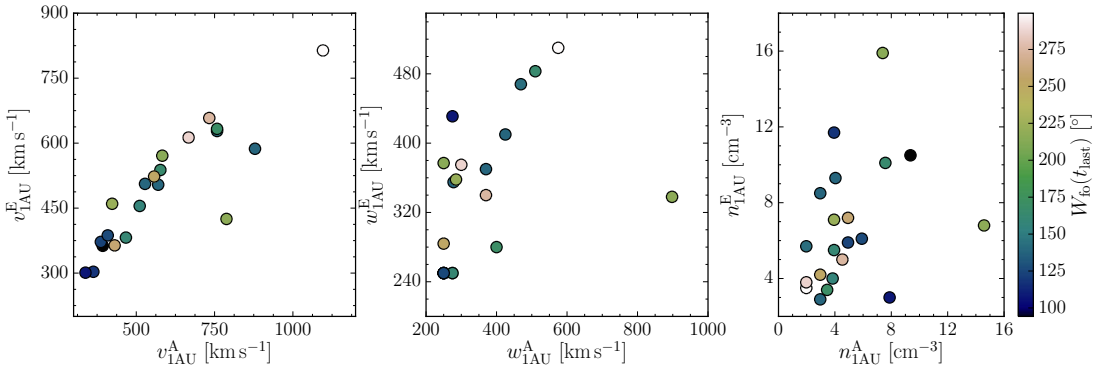

Figure (5.32) Comparison between the two DBM runs with the r-t- and r_E-t-profiles. Results of the Apex-run have the prefix A and results of the Earth-directed run the prefix E. The marker colour represents the final angular face-on width.

Since a self-similar expansion was assumed for the regime between the last remote sensing observations and L1, the CME apex speed and the Earth directed speed are connected via the ratio of the corresponding heights $c_{\mathrm{E}} = r_{\mathrm{Earth}}/r_{\mathrm{Apex}}$. This factor ranges for all events in a small interval of 0.65 to 0.96 due to the selection criteria. For this reason, the high correlation between the speeds at 1 AU of both runs, and also the CME width, is expected. A comparison between the predicted solar wind parameters of both runs shows no correlation. Since the solar wind is highly variable, this could be explained by different ambient solar wind streams for the individual CME components (Owens, Lockwood, and Barnard, 2017).

5.5 Analysis of the Initial Lorentz Force

The kinematics close to the Sun, at heights at which the accelerating Lorentz force dominates, are analysed with the TI model presented in Section 3.2.2. Since the height at which the drag becomes the dominating force is also the height at which Lorentz and drag force are equal, the Equations 3.6 and 3.13 can be equated at r_0. By using Equation 3.11 for the current at which hoop and the external Lorentz force are at equilibrium I_{eq}, the external poloidal magnetic field strength at r_{eq} can be calculated with r_0 and $a^{\mathrm{D}}(r_0)$ of the DBM solution. Additional inputs are the α-t- and κ-t-profiles to compute the GCS minor radius of the FR $b(r)$. The height at which the FR is in equilibrium r_{eq} can be approximated as $1.05\,\mathrm{R}_{\odot}$ (Sachdeva *et al.*, 2017). However, since the lowest height of the first observation in EUVI of all selected events is $r = 1.21\,\mathrm{R}_{\odot}$, there is still a gap between r_{eq} and $r(t_0)$ for which $b(r)$ is not known. Because this gap is small and it is assumed that below $r(t_0)$ the change in α and κ is low, a self similar expansion is assumed for this gap and the geometry at $r(t_0)$ is extrapolated down to r_{eq}. By knowing the value of B_{eq}, Equation 3.6 can be solved for all heights with a given decay index n.

The Lorentz force was calculated in two different ways over distances from r_{eq} to $r(t_{\mathrm{last}})$. In both runs, the equation of motion was solved using the described above method in a given range of values for the decay index starting with the critical decay index n_{cr} discussed in Section 3.2.2. At first, the final n was determined in searching for the lowest value of

n, which provides a physical correct solution. This means, a solution that is consistent with the drag-only DBM model results and satisfies the criterion $F_{\mathrm{L}} < |F_{\mathrm{D}}|$ for $r > r_0$. The resulting solution of the Lorentz force provides a lower limit for the model since with an increase of n also the maximum acceleration of the Lorentz force $a^{\mathrm{L}}_{\mathrm{max}}$ increases. In a second step the minimal n is calculated for which $a^{\mathrm{L}}_{\mathrm{max}}$ matches a_{max} derived from the r-t-profiles of the GCS modelling. The results of both calculations for all events are listed in Table 5.9 and plotted in Figure 5.33 and A.57 to A.56. Event #3 was not analysed since the CME is accelerated by the solar wind and not by a Lorentz force. To analyse the decrease of the Lorentz force, the percentage of the Lorentz acceleration at r_0 to the peak Lorentz acceleration, defined as $Fall_{\%}$, and the relative difference between drag and Lorentz acceleration, were calculated from the Lorentz profiles. Analogue to Sachdeva *et al.* (2017) the relative difference between drag and Lorentz acceleration is:

$$a_{\mathrm{diff}} = \frac{a^{\mathrm{D}} - a^{\mathrm{L}}}{a^{\mathrm{D}}} \cdot 100\%, \tag{5.9}$$

and is evaluated at a distance of $r = 40\,\mathrm{R}_{\odot}$. Generally, the results of the first run are in

Table 5.9. Results of the TI Lorentz force analysis. The results of the second run are indicated by the prefix a.

#	n	B_{eq} [G]	I_{eq} 10^{10} [A]	r_{L} [$\mathrm{R}_{\odot}$]	$Fall_{\%}$	a_{diff}	n^a	B^a_{eq} [G]	I^a_{eq} 10^{10} [A]	r^a_{L} [$\mathrm{R}_{\odot}$]	$Fall^a_{\%}$	a^a_{diff}
1	1.85	0.15	3.6	2.6	18.5	7.6	3.15	0.25	5.2	1.7	3.3	42.0
2	2.40	0.91	24.1	2.0	25.2	16.2	2.40	0.91	24.1	2.0	25.2	16.2
4	1.75	0.18	4.3	2.7	12.7	6.7	17.25	0.48	11.7	1.2	0.3	27.4
5	1.50	0.05	1.6	3.1	24.1	17.7	5.75	0.12	3.9	1.4	0.7	52.9
6	1.65	0.05	1.5	3.7	28.8	17.4	16.55	0.12	3.7	1.2	0.5	57.1
7	1.50	0.03	1.0	2.5	22.7	8.8						
8	1.90	0.22	4.5	2.2	10.1	11.6	8.15	0.54	10.8	1.4	0.5	25.3
9	3.35	1.71	52.2	1.6	1.4	4.5	3.35	1.71	52.2	1.6	1.4	4.50
10	2.80	1.39	39.6	1.7	10.2	19.4	2.80	1.39	39.6	1.7	10.2	19.4
11	1.50	0.34	8.7	2.6	34.3	23.1	9.65	0.61	15.9	1.3	1.4	74.0
12	1.50	0.19	4.3	3.7	24.2	4.6						
13	1.80	0.14	3.1	3.7	32	9.7	7.35	0.30	6.9	1.4	1.8	45.9
14	1.75	0.17	4.0	2.1	46.9	28.2	8.65	0.28	6.4	1.4	5.4	79.9
15	1.50	0.17	4.8	4.1	46.5	17.5	8.75	0.38	10.9	1.3	1.7	68.3
16	1.50	0.20	5.4	3.2	38.9	24.5	15.55	0.43	12.0	1.2	1.3	72.2
17	2.10	0.03	1.2	1.9	15.3	40.9	40.40	0.07	2.4	1.1	0.8	64.4
18	1.55	0.20	6.5	4.1	52.0	15.3	12.75	0.47	15.3	1.2	1.2	66.8
19	2.15	0.31	9.5	1.9	4.3	4.6	4.75	0.61	18.5	1.5	0.5	11.1
20	2.25	0.30	11.1	1.9	3.3	4.2	2.35	0.32	11.8	1.9	2.7	6.0
21	2.05	0.11	2.4	2.5	37.9	26.6	40.45	0.19	4.2	1.1	4.6	66.4

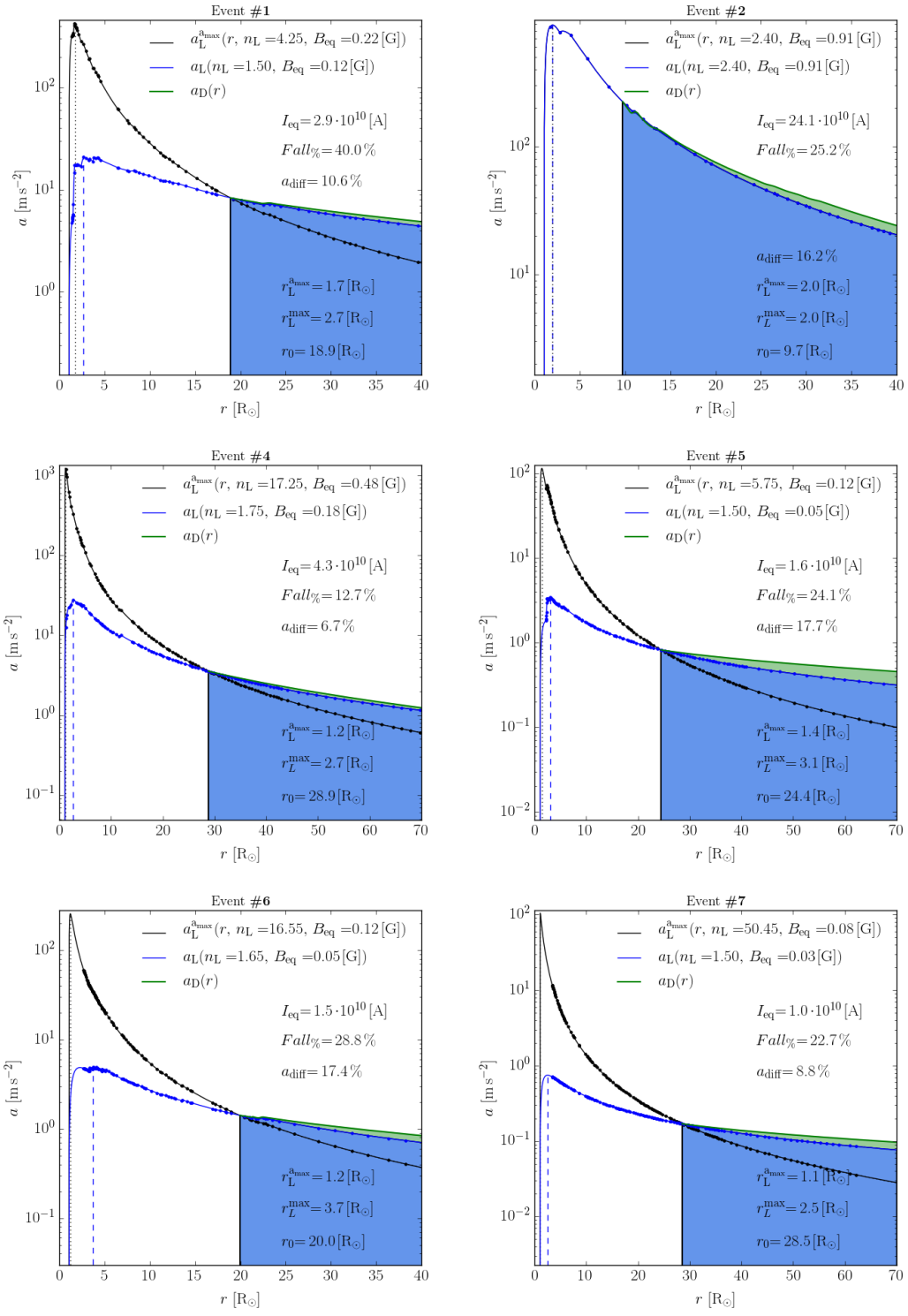

Figure (5.33) Results of the TI Lorentz force analysis for the events #1 to #7. Blue and black data are the results of the minimal n and the runs scaled to a_{max}. The results of the DBM model are shown in green and the amount of the first TI Lorentz force run in light blue comparison.

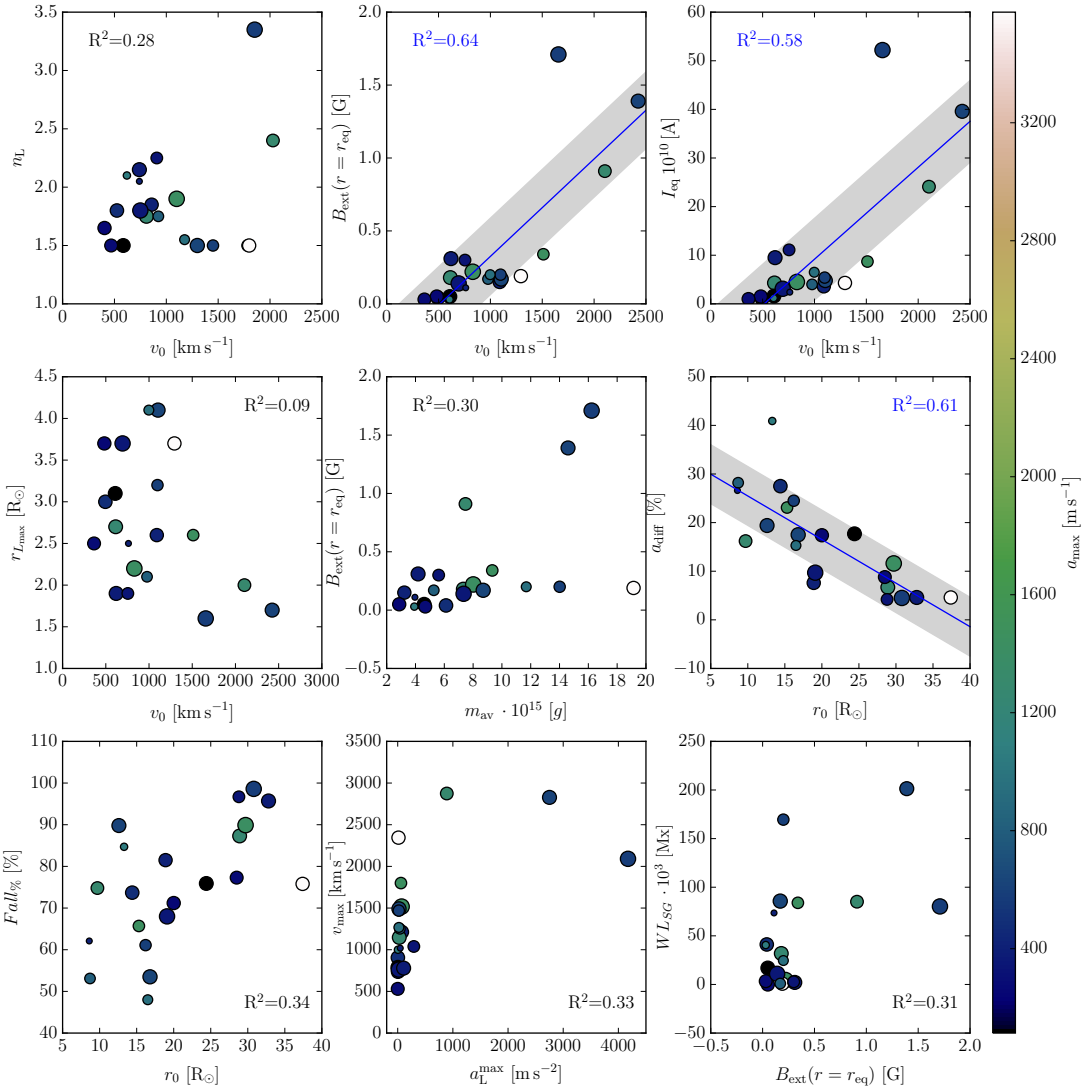

Figure (5.34) Comparison between the TI Lorentz force model results of the first run with minimal n. Marker colours indicate the maximum observed acceleration derived from GCS modelling. Linear regressions are shown by the blue lines and standard deviation by the grey areas.

the same order of magnitude as the results of Sachdeva *et al.* (2017) and Subramanian and Vourlidas (2007). Only the lower boundaries of a_{diff} is one order of magnitude lower. The range of n lies between 1.5 and 3.35, whereas the range of second run is with 2.35 to 40.45 is significantly higher.

Moreover, the level of a_{max} could not reached by increasing the value of n in an reasonable range for two events. In Table 5.9, the heights at which the Lorentz acceleration peaks are denoted for the single runs as r_{L} and r_{L}^{a}, respectively. The results of the first run lie between 1.6 and 4.1 $R_\odot$ with an average value of 2.7 $R_\odot$. In the case of the second run, the Lorentz Force peaks at significantly lower heights, namely between 1.1 and 2 $R_\odot$

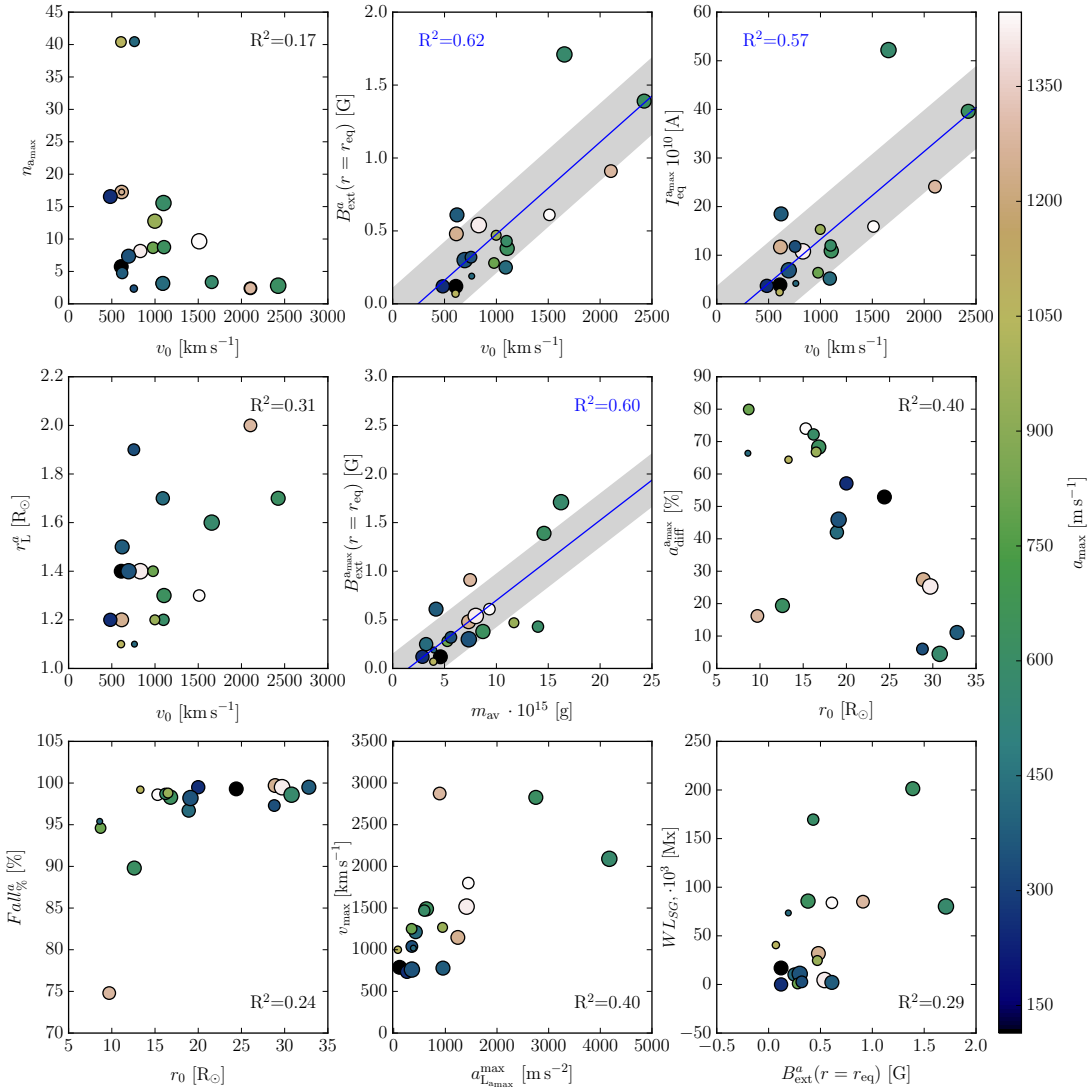

Figure (5.35) Same as Figure 5.34 but for the second run calculating the minimal n for which $a^{\mathrm{L}}_{\mathrm{max}} = a_{\mathrm{max}}$.

while the mean is at $1.4\,\mathrm{R}_\odot$.

The results of both runs of the TI Lorentz force analysis are compared in Figures 5.34 to 5.36 with the results of the preceding sections. A high correlation was found for B_{eq} and I_{eq} with the initial speed at which the drag takes over v_0 in both runs. The results of a linear regression are:

$$
\begin{aligned}
B_{\mathrm{eq}}10^{-1}[\mathrm{G}] &= (6.68 \pm 1.14) \cdot 10^{-4}\, v_0\,[\mathrm{kms}^{-1}] - (0.34 \pm 0.13) \quad R^2 = 0.64,\\
B^{\mathrm{a}}_{\mathrm{eq}}10^{-1}[\mathrm{G}] &= (6.31 \pm 1.22) \cdot 10^{-4}\, v_0\,[\mathrm{kms}^{-1}] - (0.15 \pm 0.14) \quad R^2 = 0.62,\\
I_{\mathrm{eq}}10^{10}[\mathrm{A}] &= (1.9 \pm 0.4) \cdot 10^{-2}\, v_0\,[\mathrm{kms}^{-1}] - (9.73 \pm 4.15) \qquad R^2 = 0.58,\\
I^{\mathrm{a}}_{\mathrm{eq}}10^{10}[\mathrm{A}] &= (1.8 \pm 0.3) \cdot 10^{-2}\, v_0\,[\mathrm{kms}^{-1}] - (4.8 \pm 4.6) \qquad R^2 = 0.57.
\end{aligned}
$$

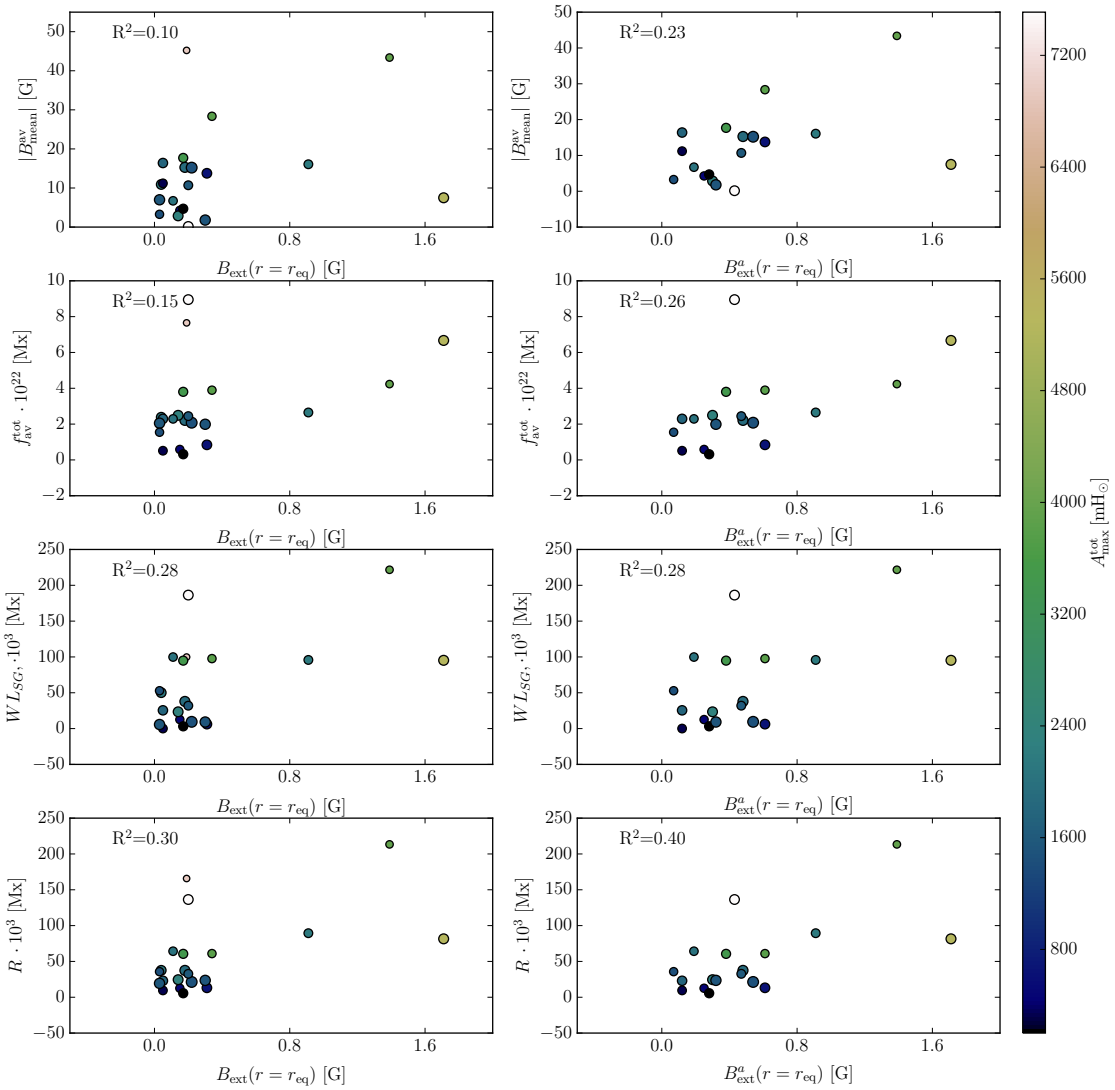

Figure (5.36) Comparison between the magnetic characteristics of the identified SRs and the calculated external magnetic field derived from the TI Lorentz force model.

These relations are close to each other for both runs. However, the other characteristics of the individual runs plotted in the Figures 5.34 and 5.35 differ a lot. The results using the minimal n show a good correlation between r_0 and a_{diff}, while for the second run, in which the maximum Lorentz acceleration matches the observed one, shows a correlation between the CME mass and B_{eq}. Using again linear regression, the following relationship was found:

$$a_{\text{diff}}[\%] = (-0.89 \pm 0.16) \cdot 10^{-4}\, r_0\,[\text{kms}^{-1}] - (34.4 \pm 3.7) \quad R^2 = 0.61,$$
$$B^{\text{a}}_{\text{eq}} 10^{-1}[\text{G}] = (8.2 \pm 1.7) \cdot 10^{-2}\, m_{\text{av}}[10^{15}\,\text{g}] - (0.12 \pm 0.15) \qquad R^2 = 0.60.$$

Similar trends for the $Fall_{\%}$ depending on r_0 can be seen for both runs, but the values

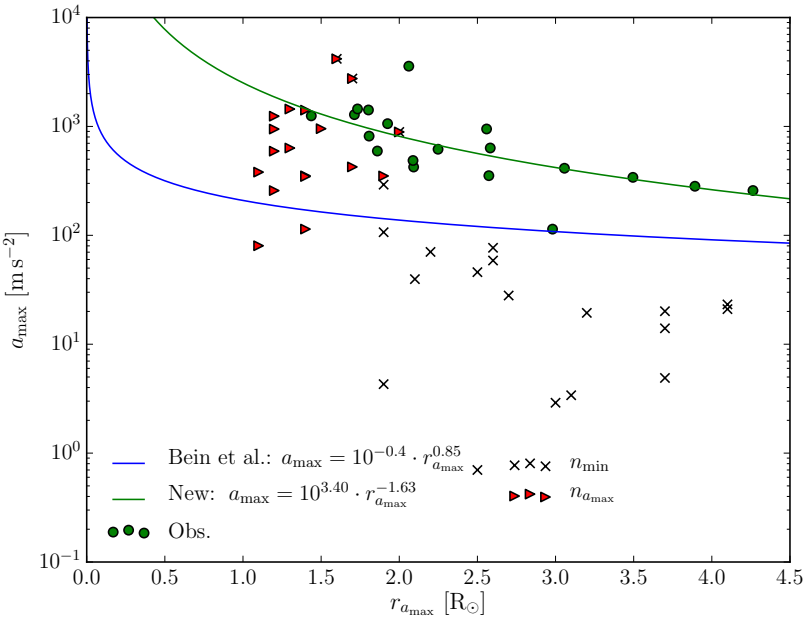

Figure (5.37) Comparison between the observed maximum CME accelerations and the computed maximum Lorentz force accelerations of both runs. The fitted relationships of this work and from Bein *et al.* (2011) are plotted in green and blue, respectively. It shall be noted that for some events the result of the first run already exceeds the observed acceleration, which is why not all data point of the second run are on the same level as the observed accelerations.

are shifted into the 95 to 100% range in the case of the second run. This is in good agreement with the findings of Sachdeva *et al.* (2017). Interestingly, the trends of the height at which the Lorentz force peaks versus v_0 are, compared between the two run, inverse to each other. A clear correlation of the parameters of the TI Lorentz force model with the maximum observed acceleration could not be found.

In a last step, the predicted magnetic field strength of the external magnetic field at r_{eq} was compared for both runs with the measured photospheric SR parameters derived from the SMART code. The comparison of both runs can be seen in Figure 5.36. In general, the results of the run in which $a_{\max}^{\mathrm{L}}$ was scaled with n to match $a_{\max}$ correlate better with the SR parameters. The strongest correlation was found with the Schrijver R value with $R^2 = 0.3$ and $R^2 = 0.4$ for the two runs.

In order to fill the "gap" between the SR analysis and the kinematic analysis with remote sensing data, the TI Lorentz force model was used to analyse the initial acceleration phase of CMEs. The results of Sachdeva *et al.* (2017) could be partially confirmed and solutions, which do not violate the DBM solutions with $|a_{\mathrm{L}}| < |a_{\mathrm{D}}|$ for $r > r_0$, were found for all events. Since the height-time profiles start below the position of the maximum Lorentz acceleration. The acceleration was compared directly with the observed ones, which was performed in a second approach. In Figure 5.37, the observed and computed accelerations are plotted versus the height at which they occur. It can be seen that neither the results of

the first run with the minimum decay index, nor the results with the scaled acceleration, match the observed accelerations. In the case of the first run the accelerations are too low, while in the second run the heights at which the acceleration takes place are too low compared to the observed ones. By considering the drag force, which is neglected at this heights in the model but still contributes to the observed acceleration balance, the TI-model results are questionable. Ideally, the Lorentz acceleration should be larger than the observed one since the drag force decelerates the CME, without considering other contributors to the total energy balance of a CME, namely the energy dissipated by the CME expansion and possible plasma heating (Kumar and Rust, 1996; Emslie *et al.*, 2012). Obviously, the simple TI-Lorentz-force model used in this work does not reproduce the observations. On the other hand, more complex MHD implementations of the TI models are successful in explaining eruptions and flare events (e.g. Wang *et al.* 2017; Baumgartner, Thalmann, and Veronig 2018). Other forms of instabilities, like the kink instability, or combinations of eruption models are also able to describe observations of FR eruptions (Hassanin and Kliem, 2016; Liu *et al.*, 2016).

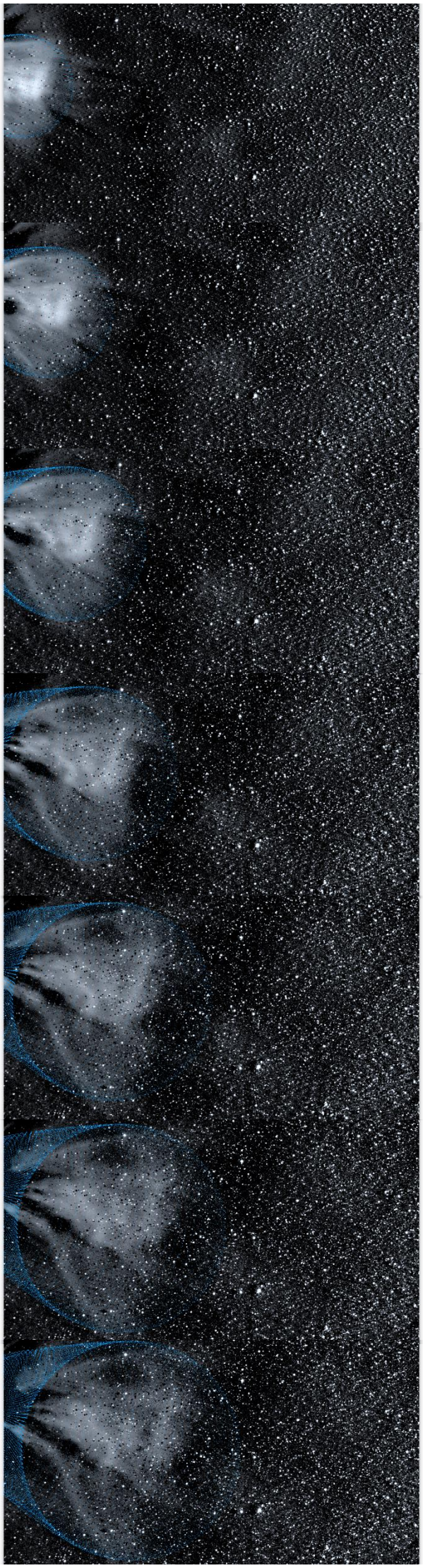

Chapter 6

Summary and Outlook

"I've had my results for a long time: but I don't know yet how I am to arrive at them."

Carl F. Gauss

Cover Figure: Time series of SECCHI/HI1 B observations of event #1. The GCS fit is shown by the blue grid.

6.1 Summary

In this thesis, a systematic study of the CME kinematics and their dependencies on the corresponding solar source regions was presented. A set of 21 events during the time period between July 2011 and November 2012 was carefully selected for this investigation. These events were chosen on the basis of the availability of multi-viewpoint coronagraph observations of the SOHO and STEREO missions as well as of the possibility of the analysis of SR properties from complementary SDO observations. Using remote sensing data of the SOHO/LASCO C2 and C3 coronagraphs and the STEREO/SECCHI suite, the 3D CME kinematics were obtained with the well established GCS modelling method using three different vantage points. This model was applied with the forward modelling technique developed for the KINCAT catalogue within the HELCATS project. For this thesis it was extended to observations taken with EUVI in a FOV close to the Sun and up to a FOV containing larger heliospheric distances with the HI1 instrument. Highly detailed 3D CME trajectories, geometries and masses could be dynamically tracked within the first $100\,R_\odot$.
By tracking the CME trajectories through the lower corona back to the photospheric ARs, the corresponding SRs of the selected CMEs were identified. These SRs were analysed with the SMART code to derive their temporally resolved magnetic properties. This analysis builds up on the findings and preliminary works of the HELCATS project. Providing the underlying data, the GCS measurements were used for a fully dynamical DBM, including the interaction between CMEs and the ambient solar wind. Since the 3D CME characteristics were modelled using multi-viewpoint observations, the Earth-directed CME components were analysed with the DBM and were compared with in-situ measurements taken by ACE of L1. In a final step, the early CME kinematics was evaluated with a TI Lorentz force model. Combining all of these steps, the full CME evolution from its origin at the Sun to a distance of 1 AU at Earth was analysed. In the following, I want to summarise the main results of this investigation.

Results of CME Dynamics:

- The GCS modelling results provide the conclusion that within the first $20\,R_\odot$ the CMEs propagation is highly dynamic. A strictly radial propagation of the CME's apex away from the Sun was not be observed within this range. The absolute total deflections in longitude were observed to range from 0° to 31.3° and in latitude between 0.4° and 18.5° (see Table 5.2). These results are in good agreement with the results reported in other studies e.g. Cremades and Bothmer (2004) and Isavnin, Vourlidas, and Kilpua (2014) with $\Delta\phi = 29°$ and $\Delta\theta = 49°$.

- In general, the deflection in latitude tends to be towards the solar equatorial plane, which was also found by Isavnin, Vourlidas, and Kilpua (2014)).

- Unambiguous rotations of the FRs ranging between $\sim 2°$ and 46° could be measured for the majority of events.

- Non-self-similar expansions by the increase of κ and α were observed and a strong correlation between both parameters with:

$$\Delta\alpha = (86.4 \pm 13.9) \cdot \Delta\kappa + (6.4 \pm 5.6),$$

was found (see Equation 5.1). Especially between heights of $r < 2\,R_\odot$ and $r \sim 5\,R_\odot$ the CME expands strongly in face-on and edge-on angular width.

Results of CME Kinematic and Mass:

- The correlation between the CME mass and speed agrees well with our analysis of the more comprehensive KINCAT catalogue within the HELCATS project (Pluta *et al.*, 2018) (see Figure 5.10).
- An important parameter to estimate the CME mass and its evolution is the CME speed at $r = 12\,\mathrm{R}_\odot$.
- Evidence for oscillation in the analysed CMEs were found and the estimated periods of 29 to 93 min support the results of Lee, Moon, and Nakariakov (2015) and Lee *et al.* (2018), who reported periods between 24 and 48 min.
- A strong correlation was found between the height at which the CME is initiated r_0^{obs} and the height at which the acceleration phase peaks (see Figure 5.7):

$$r_0^{\mathrm{obs}} = 10^{(-0.08.40\pm0.07)} \cdot r_{a_{\max}}^{(0.91\pm0.13)},$$

which is connected with $a_{\max}$ over:

$$a_{\max} = 10^{(3.40\pm0.15)} \cdot r_{a_{\max}}^{(-1.6\pm0.5)}.$$

These results differ strongly from the results of Bein *et al.* (2011), which could be explained by the different observation times with respect to the solar cycle.

DBM Results of the CME Propagation:

- The DBM gives an accurate description of the observed r-t-profiles with $R^2 > 0.99$ for all analysed events and a maximum cv of 4.29%.
- The height at which the drag force becomes the dominating force is $r_0 < 20\,\mathrm{R}_\odot$ for the majority of events and $r_0 < 40\,\mathrm{R}_\odot$ for all events, which is lower as reported by Sachdeva *et al.* (2015) and Sachdeva *et al.* (2017).
- A significant correlation between the length of the bipolar separation line of ARs and the initial height r_0 was found (see Figure 5.26).
- The height at which the drag force takes over is correlated with the initial CME latitude. CMEs originating further away from the solar equatorial plane are later dominated by the drag.
- A correlations for the initial c_{D} with v_0 as well as c_{D} at a distance of 1 AU with the CME mass were found:

$$c_{\mathrm{D}}(r_0) = (1.92 \pm 1.03)\,10^{-7}\,v_0^2 + (6.1 \pm 2.5)\,10^{-7}\,v_0 + (0.02 \pm 0.13),$$
$$c_{\mathrm{D}}(r = 1\,\mathrm{AU}) = (-2.20 \pm 6.10)\,10^{-4}\,m_{\mathrm{av}}^2 + (2.9 \pm 1.3)\,10^{-2}\,m_{\mathrm{av}} + (0.15 \pm 0.05).$$

Properties of CME SRs and correlation with CME Kinematics:

- By taking the positions of the magnetic flux weighted centre of the ARs as SR positions, an overall shift in latitude in direction to the solar equatorial plane was found for the SRs compared to the corresponding CMEs (see Figure 5.14).
- In general, the SR latitudes are shifted to the solar equatorial plane with respect to the initial CME latitudes (see Section 5.3.2):

$$\theta_{\mathrm{SR}} = (0.83 \pm 0.04) \cdot \theta_{\mathrm{CME}}.$$

- High correlations between the CME kinematics were found especially with the magnetic flux, the magnetic area, the Schrijver R value and the Falconer weighted integral over the length of the strong-gradient main neutral line. The most significant relationships are:

$$\begin{aligned}
f^{\text{-}}_{\mathrm{max}} &= (1.65 \pm 0.19)\, m_{\mathrm{av}} - (2.9 \pm 1.7), \\
A^{\text{-}}_{\mathrm{av}} &= (216 \pm 26)\, m_{\mathrm{av}} - (369 \pm 238), \\
R_{\mathrm{max}} &= (106.34 \pm 29.13)\, v(r = 12\,\mathrm{R}_{\odot}) - (30.3 \pm 25.4)\, 10^3, \\
R_{\mathrm{max}} &= (38121 \pm 4597)\, p_{\mathrm{max}} - (5.9 \pm 8.3)\, 10^3, \\
R_{\mathrm{max}} &= (288.3 \pm 32.6)\, E^{\mathrm{max}}_{\mathrm{kin}} - (19.5 \pm 6.8) \quad \text{and} \\
WL^{\mathrm{SG}}_{\mathrm{av}} &= (77.0 \pm 13.9) v(r = 12\,\mathrm{R}_{\odot}) - (26.7 \pm 17.8)\, 10^3.
\end{aligned}$$

  All parameters of these relationships are in the units which are defined in Section 5.3.4.

- The results of the temporally resolved SR analysis showed that the SRs could be divided into two groups. In the first group, the emergence of magnetic flux directly after the eruption can be observed, while a continuously cancellation of flux preceding the eruption can be seen in the other group.
- In general, the analysed events follow the trend of the "main sequence" of ARs as introduced by Falconer *et al.* (2009) (see Figure 5.24).
- It could be shown that the time of the intensity peak of accompanying flares is close to the time of the maximum acceleration of the CME with a standard deviation of 22.12 min (see Figure 5.16).
- Regarding the analysis of SXR and HXR flux, both show the strongest correlation among the CME kinematic parameters for v_{12}.

6.2 Outlook

The results presented in this thesis about a dedicated set of highly detailed CME events give an extensive insight into the complexity of the link between the kinematics of CMEs (also ICMEs) and the magnetic properties of their corresponding solar source regions. According to the discussion in Chapter 5, the results provide answers, but reveal also at

which points more data and further analysis is necessary. The CME kinematics could be connected successfully with significant correlation to the geometrical and magnetic properties of their corresponding photospheric source regions. Flare characteristics as well as the magnetic properties from ARs from which a CME originates can be used to determine important kinematic parameters such as speed, mass, momentum and kinetic energy, which in turn can be used as proxies for the ICME properties further outward into the heliosphere.

The DBM, as a simple one-dimensional propagation model, explains the interaction between the ambient solar wind and the CME well. It provides an accurate forecasting tool for the arrival of Earth-directed CMEs in L1. Since in this work high resolution and calibrated data in science data quality were used, the model has to be tested with lower resolution not fully corrected beacon data for an operational use. An opportunity is given by ESA's upcoming (Invitations to Tender) L5 modelling study, in which individual propagation models will be tested for their accuracy in a possible L5 space weather mission. Within the L5 modelling study, the different solar wind models (shown in Figure 5.31) or combinations of them could be tested systematically in the drag based model to improve the predicted ICME and solar wind parameters.

The data set should be extended and further analysed to cover a more representative statistical distribution of CMEs and ARs. Within a more comprehensive study, the focus could be to investigate in more detail the "main sequence" of ARs presented by Falconer *et al.* (2009) or to analyse further the evidences of CME oscillations, which become more concrete by several studies (Cargill, Chen, and Garren, 1994; Kim, Nakariakov, and Cho, 2014; Lee, Moon, and Nakariakov, 2015; Lee *et al.*, 2018).

The results also demonstrate how important the design of future remote sensing instruments and mission concepts in terms of FOV and cadence is. Since the most of the geometrical evolution of CMEs takes place within the first $30\,R_\odot$ and the drag becomes the dominating force below $40\,R_\odot$, this spatial range requires special attention. Multi-viewpoint observations covering a large FOV are needed to improve the accuracy of propagation models and our understanding in the dynamics of CMEs. In order to investigate the very early kinematics of CMEs i.e., their initiation and their triggering mechanisms, observations covering a FOV within the first $4\,R_\odot$ with a high cadence are crucial.

Future instruments like the *Multi Element Telescope for Imaging and Spectroscopy* (METIS, Fineschi *et al.* 2012) onboard the upcoming Solar Orbiter mission or the *Association of Spacecraft for Polarimetric and Imaging* (ASPIICS, Galano *et al.* 2018) instrument onboard the demonstration mission PROBA-3 will give new insights into the physics of CMEs and the technical possibilities in observing them. Furthermore, there is an increasing interest of more accurate space weather forecasts with the growing amount of satellite based technologies. New space weather missions and instruments, like the *Compact Coronagraph* (CCOR, Denig, Redmon, and Mulligan 2014) to replace the ageing SOHO satellite, and the Solar Coronagraph for OPErations (SCOPE, Middleton *et al.* 2016) to build up a second view from L5, are currently under development.

Bibliography

Achenbach, E.: 1972, Experiments on the flow past spheres at very high Reynolds numbers. *Journal of Fluid Mechanics* **54**, 565. DOI. ADS. (Cited on page 51.)

Antiochos, S.K., DeVore, C.R., Klimchuk, J.A.: 1999, A Model for Solar Coronal Mass Ejections. *Astrophys. J.* **510**, 485. DOI. ADS. (Cited on page 44.)

Aschwanden, M.J.: 2001, An evaluation of coronal heating models for active regions based on yohkoh, soho, and trace observations. *The Astrophysical Journal* **560**(2), 1035. DOI. http://stacks.iop.org/0004-637X/560/i=2/a=1035. (Cited on page 35.)

Aschwanden, M.J.: 2005, *Physics of the Solar Corona. An Introduction with Problems and Solutions (2nd edition)*. DOI. ADS. (Cited on pages 19, 30, 38, 42, 43, 45, and 51.)

Aschwanden, M.J., Tarbell, T.D., Nightingale, R.W., Schrijver, C.J., Title, A., Kankelborg, C.C., Martens, P., Warren, H.P.: 2000, Time Variability of the "Quiet" Sun Observed with TRACE. II. Physical Parameters, Temperature Evolution, and Energetics of Extreme-Ultraviolet Nanoflares. *Astrophys. J.* **535**, 1047. DOI. ADS. (Cited on page 19.)

Athay, R.G., Querfeld, C.W., Smartt, R.N., Landi Degl'Innocenti, E., Bommier, V.: 1983, Vector magnetic fields in prominences. III - HeI D3 Stokes profile analysis for quiescent and eruptive prominences. *Solar Phys.* **89**, 3. DOI. ADS. (Cited on page 39.)

Aulanier, G., DeLuca, E.E., Antiochos, S.K., McMullen, R.A., Golub, L.: 2000, The Topology and Evolution of the Bastille Day Flare. *Astrophys. J.* **540**, 1126. DOI. ADS. (Cited on page 44.)

Babcock, H.D.: 1959, The Sun's Polar Magnetic Field. *Astrophys. J.* **130**, 364. DOI. ADS. (Cited on page 15.)

Babcock, H.W.: 1961, The Topology of the Sun's Magnetic Field and the 22-YEAR Cycle. *Astrophys. J.* **133**, 572. DOI. ADS. (Cited on pages 15, 17, and 35.)

Baker, D.N., Balstad, R., Bodeau, J.M., Cameron, E., Fennell, J.F., Fisher, G.M., Forbes, K.F., Kintner, P.L., Leffler, L.G., Lewis, W.S., Reagan, J.B., Small III, A.A., Stansell, T.A., Strachan Jr, L., Graham, S.J., Fisher, T.M., Swisher, V., Gruber, C.A.: 2008,

Severe space weather events: Understanding societal and economic impacts: A workshop report, The National Academies Press, Washington, DC. ISBN 978-0-309-12769-1. DOI. (Cited on page 25.)

Baker, W.L., Savides, J.: 1975, The geostationary operational environmental satellite /GOES/ imaging communication system. In: *International Telemetering Conference*, 464. ADS. (Cited on page 19.)

Barnes, C.W., Simpson, J.A.: 1976, Evidence for interplanetary acceleration of nucleons in corotating interaction regions. *Astrophys. J. Lett.* **210**, L91. DOI. ADS. (Cited on page 30.)

Barnes, D., Davies, J.A., Harrison, R.A., Byrne, J.P., Perry, C.H., Bothmer, V., Eastwood, J.P., Gallagher, P.T., Kilpua, E.K.J., Möstl, C., Rodriguez, L., Rouillard, A.P., Odstrčil, D.: 2019, CMEs in the Heliosphere: II. A Statistical Analysis of the Kinematic Properties Derived from Single-Spacecraft Geometrical Modelling Techniques Applied to CMEs Detected in the Heliosphere from 2007 to 2017 by STEREO/HI-1. *Solar Phys.* **294**(5), 57. DOI. ADS. (Cited on page 75.)

Batchelor, G.K.: 2000, *An introduction to fluid dynamics*, *Cambridge Mathematical Library*, Cambridge University Press, New York. ISBN 9780511800955. DOI. (Cited on page 50.)

Bateman, G.: 1978, *MHD instabilities*. ADS. (Cited on page 48.)

Baumgartner, C., Thalmann, J.K., Veronig, A.M.: 2018, On the Factors Determining the Eruptive Character of Solar Flares. *Astrophys. J.* **853**(2), 105. DOI. ADS. (Cited on page 137.)

Bein, B.M., Berkebile-Stoiser, S., Veronig, A.M., Temmer, M., Muhr, N., Kienreich, I., Utz, D., Vršnak, B.: 2011, Impulsive Acceleration of Coronal Mass Ejections. I. Statistics and Coronal Mass Ejection Source Region Characteristics. *Astrophys. J.* **738**(2), 191. DOI. ADS. (Cited on pages 90, 93, 94, 136, and 142.)

Bertemes, F., Meller, H.: 2012, *Neolithische Kreisgrabenanlagen in Europa : internationale Arbeitstagung, 7. - 9. Mai 2004 in Goseck(Sachsen-Anhalt)*. (Cited on page 9.)

Biermann, L.: 1951, Kometenschweife und solare Korpuskularstrahlung. *Zeitschrift für Astrophysik* **29**, 274. ADS. (Cited on page 21.)

Billings, D.E.: 1966, *A guide to the solar corona*. DOI. ADS. (Cited on pages 55, 62, and 71.)

Bingert, S., Peter, H.: 2013, Nanoflare statistics in an active region 3D MHD coronal model. *Astron. Astrophys.* **550**, A30. DOI. ADS. (Cited on page 19.)

Bobra, M.G., Sun, X., Hoeksema, J.T., Turmon, M., Liu, Y., Hayashi, K., Barnes, G., Leka, K.D.: 2014, The Helioseismic and Magnetic Imager (HMI) Vector Magnetic Field Pipeline: SHARPs - Space-Weather HMI Active Region Patches. *Solar Phys.* **289**(9), 3549. DOI. ADS. (Cited on pages 79 and 103.)

Bosman, E., Bothmer, V., Nisticò, G., Vourlidas, A., Howard, R.A., Davies, J.A.: 2012, Three-dimensional properties of coronal mass ejections from stereo/secchi observations. *Solar Phys.* **281**(1), 167. DOI. ADS. (Cited on pages 26 and 74.)

Bothmer, V.: 2003, Sources of magnetic helicity over the solar cycle. In: Wilson, A. (ed.) *Solar Variability as an Input to the Earth's Environment*, *ESA SP* **535**, 419. ADS. (Cited on page 27.)

Bothmer, V., Daglis, I.A.: 2007, *Space Weather – Physics and Effects*, Springer, Berlin Heidelberg. DOI. ADS. (Cited on pages 5, 18, 21, 22, 24, and 29.)

Bothmer, V., Mrotzek, N.: 2017, Comparison of CME and ICME Structures Derived from Remote-Sensing and In Situ Observations. *Solar Phys.* **292**, 157. DOI. ADS. (Cited on pages 5, 27, 45, 93, and 106.)

Bothmer, V., Schwenn, R.: 1998, The structure and origin of magnetic clouds in the solar wind. *Ann. Geophys.* **16**, 1. DOI. ADS. (Cited on pages 5, 27, 40, 41, and 122.)

Bothmer, V., Tripathi, D.: 2007, Evolution of the photospheric magnetic field in the source regions of coronal mass ejections. In: Kneer, F., Puschmann, K.G., Wittmann, A.D. (eds.) *Modern solar facilities - advanced solar science*, 257. ADS. (Cited on pages 37 and 118.)

Bothmer, V., Zhukov, A.: 2007, In: Bothmer, V., Daglis, I.A. (eds.) *The Sun as the prime source of space weather. Space Weather- Physics and Effects*, Springer, Berlin, Heidelberg, 31. DOI. ADS. (Cited on page 25.)

Bougeret, J.L., Goetz, K., Kaiser, M.L., Bale, S.D., Kellogg, P.J., Maksimovic, M., Monge, N., Monson, S.J., Astier, P.L., Davy, S., Dekkali, M., Hinze, J.J., Manning, R.E., Aguilar-Rodriguez, E., Bonnin, X., Briand, C., Cairns, I.H., Cattell, C.A., Cecconi, B., Eastwood, J., Ergun, R.E., Fainberg, J., Hoang, S., Huttunen, K.E.J., Krucker, S., Lecacheux, A., MacDowall, R.J., Macher, W., Mangeney, A., Meetre, C.A., Moussas, X., Nguyen, Q.N., Oswald, T.H., Pulupa, M., Reiner, M.J., Robinson, P.A., Rucker, H., Salem, C., Santolik, O., Silvis, J.M., Ullrich, R., Zarka, P., Zouganelis, I.: 2008, S/WAVES: The Radio and Plasma Wave Investigation on the STEREO Mission. *Space Sci. Rev.* **136**, 487. DOI. ADS. (Cited on page 68.)

Bradshaw, P.: 1977, Compressible turbulent shear layers. *Annual Review of Fluid Mechanics* **9**, 33. DOI. ADS. (Cited on page 51.)

Brueckner, G.E., Howard, R.A., Koomen, M.J., Korendyke, C.M., Michels, D.J., Moses, J.D., Socker, D.G., Dere, K.P., Lamy, P.L., Llebaria, A., Bout, M.V., Schwenn, R., Simnett, G.M., Bedford, D.K., Eyles, C.J.: 1995, The Large Angle Spectroscopic Coronagraph (LASCO). *Solar Phys.* **162**, 357. DOI. ADS. (Cited on pages 3, 71, and 73.)

Bruno, R., Carbone, V.: 2013, The Solar Wind as a Turbulence Laboratory. *Living Reviews in Solar Physics* **10**, 2. DOI. ADS. (Cited on page 51.)

Bruno, R., Trenchi, L.: 2014, Radial Dependence of the Frequency Break between Fluid and Kinetic Scales in the Solar Wind Fluctuations. *Astrophys. J. Lett.* **787**, L24. DOI. ADS. (Cited on page 51.)

Burlaga, L., Sittler, E., Mariani, F., Schwenn, R.: 1981, Magnetic loop behind an interplanetary shock - Voyager, Helios, and IMP 8 observations. *J. Geophys. Res.* **86**, 6673. DOI. ADS. (Cited on page 27.)

Burlaga, L., Fitzenreiter, R., Lepping, R., Ogilvie, K., Szabo, A., Lazarus, A., Steinberg, J., Gloeckler, G., Howard, R., Michels, D., Farrugia, C., Lin, R.P., Larson, D.E.: 1998, A magnetic cloud containing prominence material - January 1997. *J. Geophys. Res.* **103**, 277. DOI. ADS. (Cited on page 25.)

Bushby, P., Mason, J.: 2004, Solar dynamo: Understanding the solar dynamo. *Astronomy and Geophysics* **45**(4), 4.07. DOI. ADS. (Cited on page 18.)

Byrne, J.P., Maloney, S.A., McAteer, R.T.J., Refojo, J.M., Gallagher, P.T.: 2010, Propagation of an Earth-directed coronal mass ejection in three dimensions. *Nature Communications* **1**, 74. DOI. ADS. (Cited on page 53.)

Cairns, I.H., Knock, S.A., Robinson, P.A., Kuncic, Z.: 2003, Type ii solar radio bursts: Theory and space weather implications. *Space Science Reviews* **107**(1), 27. DOI. (Cited on page 29.)

Canfield, R.C., Hudson, H.S., McKenzie, D.E.: 1999, Sigmoidal morphology and eruptive solar activity. *Geophys. Res. Lett.* **26**, 627. DOI. ADS. (Cited on page 38.)

Cargill, P.J.: 2004, On the Aerodynamic Drag Force Acting on Interplanetary Coronal Mass Ejections. *Solar Phys.* **221**, 135. DOI. ADS. (Cited on pages 4, 50, 63, and 121.)

Cargill, P.J., Chen, J., Garren, D.A.: 1994, Oscillations and Evolution of Curved Current-carrying Loops in the Solar Corona. *Astrophys. J.* **423**, 854. DOI. ADS. (Cited on pages 95 and 144.)

Cargill, P.J., Chen, J., Spicer, D.S., Zalesak, S.T.: 1996, Magnetohydrodynamic simulations of the motion of magnetic flux tubes through a magnetized plasma. *J. Geophys. Res.* **101**(A3), 4855. DOI. ADS. (Cited on pages 50, 63, and 128.)

Carley, E.P., McAteer, R.T.J., Gallagher, P.T.: 2012, Coronal Mass Ejection Mass, Energy, and Force Estimates Using STEREO. *Astrophys. J.* **752**, 36. DOI. ADS. (Cited on pages 50, 52, and 63.)

Carmichael, H.: 1964, A Process for Flares. *NASA Special Publication* **50**, 451. ADS. (Cited on pages 4 and 42.)

Carrington, R.C.: 1859, Description of a Singular Appearance seen in the Sun on September 1, 1859. *Mon. Not. Roy. Astron. Soc.* **20**, 13. DOI. ADS. (Cited on page 18.)

Carroll, B.W., Ostlie, D.A.: 2006, *An introduction to modern astrophysics and cosmology*. ADS. (Cited on pages 11, 12, and 13.)

Chen, J.: 1989, Effects of toroidal forces in current loops embedded in a background plasma. *Astrophys. J.* **338**, 453. DOI. ADS. (Cited on pages 47 and 48.)

Chen, J.: 2017, Physics of erupting solar flux ropes: Coronal mass ejections (CMEs)—Recent advances in theory and observation. *Physics of Plasmas* **24**(9), 090501. DOI. ADS. (Cited on page 44.)

Chen, J., Krall, J.: 2003, Acceleration of Coronal Mass Ejections. In: *AAS/Solar Physics Division Meeting #34, Bulletin of the American Astronomical Society* **35**, 852. ADS. (Cited on page 50.)

Chen, P.F., Shibata, K.: 2000, An Emerging Flux Trigger Mechanism for Coronal Mass Ejections. *Astrophys. J.* **545**, 524. DOI. ADS. (Cited on pages 43, 45, and 118.)

Clette, F., Lefèvre, L.: 2016, The new sunspot number: Assembling all corrections. *Solar Physics* **291**(9), 2629. DOI. (Cited on page 16.)

Clette, F., Svalgaard, L., Vaquero, J.M., Cliver, E.W.: 2014, Revisiting the sunspot number. *Space Science Reviews* **186**(1), 35. DOI. (Cited on pages 14 and 16.)

Colaninno, R.C., Vourlidas, A.: 2009, First Determination of the True Mass of Coronal Mass Ejections: A Novel Approach to Using the Two STEREO Viewpoints. *Astrophys. J.* **698**, 852. DOI. ADS. (Cited on pages 60, 62, and 95.)

Cowling, T.G.: 1945, On the Sun's general magnetic field. *Mon. Not. Roy. Astron. Soc.* **105**, 166. DOI. ADS. (Cited on page 19.)

Cremades, H., Bothmer, V.: 2004, On the three-dimensional configuration of coronal mass ejections. *Astron. Astrophys.* **422**, 307. DOI. ADS. (Cited on pages 3, 4, 27, 57, 58, 59, 90, 106, and 141.)

Daglis, I.A., Thorne, R.M., Baumjohann, W., Orsini, S.: The terrestrial ring current: Origin, formation, and decay. *Reviews of Geophysics* **37**(4), 407. DOI. (Cited on page 24.)

Dal Lago, A., Vieira, L.E.A., Echer, E., Gonzalez, W.D., de Gonzalez, A.L.C., Guarnieri, F.L., Schuch, N.J., Schwenn, R.: 2004, Comparison Between Halo cme Expansion Speeds Observed on the Sun, the Related Shock Transit Speeds to Earth and Corresponding Ejecta Speeds at 1 au. *Solar Phys.* **222**, 323. DOI. ADS. (Cited on page 3.)

Davila, J.M., Rust, D.M., Pizzo, V.J., Liewer, P.C.: 1996, Solar Terrestrial Relations Observatory (STEREO). In: Rust, D.M. (ed.) *Missions to the Sun, Proc. SPIE* **2804**, 34. ADS. (Cited on pages 3 and 73.)

DeForest, C.E., Howard, T.A., McComas, D.J.: 2013, Tracking Coronal Features from the Low Corona to Earth: A Quantitative Analysis of the 2008 December 12 Coronal Mass Ejection. *Astrophys. J.* **769**, 43. DOI. ADS. (Cited on page 68.)

Denig, W., Redmon, R., Mulligan, P.: 2014, NOAA Operational Space Environmental Monitoring - Current Capabilities and Future Directions. In: *EGU General Assembly Conference Abstracts, EGU General Assembly Conference Abstracts*, 4525. ADS. (Cited on page 144.)

Dikpati, M., Gilman, P.A.: 2007, Global solar dynamo models: simulations and predictions of cyclic photospheric fields and long-term non-reversing interior fields. *New Journal of Physics* **9**(8), 297. DOI. ADS. (Cited on page 17.)

Domingo, V., Fleck, B., Poland, A.I.: 1995, SOHO: The Solar and Heliospheric Observatory. *Space Sci. Rev.* **72**, 81. DOI. ADS. (Cited on pages 3 and 73.)

Druckmüller, M.: 2013, A noise adaptive fuzzy equalization method for processing solar extreme ultraviolet images. *The Astrophysical Journal Supplement Series* **207**(2), 25. DOI. http://stacks.iop.org/0067-0049/207/i=2/a=25. (Cited on pages 38 and 103.)

Eddy, J.A.: 1974, A Nineteenth-century Coronal Transient. *Astron. Astrophys.* **34**, 235. ADS. (Cited on page 3.)

Eduardo, S.-D., P., R.A., Benoit, L., Kevin, S., Chihiro, T., Rui, P., R., S.N., Illya, P.: The very slow solar wind: Properties, origin and variability. *Journal of Geophysical Research: Space Physics* **121**(4), 2830. DOI. (Cited on page 21.)

Emslie, A.G., Dennis, B.R., Shih, A.Y., Chamberlin, P.C., Mewaldt, R.A., Moore, C.S., Share, G.H., Vourlidas, A., Welsch, B.T.: 2012, Global Energetics of Thirty-eight Large Solar Eruptive Events. *Astrophys. J.* **759**(1), 71. DOI. ADS. (Cited on page 137.)

Evans, J.W.: 1948, Photometer for measurement of sky brightness near the sun. *Journal of the Optical Society of America (1917-1983)* **38**(12), 1083. ADS. (Cited on page 70.)

Eyles, C.J., Harrison, R.A., Davis, C.J., Waltham, N.R., Shaughnessy, B.M., Mapson-Menard, H.C.A., Bewsher, D., Crothers, S.R., Davies, J.A., Simnett, G.M., Howard, R.A., Moses, J.D., Newmark, J.S., Socker, D.G., Halain, J.-P., Defise, J.-M., Mazy, E., Rochus, P.: 2009, The Heliospheric Imagers Onboard the STEREO Mission. *Solar Phys.* **254**(2), 387. DOI. ADS. (Cited on pages 72 and 77.)

Falconer, D.A., Moore, R.L., Gary, G.A.: 2008, Magnetogram Measures of Total Nonpotentiality for Prediction of Solar Coronal Mass Ejections from Active Regions of Any Degree of Magnetic Complexity. *Astrophys. J.* **689**, 1433. DOI. ADS. (Cited on pages 36 and 79.)

Falconer, D.A., Moore, R.L., Gary, G.A., Adams, M.: 2009, THE "MAIN SEQUENCE" OF EXPLOSIVE SOLAR ACTIVE REGIONS: DISCOVERY AND INTERPRETATION. *The Astrophysical Journal* **700**(2), L166. DOI. https://doi.org/10.1088%2F0004-637x%2F700%2F2%2Fl166. (Cited on pages 119, 143, and 144.)

Feynman, J., Martin, S.F.: 1995, The initiation of coronal mass ejections by newly emerging magnetic flux. *J. Geophys. Res.* **100**, 3355. DOI. ADS. (Cited on page 39.)

Fineschi, S., Antonucci, E., Naletto, G., Romoli, M., Spadaro, D., Nicolini, G., Abbo, L., Andretta, V., Bemporad, A., Berlicki, A., Capobianco, G., Crescenzio, G., Da Deppo, V., Focardi, M., Landini, F., Massone, G., Malvezzi, M.A., Moses, J.D., Nicolosi, P., Pancrazzi, M., Pelizzo, M.-G., Poletto, L., Schühle, U.H., Solanki, S.K., Telloni, D., Teriaca, L., Uslenghi, M.: 2012, *METIS: a novel coronagraph design for the Solar Orbiter mission*, *Society of Photo-Optical Instrumentation Engineers (SPIE) Conference Series* **8443**, 84433H. DOI. ADS. (Cited on page 144.)

Fisher, G.H., Fan, Y., Howard, R.F.: 1995, Comparisons between theory and observation of active region tilts. *Astrophys. J.* **438**, 463. DOI. ADS. (Cited on page 35.)

Fisher, R.R., Poland, A.I.: 1981, Coronal activity below 2 solar radii - 1980 February 15-17. *Astrophys. J.* **246**, 1004. DOI. ADS. (Cited on page 27.)

Fleck, B.: 2005, Eight years of SOHO: some highlights. In: Hanslmeier, A., Veronig, A., Messerotti, M. (eds.) *Solar Magnetic Phenomena*, *Astrophysics and Space Science Library* **320**, 139. DOI. ADS. (Cited on page 67.)

Forbes, T.G.: 2000, A review on the genesis of coronal mass ejections. *J. Geophys. Res.* **105**, 23153. DOI. ADS. (Cited on page 43.)

Forbes, T.G., Isenberg, P.A.: 1991, A catastrophe mechanism for coronal mass ejections. *Astrophys. J.* **373**, 294. DOI. ADS. (Cited on page 46.)

Forbes, T.G., Priest, E.R.: 1984, Numerical simulation of reconnection in an emerging magnetic flux region. *Solar Phys.* **94**, 315. DOI. ADS. (Cited on page 43.)

Forbes, T.G., Priest, E.R.: 1995, Photospheric Magnetic Field Evolution and Eruptive Flares. *Astrophys. J.* **446**, 377. DOI. ADS. (Cited on page 44.)

Forbes, T.G., Priest, E.R., Isenberg, P.A.: 1994, On the maximum energy release in flux-rope models of eruptive flares. *Solar Physics* **150**(1), 245. DOI. (Cited on page 37.)

Forbes, T.G., Linker, J.A., Chen, J., Cid, C., Kóta, J., Lee, M.A., Mann, G., Mikić, Z., Potgieter, M.S., Schmidt, J.M., Siscoe, G.L., Vainio, R., Antiochos, S.K., Riley, P.: 2006, CME Theory and Models. *Space Sci. Rev.* **123**, 251. DOI. ADS. (Cited on pages 33 and 46.)

Forsyth, R.J., Bothmer, V., Cid, C., Crooker, N.U., Horbury, T.S., Kecskemety, K., Klecker, B., Linker, J.A., Odstrcil, D., Reiner, M.J., Richardson, I.G., Rodriguez-Pacheco, J., Schmidt, J.M., Wimmer-Schweingruber, R.F.: 2006, ICMEs in the Inner Heliosphere: Origin, Evolution and Propagation Effects. Report of Working Group G. *Space Sci. Rev.* **123**(1-3), 383. DOI. ADS. (Cited on page 3.)

Fox, N.J., Velli, M.C., Bale, S.D., Decker, R., Driesman, A., Howard, R.A., Kasper, J.C., Kinnison, J., Kusterer, M., Lario, D., Lockwood, M.K., McComas, D.J., Raouafi, N.E., Szabo, A.: 2016, The solar probe plus mission: Humanity's first visit to our star. *Space Science Reviews* **204**(1), 7. DOI. (Cited on page 23.)

Galano, D., Bemporad, A., Buckley, S., Cernica, I., Dániel, V., Denis, F., de Vos, L., Fineschi, S., Galy, C., Graczyk, R., Horodyska, P., Jacob, J., Jansen, R., Kranitis, N., Kurowski, M., Ladno, M., Ledent, P., Loreggia, D., Melich, R., Mollet, D., Mosdorf, M., Paschalis, A., Peresty, R., Purica, M., Radzik, B., Rataj, M., Rougeot, R., Salvador, L., Thizy, C., Versluys, J., Walczak, T., Zarzycka, A., Zender, J., Zhukov, A.: 2018, Development of ASPIICS: a coronagraph based on Proba-3 formation flying mission. In: *Proc. SPIE*, *Society of Photo-Optical Instrumentation Engineers (SPIE) Conference Series* **10698**, 106982Y. DOI. ADS. (Cited on page 144.)

Galvin, A.B., Kistler, L.M., Popecki, M.A., Farrugia, C.J., Simunac, K.D.C., Ellis, L., Möbius, E., Lee, M.A., Boehm, M., Carroll, J., Crawshaw, A., Conti, M., Demaine, P., Ellis, S., Gaidos, J.A., Googins, J., Granoff, M., Gustafson, A., Heirtzler, D., King, B., Knauss, U., Levasseur, J., Longworth, S., Singer, K., Turco, S., Vachon, P., Vosbury, M., Widholm, M., Blush, L.M., Karrer, R., Bochsler, P., Daoudi, H., Etter, A., Fischer, J., Jost, J., Opitz, A., Sigrist, M., Wurz, P., Klecker, B., Ertl, M., Seidenschwang, E., Wimmer-Schweingruber, R.F., Koeten, M., Thompson, B., Steinfeld, D.: 2008, The

Plasma and Suprathermal Ion Composition (PLASTIC) Investigation on the STEREO Observatories. *Space Sci. Rev.* **136**, 437. DOI. ADS. (Cited on page 68.)

Gary, G.A.: 2001, Plasma Beta above a Solar Active Region: Rethinking the Paradigm. *Solar Phys.* **203**(1), 71. DOI. ADS. (Cited on page 47.)

Gleissberg, W.: 1939, A long-periodic fluctuation of the sun-spot numbers. *The Observatory* **62**, 158. ADS. (Cited on page 14.)

Goldstein, H.: 1983, On the field configuration in magnetic clouds. In: *NASA Conference Publication*, *NASA Conference Publication* **228**. ADS. (Cited on page 27.)

Gopalswamy, N.: 2013, STEREO and SOHO contributions to coronal mass ejection studies: Some recent results. In: *Astronomical Society of India Conference Series*, *Astronomical Society of India Conference Series* **10**. ADS. (Cited on page 50.)

Gopalswamy, N., Lara, A., Lepping, R.P., Kaiser, M.L., Berdichevsky, D., St. Cyr, O.C.: 2000, Interplanetary acceleration of coronal mass ejections. *Geophys. Res. Lett.* **27**, 145. DOI. ADS. (Cited on page 3.)

Gopalswamy, N., Xie, H., Yashiro, S., Usoskin, I.: 2005, Coronal Mass Ejections and Ground Level Enhancements. *International Cosmic Ray Conference* **1**, 169. ADS. (Cited on page 25.)

Gopalswamy, N., Mikić, Z., Maia, D., Alexander, D., Cremades, H., Kaufmann, P., Tripathi, D., Wang, Y.-M.: 2006, The Pre-CME Sun. *Space Sci. Rev.* **123**, 303. DOI. ADS. (Cited on page 25.)

Gopalswamy, N., Mäkelä, P., Xie, H., Akiyama, S., Yashiro, S.: 2009, CME interactions with coronal holes and their interplanetary consequences. *Journal of Geophysical Research (Space Physics)* **114**(A3), A00A22. DOI. ADS. (Cited on page 90.)

Gosling, J.T.: 1993, The solar flare myth. *J. Geophys. Res.* **98**. ADS. (Cited on page 29.)

Gosling, J.T., Hildner, E., MacQueen, R.M., Munro, R.H., Poland, A.I., Ross, C.L.: 1974, Mass ejections from the sun - A view from SKYLAB. *J. Geophys. Res.* **79**, 4581. DOI. ADS. (Cited on page 26.)

Hale, G.E.: 1908, On the Probable Existence of a Magnetic Field in Sun-Spots. *Astrophys. J.* **28**, 315. DOI. ADS. (Cited on pages 14 and 69.)

Hale, G.E., Ellerman, F., Nicholson, S.B., Joy, A.H.: 1919, The Magnetic Polarity of Sun-Spots. *Astrophys. J.* **49**, 153. DOI. ADS. (Cited on pages 14, 34, and 35.)

Hansen, R.T., Garcia, C.J., Grognard, R.J.-M., Sheridan, K.V.: 1971, A coronal disturbance observed simultaneously with a white-light corona-meter and the 80 MHz Culgoora radioheliograph. *Proceedings of the Astronomical Society of Australia* **2**, 57. ADS. (Cited on page 3.)

Harrison, R.A., Davies, J.A., Barnes, D., Byrne, J.P., Perry, C.H., Bothmer, V., Eastwood, J.P., Gallagher, P.T., Kilpua, E.K.J., Möstl, C., Rodriguez, L., Rouillard, A.P., Odstrčil, D.: 2018, CMEs in the Heliosphere: I. A Statistical Analysis of the Observational Properties of CMEs Detected in the Heliosphere from 2007 to 2017 by STEREO/HI-1. *Solar Phys.* **293**(5), 77. DOI. ADS. (Cited on page 75.)

Harvey, K.L.: 1993, Magnetic Bipoles on the Sun. PhD thesis, , Univ. Utrecht, (1993). ADS. (Cited on page 35.)

Harvey, K.L., Martin, S.F.: 1973, Ephemeral Active Regions. *Solar Phys.* **32**(2), 389. DOI. ADS. (Cited on page 18.)

Hassanin, A., Kliem, B.: 2016, Helical Kink Instability in a Confined Solar Eruption. *Astrophys. J.* **832**(2), 106. DOI. ADS. (Cited on page 137.)

Hathaway, D.H.: 2015, The solar cycle. *Living Reviews in Solar Physics* **12**(1), 4. DOI. (Cited on page 14.)

Heinzel, P., Anzer, U.: 2003, 2D Radiative Transfer in Magnetically Confined Structures. In: Hubeny, I., Mihalas, D., Werner, K. (eds.) *Stellar Atmosphere Modeling*, *Astronomical Society of the Pacific Conference Series* **288**, 441. ADS. (Cited on page 39.)

Heyvaerts, J., Priest, E.R., Rust, D.M.: 1977, An emerging flux model for the solar flare phenomenon. *Astrophys. J.* **216**, 123. DOI. ADS. (Cited on pages 43 and 118.)

Higgins, P.A., Gallagher, P.T., McAteer, R.T.J., Bloomfield, D.S.: 2011, Solar magnetic feature detection and tracking for space weather monitoring. *Advances in Space Research* **47**, 2105. DOI. ADS. (Cited on pages 6, 79, and 108.)

Hildner, E., Gosling, J.T., Hansen, R.T., Bohlin, J.D.: 1975, The sources of material comprising a mass ejection coronal transient. *Solar Phys.* **45**, 363. DOI. ADS. (Cited on pages 62 and 95.)

Hirayama, T.: 1974, Theoretical Model of Flares and Prominences. I: Evaporating Flare Model. *Solar Phys.* **34**, 323. DOI. ADS. (Cited on pages 4 and 42.)

Holder, Z.A., Canfield, R.C., McMullen, R.A., Nandy, D., Howard, R.F., Pevtsov, A.A.: 2004, On the Tilt and Twist of Solar Active Regions. *Astrophys. J.* **611**, 1149. DOI. ADS. (Cited on page 35.)

Hood, A.W., Priest, E.R.: 1979, Kink instability of solar coronal loops as the cause of solar flares. *Solar Phys.* **64**, 303. DOI. ADS. (Cited on page 47.)

Howard, R.A., Sheeley Jr., N.R., Koomen, M.J., Michels, D.J.: 1985, Coronal mass ejections: 1979–1981. *Journal of Geophysical Research: Space Physics* **90**(A9), 8173. DOI. ADS. (Cited on page 60.)

Howard, R.A., Moses, J.D., Vourlidas, A., Newmark, J.S., Socker, D.G., Plunkett, S.P., Korendyke, C.M., Cook, J.W., Hurley, A., Davila, J.M., Thompson, W.T., St Cyr, O.C., Mentzell, E., Mehalick, K., Lemen, J.R., Wuelser, J.P., Duncan, D.W., Tarbell, T.D., Wolfson, C.J., Moore, A., Harrison, R.A., Waltham, N.R., Lang, J., Davis, C.J., Eyles, C.J., Mapson-Menard, H., Simnett, G.M., Halain, J.P., Defise, J.M., Mazy, E., Rochus, P., Mercier, R., Ravet, M.F., Delmotte, F., Auchere, F., Delaboudiniere, J.P., Bothmer, V., Deutsch, W., Wang, D., Rich, N., Cooper, S., Stephens, V., Maahs, G., Baugh, R., McMullin, D., Carter, T.: 2008, Sun Earth Connection Coronal and Heliospheric Investigation (SECCHI). *Space Sci. Rev.* **136**, 67. DOI. ADS. (Cited on pages 3, 70, 71, 73, and 76.)

Howard, T.: 2011, *Coronal Mass Ejections*, *Astrophysics and Space Science Library* **376**. DOI. ADS. (Cited on pages 29 and 38.)

Howard, T.A., Tappin, S.J.: 2009, Interplanetary Coronal Mass Ejections Observed in the Heliosphere: 3. Physical Implications. *Space Sci. Rev.* **147**, 89. DOI. ADS. (Cited on pages 53, 54, 55, and 56.)

Howe, R., Christensen-Dalsgaard, J., Hill, F., Komm, R.W., Larsen, R.M., Schou, J., Thompson, M.J., Toomre, J.: 2000, Dynamic Variations at the Base of the Solar Convection Zone. *Science* **287**, 2456. DOI. ADS. (Cited on page 16.)

Hudson, H.S.: 2007, The Unpredictability of the Most Energetic Solar Events. *Astrophys. J. Lett.* **663**, L45. DOI. ADS. (Cited on page 19.)

Hundhausen, A.J., Stanger, A.L., Serbicki, S.A.: 1994, Mass and energy contents of coronal mass ejections: SMM results from 1980 and 1984-1988. In: Hunt, J.J. (ed.) *Solar Dynamic Phenomena and Solar Wind Consequences, the Third SOHO Workshop*, *ESA Special Publication* **373**, 409. ADS. (Cited on page 60.)

Illing, R.M.E., Hundhausen, A.J.: 1985, Observation of a coronal transient from 1.2 to 6 solar radii. *J. Geophys. Res.* **90**, 275. DOI. ADS. (Cited on page 27.)

Isavnin, A., Vourlidas, A., Kilpua, E.K.J.: 2014, Three-Dimensional Evolution of Flux-Rope CMEs and Its Relation to the Local Orientation of the Heliospheric Current Sheet. *Solar Phys.* **289**(6), 2141. DOI. ADS. (Cited on pages 5, 89, and 141.)

Jackson, J.D.: 1975, *Classical electrodynamics*. ADS. (Cited on pages 53 and 55.)

Jaeggli, S.A., Norton, A.A.: 2016, The Magnetic Classification of Solar Active Regions 1992-2015. *Astrophys. J. Lett.* **820**, L11. DOI. ADS. (Cited on pages 34 and 103.)

Jian, L., Russell, C.T., Luhmann, J.G., Skoug, R.M.: 2006, Properties of Interplanetary Coronal Mass Ejections at One AU During 1995 2004. *Solar Phys.* **239**, 393. DOI. ADS. (Cited on page 51.)

Kaiser, M.L., Kucera, T.A., Davila, J.M., St. Cyr, O.C., Guhathakurta, M., Christian, E.: 2008, The STEREO Mission: An Introduction. *Space Sci. Rev.* **136**, 5. DOI. ADS. (Cited on pages 67 and 68.)

Kane, R.P.: 2002, Some Implications Using the Group Sunspot Number Reconstruction. *Solar Phys.* **205**(2), 383. DOI. ADS. (Cited on page 14.)

Kasper, J.C., Maruca, B.A., Stevens, M.L., Zaslavsky, A.: 2013, Sensitive Test for Ion-Cyclotron Resonant Heating in the Solar Wind. *Physical Review Letters* **110**(9), 091102. DOI. ADS. (Cited on page 69.)

Kiepenheuer, K.O.: 1968, Preface and Introduction. In: Kiepenheuer, K.O. (ed.) *Structure and Development of Solar Active Regions*, *IAU Symposium* **35**, 3. ADS. (Cited on page 34.)

Kilpua, E.K.J., Madjarska, M.S., Karna, N., Wiegelmann, T., Farrugia, C., Yu, W., Andreeova, K.: 2016, Sources of the slow solar wind during the solar cycle 23/24 minimum. *Solar Physics* **291**(8), 2441. DOI. (Cited on page 21.)

Kim, S., Nakariakov, V.M., Cho, K.-S.: 2014, VERTICAL KINK OSCILLATION OF a MAGNETIC FLUX ROPE STRUCTURE IN THE SOLAR CORONA. *The Astrophysical Journal* **797**(2), L22. DOI. https://doi.org/10.1088%2F2041-8205%2F797%2F2%2Fl22. (Cited on pages 95 and 144.)

King, J.H., Papitashvili, N.E.: 2005, Solar wind spatial scales in and comparisons of hourly Wind and ACE plasma and magnetic field data. *Journal of Geophysical Research (Space Physics)* **110**, A02104. DOI. ADS. (Cited on page 23.)

Kirichenko, A.S., Bogachev, S.A.: 2017, Plasma heating in solar microflares: Statistics and analysis. *The Astrophysical Journal* **840**(1), 45. (Cited on page 19.)

Kliem, B., Török, T.: 2006, Torus Instability. *Physical Review Letters* **96**(25), 255002. DOI. ADS. (Cited on pages 47 and 48.)

Koomen, M.J., Detwiler, C.R., Brueckner, G.E., Cooper, H.W., Tousey, R.: 1975, White light coronagraph in OSO-7. *Applied Optics* **14**, 743. DOI. ADS. (Cited on page 26.)

Kopp, R.A., Pneuman, G.W.: 1976, Magnetic reconnection in the corona and the loop prominence phenomenon. *Solar Phys.* **50**, 85. DOI. ADS. (Cited on pages 4 and 42.)

Kosovichev, A.G., Zharkova, V.V.: 1998, X-ray flare sparks quake inside Sun. *Nature* **393**, 317. DOI. ADS. (Cited on page 67.)

Kumar, A., Rust, D.M.: 1996, Interplanetary magnetic clouds, helicity conservation, and current-core flux-ropes. *J. Geophys. Res.* **101**(A7), 15667. DOI. ADS. (Cited on page 137.)

Künzel, H.: 1965, Zur Klassifikation von Sonnenfleckengruppen. *Astronomische Nachrichten* **288**, 177. ADS. (Cited on page 34.)

Kuzmenko, I.V., Grechnev, V.V.: 2017, Development and Parameters of a Non-Self-Similar CME Caused by the Eruption of a Quiescent Prominence. *Solar Phys.* **292**(10), 143. DOI. ADS. (Cited on page 90.)

Landau, L.D., Lifshitz, E.M.: 1987, *Fluid mechanics, second edition: Volume 6 (course of theoretical physics)*, 2nd edn., *Course of theoretical physics / by L. D. Landau and E. M. Lifshitz, Vol. 6*, Butterworth-Heinemann, Burlington. ISBN 0750627670. http://www.worldcat.org/isbn/0750627670. (Cited on pages 50 and 63.)

Lang, K.R.: 2009, *The Sun from Space*. DOI. ADS. (Cited on pages 21, 24, 29, and 30.)

Lawrence, J.D.: 1972, *A catalog of special plane curves*, *Dover books on advanced mathematics*, Dover Publications, New York. ISBN 9780486602882. https://books.google.de/books?id=F0DvAAAAMAAJ. (Cited on page 59.)

Leblanc, Y., Dulk, G.A., Bougeret, J.-L.: 1998, Tracing the Electron Density from the Corona to 1au. *Solar Phys.* **183**, 165. DOI. ADS. (Cited on pages 23, 128, and 129.)

Lee, H., Moon, Y.-J., Nakariakov, V.: 2015, Radial and Azimuthal Oscillations in Halo Coronal Mass Ejections. In: *AAS/AGU Triennial Earth-Sun Summit*, *AAS/AGU Triennial Earth-Sun Summit*, 310.02. ADS. (Cited on pages 94, 142, and 144.)

Lee, H., Moon, Y.-J., Nakariakov, V.M., Na, H., Cho, I.-H., Park, E.: 2018, Three-dimensional Oscillations of 21 Halo Coronal Mass Ejections Using Multi-spacecraft Data. *Astrophys. J.* **868**(1), 18. DOI. ADS. (Cited on pages 94, 95, 142, and 144.)

Leighton, R.B.: 1969, A Magneto-Kinematic Model of the Solar Cycle. *Astrophys. J.* **156**, 1. DOI. ADS. (Cited on pages 17 and 35.)

Leka, K.D., Canfield, R.C., McClymont, A.N., van Driel-Gesztelyi, L.: 1996, Evidence for Current-carrying Emerging Flux. *Astrophys. J.* **462**, 547. DOI. ADS. (Cited on page 36.)

Lemen, J.R., Title, A.M., Akin, D.J., Boerner, P.F., Chou, C., Drake, J.F., Duncan, D.W., Edwards, C.G., Friedlaender, F.M., Heyman, G.F., Hurlburt, N.E., Katz, N.L., Kushner, G.D., Levay, M., Lindgren, R.W., Mathur, D.P., McFeaters, E.L., Mitchell, S., Rehse, R.A., Schrijver, C.J., Springer, L.A., Stern, R.A., Tarbell, T.D., Wuelser, J.-P., Wolfson, C.J., Yanari, C., Bookbinder, J.A., Cheimets, P.N., Caldwell, D., Deluca, E.E., Gates, R., Golub, L., Park, S., Podgorski, W.A., Bush, R.I., Scherrer, P.H., Gummin, M.A., Smith, P., Auker, G., Jerram, P., Pool, P., Soufli, R., Windt, D.L., Beardsley, S., Clapp, M., Lang, J., Waltham, N.: 2012, The Atmospheric Imaging Assembly (AIA) on the Solar Dynamics Observatory (SDO). *Solar Phys.* **275**, 17. DOI. ADS. (Cited on pages 13, 70, and 73.)

Lin, J., Raymond, J.C., van Ballegooijen, A.A.: 2004, The role of magnetic reconnection in the observable features of solar eruptions. *The Astrophysical Journal* **602**(1), 422. http://stacks.iop.org/0004-637X/602/i=1/a=422. (Cited on page 37.)

Lin, J., Forbes, T.G., Isenberg, P.A., Démoulin, P.: 1998, The effect of curvature on flux-rope models of coronal mass ejections. *The Astrophysical Journal* **504**(2), 1006. http://stacks.iop.org/0004-637X/504/i=2/a=1006. (Cited on page 37.)

Lindsay, G.M., Luhmann, J.G., Russell, C.T., Gosling, J.T.: 1999, Relationships between coronal mass ejection speeds from coronagraph images and interplanetary characteristics of associated interplanetary coronal mass ejections. *J. Geophys. Res.* **104**, 12515. DOI. ADS. (Cited on page 3.)

Linker, J.A., Mikić, Z., Lionello, R., Riley, P., Amari, T., Odstrcil, D.: 2003, Flux cancellation and coronal mass ejections. *Physics of Plasmas* **10**(5), 1971. DOI. https://doi.org/10.1063/1.1563668. (Cited on pages 37 and 118.)

Liu, R., Kliem, B., Titov, V.S., Chen, J., Wang, Y., Wang, H., Liu, C., Xu, Y., Wiegelmann, T.: 2016, Structure, Stability, and Evolution of Magnetic Flux Ropes from the Perspective of Magnetic Twist. *Astrophys. J.* **818**(2), 148. DOI. ADS. (Cited on page 137.)

Livi, S.H.B., Wang, J., Martin, S.F.: 1985, The cancellation of magnetic flux. I - On the quiet sun. *Australian Journal of Physics* **38**, 855. DOI. ADS. (Cited on page 36.)

Livi, S.H.B., Martin, S., Wang, H., Ai, G.: 1989, The association of flares to cancelling magnetic features on the sun. *Solar Phys.* **121**, 197. DOI. ADS. (Cited on pages 37 and 118.)

Llebaria, A., Lamy, P.L., Bout, M.V.: 2004, Lessons learned from the SOHO/LASCO-C2 calibration. In: Fineschi, S., Gummin, M.A. (eds.) *Proc. SPIE, Society of Photo-Optical Instrumentation Engineers (SPIE) Conference Series* **5171**, 26. DOI. ADS. (Cited on page 77.)

Low, B.C.: 1996, Solar Activity and the Corona. *Solar Phys.* **167**, 217. DOI. ADS. (Cited on page 27.)

Lugaz, N., Manchester, W.B. IV, Gombosi, T.I.: 2005, The Evolution of Coronal Mass Ejection Density Structures. *Astrophys. J.* **627**, 1019. DOI. ADS. (Cited on page 62.)

Lugaz, N., Farrugia, C.J., Davies, J.A., Möstl, C., Davis, C.J., Roussev, I.I., Temmer, M.: 2012, The Deflection of the Two Interacting Coronal Mass Ejections of 2010 May 23-24 as Revealed by Combined in Situ Measurements and Heliospheric Imaging. *Astrophys. J.* **759**(1), 68. DOI. ADS. (Cited on page 90.)

Luhmann, J.G., Curtis, D.W., Schroeder, P., McCauley, J., Lin, R.P., Larson, D.E., Bale, S.D., Sauvaud, J.-A., Aoustin, C., Mewaldt, R.A., Cummings, A.C., Stone, E.C., Davis, A.J., Cook, W.R., Kecman, B., Wiedenbeck, M.E., von Rosenvinge, T., Acuna, M.H., Reichenthal, L.S., Shuman, S., Wortman, K.A., Reames, D.V., Mueller-Mellin, R., Kunow, H., Mason, G.M., Walpole, P., Korth, A., Sanderson, T.R., Russell, C.T., Gosling, J.T.: 2008, STEREO IMPACT Investigation Goals, Measurements, and Data Products Overview. *Space Sci. Rev.* **136**, 117. DOI. ADS. (Cited on page 68.)

Lyot, B.: 1939, The study of the solar corona and prominences without eclipses (George Darwin Lecture, 1939). *Mon. Not. Roy. Astron. Soc.* **99**, 580. DOI. ADS. (Cited on page 70.)

MacQueen, R.M., Eddy, J.A., Gosling, J.T., Hildner, E., Munro, R.H., Newkirk, G.A. Jr., Poland, A.I., Ross, C.L.: 1974, The Outer Solar Corona as Observed from Skylab: Preliminary Results. *Astrophys. J. Lett.* **187**, L85. DOI. ADS. (Cited on page 3.)

MacQueen, R.M., Csoeke-Poeckh, A., Hildner, E., House, L., Reynolds, R., Stanger, A., Tepoel, H., Wagner, W.: 1980, The High Altitude Observatory Coronagraph/Polarimeter on the Solar Maximum Mission. *Solar Phys.* **65**, 91. DOI. ADS. (Cited on page 26.)

Maloney, S.A., Gallagher, P.T., McAteer, R.T.J.: 2009, Reconstructing the 3-D Trajectories of CMEs in the Inner Heliosphere. *Solar Phys.* **256**, 149. DOI. ADS. (Cited on page 50.)

Martin, S.F., Livi, S.H.B., Wang, J.: 1985, The cancellation of magnetic flux. II - In a decaying active region. *Australian Journal of Physics* **38**, 929. DOI. ADS. (Cited on page 36.)

Marubashi, K., Akiyama, S., Yashiro, S., Gopalswamy, N., Cho, K.-S., Park, Y.-D.: 2015, Geometrical Relationship Between Interplanetary Flux Ropes and Their Solar Sources. *Solar Phys.* **290**, 1371. DOI. ADS. (Cited on pages 3, 28, and 123.)

Mason, E.I., Antiochos, S.K., Viall, N.M.: 2019, Observations of Solar Coronal Rain in Null Point Topologies. *Astrophys. J. Lett.* **874**, L33. DOI. ADS. (Cited on page 69.)

Mays, L., Verbeke, C., Taktakishvili, A., Riley, P., CME Arrival Time Working Team Members: 2018, CME Arrival Time and Impact Working Team. In: *Solar Heliospheric and INterplanetary Environment (SHINE 2018)*, 122. ADS. (Cited on page 5.)

McClintock, B.H., Norton, A.A.: 2013, Recovering Joy's Law as a Function of Solar Cycle, Hemisphere, and Longitude. *Solar Phys.* **287**, 215. DOI. ADS. (Cited on page 35.)

McComas, D.J., Bame, S.J., Barker, P., Feldman, W.C., Phillips, J.L., Riley, P., Griffee, J.W.: 1998a, Solar Wind Electron Proton Alpha Monitor (SWEPAM) for the Advanced Composition Explorer. *Space Sci. Rev.* **86**, 563. DOI. ADS. (Cited on page 73.)

McComas, D.J., Bame, S.J., Barraclough, B.L., Feldman, W.C., Funsten, H.O., Gosling, J.T., Riley, P., Skoug, R., Balogh, A., Forsyth, R., Goldstein, B.E., Neugebauer, M.: 1998b, Ulysses' return to the slow solar wind. *Geophys. Res. Lett.* **25**, 1. DOI. ADS. (Cited on page 22.)

Middleton, K.F., Heiko Anwand, H., Bothmer, V., Davies, J.A., Ergenzinger, K., J., E., Halain, J., Hardie, R., Hellin, M., Hinrichs, J., Huke, P., Kennedy, K.V. N., P., J., McQuirk, C., Nicula, B., Renotte, E., Shaugnessy, B.M., Stopfkuchen, L., Tappin, S.J., Tosh, I.A.J., Waltham, N.R., West, M.J.: 2016, A Coronagraph for Operational Space Weather Prediction. In: *International Conference on Space Optics*, *International Conference on Space Optics* **18**. (Cited on page 144.)

Millward, G., Biesecker, D., Pizzo, V., de Koning, C.A.: 2013, An operational software tool for the analysis of coronagraph images: Determining CME parameters for input into the WSA-Enlil heliospheric model. *Space Weather* **11**, 57. DOI. ADS. (Cited on page 59.)

Minnaert, M.: 1930, On the continuous spectrum of the corona and its polarisation. With 3 figures. (Received July 30, 1930). *Zeitschrift fuer Astrophysik* **1**, 209. ADS. (Cited on page 55.)

Mishra, W., Srivastava, N., Singh, T.: 2015, Kinematics of interacting CMEs of 25 and 28 September 2012. *Journal of Geophysical Research (Space Physics)* **120**(12), 10,221. DOI. ADS. (Cited on page 85.)

Morrill, J.S., Korendyke, C.M., Brueckner, G.E., Giovane, F., Howard, R.A., Koomen, M., Moses, D., Plunkett, S.P., Vourlidas, A., Esfandiari, E., Rich, N., Wang, D., Thernisien, A.F., Lamy, P., Llebaria, A., Biesecker, D., Michels, D., Gong, Q., Andrews, M.: 2006, Calibration of the Soho/Lasco C3 White Light Coronagraph. *Solar Phys.* **233**(2), 331. DOI. ADS. (Cited on page 77.)

Möstl, C., Rollett, T., Frahm, R.A., Liu, Y.D., Long, D.M., Colaninno, R.C., Reiss, M.A., Temmer, M., Farrugia, C.J., Posner, A., Dumbović, M., Janvier, M., Démoulin, P., Boakes, P., Devos, A., Kraaikamp, E., Mays, M.L., Vršnak, B.: 2015, Strong coronal channelling and interplanetary evolution of a solar storm up to Earth and Mars. *Nature Communications* **6**, 7135. DOI. ADS. (Cited on page 90.)

Mouschovias, T.C., Poland, A.I.: 1978, Expansion and broadening of coronal loop transients - A theoretical explanation. *Astrophys. J.* **220**, 675. DOI. ADS. (Cited on page 3.)

Müller, D., Marsden, R.G., St. Cyr, O.C., Gilbert, H.R.: 2013, Solar orbiter. *Solar Physics* **285**(1), 25. DOI. (Cited on page 23.)

Mulligan, T., Russell, C.T., Luhmann, J.G.: 1998, Solar cycle evolution of the structure of magnetic clouds in the inner heliosphere. *Geophys. Res. Lett.* **25**, 2959. DOI. ADS. (Cited on pages 5 and 40.)

Munro, R.H., Gosling, J.T., Hildner, E., MacQueen, R.M., Poland, A.I., Ross, C.L.: 1979, The association of coronal mass ejection transients with other forms of solar activity. *Solar Phys.* **61**, 201. DOI. ADS. (Cited on page 33.)

Murray, S.A., Guerra, J.A., Zucca, P., Park, S.-H., Carley, E.P., Gallagher, P.T., Vilmer, N., Bothmer, V.: 2018, Connecting Coronal Mass Ejections to Their Solar Active Region Sources: Combining Results from the HELCATS and FLARECAST Projects. *Solar Phys.* **293**, 60. DOI. ADS. (Cited on pages 34, 75, 79, 108, and 109.)

NIST `https://www.nist.gov/data`. (Cited on page III.)

Nisticò, G., Vladimirov, V., Nakariakov, V.M., Battams, K., Bothmer, V.: 2018, Oscillations of cometary tails: a vortex shedding phenomenon? *ArXiv e-prints*. ADS. (Cited on page 21.)

Ogilvie, K.W., Desch, M.D.: 1997, The wind spacecraft and its early scientific results. *Advances in Space Research* **20**(4-5), 559. DOI. ADS. (Cited on page 69.)

Opgenoorth, H., Pulkkinen, A., Buchert, S., Monstein, C., Klein, K.L., Marqué, C., Krucker, S.: 2016, Solar activity during the space weather incident of Nov 4., 2015 - Complex data and lessons learned. In: *EGU General Assembly Conference Abstracts*, *EGU General Assembly Conference Abstracts* **18**, EPSC2016. ADS. (Cited on page 20.)

Owens, M.J., Lockwood, M., Barnard, L.A.: 2017, Coronal mass ejections are not coherent magnetohydrodynamic structures. *Scientific Reports* **7**, 4152. DOI. ADS. (Cited on pages 90, 129, and 130.)

Palmerio, E., Kilpua, E.K.J., James, A.W., Green, L.M., Pomoell, J., Isavnin, A., Valori, G.: 2017, Determining the Intrinsic CME Flux Rope Type Using Remote-sensing Solar Disk Observations. *Solar Phys.* **292**, 39. DOI. ADS. (Cited on pages 5, 38, 40, and 106.)

Palmerio, E., Kilpua, E.K.J., Möstl, C., Bothmer, V., James, A.W., Green, L.M., Isavnin, A., Davies, J.A., Harrison, R.A.: 2018, Coronal Magnetic Structure of Earthbound CMEs and In Situ Comparison. *Space Weather* **16**, 442. DOI. ADS. (Cited on pages 5, 40, and 106.)

Parker, E.: 1959, Extension of the Solar Corona into Interplanetary Space. *J. Geophys. Res.* **64**, 1675. DOI. ADS. (Cited on page 21.)

Parker, E.N.: 1955, Hydromagnetic Dynamo Models. *Astrophys. J.* **122**, 293. DOI. ADS. (Cited on page 16.)

Parker, E.N.: 1983, Direct coronal heating from dissipation of magnetic field. In: *NASA Conference Publication*, *NASA Conference Publication* **228**. ADS. (Cited on page 19.)

Pesnell, W.D., Thompson, B.J., Chamberlin, P.C.: 2012, The Solar Dynamics Observatory (SDO). *Solar Phys.* **275**, 3. DOI. ADS. (Cited on pages 6 and 73.)

Pluta, A., Mrotzek, N., Vourlidas, A., Bothmer, V., Savani, N.: 2018, Combined geometrical modelling and white-light mass determination of coronal mass ejections. *Astron. Astrophys.*. DOI. (Cited on pages 26, 50, 61, 62, 75, 90, 92, 97, 98, 99, 100, and 142.)

Poland, A.I., Howard, R.A., Koomen, M.J., Michels, D.J., Sheeley, N.R.: 1981, Coronal transients near sunspot maximum. *Solar Physics* **69**(1), 169. DOI. https://doi.org/10.1007/BF00151264. (Cited on page 60.)

Priest, E.R.: 1989, Book-Review - Dynamics and Structure of Quiescent Solar Prominences. *Journal of the British Astronomical Association* **99**, 152. ADS. (Cited on page 39.)

Priest, E.R., Forbes, T.G.: 1990, Magnetic field evolution during prominence eruptions and two-ribbon flares. *Solar Phys.* **126**, 319. DOI. ADS. (Cited on page 46.)

Reames, D.V., Kahler, S.W., Ng, C.K.: 1997, Spatial and Temporal Invariance in the Spectra of Energetic Particles in Gradual Solar Events. *Astrophys. J.* **491**, 414. DOI. ADS. (Cited on page 29.)

Reid, H.A.S., Ratcliffe, H.: 2014, A review of solar type III radio bursts. *Research in Astronomy and Astrophysics* **14**, 773. DOI. ADS. (Cited on page 29.)

Reinard, A.A.: 2008, Analysis of Interplanetary Coronal Mass Ejection Parameters as a Function of Energetics, Source Location, and Magnetic Structure. *Astrophys. J.* **682**, 1289. DOI. ADS. (Cited on page 95.)

Richardson, I.G., Cane, H.V.: 2010, Near-Earth Interplanetary Coronal Mass Ejections During Solar Cycle 23 (1996 - 2009): Catalog and Summary of Properties. *Solar Phys.* **264**, 189. DOI. ADS. (Cited on page 28.)

Rickett, B.J., Coles, W.A.: 1980, Solar cycle changes in the high latitude solar wind. In: *NASA Conference Publication*, *NASA Conference Publication* **2098**. ADS. (Cited on page 23.)

Rickett, B.J., Coles, W.A.: 1991, Evolution of the solar wind structure over a solar cycle - Interplanetary scintillation velocity measurements compared with coronal observations. *J. Geophys. Res.* **96**, 1717. DOI. ADS. (Cited on page 23.)

Riley, P., Lionello, R., Mikić, Z., Linker, J.: 2008, Using Global Simulations to Relate the Three-Part Structure of Coronal Mass Ejections to In Situ Signatures. *Astrophys. J.* **672**, 1221. DOI. ADS. (Cited on page 27.)

Riley, P., Mays, M.L., Andries, J., Amerstorfer, T., Biesecker, D., Delouille, V., Dumbović, M., Feng, X., Henley, E., Linker, J.A., Möstl, C., Nuñez, M., Pizzo, V., Temmer, M., Tobiska, W.K., Verbeke, C., West, M.J., Zhao, X.: 2018, Forecasting the Arrival Time of Coronal Mass Ejections: Analysis of the CCMC CME Scoreboard. *Space Weather* **16**, 1245. DOI. ADS. (Cited on page 5.)

Rollett, T., Möstl, C., Isavnin, A., Davies, J.A., Kubicka, M., Amerstorfer, U.V., Harrison, R.A.: 2016, ElEvoHI: A Novel CME Prediction Tool for Heliospheric Imaging Combining an Elliptical Front with Drag-based Model Fitting. *Astrophys. J.* **824**, 131. DOI. ADS. (Cited on page 53.)

Rosenbauer, H., Schwenn, R., Marsch, E., Meyer, B., Miggenrieder, H., Montgomery, M.D., Muehlhaeuser, K.H., Pilipp, W., Voges, W., Zink, S.M.: 1977, A survey on initial results of the HELIOS plasma experiment. *Journal of Geophysics Zeitschrift Geophysik* **42**, 561. ADS. (Cited on pages 23 and 24.)

Russell, C.T., Shinde, A.A., Jian, L.: 2005, A new parameter to define interplanetary coronal mass ejections. *Advances in Space Research* **35**, 2178. DOI. ADS. (Cited on page 51.)

Rust, D.M.: 1994, Spawning and shedding helical magnetic fields in the solar atmosphere. *Geophys. Res. Lett.* **21**, 241. DOI. ADS. (Cited on page 35.)

Rust, D.M., Kumar, A.: 1994, Helical magnetic fields in filaments. *Solar Phys.* **155**, 69. DOI. ADS. (Cited on page 39.)

Rybanský, M., Rušin, V., Minarovjech, M.: 2001, Coronal index of solar activity – solar-terrestrial research. *Space Science Reviews* **95**(1), 227. DOI. (Cited on page 14.)

Sachdeva, N., Subramanian, P., Colaninno, R., Vourlidas, A.: 2015, CME Propagation: Where does Aerodynamic Drag 'Take Over'? *Astrophys. J.* **809**, 158. DOI. ADS. (Cited on pages 4, 51, 122, and 142.)

Sachdeva, N., Subramanian, P., Vourlidas, A., Bothmer, V.: 2017, CME Dynamics Using STEREO and LASCO Observations: The Relative Importance of Lorentz Forces and Solar Wind Drag. *Solar Phys.* **292**, 118. DOI. ADS. (Cited on pages 4, 51, 53, 121, 122, 130, 131, 133, 136, and 142.)

Sakurai, T.: 1976, Magnetohydrodynamic interpretation of the motion of prominences. *Pub. Astron. Soc. Japan* **28**, 177. ADS. (Cited on page 47.)

Savani, N.P., Vourlidas, A., Pulkkinen, A., Nieves-Chinchilla, T., Lavraud, B., Owens, M.J.: 2013, Tracking the momentum flux of a CME and quantifying its influence on geomagnetically induced currents at Earth. *Space Weather* **11**, 245. DOI. ADS. (Cited on page 77.)

Scherrer, P.H., Schou, J., Bush, R.I., Kosovichev, A.G., Bogart, R.S., Hoeksema, J.T., Liu, Y., Duvall, T.L., Zhao, J., Title, A.M., Schrijver, C.J., Tarbell, T.D., Tomczyk, S.: 2012, The Helioseismic and Magnetic Imager (HMI) Investigation for the Solar Dynamics Observatory (SDO). *Solar Phys.* **275**(1-2), 207. DOI. ADS. (Cited on page 69.)

Scherrer, R.S. P. H.and Bogart, Bush, R.I., Hoeksema, J.T., Kosovichev, A.G., Schou, J., Rosenberg, W., Springer, L., Tarbell, T.D., Title, A., Wolfson, C.J., Zayer, I.: 1995, The Solar Oscillations Investigation - Michelson Doppler Imager. *Solar Phys.* **162**(1), 129. DOI. ADS. (Cited on page 69.)

Schou, J., Scherrer, P.H., Bush, R.I., Wachter, R., Couvidat, S., Rabello-Soares, M.C., Bogart, R.S., Hoeksema, J.T., Liu, Y., Duvall, T.L., Akin, D.J., Allard, B.A., Miles, J.W., Rairden, R., Shine, R.A., Tarbell, T.D., Title, A.M., Wolfson, C.J., Elmore, D.F., Norton, A.A., Tomczyk, S.: 2012, Design and Ground Calibration of the Helioseismic and Magnetic Imager (HMI) Instrument on the Solar Dynamics Observatory (SDO). *Solar Phys.* **275**(1), 229. DOI. ADS. (Cited on pages 69 and 73.)

Schrijver, C.J.: 2007, A Characteristic Magnetic Field Pattern Associated with All Major Solar Flares and Its Use in Flare Forecasting. *Astrophys. J. Lett.* **655**, L117. DOI. ADS. (Cited on pages 36 and 79.)

Schwabe, H.: 1844, Sonnenbeobachtungen im Jahre 1843. Von Herrn Hofrath Schwabe in Dessau. *Astronomische Nachrichten* **21**, 233. DOI. ADS. (Cited on page 14.)

Schwenn, R., Marsch, E.: 1990, *Physics of the Inner Heliosphere I. Large-Scale Phenomena.*, 103. ADS. (Cited on pages 21 and 24.)

Shafranov, V.D.: 1966, Plasma Equilibrium in a Magnetic Field. *Reviews of Plasma Physics* **2**, 103. ADS. (Cited on page 47.)

Sheeley, N.R., Wang, Y.-M., Hawley, S.H., Brueckner, G.E., Dere, K.P., Howard, R.A., Koomen, M.J., Korendyke, C.M., Michels, D.J., Paswaters, S.E., Socker, D.G., St. Cyr, O.C., Wang, D., Lamy, P.L., Llebaria, A., Schwenn, R., Simnett, G.M., Plunkett, S., Biesecker, D.A.: 1997, Measurements of Flow Speeds in the Corona Between 2 and 30 $R_{\odot}$. *Astrophys. J.* **484**, 472. DOI. ADS. (Cited on pages 23, 128, and 129.)

Smith, C.W., L'Heureux, J., Ness, N.F., Acuña, M.H., Burlaga, L.F., Scheifele, J.: 1998, The ACE Magnetic Fields Experiment. *Space Sci. Rev.* **86**, 613. DOI. ADS. (Cited on page 73.)

Socker, D.G., Howard, R.A., Korendyke, C.M., Simnett, G.M., Webb, D.F.: 2000, NASA Solar Terrestrial Relations Observatory (STEREO) mission heliospheric imager. In: Fineschi, S., Korendyke, C.M., Siegmund, O.H., Woodgate, B.E. (eds.) *Proc. SPIE, Society of Photo-Optical Instrumentation Engineers (SPIE) Conference Series* **4139**, 284. DOI. ADS. (Cited on page 72.)

Spiegel, E.A., Zahn, J.-P.: 1992, The solar tachocline. *Astron. Astrophys.* **265**, 106. ADS. (Cited on page 12.)

Stewart, M.K. R. T.and McCabe, Koomen, M.J., Hansen, R.T., Dulk, G.A.: 1974, Observations of coronal disturbances from 1 to 9 r. *Solar Physics* **36**(1), 203. DOI. https://doi.org/10.1007/BF00151561. (Cited on page 60.)

Stix, M.: 2004, *The Sun : An Introduction*. ADS. (Cited on pages III, IV, and 11.)

Stone, E.C., Frandsen, A.M., Mewaldt, R.A., Christian, E.R., Margolies, D., Ormes, J.F., Snow, F.: 1998, The Advanced Composition Explorer. *Space Sci. Rev.* **86**, 1. DOI. ADS. (Cited on pages 69 and 73.)

Sturrock, P.A.: 1966, Model of the High-Energy Phase of Solar Flares. *Nature* **211**, 695. DOI. ADS. (Cited on pages 4 and 42.)

Subramanian, P., Dere, K.P.: 2001, Source Regions of Coronal Mass Ejections. *Astrophys. J.* **561**, 372. DOI. ADS. (Cited on pages 33 and 36.)

Subramanian, P., Vourlidas, A.: 2007, Energetics of solar coronal mass ejections. *Astron. Astrophys.* **467**(2), 685. DOI. ADS. (Cited on pages 61 and 133.)

Subramanian, P., Lara, A., Borgazzi, A.: 2012, Can solar wind viscous drag account for coronal mass ejection deceleration? *Geophys. Res. Lett.* **39**, L19107. DOI. ADS. (Cited on page 51.)

Subramanian, S., Madjarska, M.S., Doyle, J.G.: 2010, Coronal hole boundaries evolution at small scales. II. XRT view. Can small-scale outflows at CHBs be a source of the slow solar wind. *Astron. Astrophys.* **516**, A50. DOI. ADS. (Cited on page 21.)

Suess, H.E.: 1980, The Radiocarbon Record in Tree Rings of the Last 8000 Years. *Radiocarbon* **22**(2), 200–209. DOI. (Cited on page 14.)

Temmer, M.: 2010, Statistical Properties of Flares and Sunspots over the Solar Cycle. In: Cranmer, S.R., Hoeksema, J.T., Kohl, J.L. (eds.) *SOHO-23: Understanding a Peculiar Solar Minimum*, *Astronomical Society of the Pacific Conference Series* **428**, 161. ADS. (Cited on pages 19 and 90.)

Temmer, M., Rollett, T., Möstl, C., Veronig, A.M., Vršnak, B., Odstrčil, D.: 2011, Influence of the Ambient Solar Wind Flow on the Propagation Behavior of Interplanetary Coronal Mass Ejections. *Astrophys. J.* **743**, 101. DOI. ADS. (Cited on pages 4 and 53.)

Temmer, M., Vršnak, B., Rollett, T., Bein, B., de Koning, C.A., Liu, Y., Bosman, E., Davies, J.A., Möstl, C., Žic, T., Veronig, A.M., Bothmer, V., Harrison, R., Nitta, N., Bisi, M., Flor, O., Eastwood, J., Odstrcil, D., Forsyth, R.: 2012, Characteristics of Kinematics of a Coronal Mass Ejection during the 2010 August 1 CME-CME Interaction Event. *Astrophys. J.* **749**, 57. DOI. ADS. (Cited on page 4.)

Thernisien, A.: 2011, Implementation of the Graduated Cylindrical Shell Model for the Three-dimensional Reconstruction of Coronal Mass Ejections. *Astrophys. J. Supp.* **194**, 33. DOI. ADS. (Cited on pages 58, 59, 60, and 89.)

Thernisien, A., Vourlidas, A., Howard, R.A.: 2009, Forward modeling of coronal mass ejections using stereo/secchi data. *Solar Physics* **256**(1), 111. DOI. ADS. (Cited on page 85.)

Thernisien, A.F.R., Howard, R.A., Vourlidas, A.: 2006, Modeling of Flux Rope Coronal Mass Ejections. *Astrophys. J.* **652**, 763. DOI. ADS. (Cited on pages 6, 53, 57, 58, 59, and 85.)

Tian, L., Liu, Y., Wang, H.: 2003, Latitude and Magnetic Flux Dependence of the Tilt Angle of Bipolar Regions. *Solar Phys.* **215**, 281. DOI. ADS. (Cited on page 35.)

Titov, V.S., Démoulin, P.: 1999, Basic topology of twisted magnetic configurations in solar flares. *Astron. Astrophys.* **351**, 707. ADS. (Cited on page 49.)

Tiwari, S.K., Falconer, D.A., Moore, R.L., Venkatakrishnan, P., Winebarger, A.R., Khazanov, I.G.: 2015, Near-sun speed of cmes and the magnetic nonpotentiality of their source active regions. *Geophysical Research Letters* **42**(14), 5702. DOI. https://agupubs.onlinelibrary.wiley.com/doi/abs/10.1002/2015GL064865. (Cited on pages 36 and 117.)

Török, T., Kliem, B.: 2005, Confined and Ejective Eruptions of Kink-unstable Flux Ropes. *Astrophys. J. Lett.* **630**, L97. DOI. ADS. (Cited on page 47.)

Tousey, R.: 1973, The solar corona. In: Rycroft, M.J., Runcorn, S.K. (eds.) *Space Research Conference*, *Space Research Conference* **2**, 713. ADS. (Cited on pages 3 and 26.)

Tousey, R., Howard, R.A., Koomen, M.J.: 1974, The Frequency and Nature of Coronal Transient Events Observed by OSO-7*. In: *Bulletin of the American Astronomical Society*, *Bul. of the Amer. Astron. Soc.* **6**, 295. ADS. (Cited on page 26.)

Tripathi, D., Bothmer, V., Cremades, H.: 2004a, The basic characteristics of EUV posteruptive arcades and their role as tracers of coronal mass ejection source regions. *Astron. Astrophys.* **422**, 337. DOI. ADS. (Cited on page 38.)

Tripathi, D., Bothmer, V., Cremades, H.: 2004b, The basic characteristics of EUV posteruptive arcades and their role as tracers of coronal mass ejection source regions. *Astron. Astrophys.* **422**, 337. DOI. ADS. (Cited on page 106.)

Tsuneta, S.: 1996, Structure and Dynamics of Magnetic Reconnection in a Solar Flare: Erratum. *Astrophys. J.* **464**, 1055. DOI. ADS. (Cited on page 42.)

Tsuneta, S.: 1997, Moving Plasmoid and Formation of the Neutral Sheet in a Solar Flare. *Astrophys. J.* **483**, 507. DOI. ADS. (Cited on page 42.)

Uchida, Y., Hirose, S., Cable, S., Uemura, S., Fujisaki, K., Torii, M., Morita, S.: 1998, MHD Simulation of Dark Filament Eruption in the Quadrupole Source Model. In: Webb, D.F., Schmieder, B., Rust, D.M. (eds.) *IAU Colloq. 167: New Perspectives on Solar Prominences*, *Astronomical Society of the Pacific Conference Series* **150**, 384. ADS. (Cited on page 43.)

Uchida, Y., Hirose, S., Morita, S., Torii, M., Tanaka, T., Yabiku, T., Miyagoshi, T., Uemura, S., Yamaguchi, T.: 1999, Observations of Flares and Active Regions from Yohkoh, and Magnetodynamic Models Explaining Them. *Astrophys. Space Sci.* **264**, 145. DOI. ADS. (Cited on page 43.)

van Ballegooijen, A.A., Martens, P.C.H.: 1989, Formation and eruption of solar prominences. *Astrophys. J.* **343**, 971. DOI. ADS. (Cited on page 37.)

van de Hulst, H.C.: 1950, The electron density of the solar corona. *Bull. Astro. Inst. of the Neth.* **11**, 135. ADS. (Cited on page 55.)

van Driel-Gesztelyi, L., Green, L.M.: 2015, Evolution of active regions. *Living Reviews in Solar Physics* **12**(1), 1. DOI. https://doi.org/10.1007/lrsp-2015-1. (Cited on pages 34, 35, 36, 37, and 38.)

Vanninathan, K., Madjarska, M.S., Galsgaard, K., Huang, Z., Doyle, J.G.: 2015, Active region upflows. I. Multi-instrument observations. *Astron. Astrophys.* **584**, A38. DOI. ADS. (Cited on page 21.)

Venkatakrishnan, P., Ravindra, B.: 2003, Relationship between cme velocity and active region magnetic energy. *Geophysical Research Letters* **30**(23). DOI. https://agupubs.onlinelibrary.wiley.com/doi/abs/10.1029/2003GL018100. (Cited on page 117.)

Venzmer, M.S., Bothmer, V.: 2018, Solar-wind predictions for the Parker Solar Probe orbit. Near-Sun extrapolations derived from an empirical solar-wind model based on Helios and OMNI observations. *Astron. Astrophys.* **611**, A36. DOI. ADS. (Cited on pages 23, 128, and 129.)

Verbeke, C., Mays, M.L., Temmer, M., Bingham, S., Steenburgh, R., Dumbović, M., Núñez, M., Jian, L.K., Hess, P., Wiegand, C., Taktakishvili, A., Andries, J.: Benchmarking cme arrival time and impact: Progress on metadata, metrics, and events. *Space Weather* **17**(1), 6. DOI. https://agupubs.onlinelibrary.wiley.com/doi/abs/10.1029/2018SW002046. (Cited on page 5.)

Verbeke, C., Mays, M.L., Taktakishvilli, A., Kuznetsova, M.: 2018, Defining metrics and tracking progress for predicting CME arrival and parameters at L1: Highlights from the International Forum on Space Weather Capabilities Assessment. In: *42nd COSPAR Scientific Assembly, COSPAR Meeting* **42**, PSW.1. ADS. (Cited on page 5.)

Vourlidas, A.: 2014, The flux rope nature of coronal mass ejections. *Plasma Phys. and Contr. F.* **56**(6), 064001. DOI. ADS. (Cited on page 27.)

Vourlidas, A., Howard, R.A.: 2006, The Proper Treatment of Coronal Mass Ejection Brightness: A New Methodology and Implications for Observations. *Astrophys. J.* **642**, 1216. DOI. ADS. (Cited on page 56.)

Vourlidas, A., Subramanian, P., Dere, K.P., Howard, R.A.: 2000, Large-Angle Spectrometric Coronagraph Measurements of the Energetics of Coronal Mass Ejections. *Astrophys. J.* **534**, 456. DOI. ADS. (Cited on pages 62 and 99.)

Vourlidas, A., Buzasi, D., Howard, R.A., Esfandiari, E.: 2002, Mass and energy properties of LASCO CMEs. In: Wilson, A. (ed.) *Solar Variability: From Core to Outer Frontiers, ESA Special Publication* **506**, 91. ADS. (Cited on page 27.)

Vourlidas, A., Howard, R.A., Esfandiari, E., Patsourakos, S., Yashiro, S., Michalek, G.: 2010, Comprehensive Analysis of Coronal Mass Ejection Mass and Energy Properties Over a Full Solar Cycle. *Astrophys. J.* **722**, 1522. DOI. ADS. (Cited on pages 25, 26, 61, 62, 77, 95, and 99.)

Vourlidas, A., Howard, R.A., Esfandiari, E., Patsourakos, S., Yashiro, S., Michalek, G.: 2011, Erratum: "Comprehensive Analysis of Coronal Mass Ejection Mass and Energy Properties Over a Full Solar Cycle" ¡A href="/abs/2010ApJ...722.1522V"¿(2010, ApJ, 722, 1522)¡/A¿. *Astrophys. J.* **730**, 59. DOI. ADS. (Cited on pages 26 and 99.)

Vourlidas, A., Lynch, B.J., Howard, R.A., Li, Y.: 2013, How Many CMEs Have Flux Ropes? Deciphering the Signatures of Shocks, Flux Ropes, and Prominences in Coronagraph Observations of CMEs. *Solar Phys.* **284**, 179. DOI. ADS. (Cited on pages 3, 27, and 28.)

Vourlidas, A., Balmaceda, L.A., Stenborg, G., Dal Lago, A.: 2017, Multi-viewpoint Coronal Mass Ejection Catalog Based on STEREO COR2 Observations. *Astrophys. J.* **838**, 141. DOI. ADS. (Cited on page 26.)

Vršnak, B.: 2006, Forces governing coronal mass ejections. *Advances in Space Research* **38**, 431. DOI. ADS. (Cited on page 52.)

Vršnak, B., Žic, T., Falkenberg, T.V., Möstl, C., Vennerstrom, S., Vrbanec, D.: 2010, The role of aerodynamic drag in propagation of interplanetary coronal mass ejections. *Astron. Astrophys.* **512**, A43. DOI. ADS. (Cited on page 50.)

Vršnak, B., Žic, T., Vrbanec, D., Temmer, M., Rollett, T., Möstl, C., Veronig, A., Čalogović, J., Dumbović, M., Lulić, S., Moon, Y.-J., Shanmugaraju, A.: 2013, Propagation of Interplanetary Coronal Mass Ejections: The Drag-Based Model. *Solar Phys.* **285**, 295. DOI. ADS. (Cited on pages 4, 53, 120, and 121.)

Vršnak, B., Temmer, M., Žic, T., Taktakishvili, A., Dumbović, M., Möstl, C., Veronig, A.M., Mays, M.L., Odstrčil, D.: 2014, Heliospheric Propagation of Coronal Mass Ejections: Comparison of Numerical WSA-ENLIL+Cone Model and Analytical Drag-based Model. *ApJS* **213**, 21. DOI. ADS. (Cited on page 4.)

Žic, T., Vršnak, B., Temmer, M.: 2015, Heliospheric Propagation of Coronal Mass Ejections: Drag-based Model Fitting. *ApJS* **218**(2), 32. DOI. ADS. (Cited on page 80.)

Wang, D., Liu, R., Wang, Y., Liu, K., Chen, J., Liu, J., Zhou, Z., Zhang, M.: 2017, Critical Height of the Torus Instability in Two-ribbon Solar Flares. *Astrophys. J. Lett.* **843**(1), L9. DOI. ADS. (Cited on page 137.)

Wang, J., Hoeksema, J.T., Liu, S.: 2019, On Deflection of Solar Coronal Mass Ejections by the Ambient Coronal Magnetic Field Configuration. *arXiv e-prints*, arXiv:1909.06410. ADS. (Cited on page 90.)

Wang, Y.-M.: 2001, On the relationship between he ii 304 prominences and the photospheric magnetic field. *The Astrophysical Journal* **560**(1), 456. http://stacks.iop.org/0004-637X/560/i=1/a=456. (Cited on page 36.)

Wang, Y.-M., Sheeley, N.R. Jr.: 1989, Average properties of bipolar magnetic regions during sunspot cycle 21. *Solar Phys.* **124**, 81. DOI. ADS. (Cited on page 35.)

Wang, Y.-M., Sheeley, N.R. Jr.: 1990, Solar wind speed and coronal flux-tube expansion. *Astrophys. J.* **355**, 726. DOI. ADS. (Cited on page 21.)

Wang, Y.-M., Sheeley, N.R. Jr.: 1991, Magnetic flux transport and the sun's dipole moment - New twists to the Babcock-Leighton model. *Astrophys. J.* **375**, 761. DOI. ADS. (Cited on page 35.)

Wang, Y.-M., Sheeley, N.R. Jr., Walters, J.H., Brueckner, G.E., Howard, R.A., Michels, D.J., Lamy, P.L., Schwenn, R., Simnett, G.M.: 1998, Origin of Streamer Material in the Outer Corona. *Astrophys. J. Lett.* **498**, L165. DOI. ADS. (Cited on page 21.)

Wang, Y., Shen, C., Wang, S., Ye, P.: 2004, Deflection of coronal mass ejection in the interplanetary medium. *Solar Phys.* **222**(2), 329. DOI. ADS. (Cited on page 90.)

Wang, Y., Chen, C., Gui, B., Shen, C., Ye, P., Wang, S.: 2011, Statistical study of coronal mass ejection source locations: Understanding CMEs viewed in coronagraphs. *Journal of Geophysical Research (Space Physics)* **116**(A4), A04104. DOI. ADS. (Cited on page 93.)

Webb, D.F., Howard, T.A.: 2012, Coronal Mass Ejections: Observations. *Living Rev. in Solar Phys.* **9**, 3. DOI. ADS. (Cited on pages 3, 25, 26, 33, 42, and 52.)

Webb, D.F., Hundhausen, A.J.: 1987, Activity associated with the solar origin of coronal mass ejections. *Solar Phys.* **108**, 383. DOI. ADS. (Cited on pages 25 and 33.)

Welsch, B.T.: 2018, Flux Accretion and Coronal Mass Ejection Dynamics. *Solar Phys.* **293**, 113. DOI. ADS. (Cited on page 47.)

Wiegelmann, T., Sakurai, T.: 2012, Solar Force-free Magnetic Fields. *Living Reviews in Solar Physics* **9**(1), 5. DOI. ADS. (Cited on page 47.)

Wiegelmann, T., Neukirch, T., Nickeler, D.H., Solanki, S.K., Martínez Pillet, V., Borrero, J.M.: 2015, Magneto-static Modeling of the Mixed Plasma Beta Solar Atmosphere Based on Sunrise/IMaX Data. *Astrophys. J.* **815**(1), 10. DOI. ADS. (Cited on page 47.)

Wild, J.P.: 1950, Observations of the Spectrum of High-Intensity Solar Radiation at Metre Wavelengths. III. Isolated Bursts. *Australian Journal of Scientific Research A Physical Sciences* **3**, 541. DOI. ADS. (Cited on page 29.)

Wild, J.P., Smerd, S.F., Weiss, A.A.: 1963, Solar Bursts. *Annual Review of Astronomy and Astrophysics* **1**, 291. DOI. ADS. (Cited on page 29.)

Wolf, R.: 1856, Mittheilungen über die Sonnenflecken I. *Astronomische Mitteilungen der Eidgenössischen Sternwarte Zurich* **1**, 3. ADS. (Cited on page 14.)

Woods, T.N., Eparvier, F.G., Hock, R., Jones, A.R., Woodraska, D., Judge, D., Didkovsky, L., Lean, J., Mariska, J., Warren, H., McMullin, D., Chamberlin, P., Berthiaume, G., Bailey, S., Fuller-Rowell, T., Sojka, J., Tobiska, W.K., Viereck, R.: 2012, Extreme Ultraviolet Variability Experiment (EVE) on the Solar Dynamics Observatory (SDO): Overview of Science Objectives, Instrument Design, Data Products, and Model Developments. *Solar Phys.* **275**, 115. DOI. ADS. (Cited on page 69.)

Xie, H., Ofman, L., Lawrence, G.: 2004, Cone model for halo CMEs: Application to space weather forecasting. *Journal of Geophysical Research (Space Physics)* **109**, A03109. DOI. ADS. (Cited on page 59.)

Yashiro, S., Gopalswamy, N., Michalek, G., St. Cyr, O.C., Plunkett, S.P., Rich, N.B., Howard, R.A.: 2004, A catalog of white light coronal mass ejections observed by the soho spacecraft. *Journal of Geophysical Research: Space Physics* **109**(A7). DOI. (Cited on page 27.)

Yurchyshyn, V., Yashiro, S., Abramenko, V., Wang, H., Gopalswamy, N.: 2005, Statistical Distributions of Speeds of Coronal Mass Ejections. *Astrophys. J.* **619**(1), 599. DOI. ADS. (Cited on page 93.)

Zank, G.P., Adhikari, L., Hunana, P., Shiota, D., Bruno, R., Telloni, D.: 2016, A Nearly Incompressible Description of Low-Frequency Turbulence in the Solar Wind. *AGU Fall Meeting Abstracts*, SH44A. ADS. (Cited on page 51.)

Zhang, J., Dere, K.P.: 2006, A Statistical Study of Main and Residual Accelerations of Coronal Mass Ejections. *Astrophys. J.* **649**, 1100. DOI. ADS. (Cited on page 52.)

Zhao, X.P., Plunkett, S.P., Liu, W.: 2002, Determination of geometrical and kinematical properties of halo coronal mass ejections using the cone model. *Journal of Geophysical Research (Space Physics)* **107**, 1223. DOI. ADS. (Cited on page 59.)

Zurbuchen, T.H., Richardson, I.G.: 2006, In-Situ Solar Wind and Magnetic Field Signatures of Interplanetary Coronal Mass Ejections. *Space Sci. Rev.* **123**(1-3), 31. DOI. ADS. (Cited on page 28.)

Zwaan, C.: 1987, Elements and patterns in the solar magnetic field. *Annual Review of Astronomy and Astrophysics* **25**, 83. DOI. ADS. (Cited on page 35.)

Appendix

A.1 Tables

Table A.1. Results of the DBM analysis. Variables from the Earth directed analysis are indicated with an E.

#	R_2	cv[%]	s	R_E^2	cv_E	s_E
1	0.995	2.70	0.94	0.999	0.67	0.30
2	0.998	2.49	1.13	0.992	1.44	0.66
3	0.999	1.35	0.25	0.996	2.32	0.58
4	0.999	0.46	0.21	0.997	3.07	1.18
5	0.997	2.41	1.15	0.998	1.85	0.84
6	0.995	2.97	1.44	0.992	3.52	1.80
7	0.999	0.50	0.21	1.000	0.65	0.17
8	0.999	0.84	0.37	0.999	0.58	0.23
9	0.999	1.18	0.72	0.995	3.63	2.13
10	0.992	4.29	2.40	1.000	0.82	0.53
11	0.999	1.53	0.88	0.998	1.37	0.63
12	0.999	1.61	1.24	0.999	1.30	0.81
13	0.998	1.53	0.71	0.999	1.43	0.51
14	0.999	0.68	0.39	0.999	1.78	0.54
15	0.999	1.17	0.65	0.999	1.41	0.74
16	0.999	1.54	0.77	0.999	2.14	1.14
17	0.998	1.94	1.01	0.999	1.83	0.91
18	0.999	0.60	0.34	1.000	0.57	0.34
19	0.999	1.02	0.77	0.997	1.80	1.12
20	0.999	0.78	0.49	0.998	1.79	1.09
21	0.999	1.42	0.52	0.999	1.51	0.55

A.2 Graphics

A.2.1 GCS Modelling Results

The following mosaics are selected observations from the image sequences used for GCS modelling. It should be noted that the single STEREO and SOHO observations from different perspectives are not always concurrent. Times are in UTC.

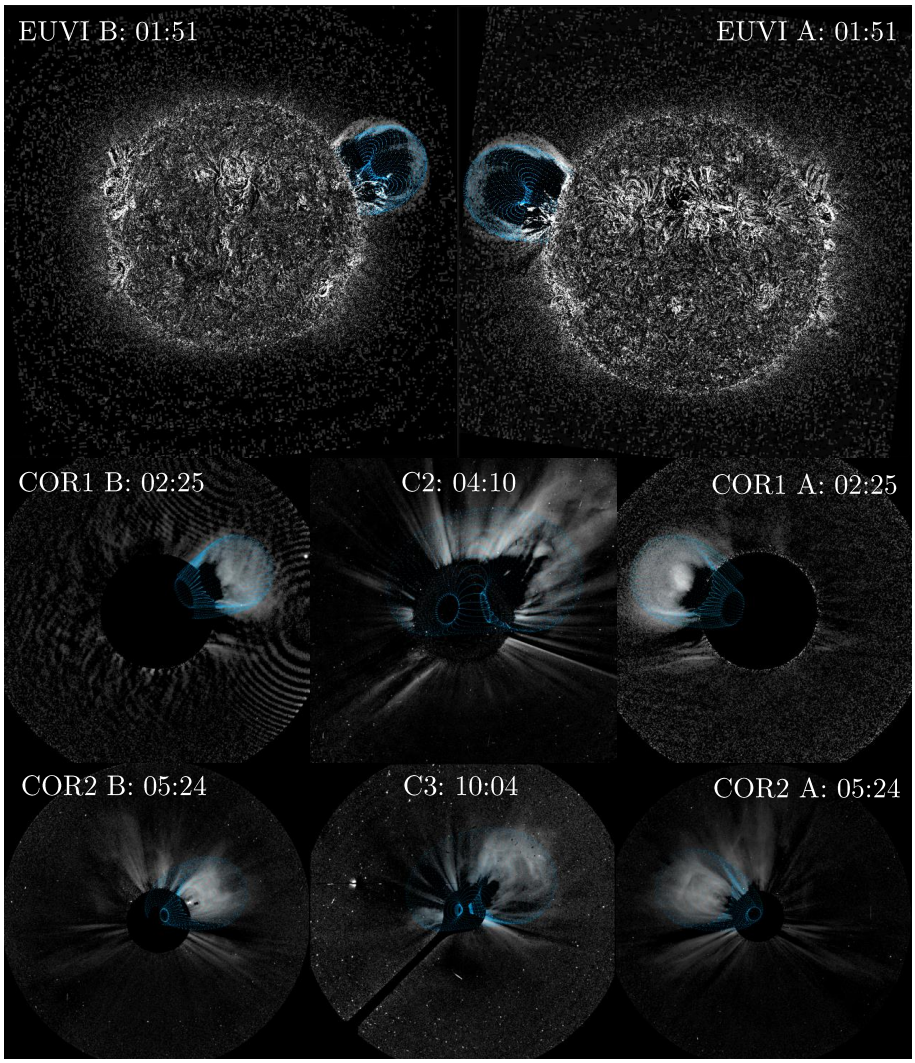

Figure (A.1) Same as Figure 5.1 for Event #3 at September 6, 2011.

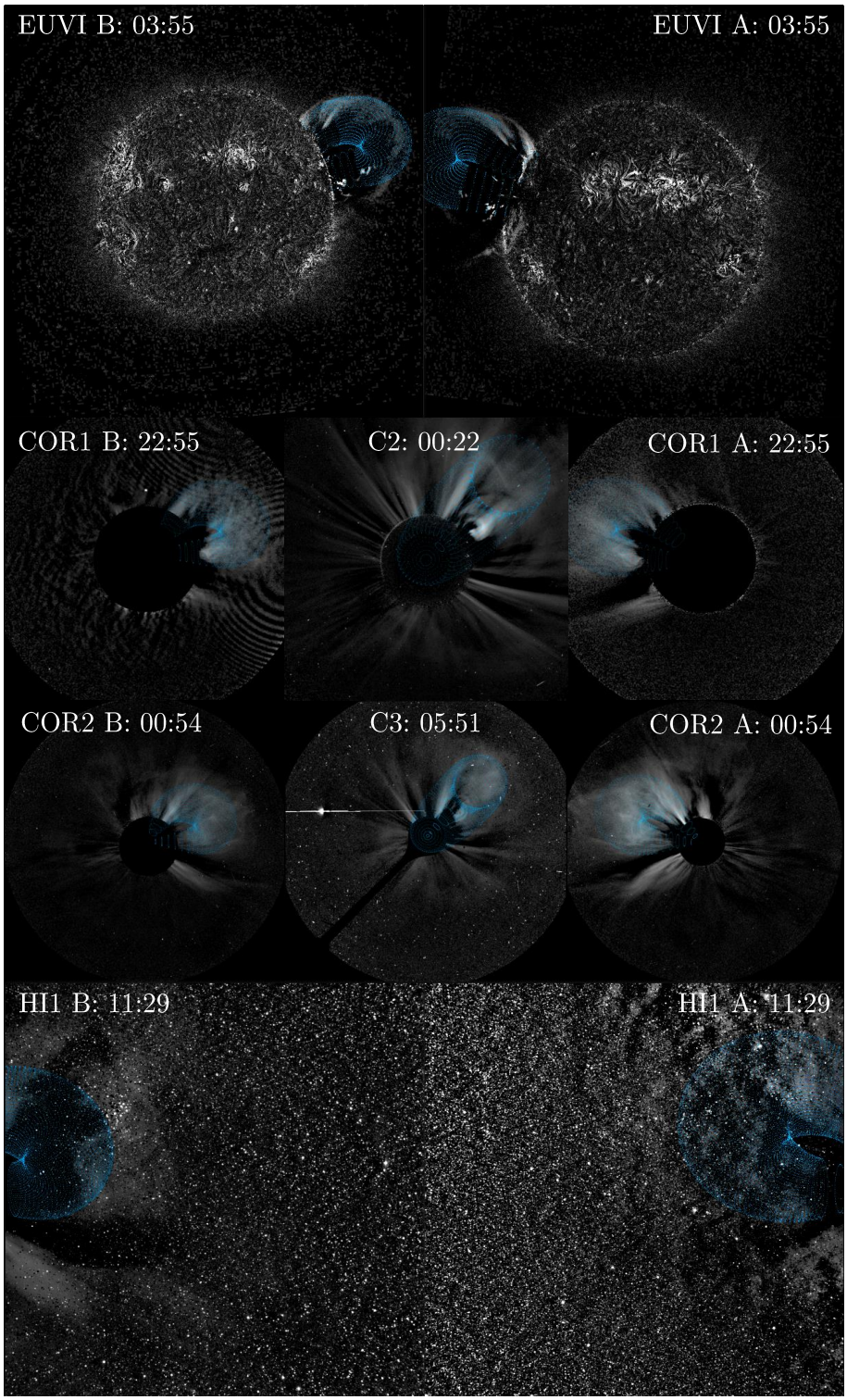

Figure (A.2) Same as Figure 5.1 for Event #4 at September 6, 2011.

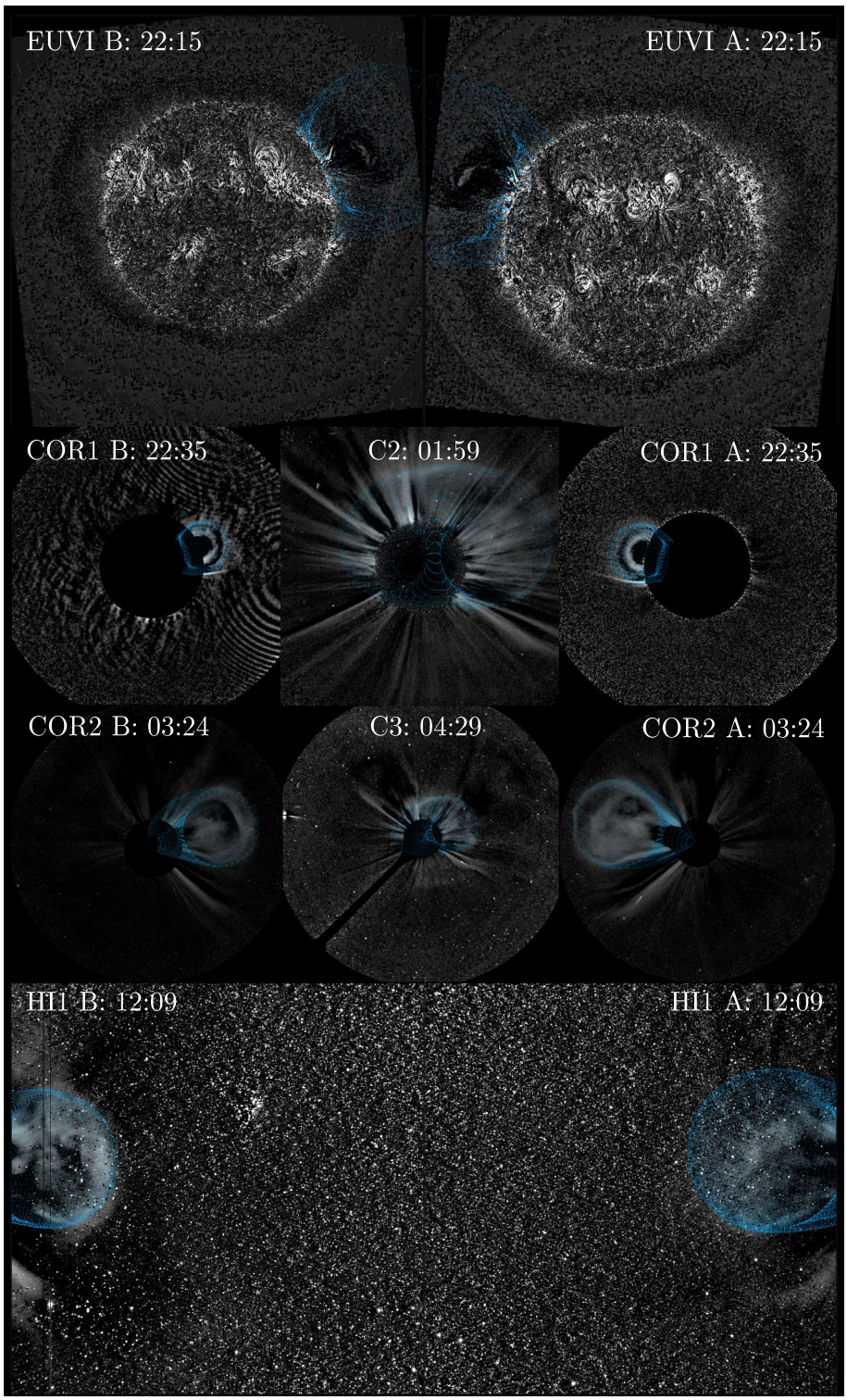

Figure (A.3) Same as Figure 5.1 for Event #5 at September 13, 2011.

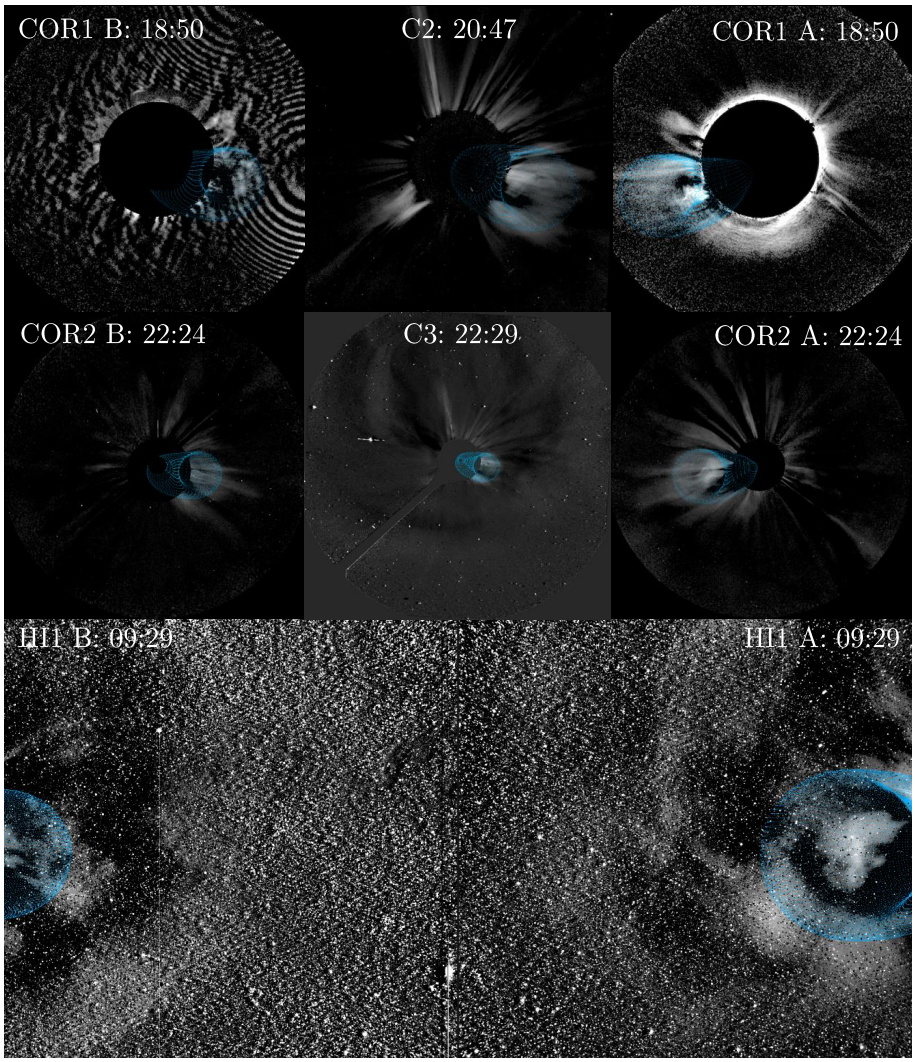

Figure (A.4) Same as Figure 5.1 for Event #6 at October 4, 2011.

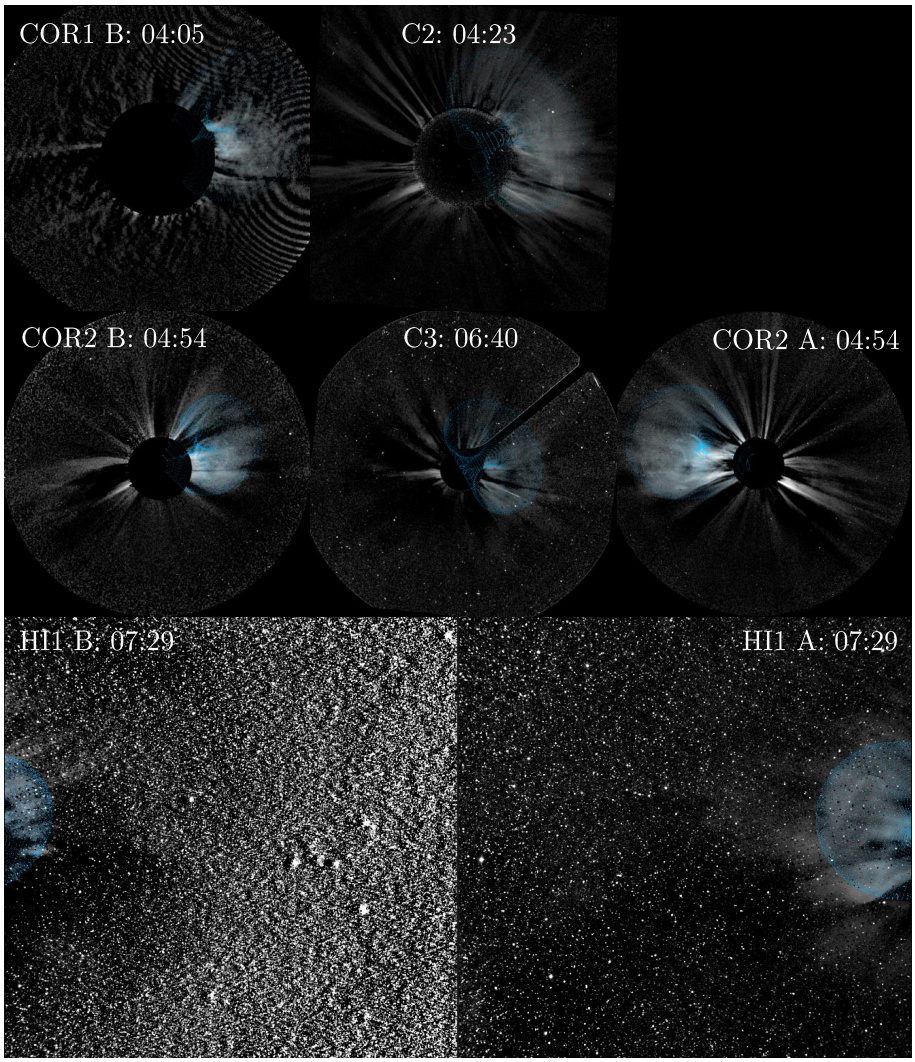

Figure (A.5) Same as Figure 5.1 for Event #7 at October 26, 2011.

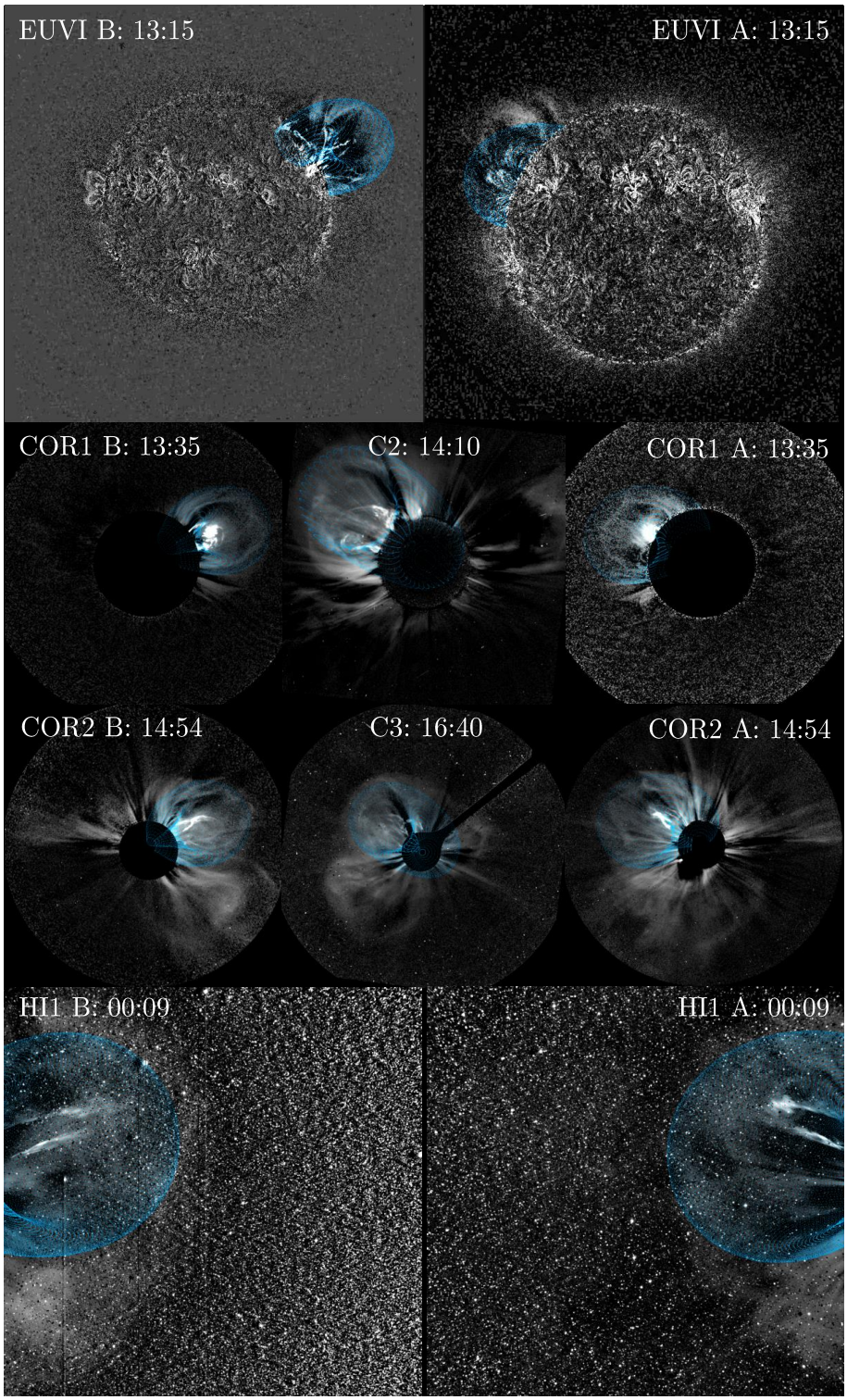

Figure (A.6) Same as Figure 5.1 for Event #8 at November 9, 2011.

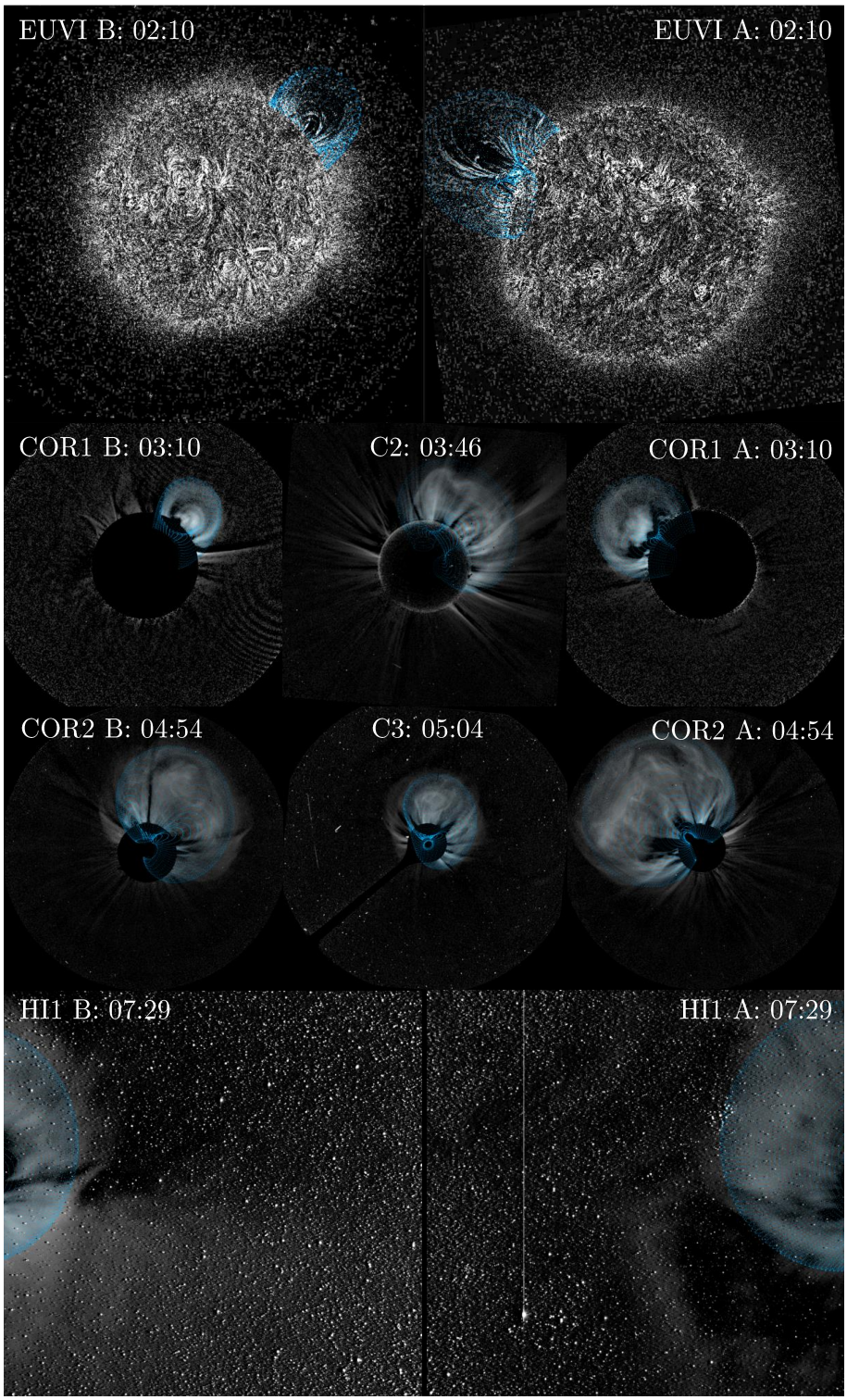

Figure (A.7) Same as Figure 5.1 for Event #9 at January 23, 2012.

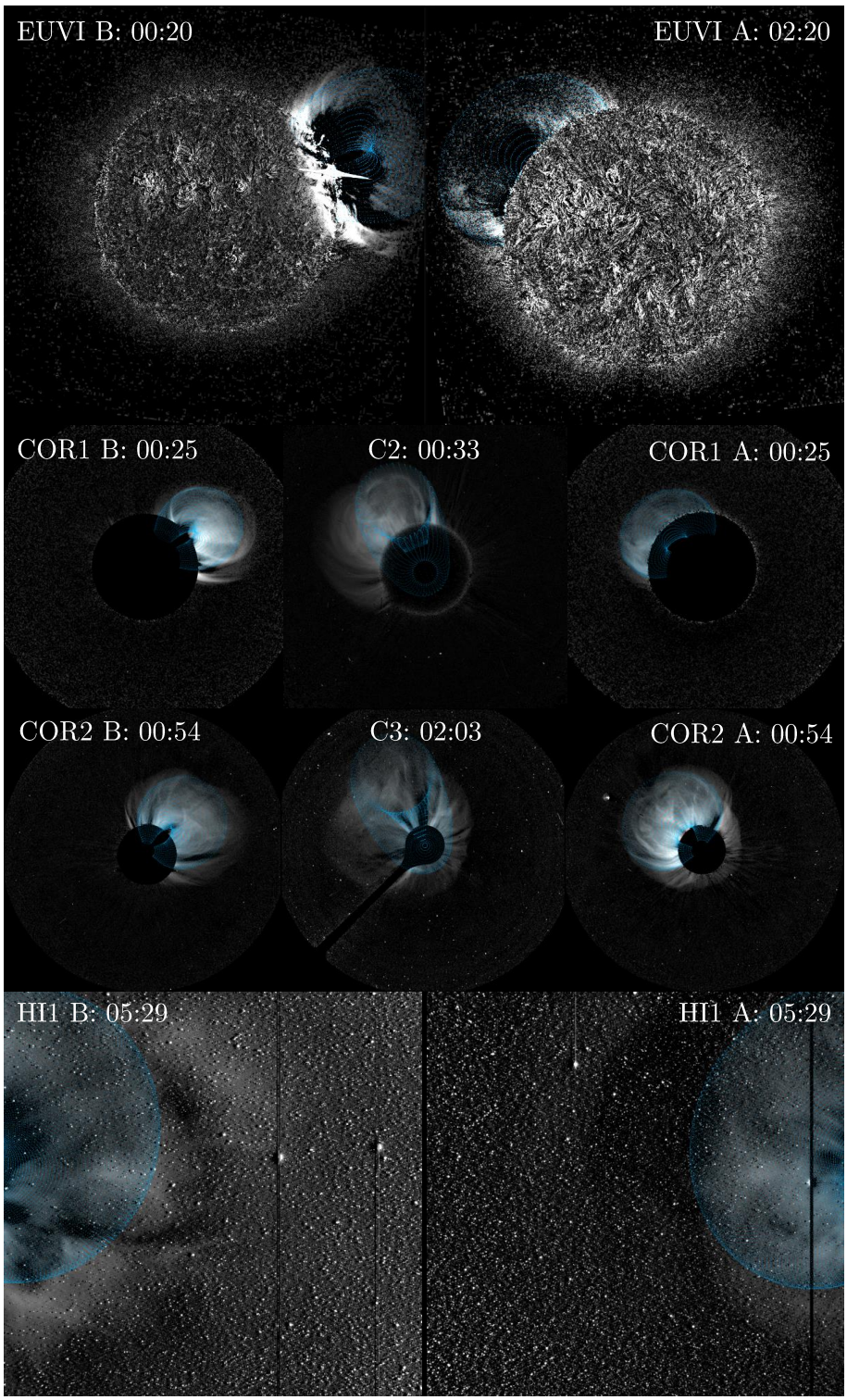

Figure (A.8) Same as Figure 5.1 for Event #10 at March 7, 2012.

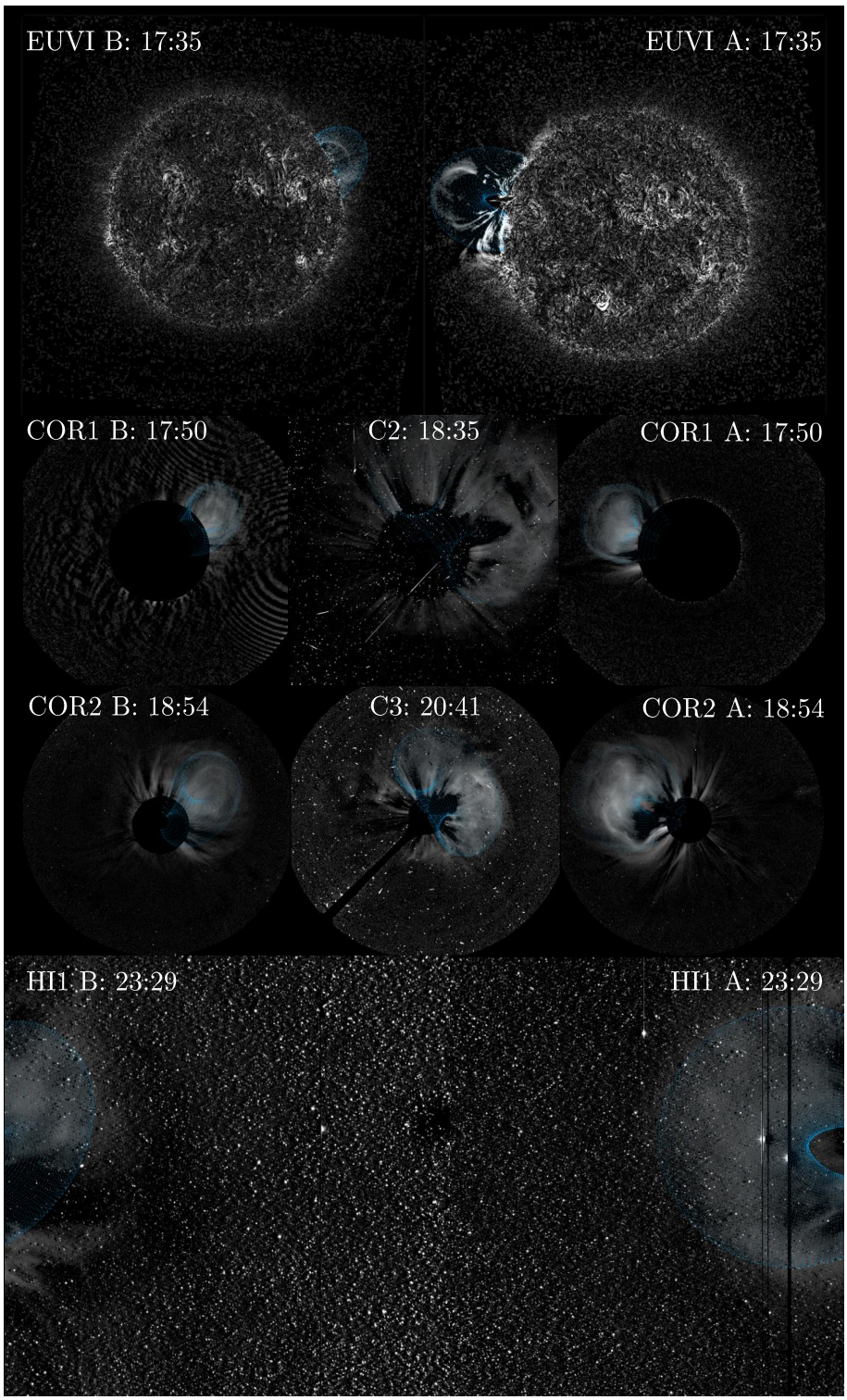

Figure (A.9) Same as Figure 5.1 for Event #11 at March 10, 2012.

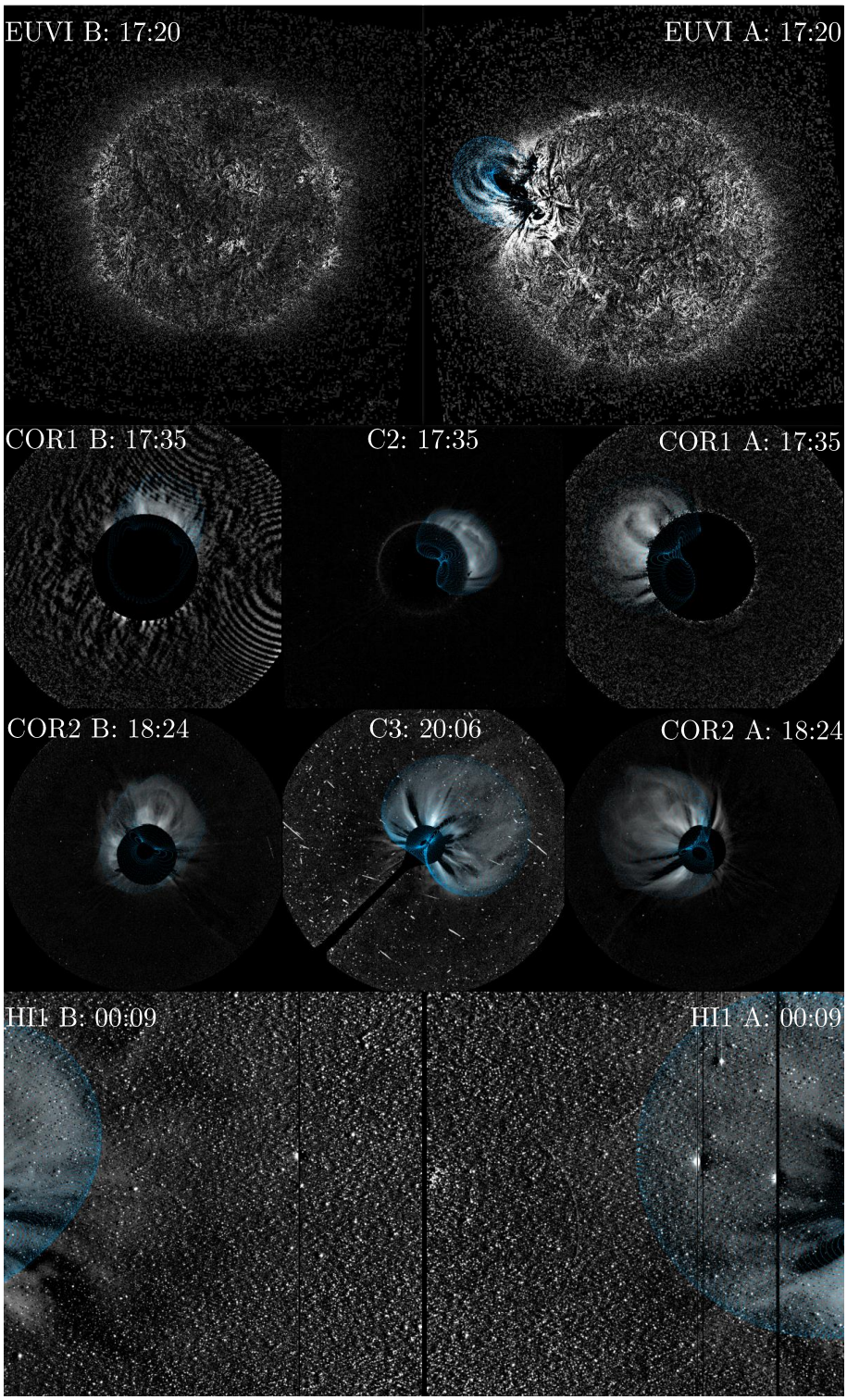

Figure (A.10) Same as Figure 5.1 for Event #12 at March 13, 2012.

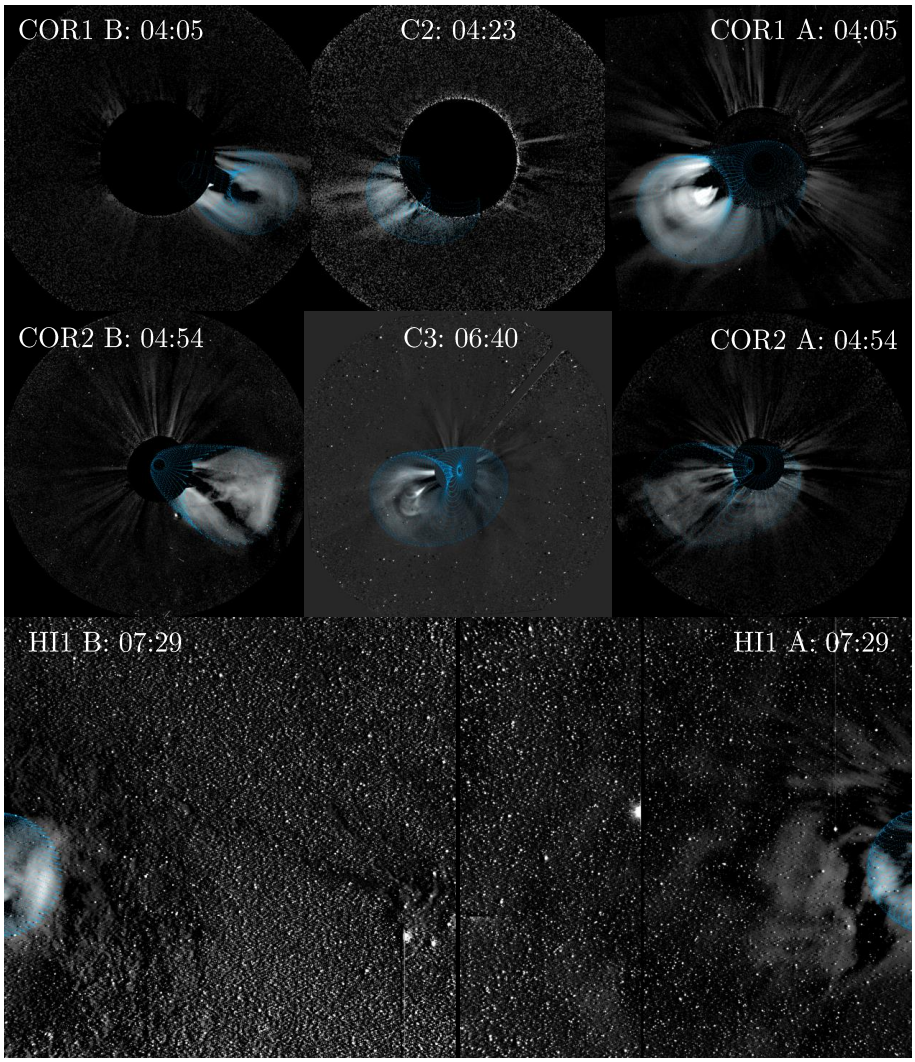

Figure (A.11) Same as Figure 5.1 for Event #13 at April 19, 2012.

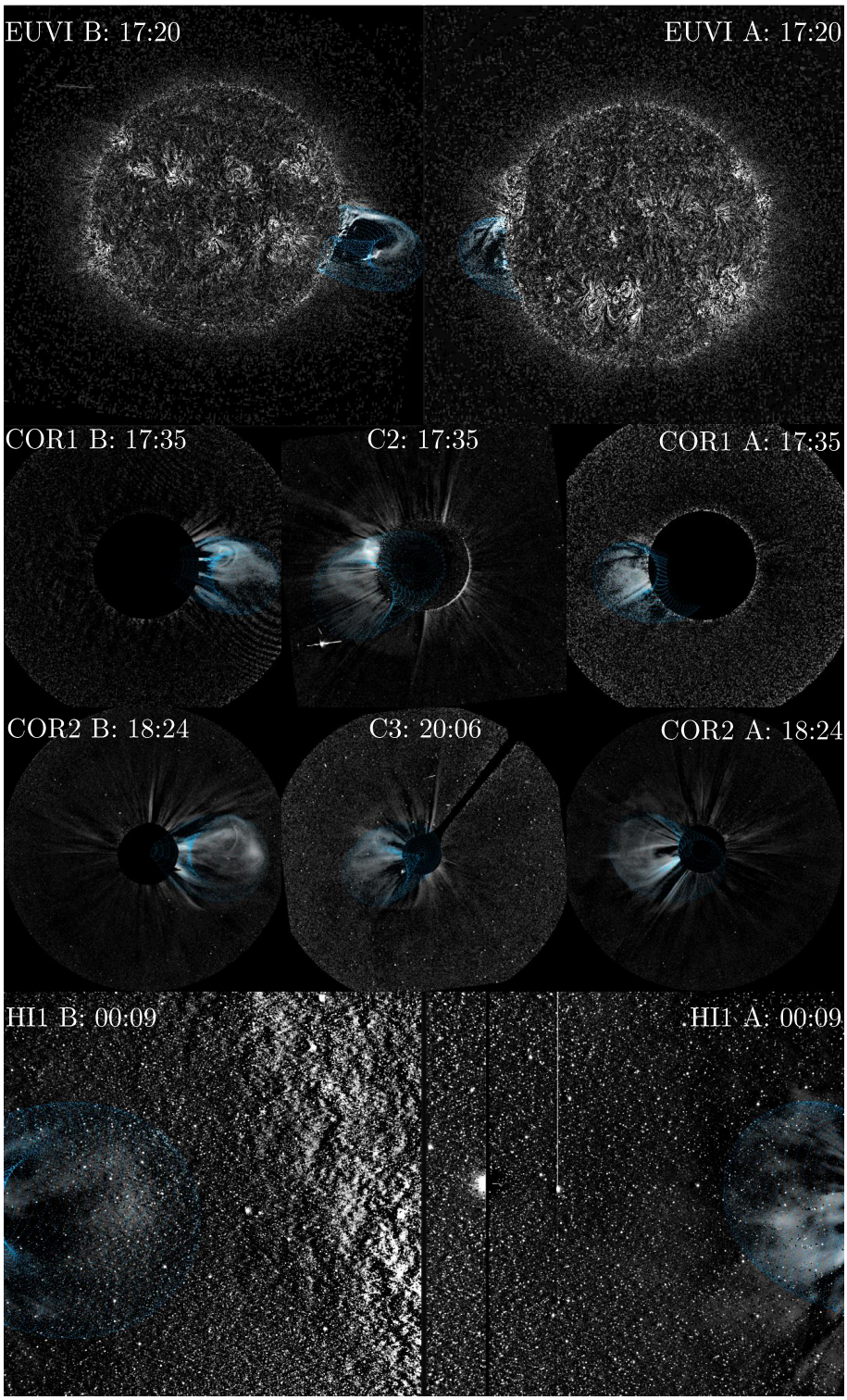

Figure (A.12) Same as Figure 5.1 for Event #14 at May 11, 2012.

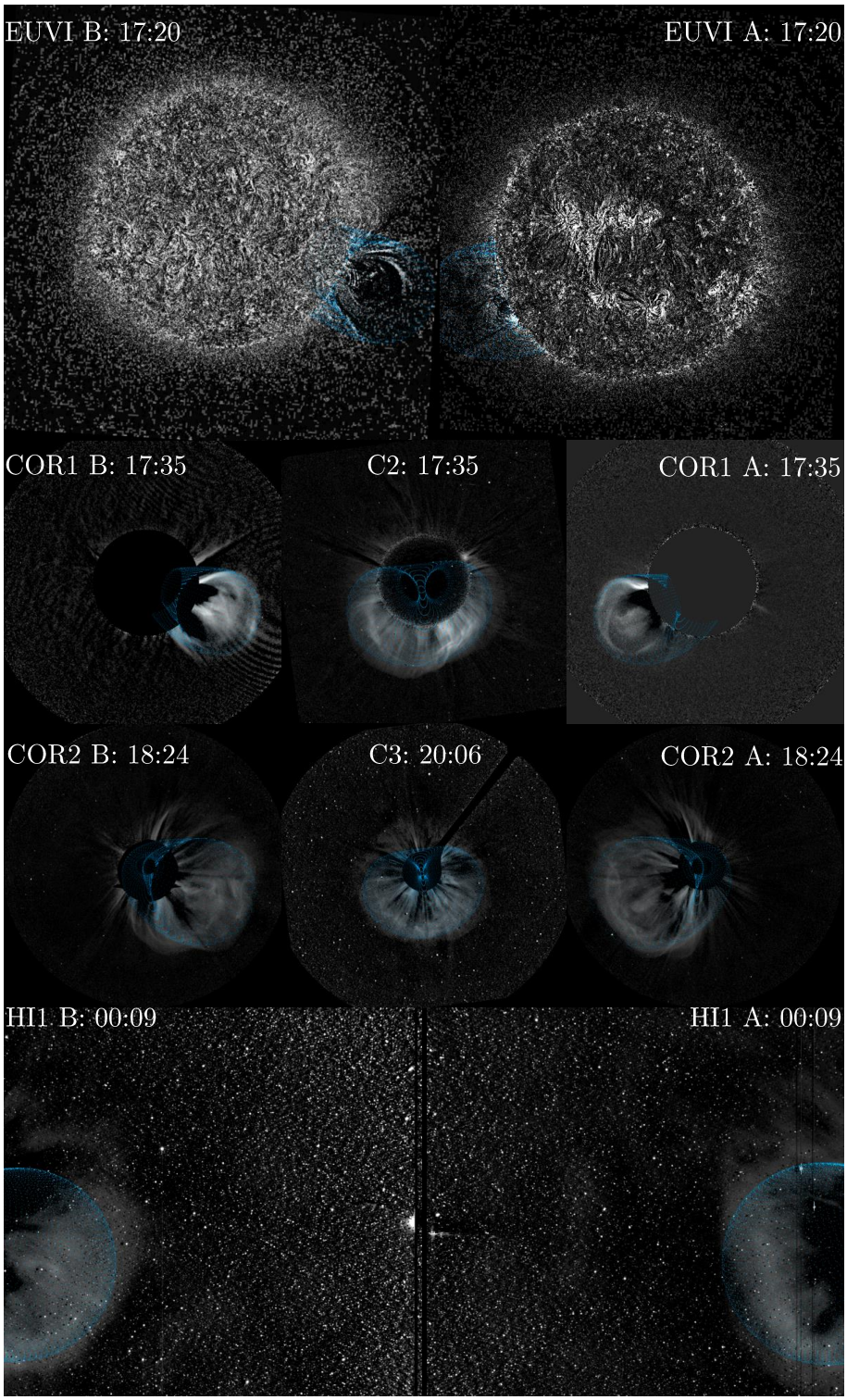

Figure (A.13) Same as Figure 5.1 for Event #15 at June 12, 2012.

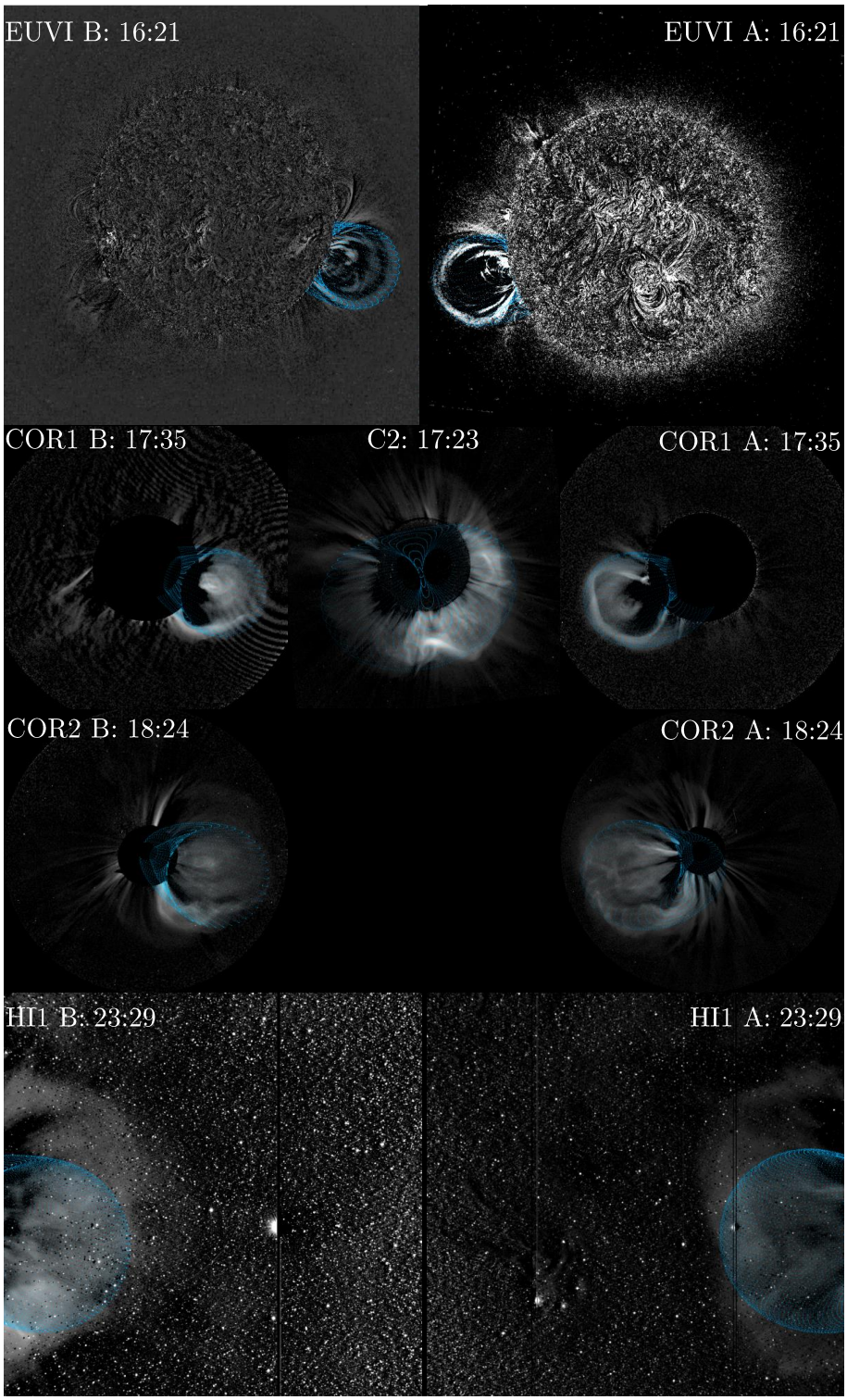

Figure (A.14) Same as Figure 5.1 for Event #16 at July 12, 2012.

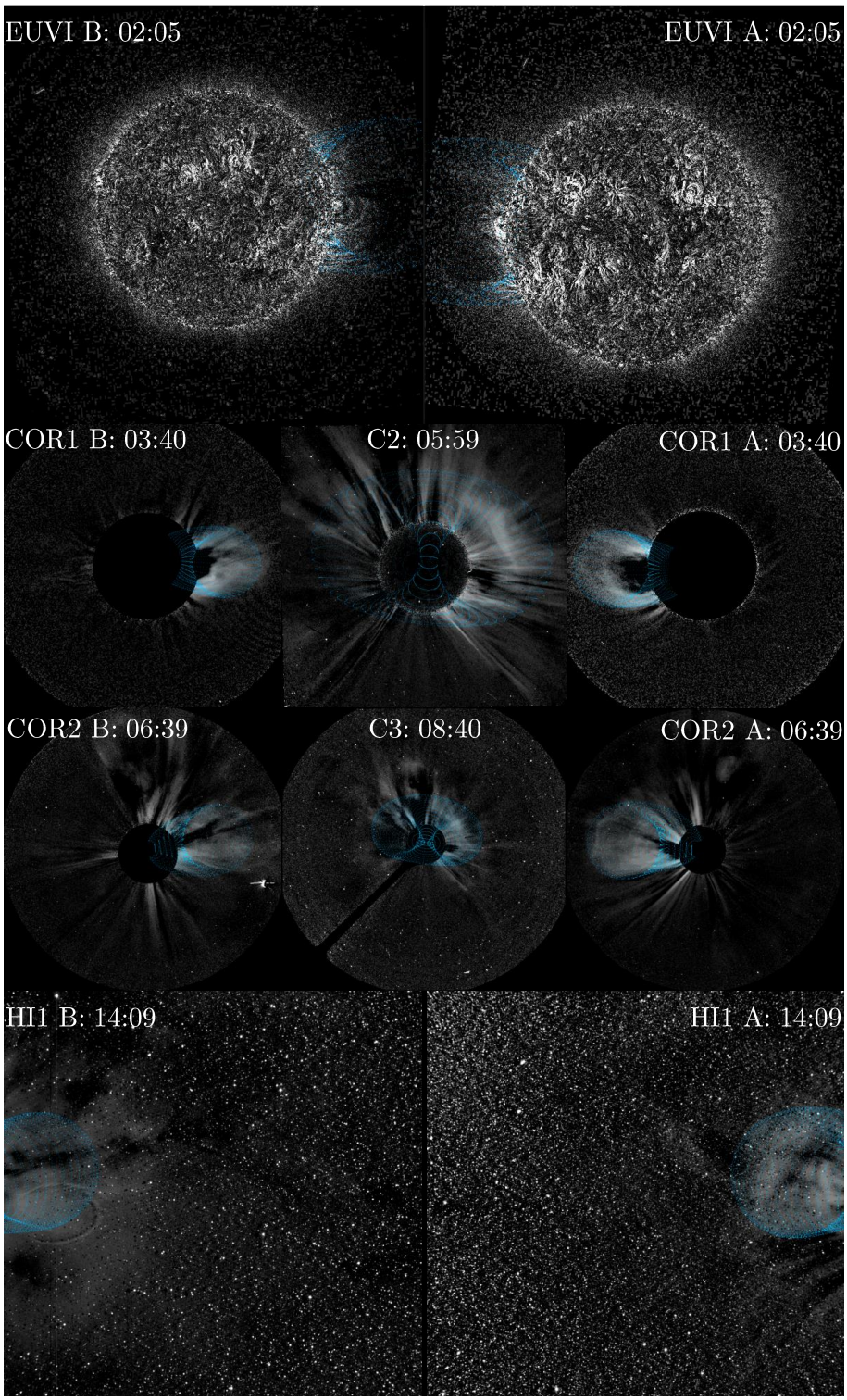

Figure (A.15) Same as Figure 5.1 for Event #17 at September 2, 2012.

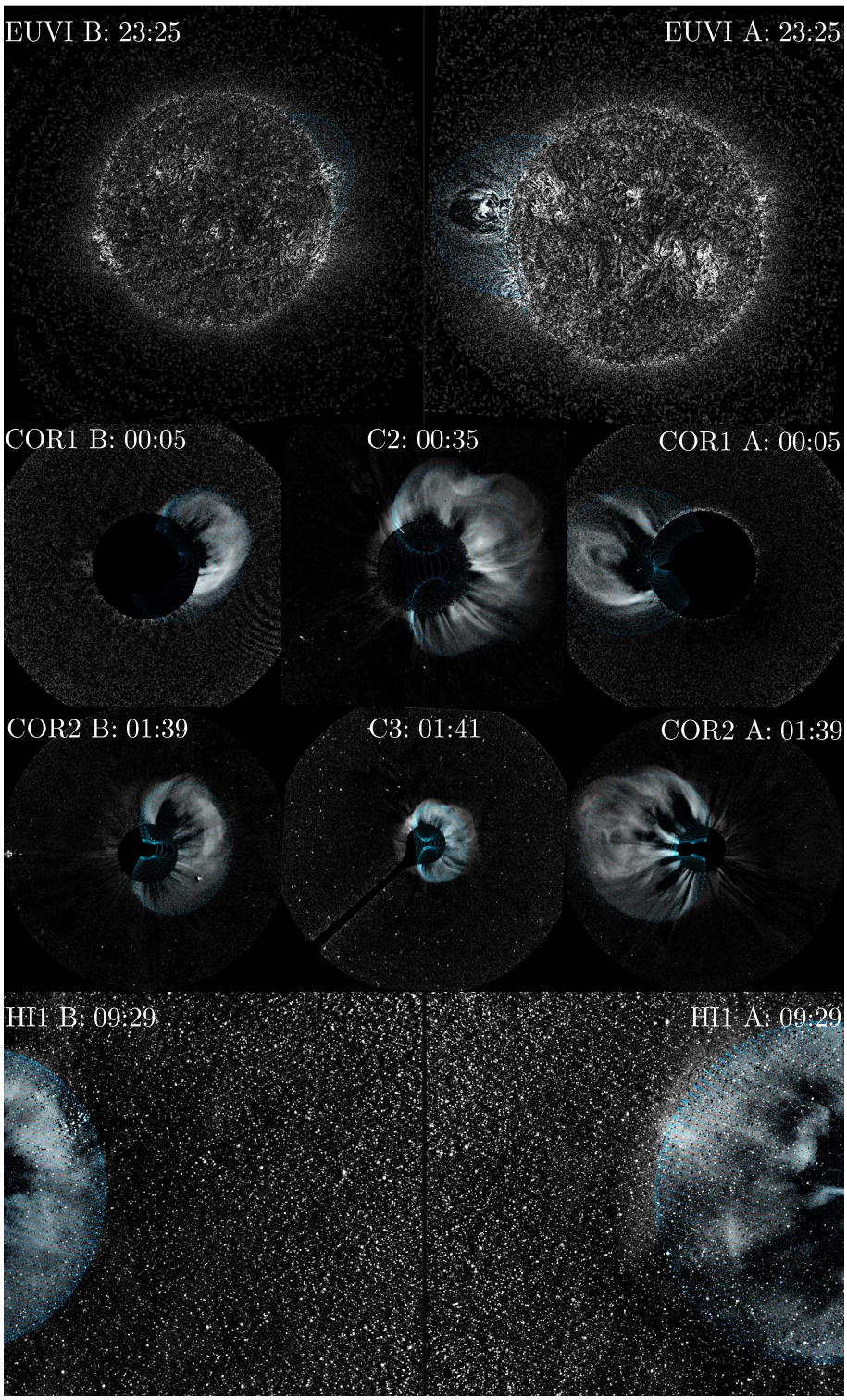

Figure (A.16) Same as Figure 5.1 for Event #18 at September 9, 2012.

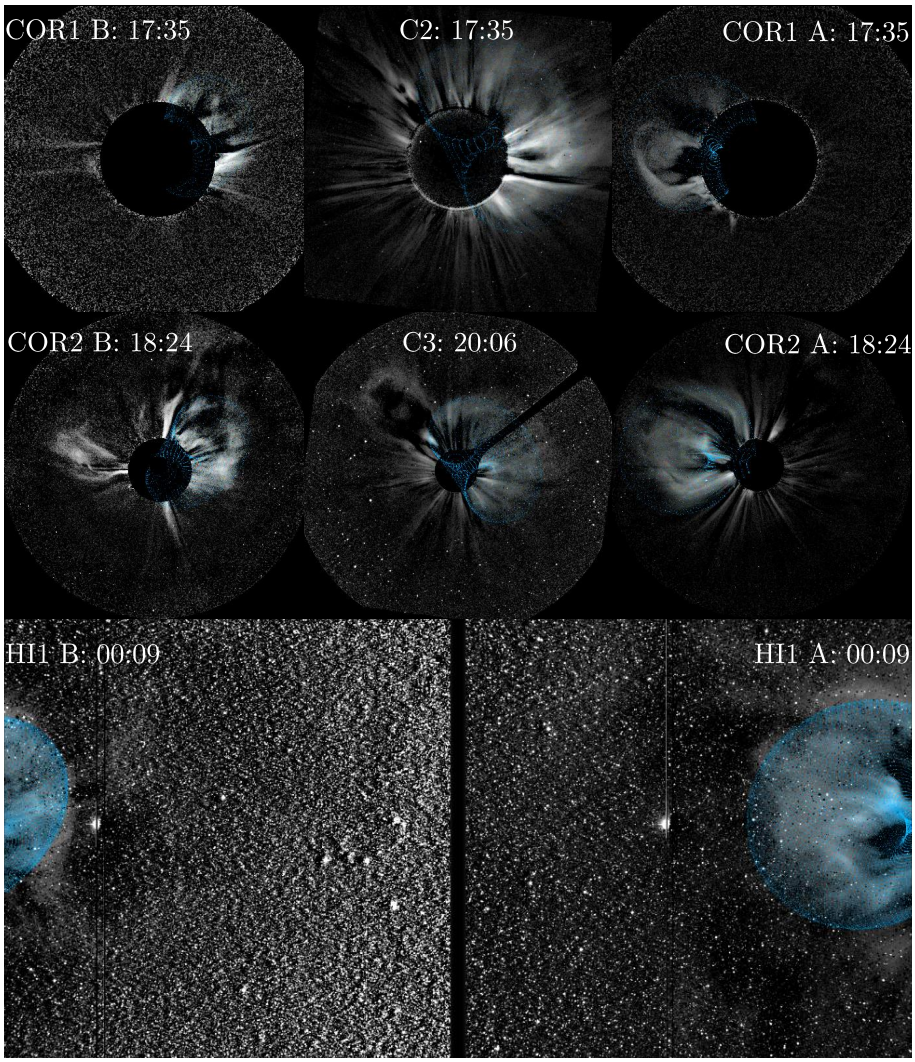

Figure (A.17) Same as Figure 5.1 for Event #19 at September 27, 2012.

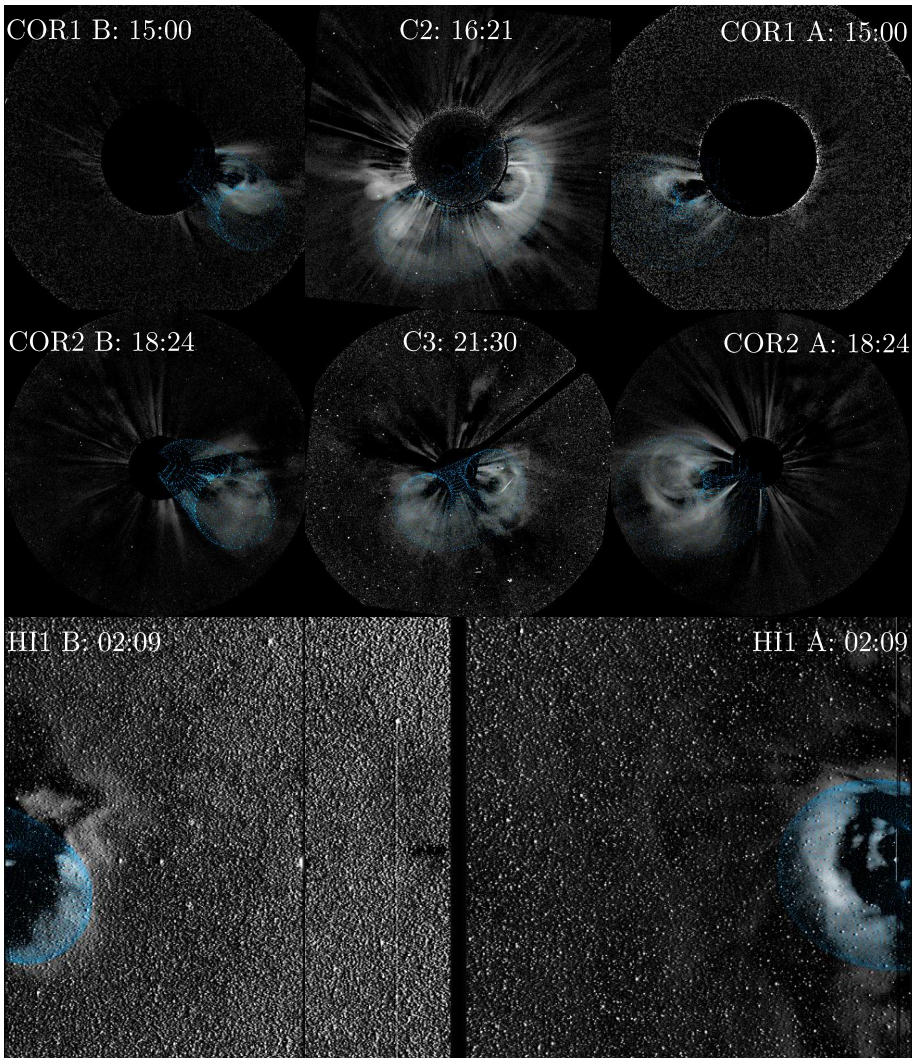

Figure (A.18) Same as Figure 5.1 for Event #19 at November 20, 2012.

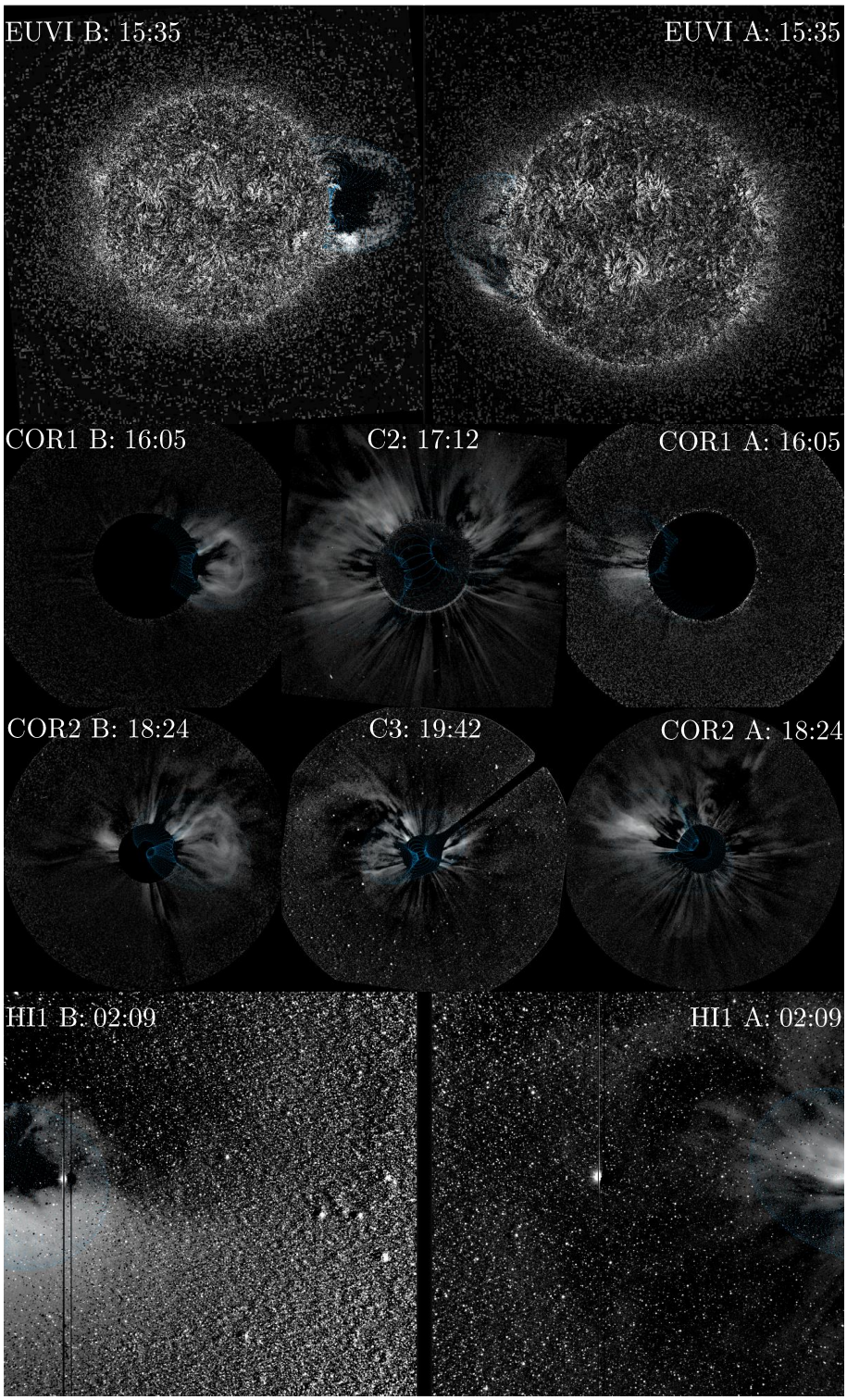

Figure (A.19) Same as Figure 5.1 for Event #19 at November 21, 2012.

A.2.2

A.2.2 GCS Geometries

All fitted GCS parameters are plotted versus the fitted solar distance r_{CME} for the events #3 to #21 in the Figures A.20 to A.21. For every GCS parameter evolution the height at which the parameter stays constant is labelled. The single errors, marked by the grey area, are listed in Table 5.1.

(a)

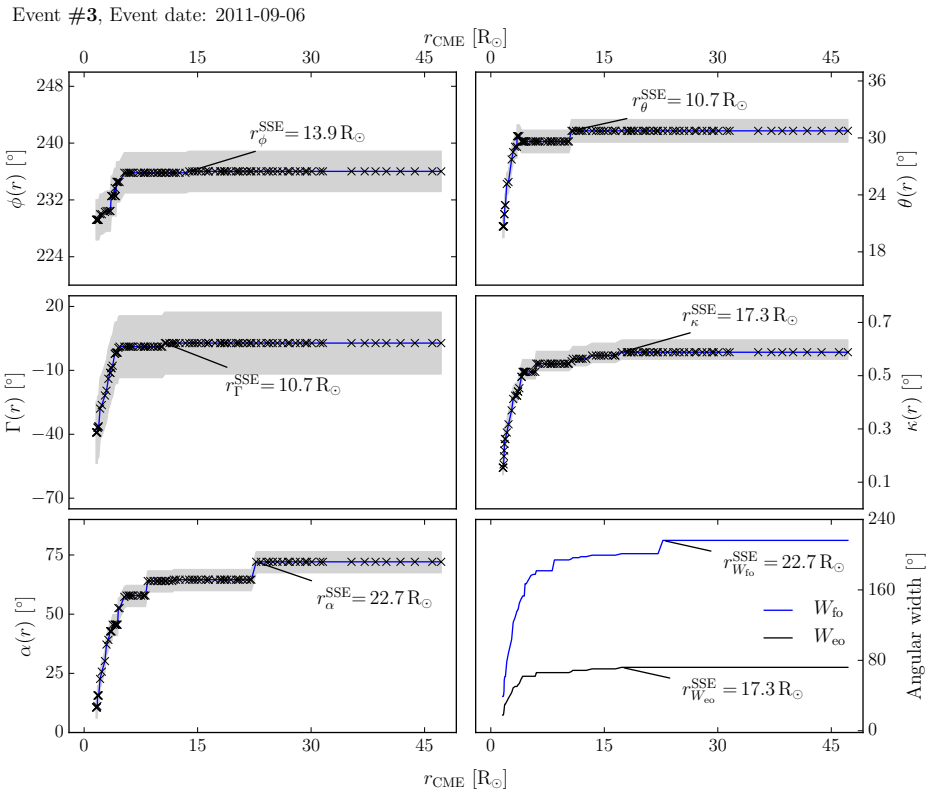

Figure (A.20) Geometrical results of the GCS modelling of event #3. Same colours and markers as in Figure 5.4.

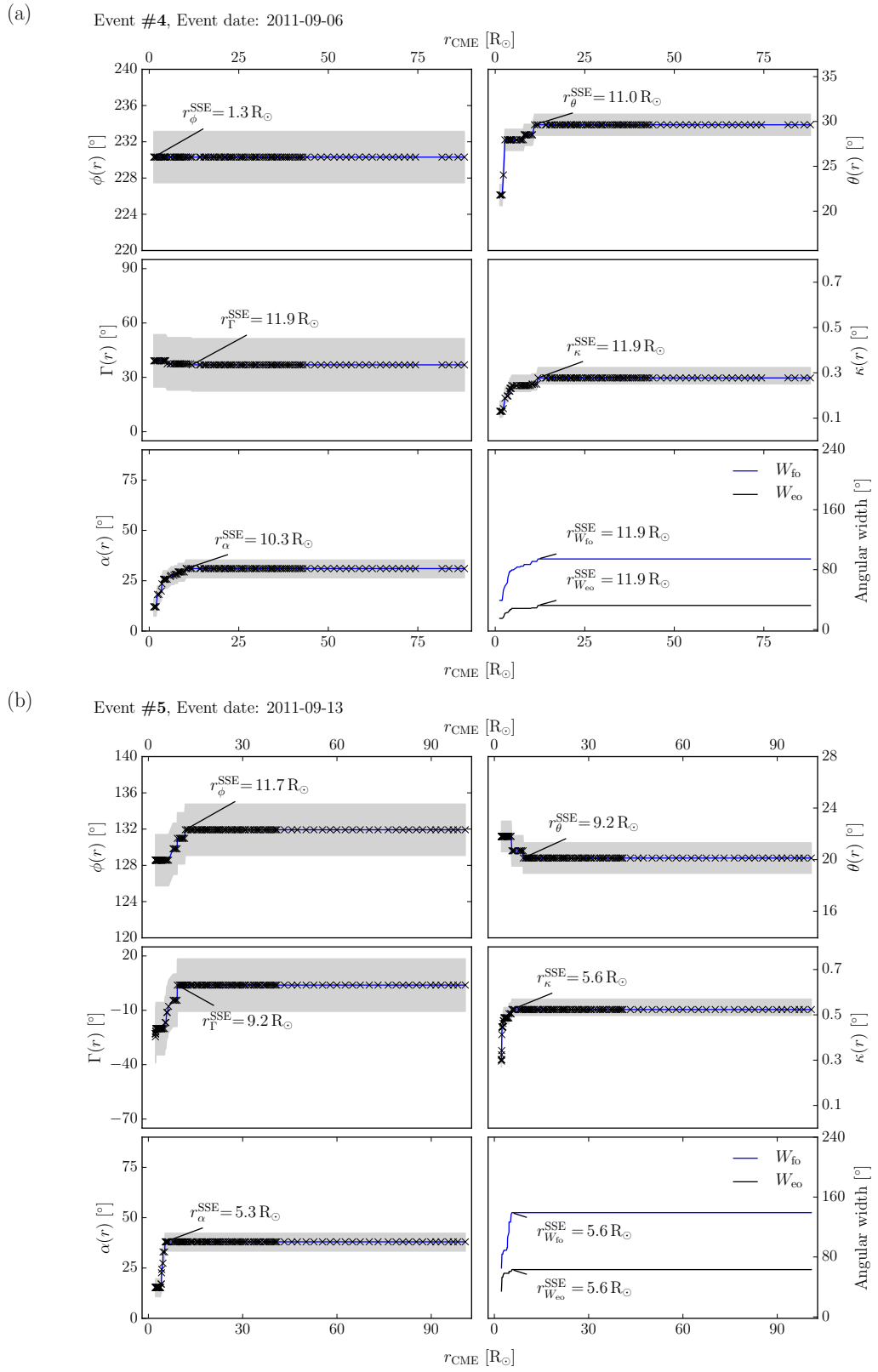

Figure (A.21) Geometrical results of the GCS modelling of the events #4 (a) and #5 (b). Same colours and markers as in Figure 5.4.

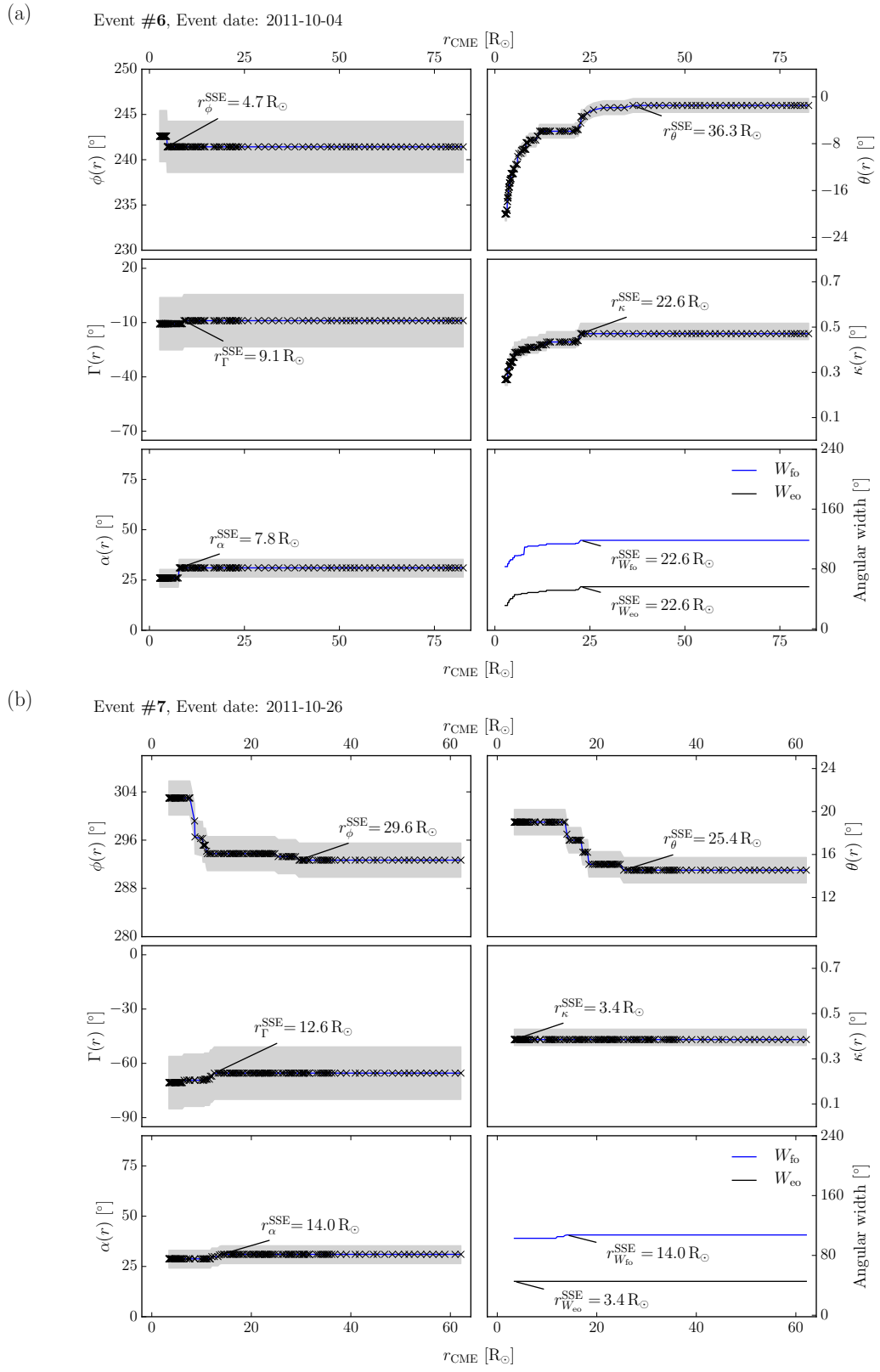

Figure (A.22) Geometrical results of the GCS modelling of the events #6 (a) and #7 (b). Same colours and markers as in Figure 5.4.

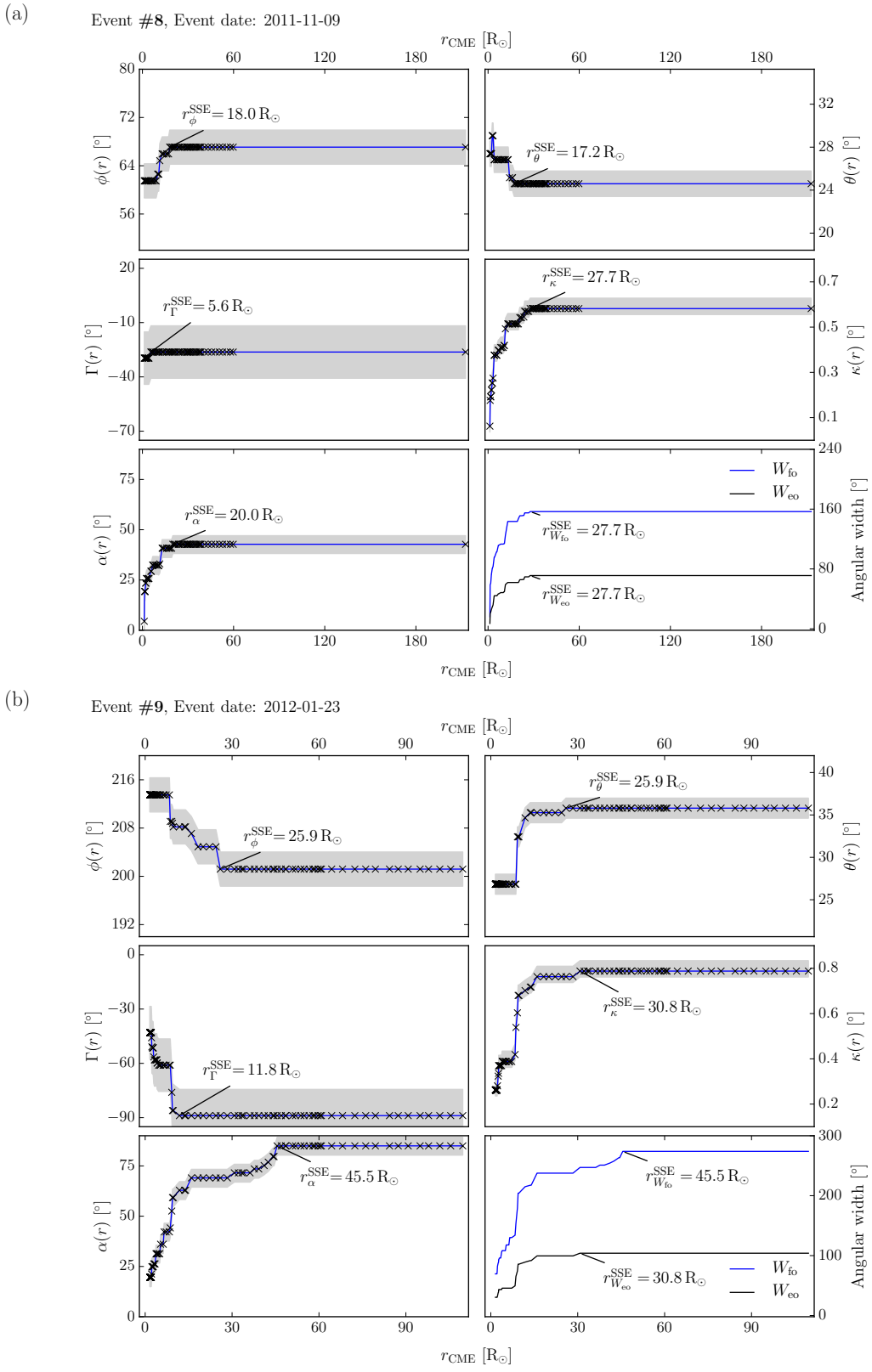

Figure (A.23) Geometrical results of the GCS modelling of the events #8 (a) and #9 (b). Same colours and markers as in Figure 5.4.

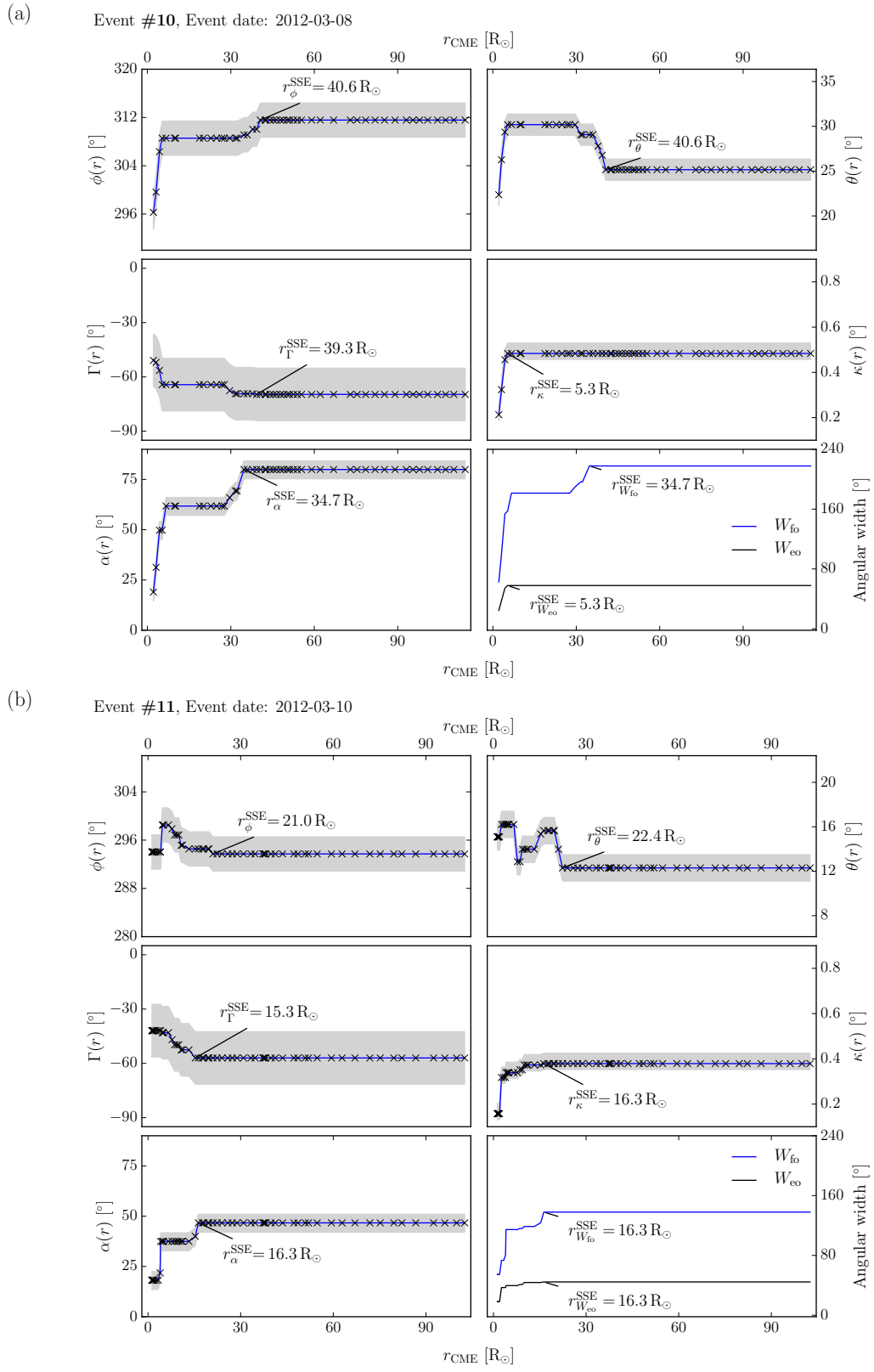

Figure (A.24) Geometrical results of the GCS modelling of the events #10 (a) and #11 (b). Same colours and markers as in Figure 5.4.

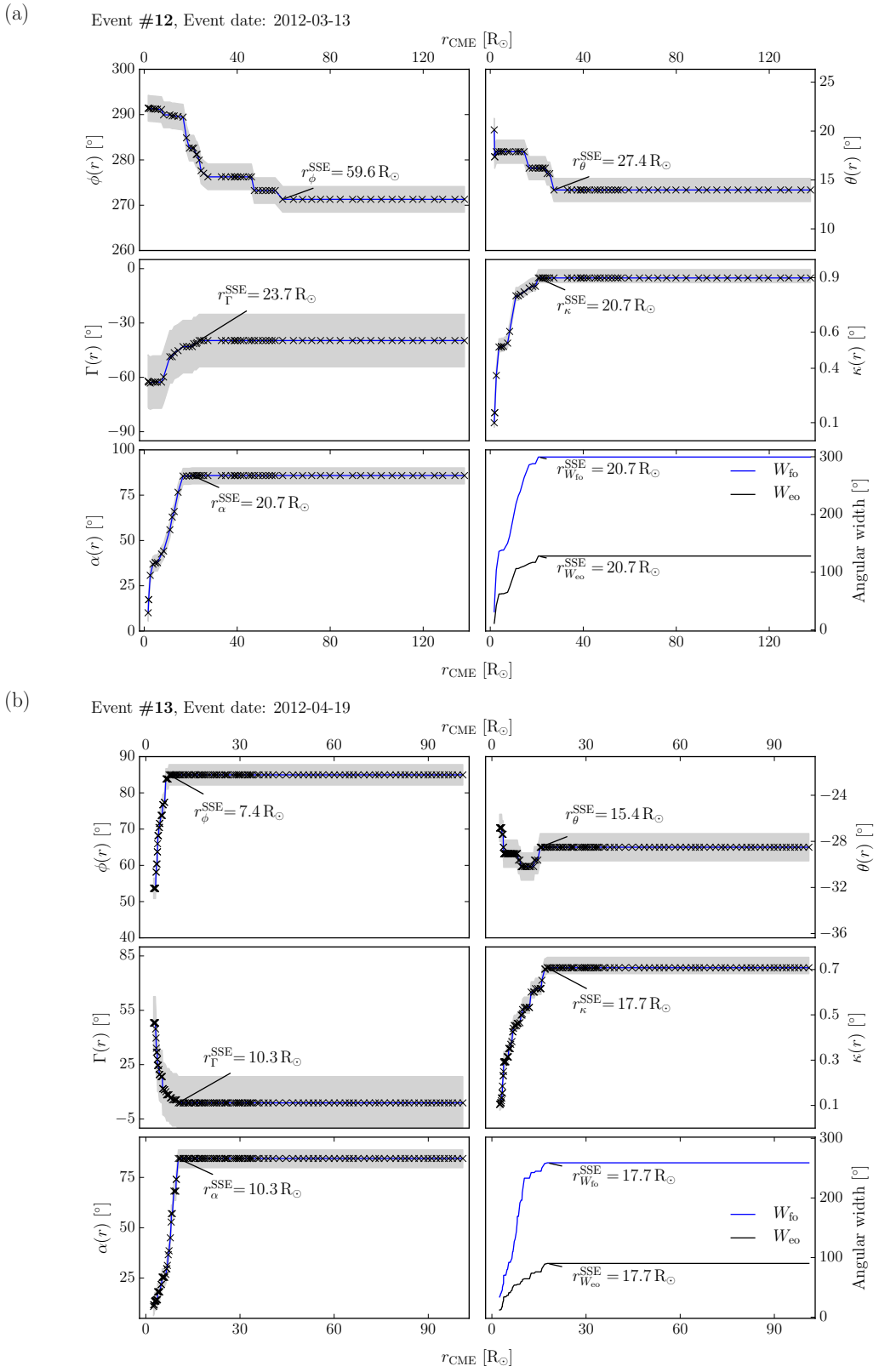

Figure (A.25) Geometrical results of the GCS modelling of the events #12 (a) and #13 (b). Same colours and markers as in Figure 5.4.

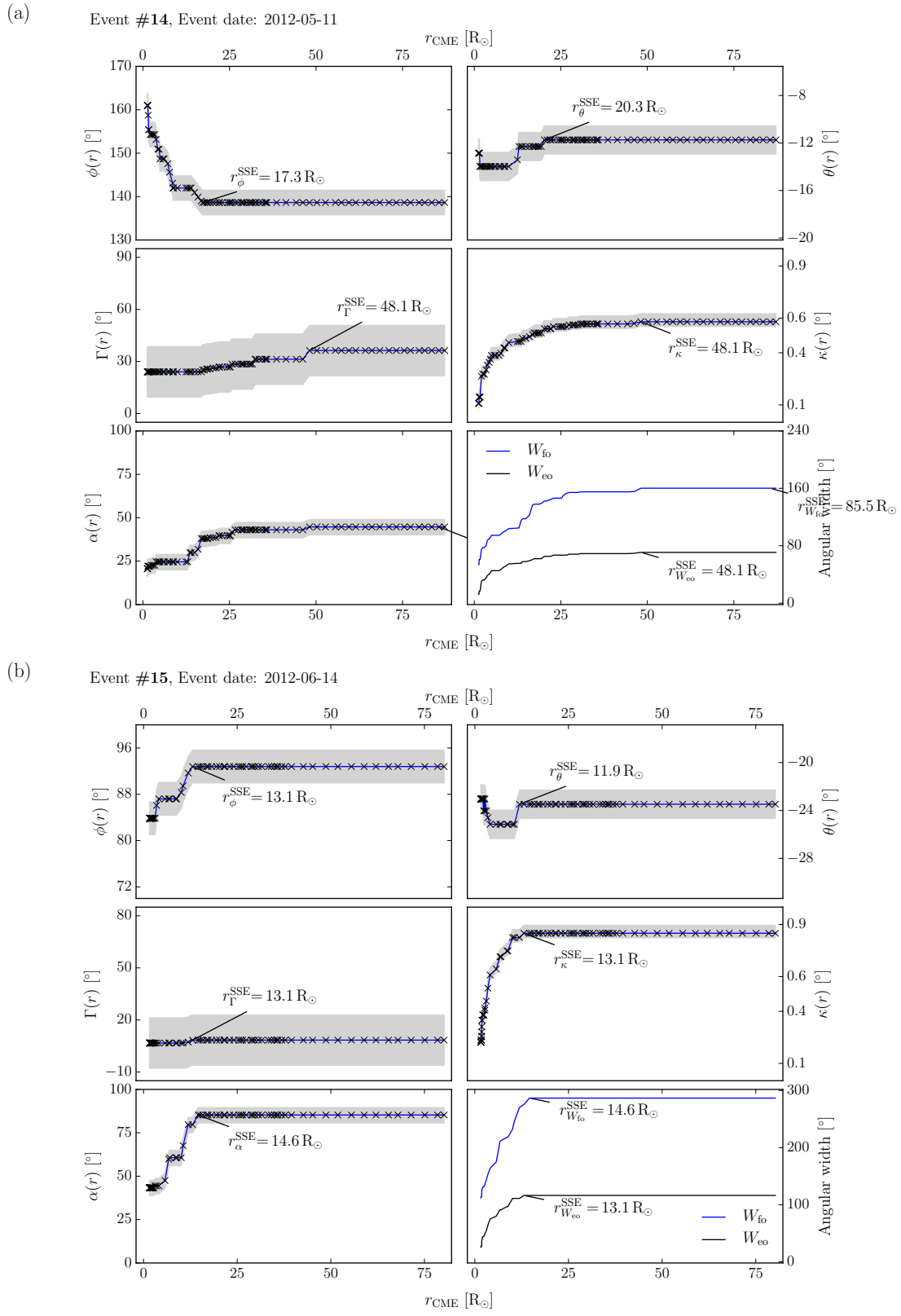

Figure (A.26) Geometrical results of the GCS modelling of the events #14 (a) and #15 (b). Same colours and markers as in Figure 5.4.

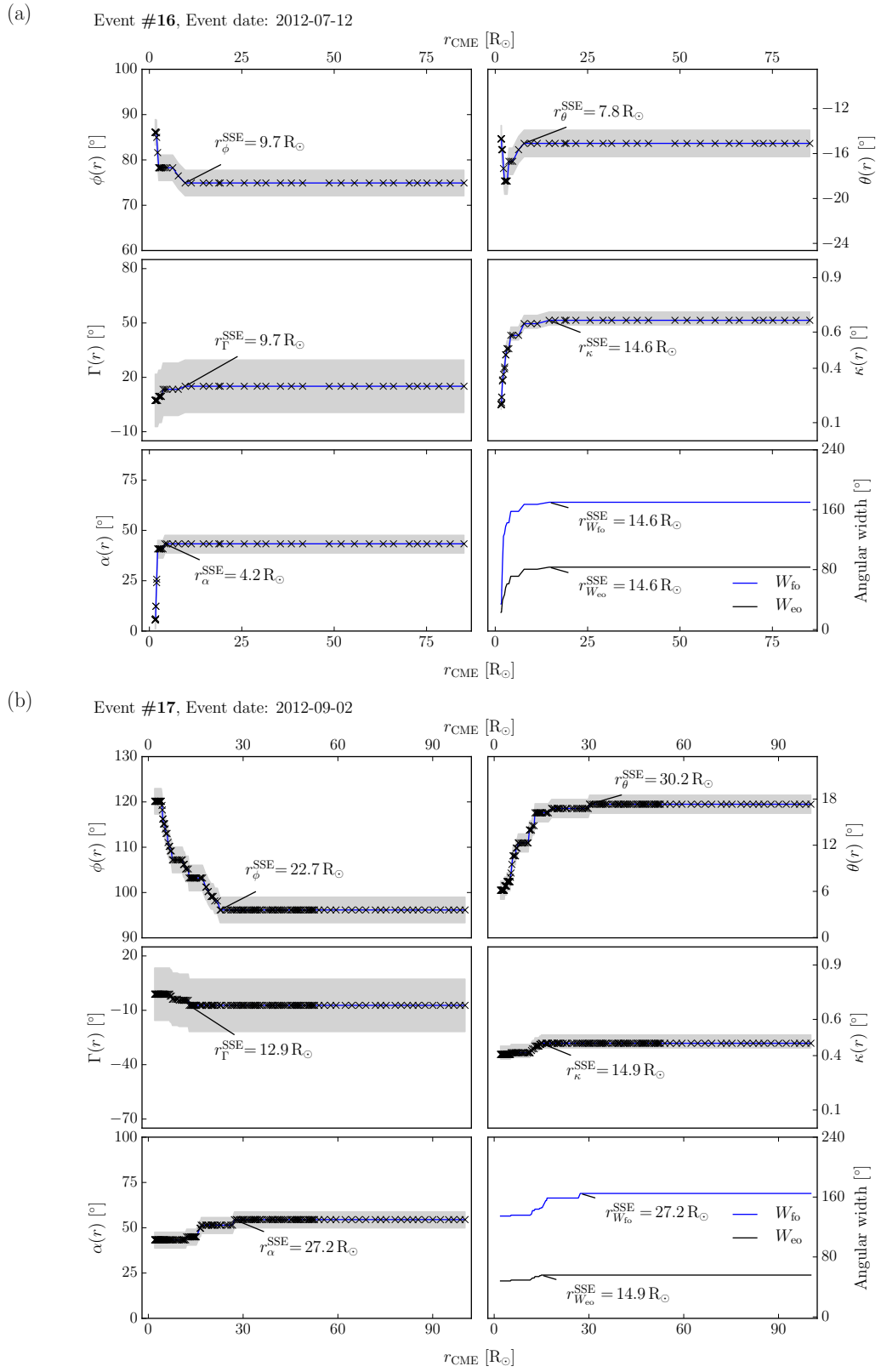

Figure (A.27) Geometrical results of the GCS modelling of the events #16 (a) and #17 (b). Same colours and markers as in Figure 5.4.

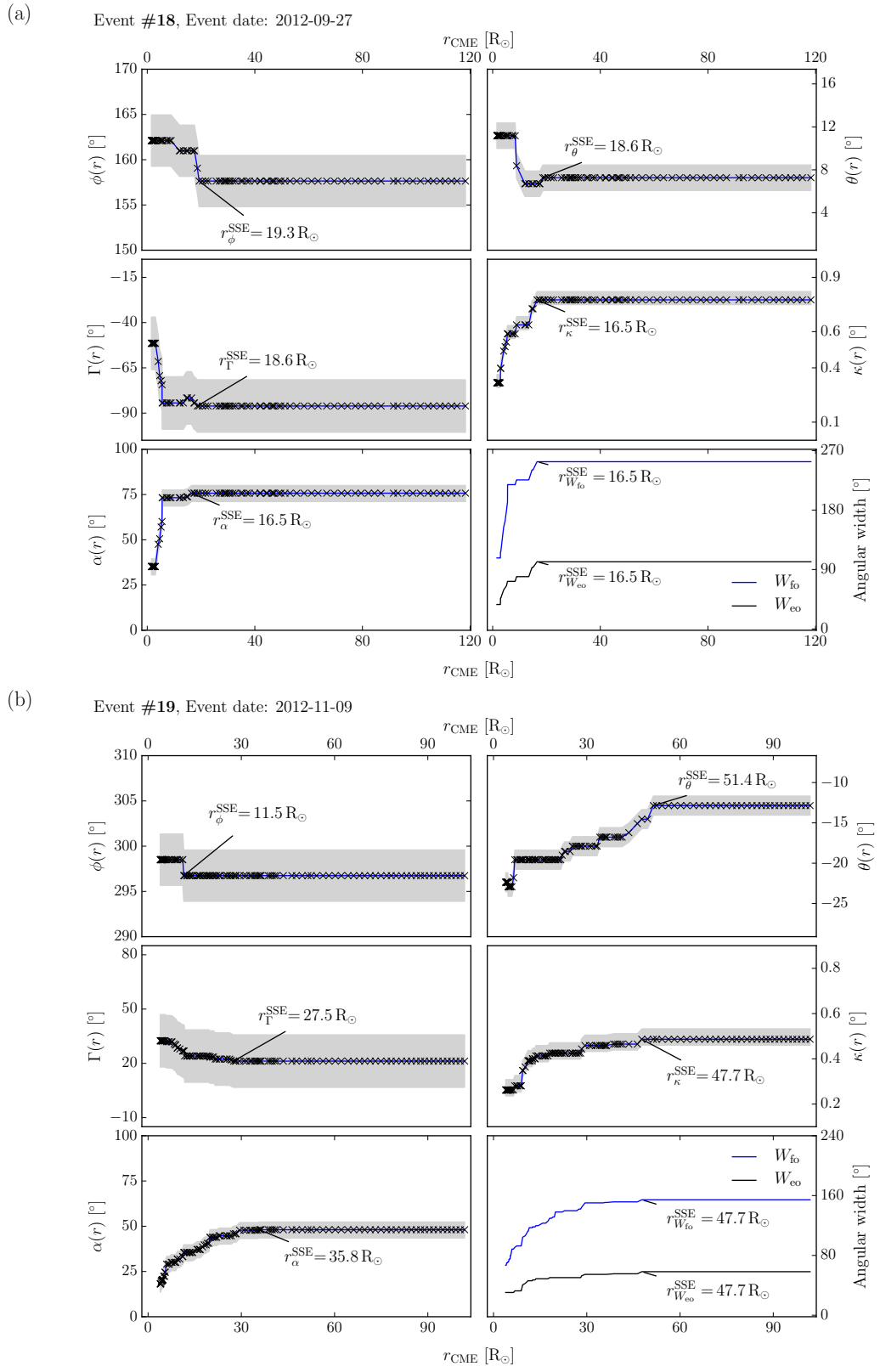

Figure (A.28) Geometrical results of the GCS modelling of the events #18 (a) and #19 (b). Same colours and markers as in Figure 5.4.

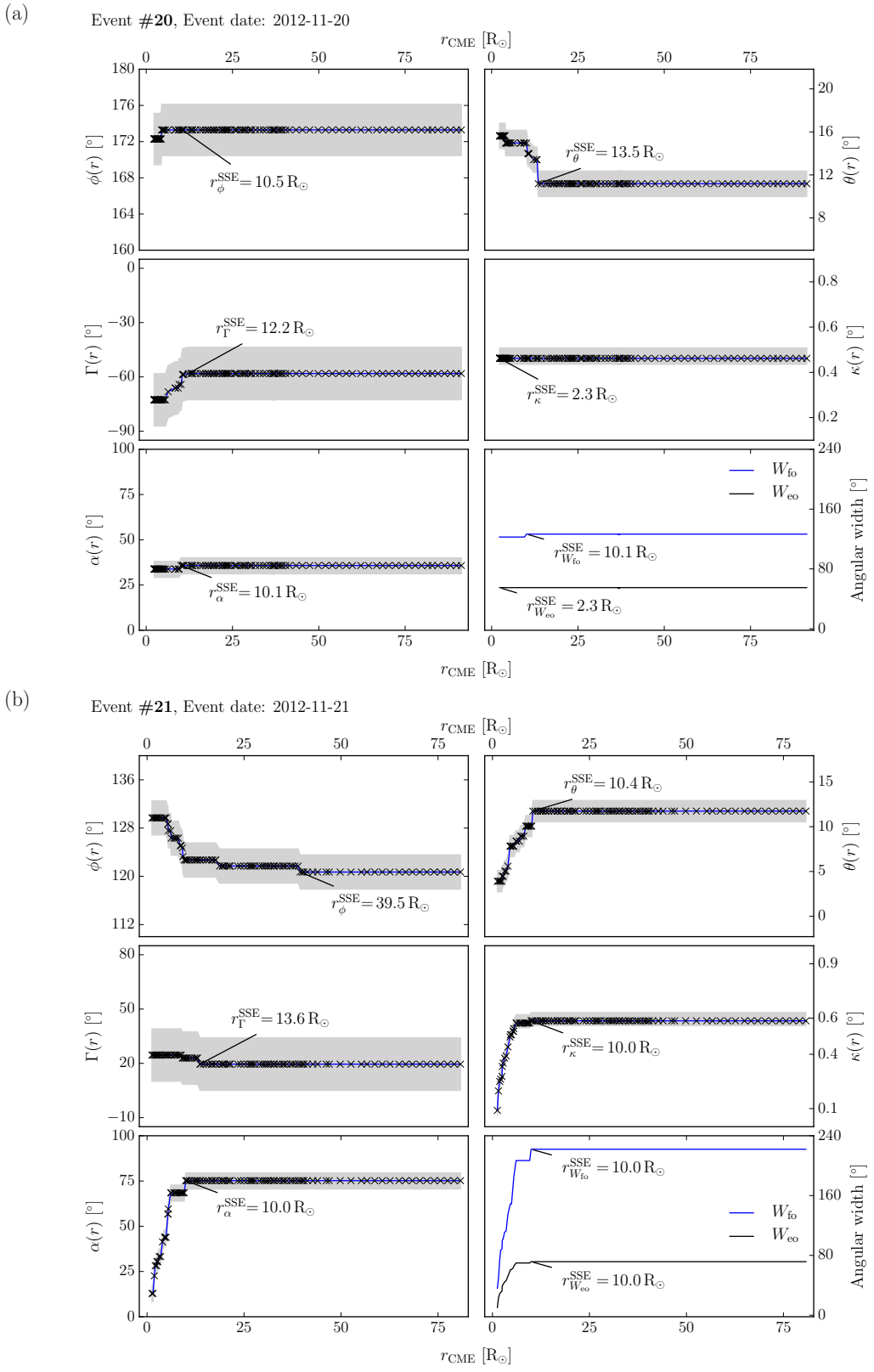

Figure (A.29) Geometrical results of the GCS modelling of the events #20 (a) and #21 (b). Same colours and markers as in Figure 5.4.

A.2.3

A.2.3 Kinematic Profiles

The r-t-profiles derived from the GCS modelling are shown in the first row of the Figures A.30 to A.39 for the events #3 to #21. In the second and third row, the v-t- and a-t-profiles computed from the r-t-profiles are shown. Using different spline methods, the fitted curves of $r(t)$, $v(t)$ and $a(t)$ are plotted in blue and light blue. A three-point moving average calculated from the GCS measurements can be seen by the blue triangles.

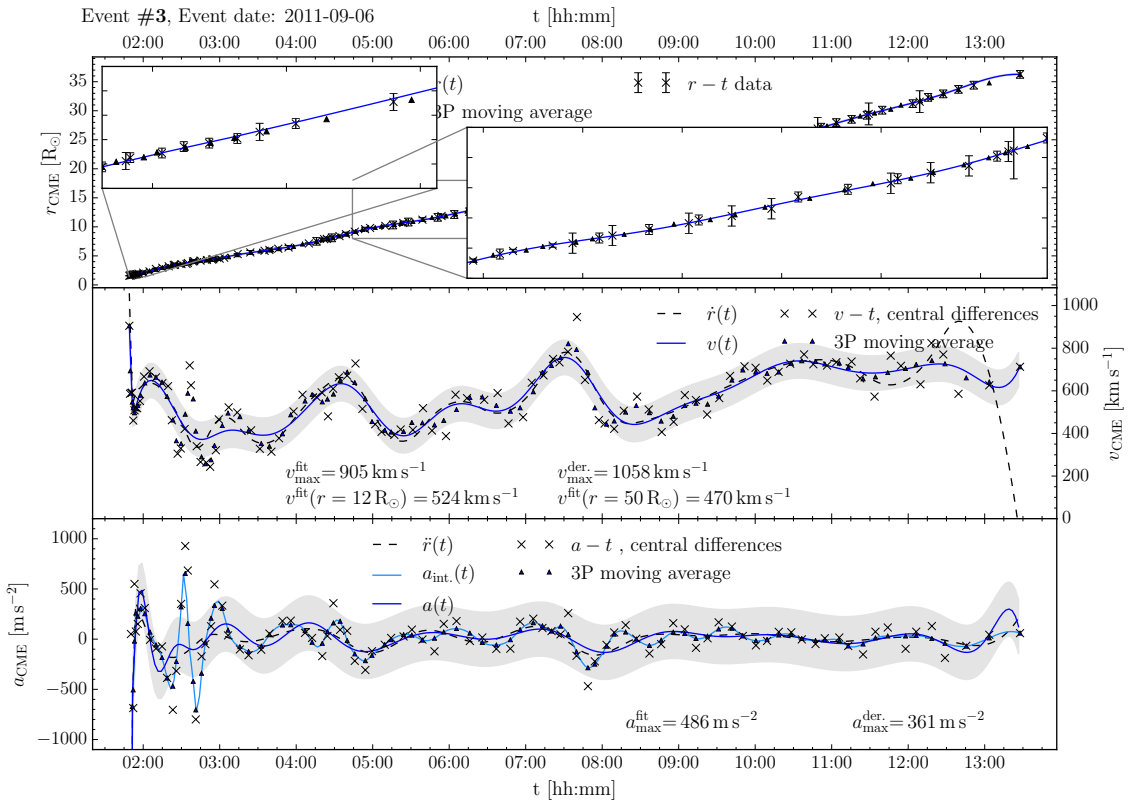

Figure (A.30) Kinematic results of the events #3. Same colours and markers as in Figure 5.8.

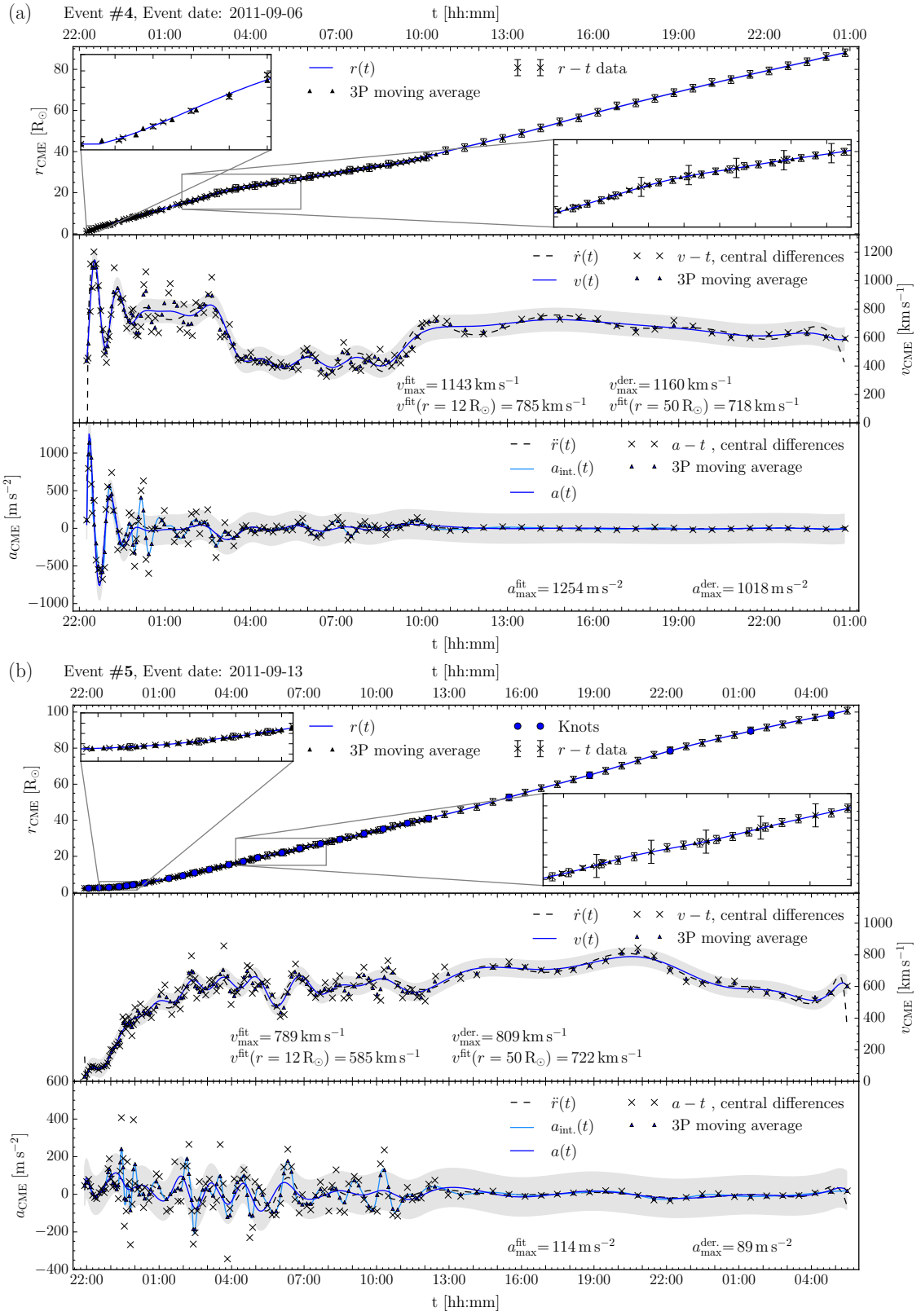

Figure (A.31) Kinematic results of the events #4 (a) and #5 (b). Same colours and markers as in Figure 5.8.

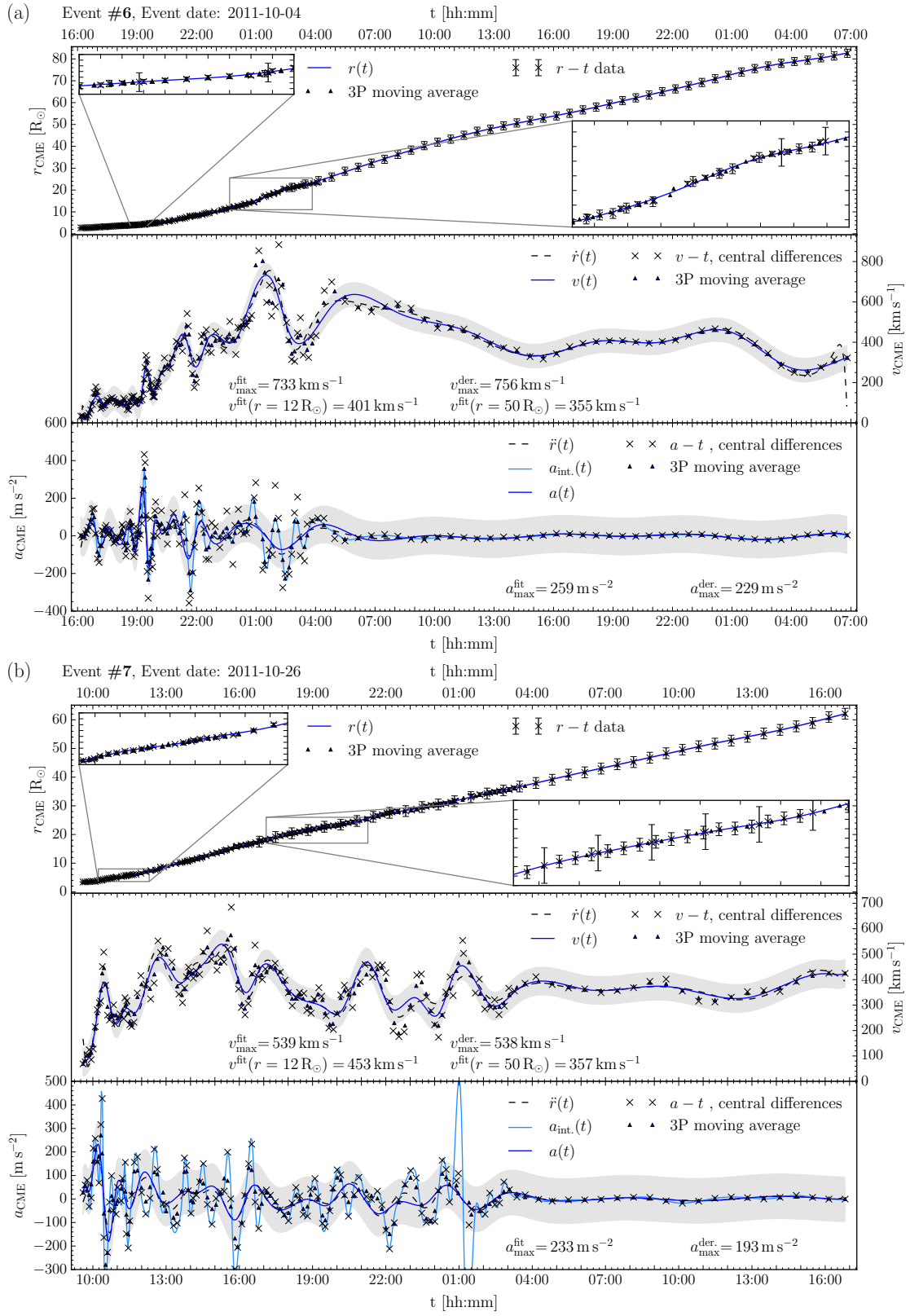

Figure (A.32) Kinematic results of the events #6 (a) and #7 (b). Same colours and markers as in Figure 5.8.

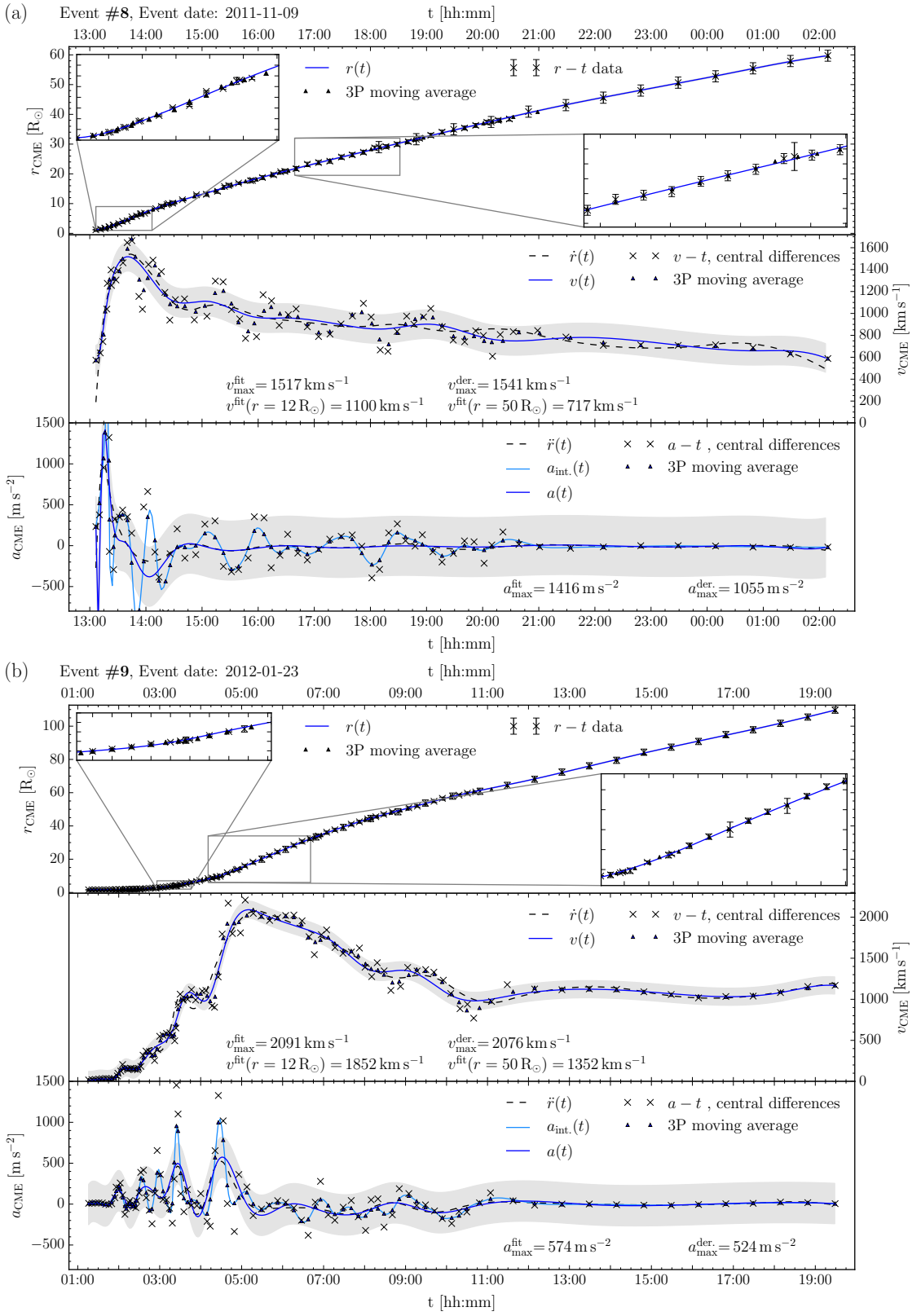

Figure (A.33) Kinematic results of the events #8 (a) and #9 (b). Same colours and markers as in Figure 5.8.

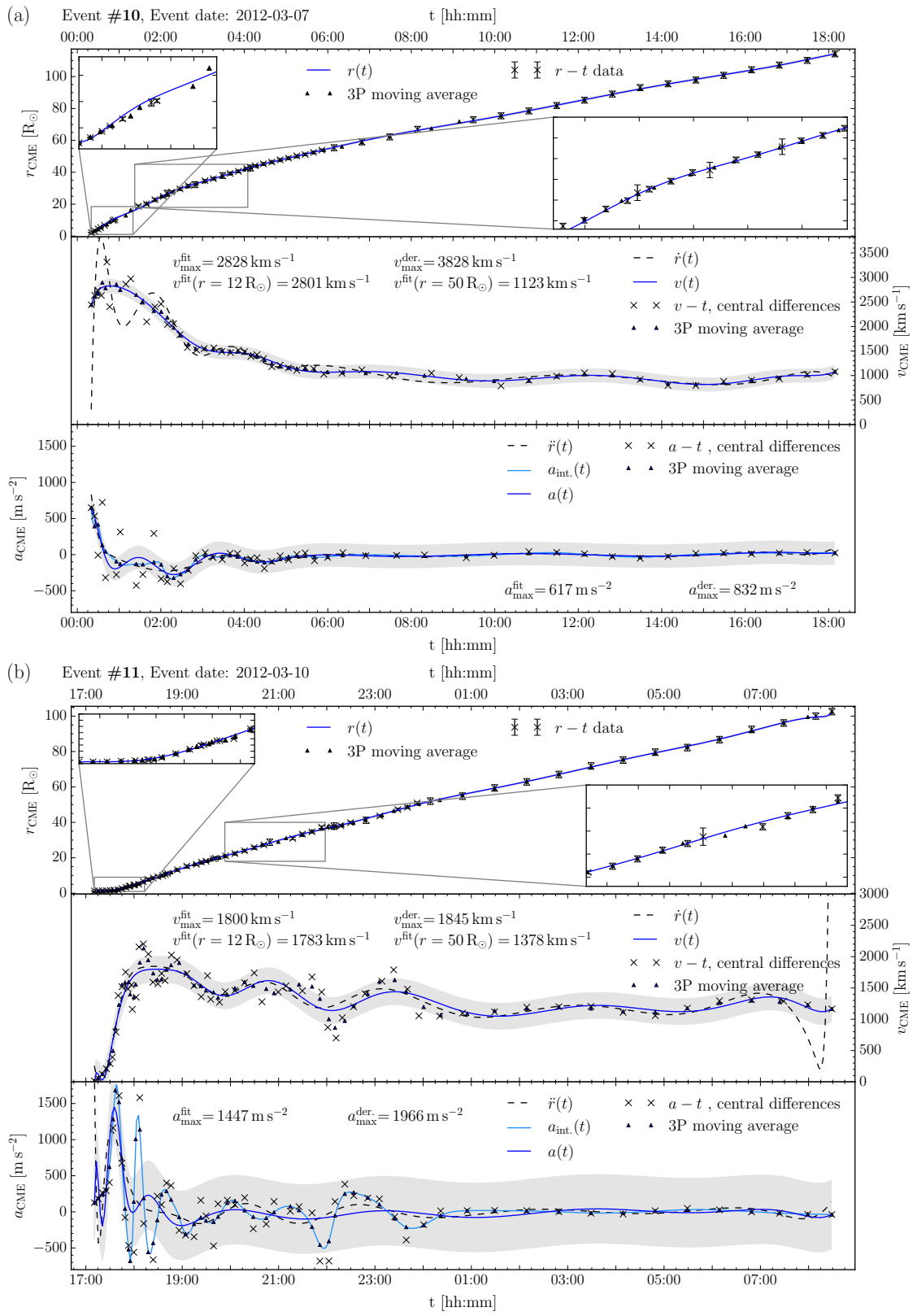

Figure (A.34) Kinematic results of the events #10 (a) and #11 (b). Same colours and markers as in Figure 5.8.

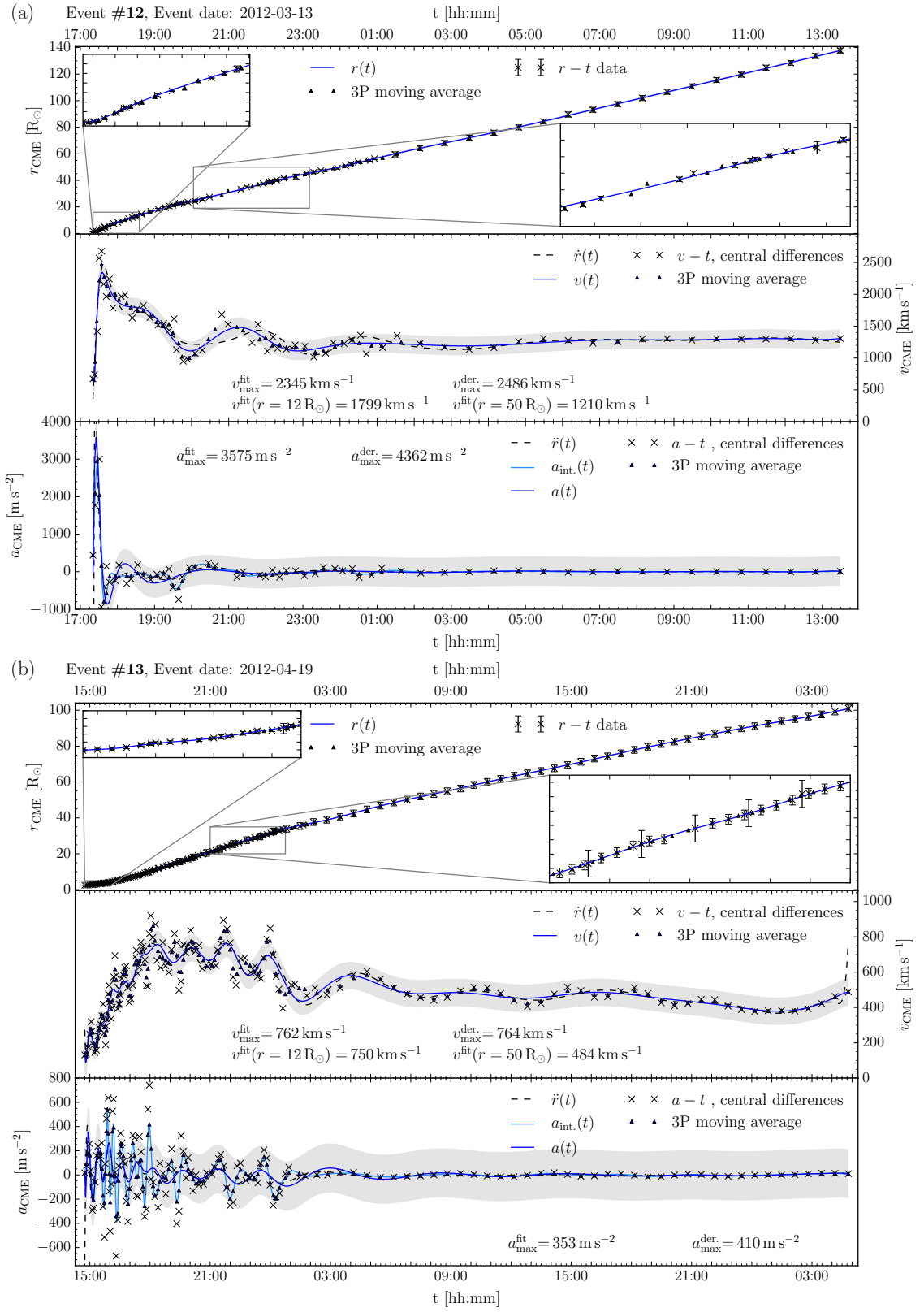

Figure (A.35) Kinematic results of the events #12 (a) and #13 (b). Same colours and markers as in Figure 5.8.

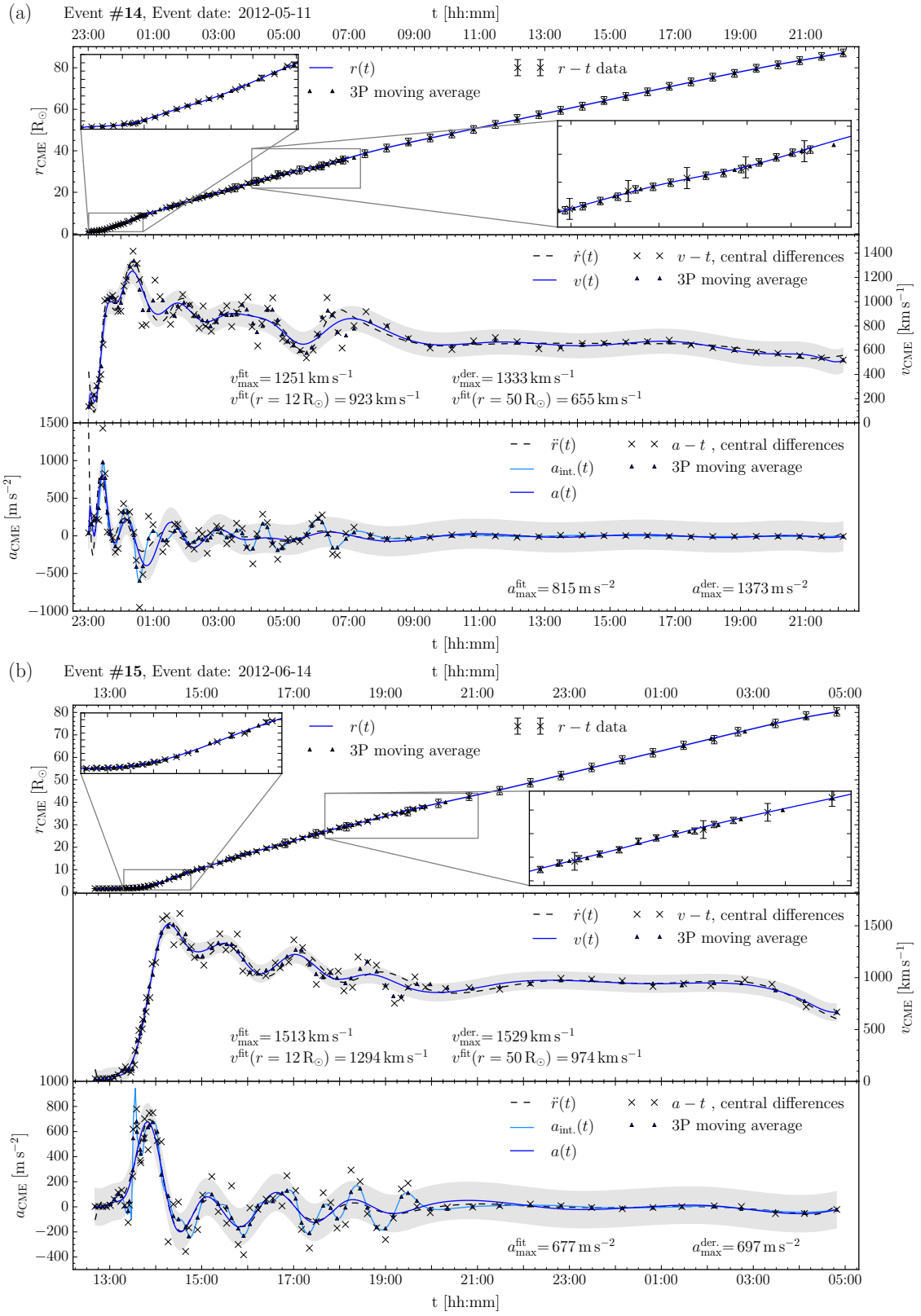

Figure (A.36) Kinematic results of the events #14 (a) and #15 (b). Same colours and markers as in Figure 5.8.

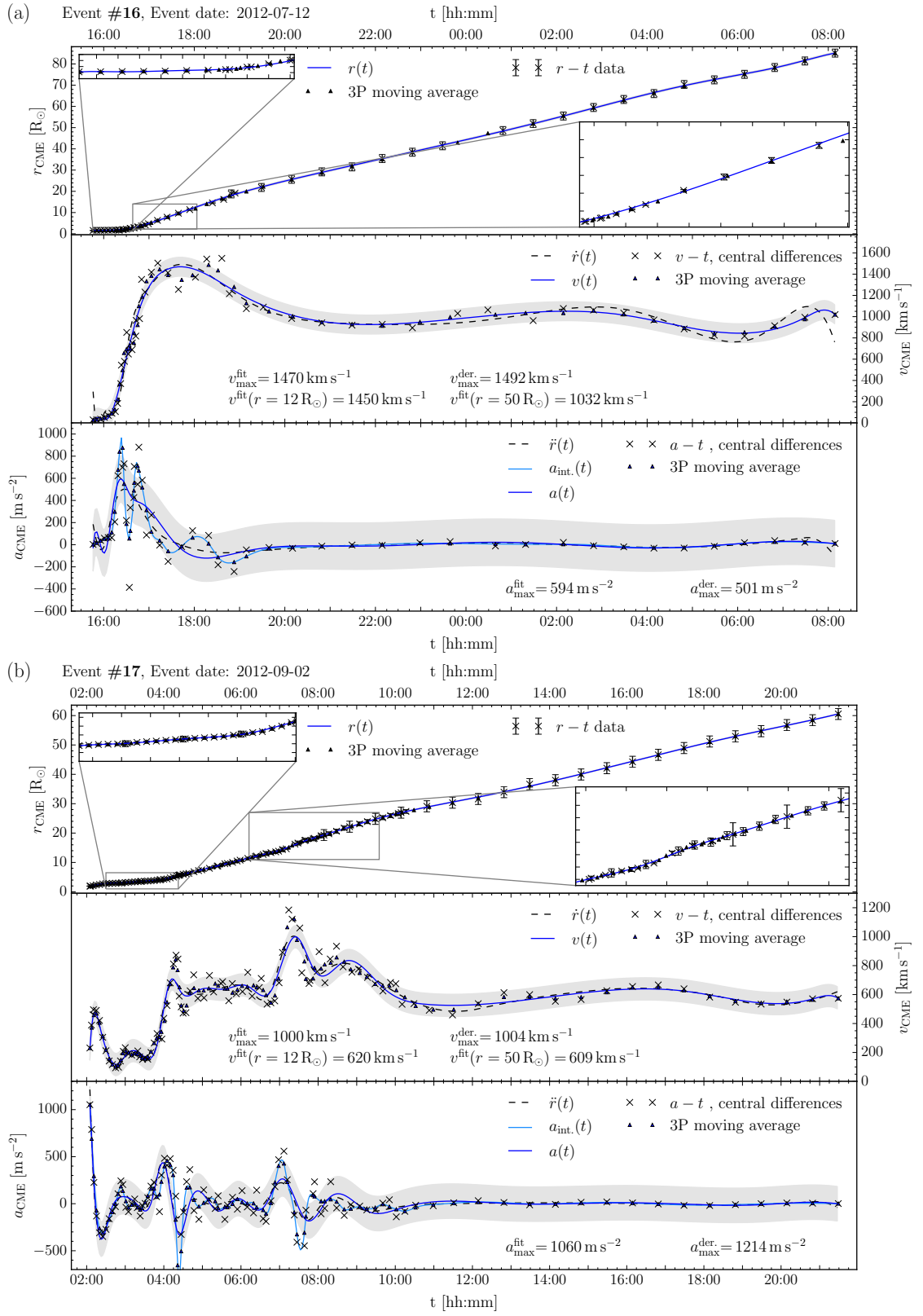

Figure (A.37) Kinematic results of the events #16 (a) and #17 (b). Same colours and markers as in Figure 5.8.

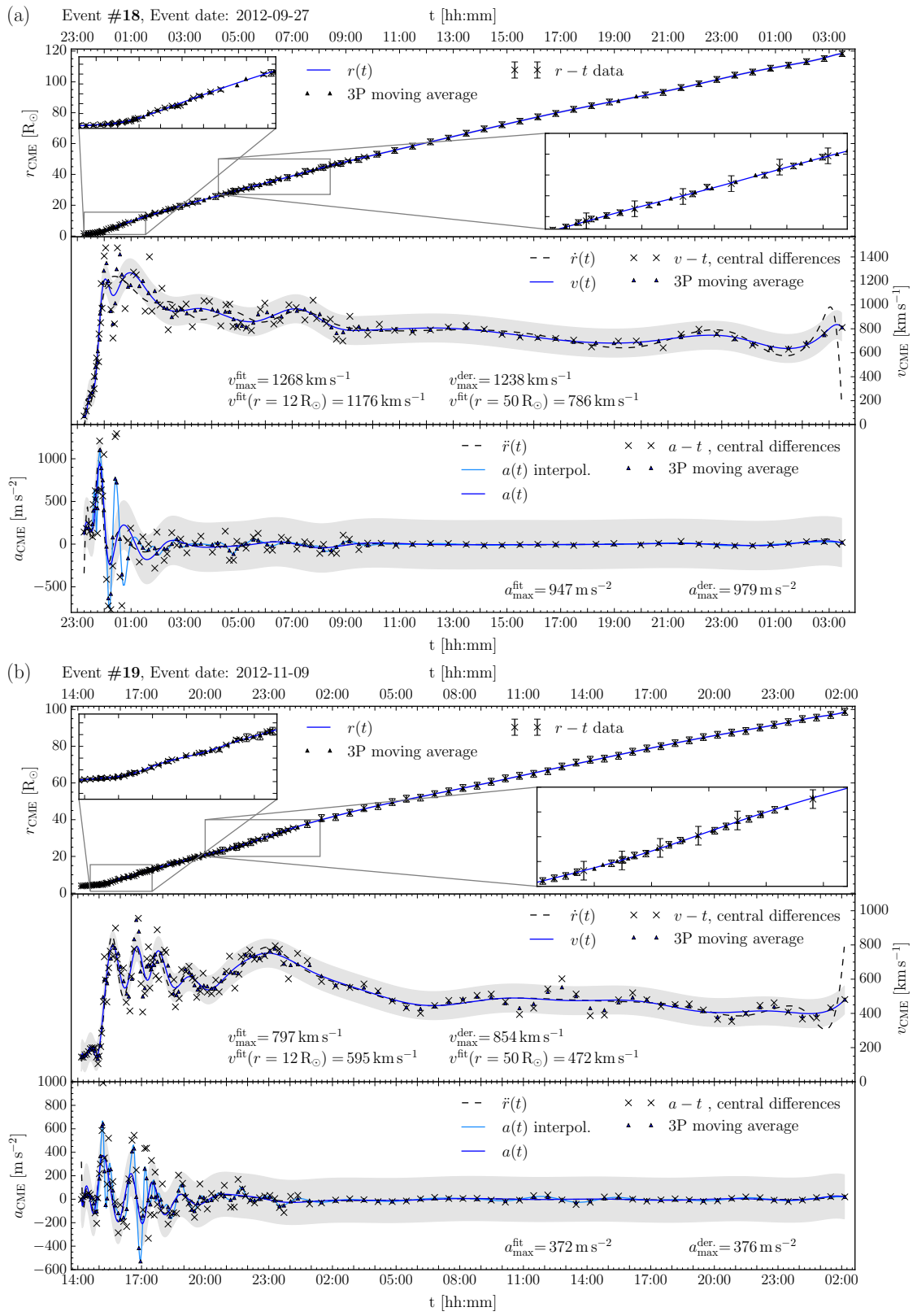

Figure (A.38) Kinematic results of the events #18 (a) and #19 (b). Same colours and markers as in Figure 5.8.

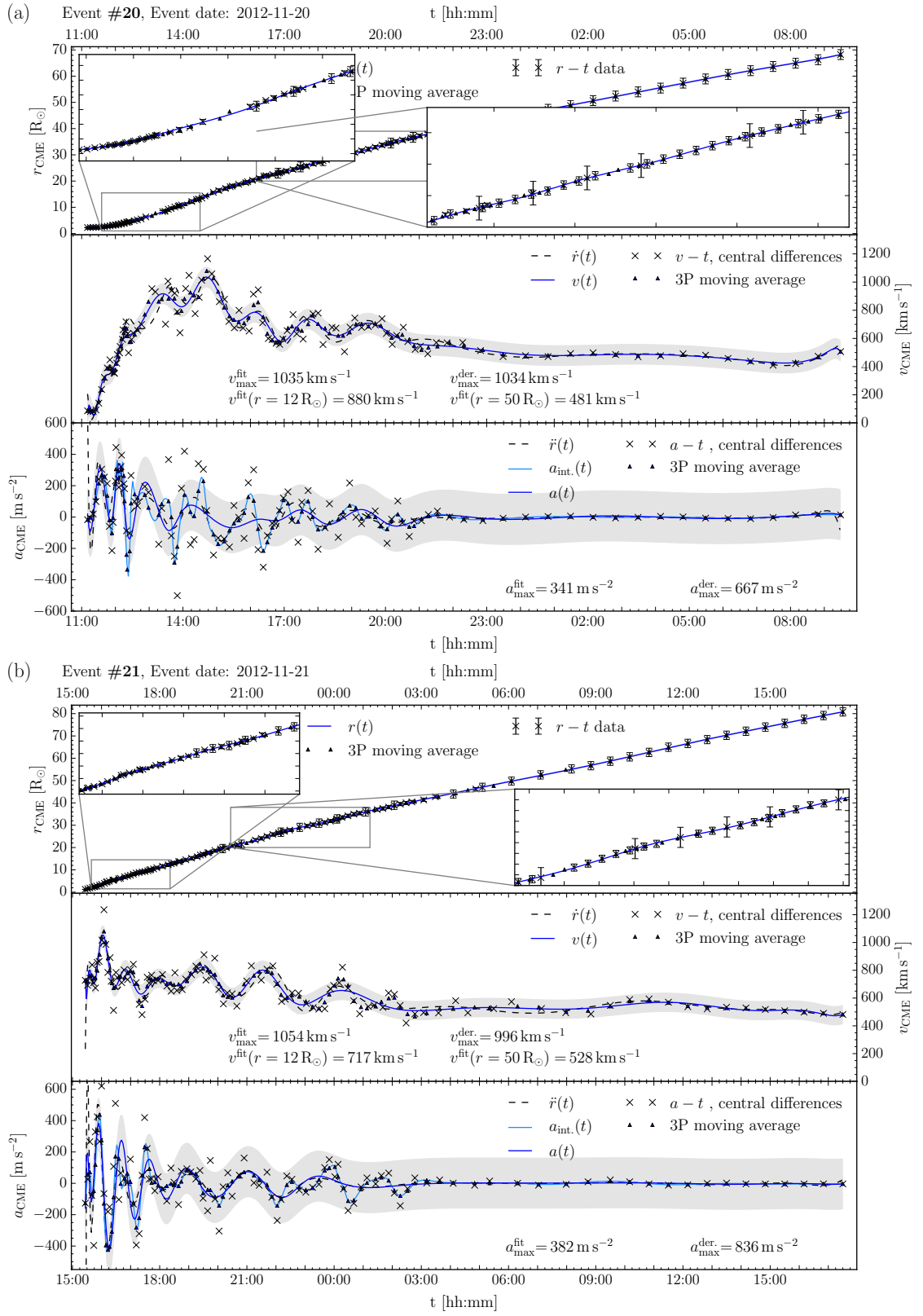

Figure (A.39) Kinematic results of the events #20 (a) and #21 (b). Same colours and markers as in Figure 5.8.

A.2.4

A.2.4 CME Masses

The determined CME masses form observations of the individual satellites are shown in Figures 5.12 and A.40 to A.42. STEREO A and B data are shown in red and blue, respectively. SOHO data can be seen in green. Partial and full halo events as well as streamer interactions have additional prefixes pH, fH and S. These events are also indicated by dashed and dotted lines, which representing the fit results to the corresponding data points.

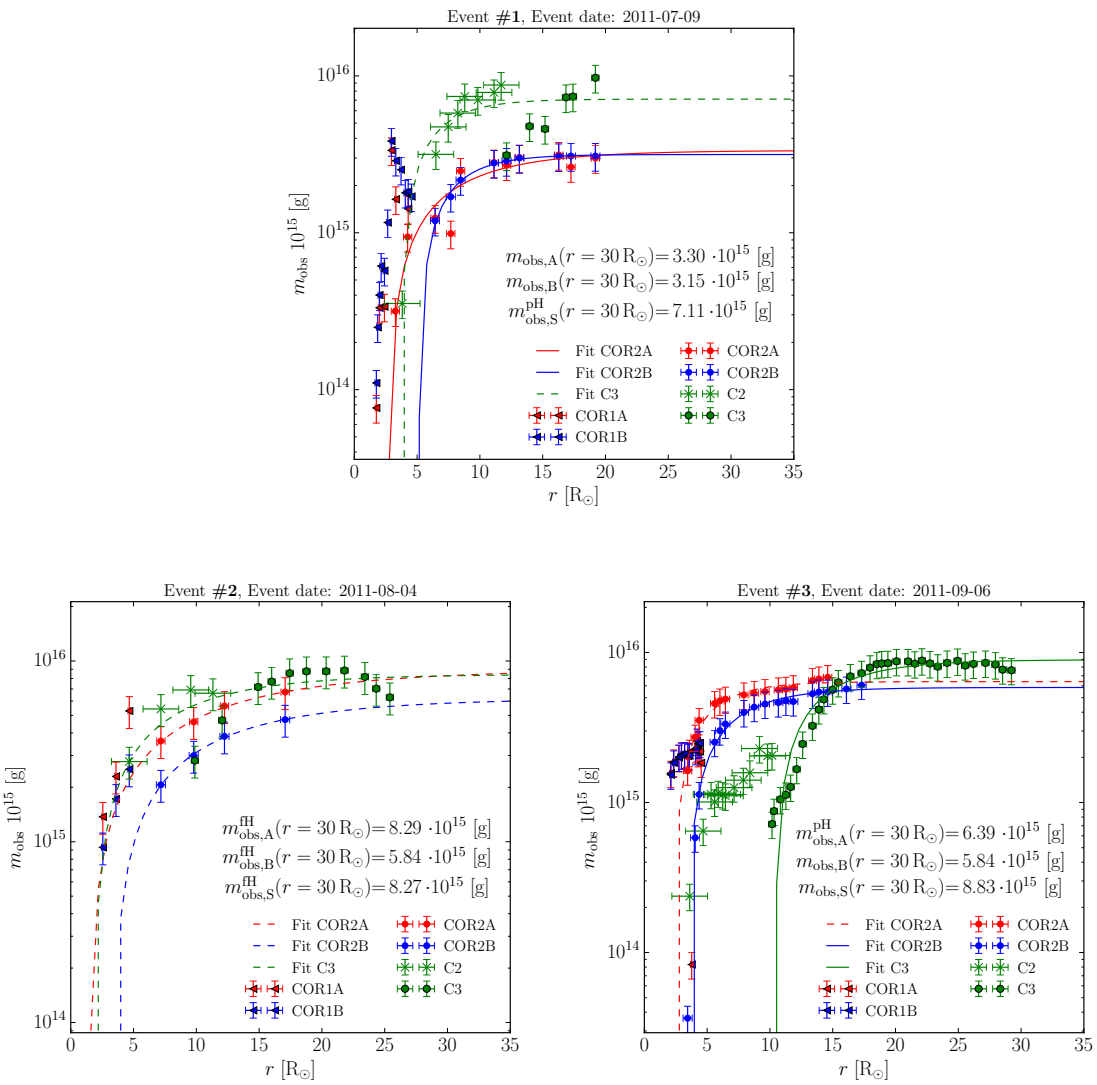

Figure (A.40) Results of the mass determination of the events #1 to #3. See Figure 5.12 for more details.

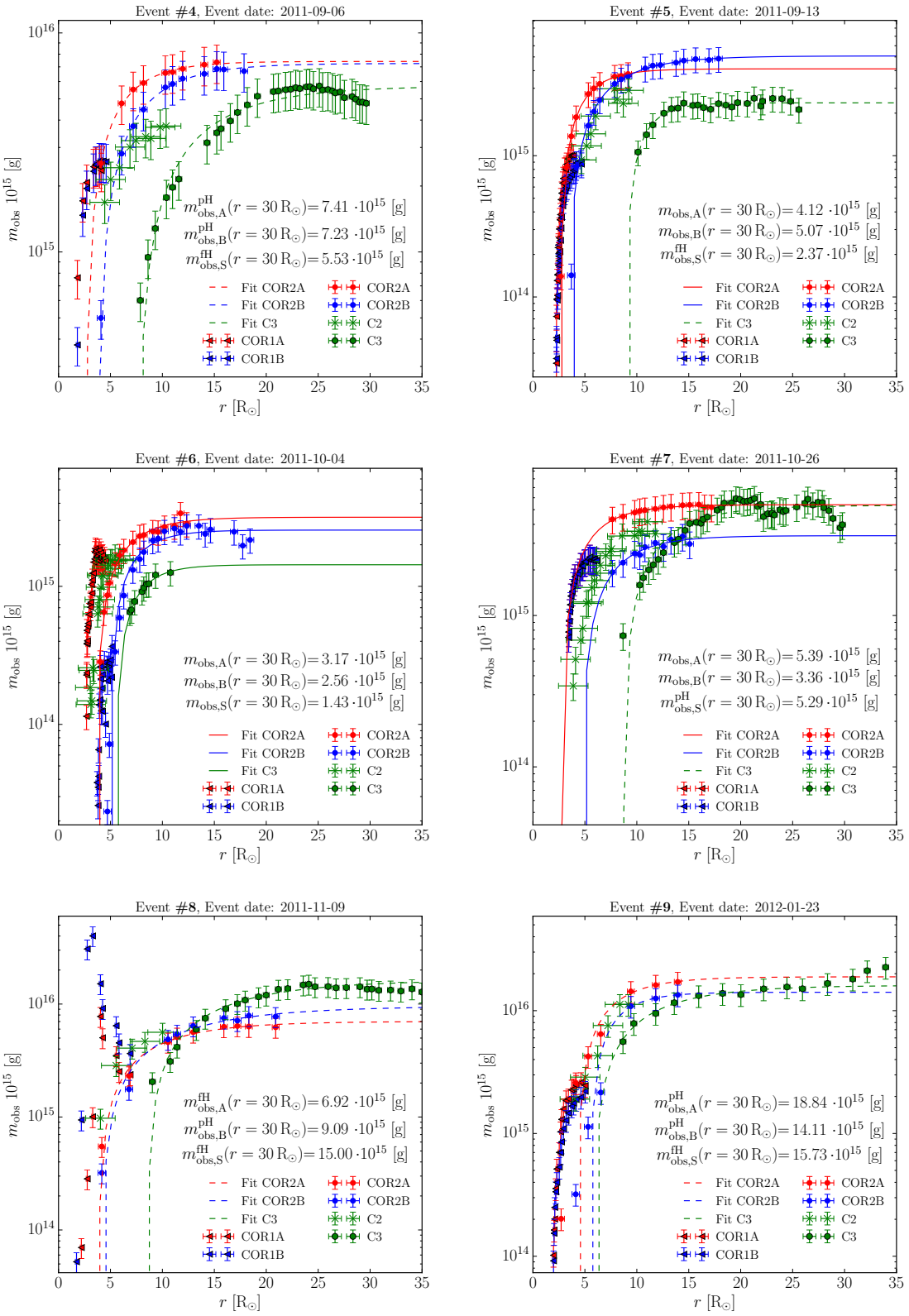

Figure (A.41) Results of the mass determination of the events #4 to #9. See Figure 5.12 for more details.

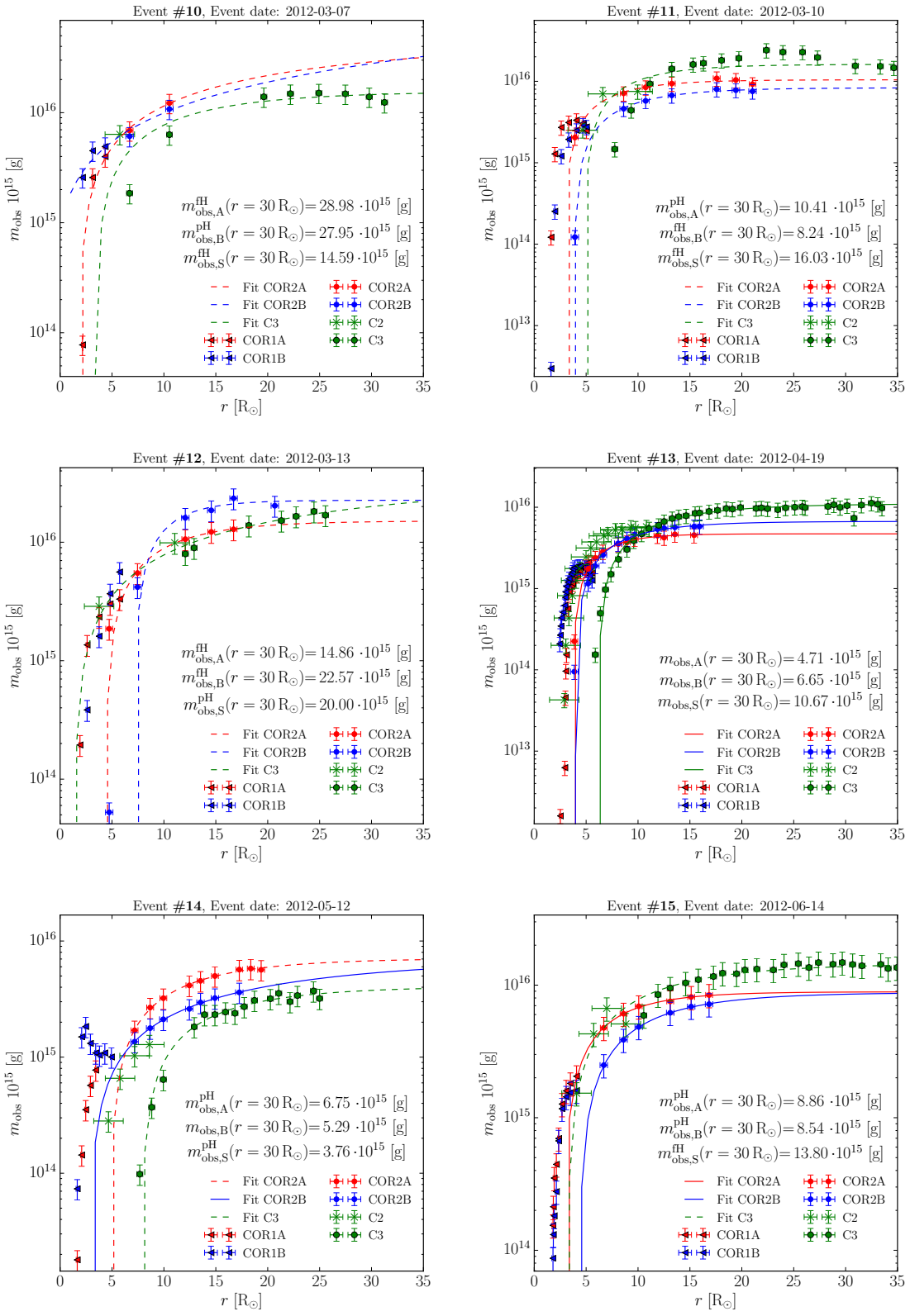

Figure (A.42) Results of the mass determination of the events #10 to #15. See Figure 5.12 for more details.

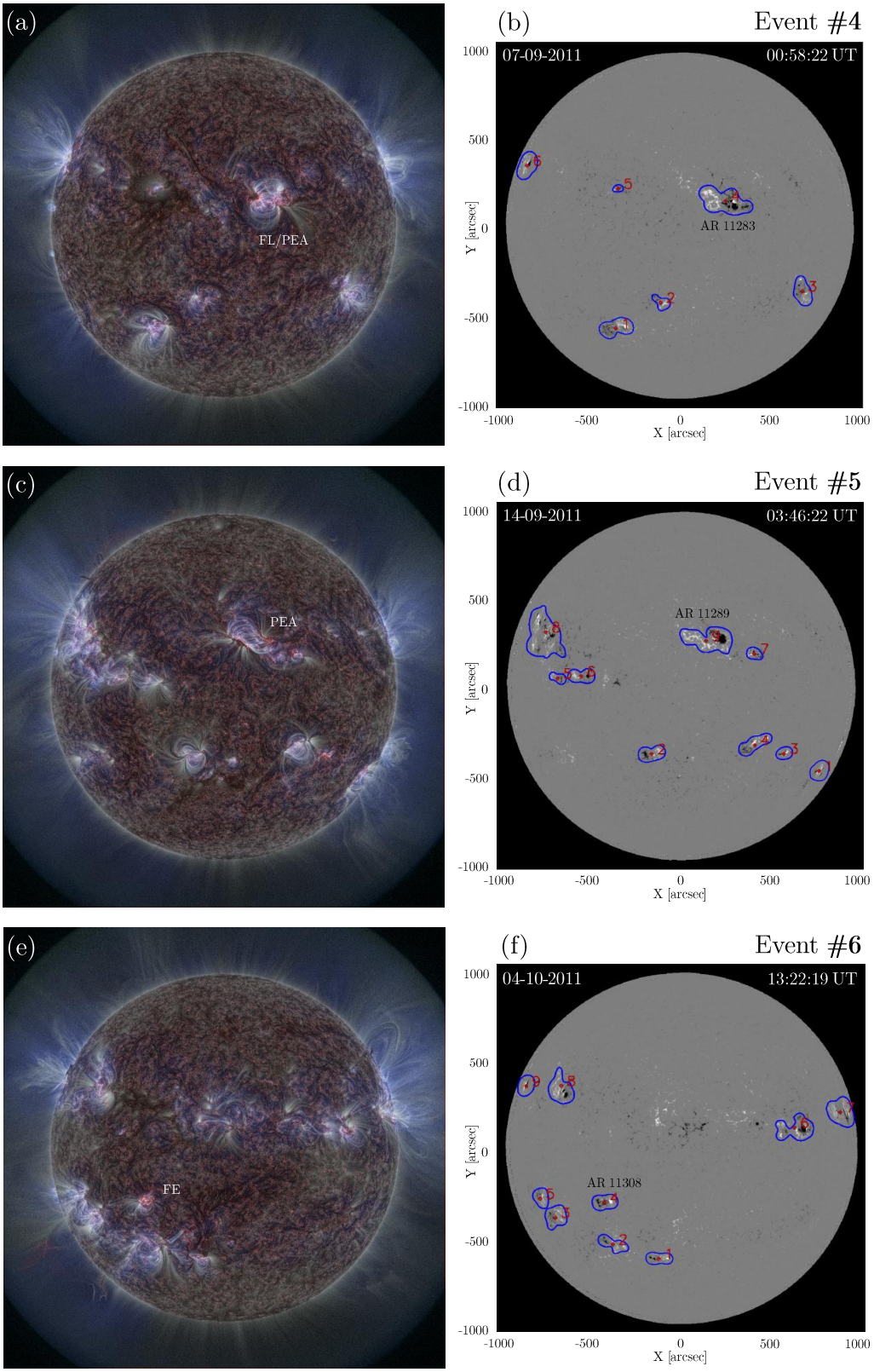

Figure (A.43) Same as Figure 5.13 but for the events #4,#5 and #6.

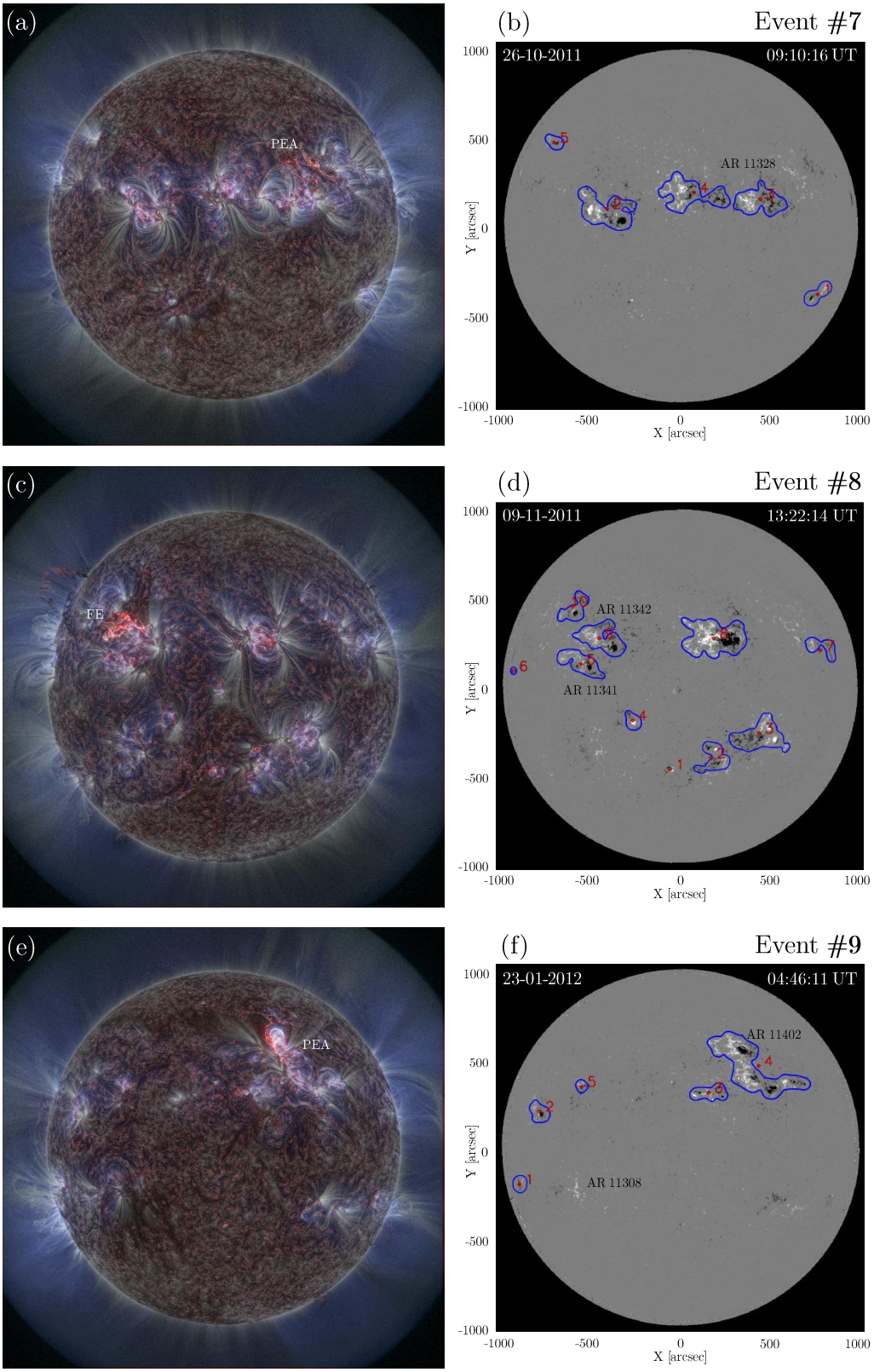

Figure (A.44) Same as Figure 5.13 but for the events #7,#8 and #9.

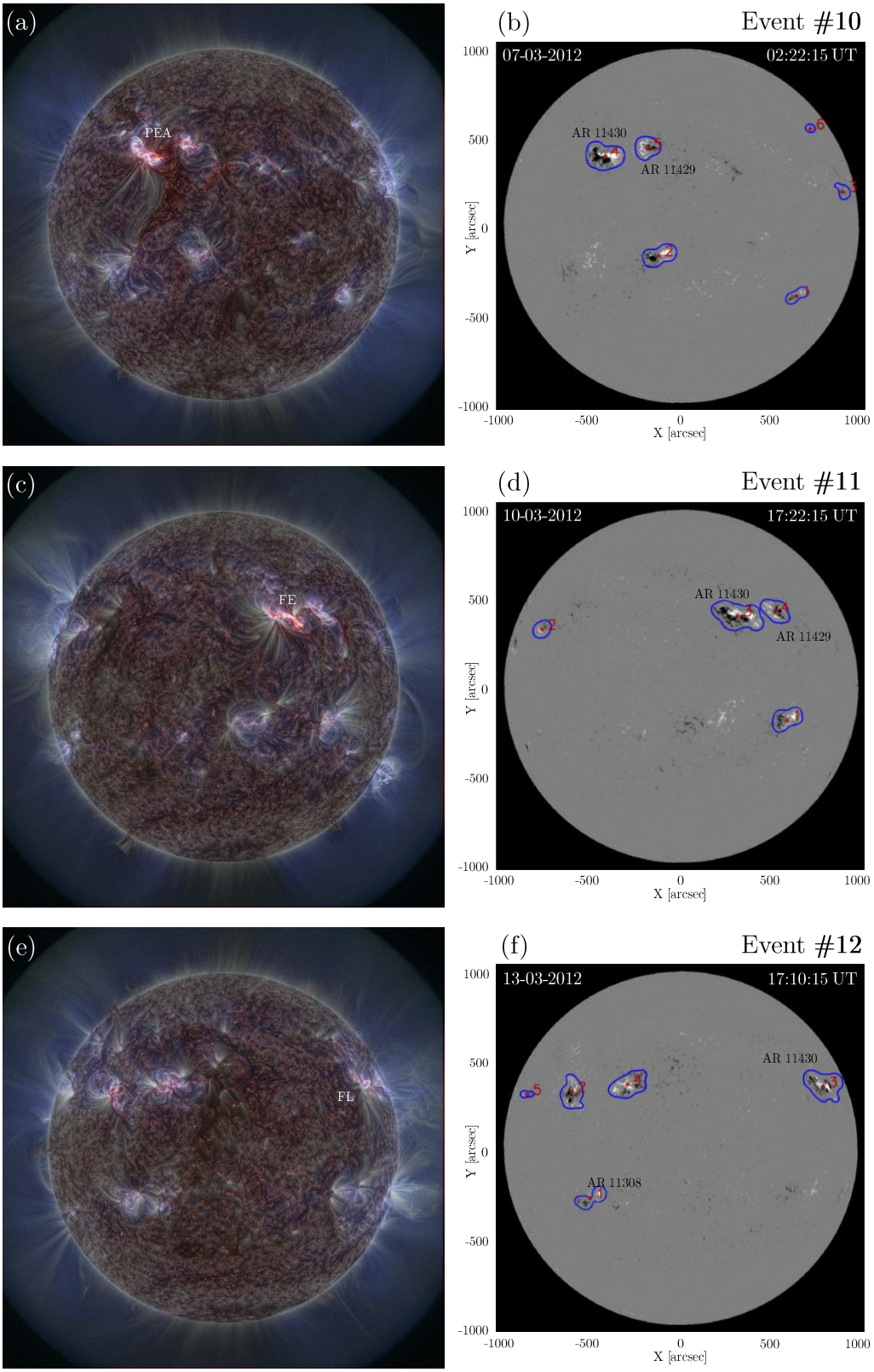

Figure (A.45) Same as Figure 5.13 but for the events #10,#11 and #12.

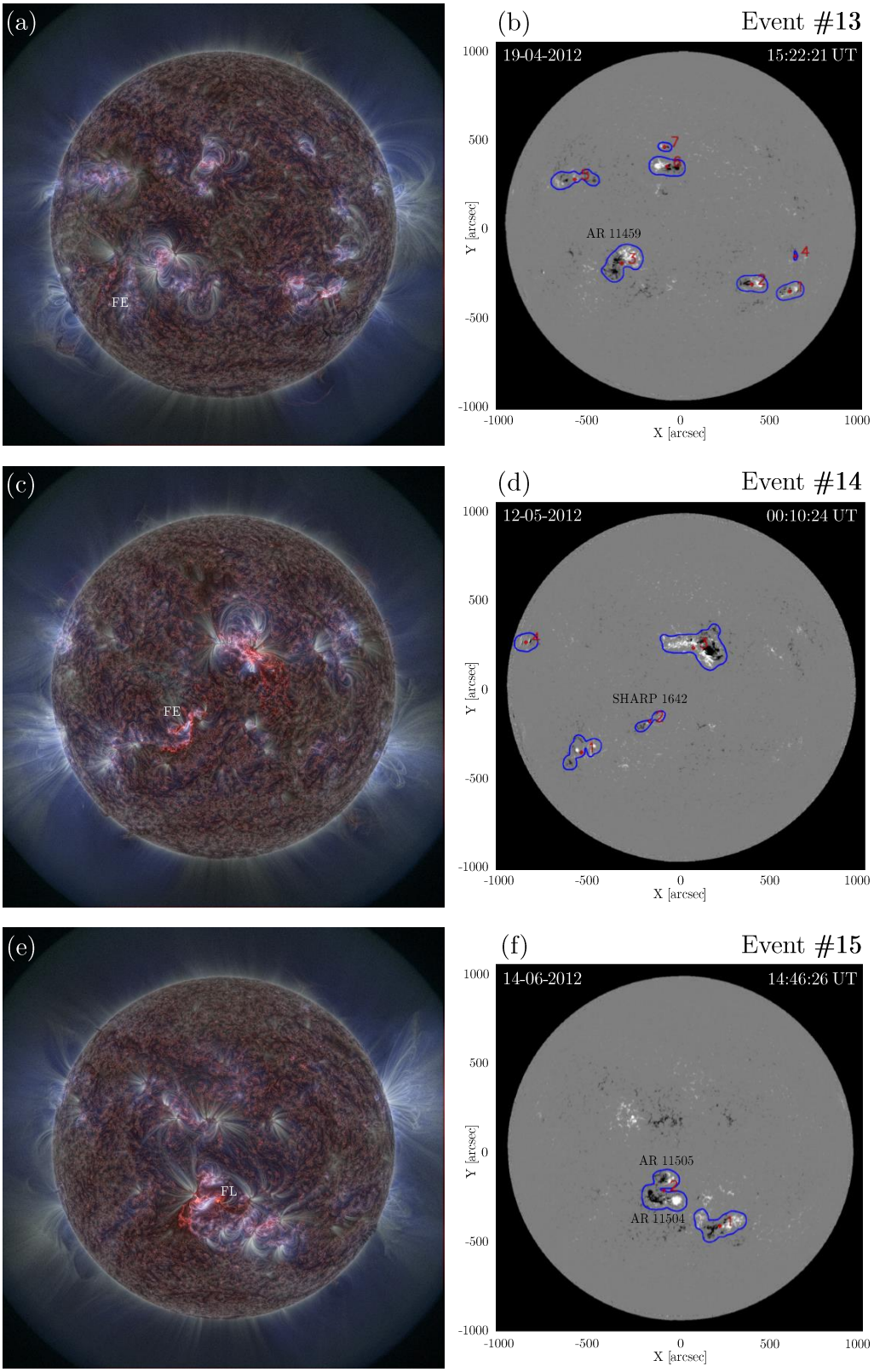

Figure (A.46) Same as Figure 5.13 but for the events #13,#14 and #15.

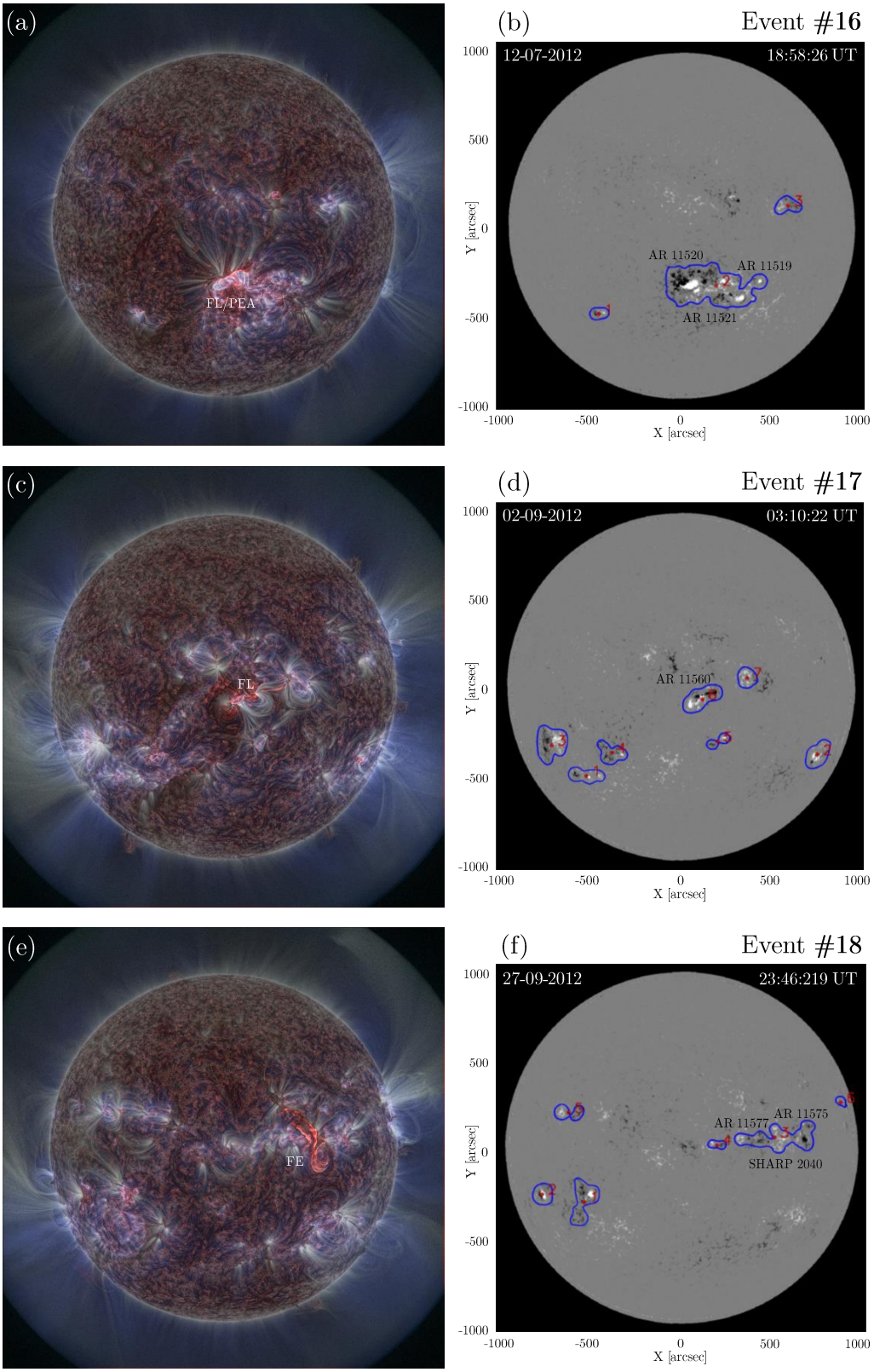

Figure (A.47) Same as Figure 5.13 but for the events #16,#17 and #18.

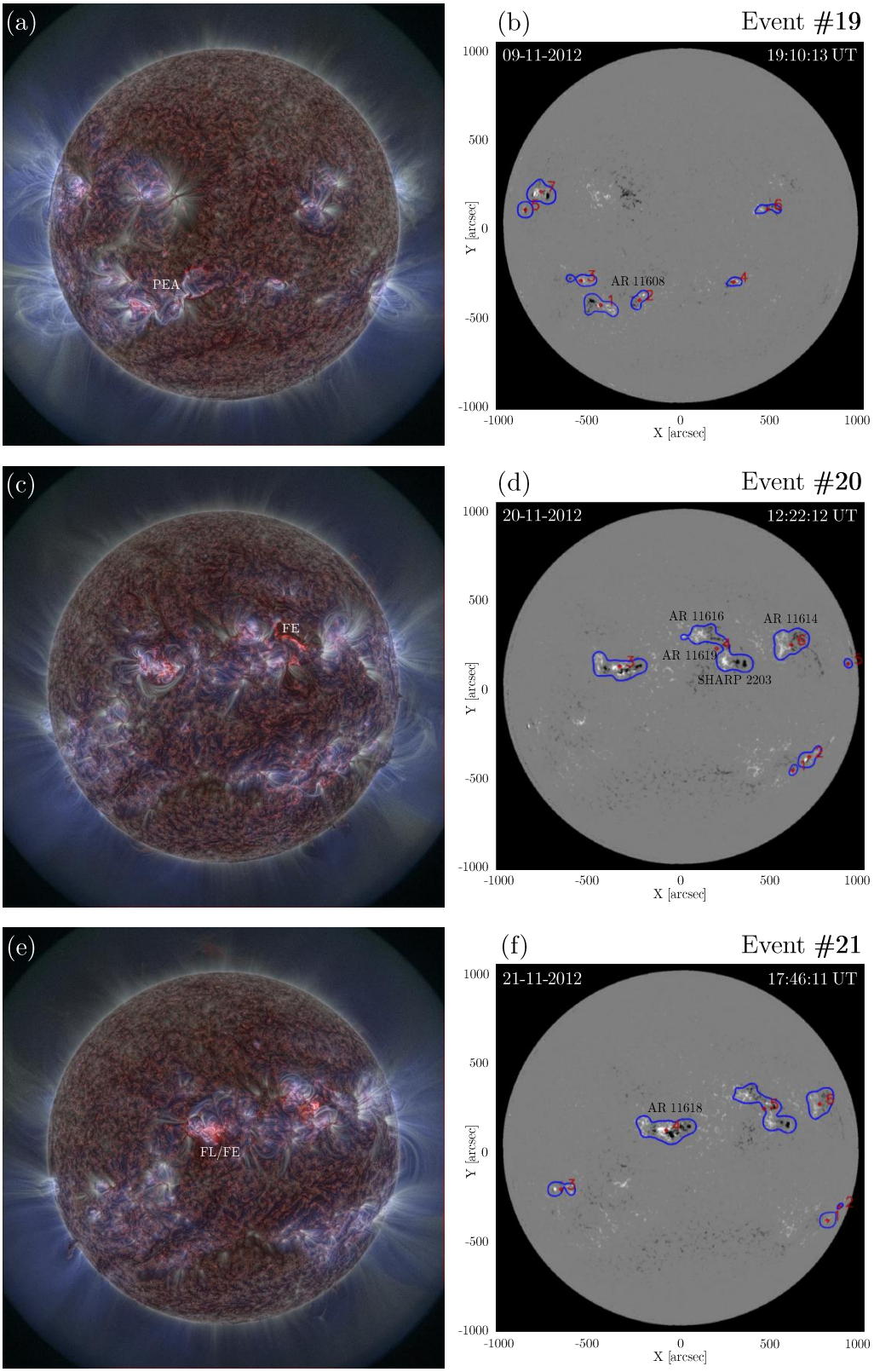

Figure (A.48) Same as Figure 5.13 but for the events #19,#20 and #21.

A.2.5 DBM Analysis Results

In the following plots, the DBM results of the r-t-profiles of the CME apex and the Earth-directed CME component are shown. The Earth-symbol represents the time at which a distance of 1 AU is reached. Linear fits of the data below the HI FOV and above the COR2 FOV are shown by the red and yellow dashed lines.

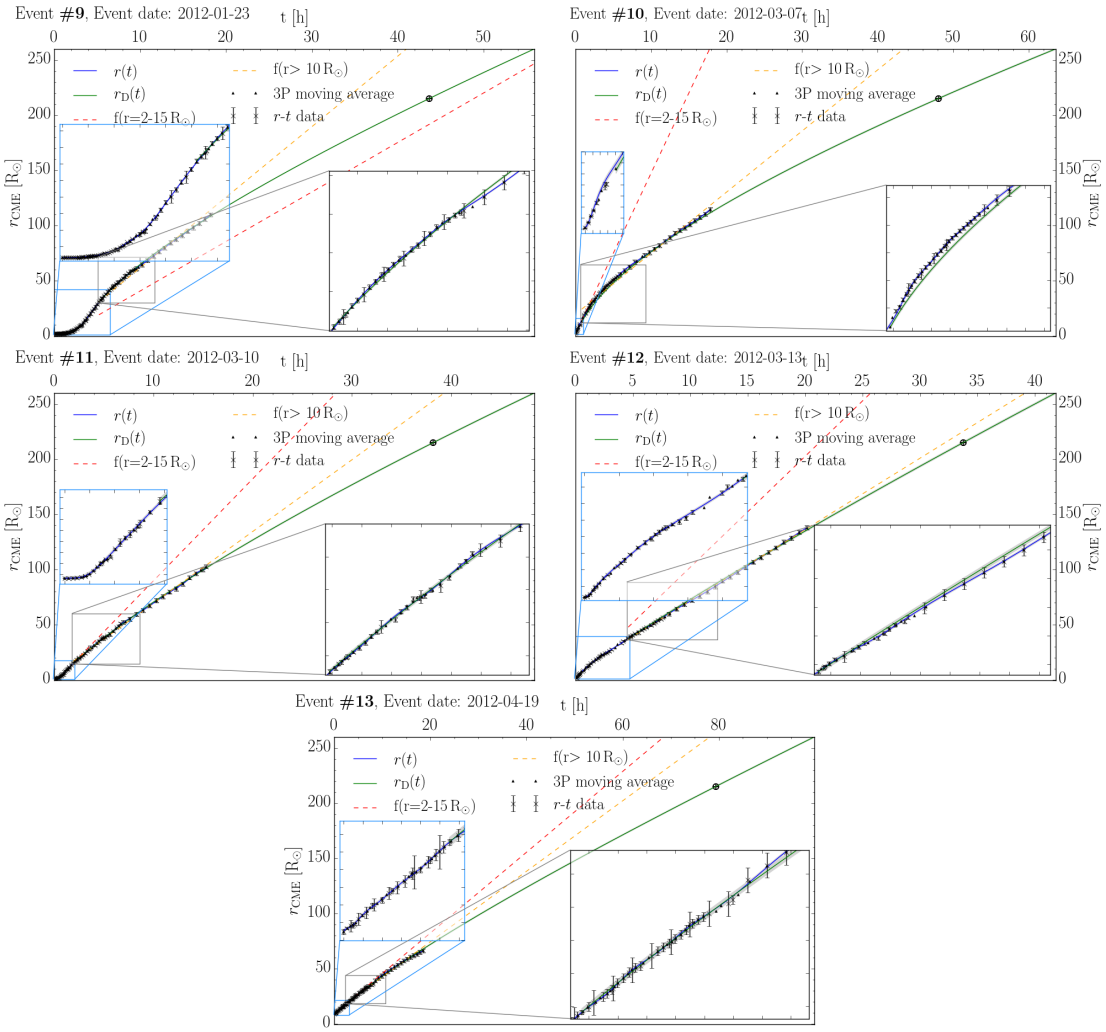

Figure (A.49) Same as Figure 5.27 but for events #9 to #13.

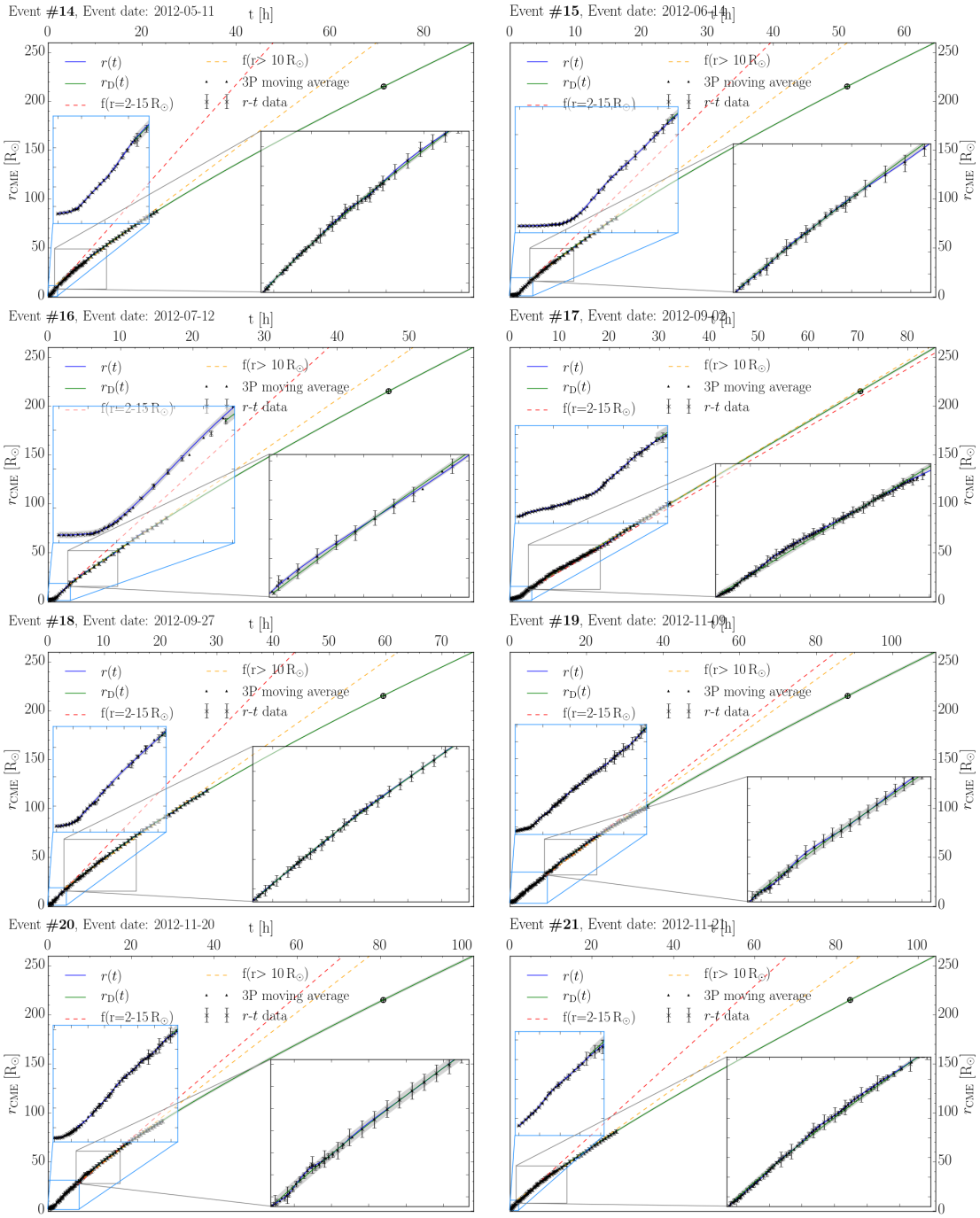

Figure (A.50) Same as Figure 5.27 but for events #14 to #21.

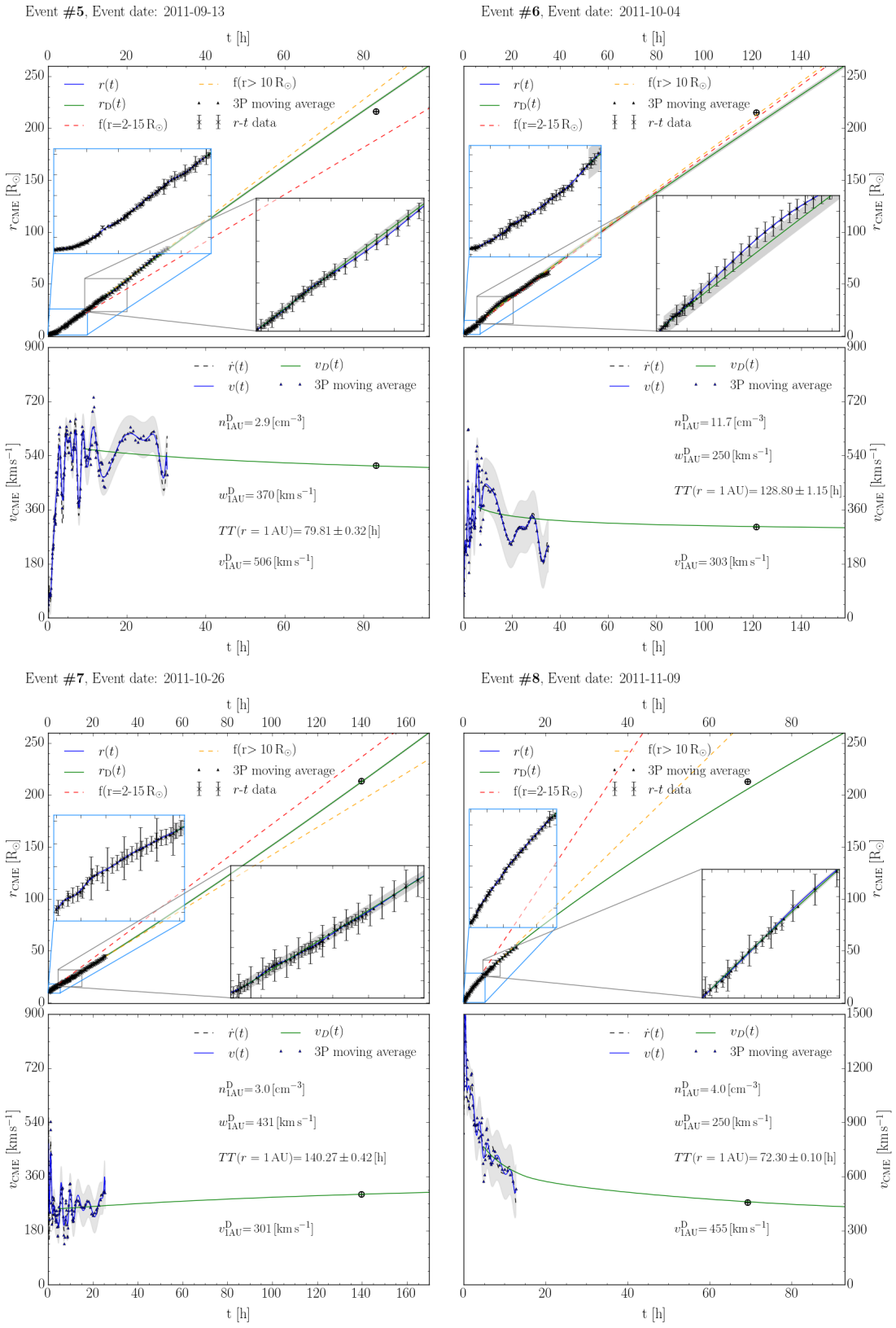

Figure (A.51) Same as Figure 5.29 but for the events #5 to #8.

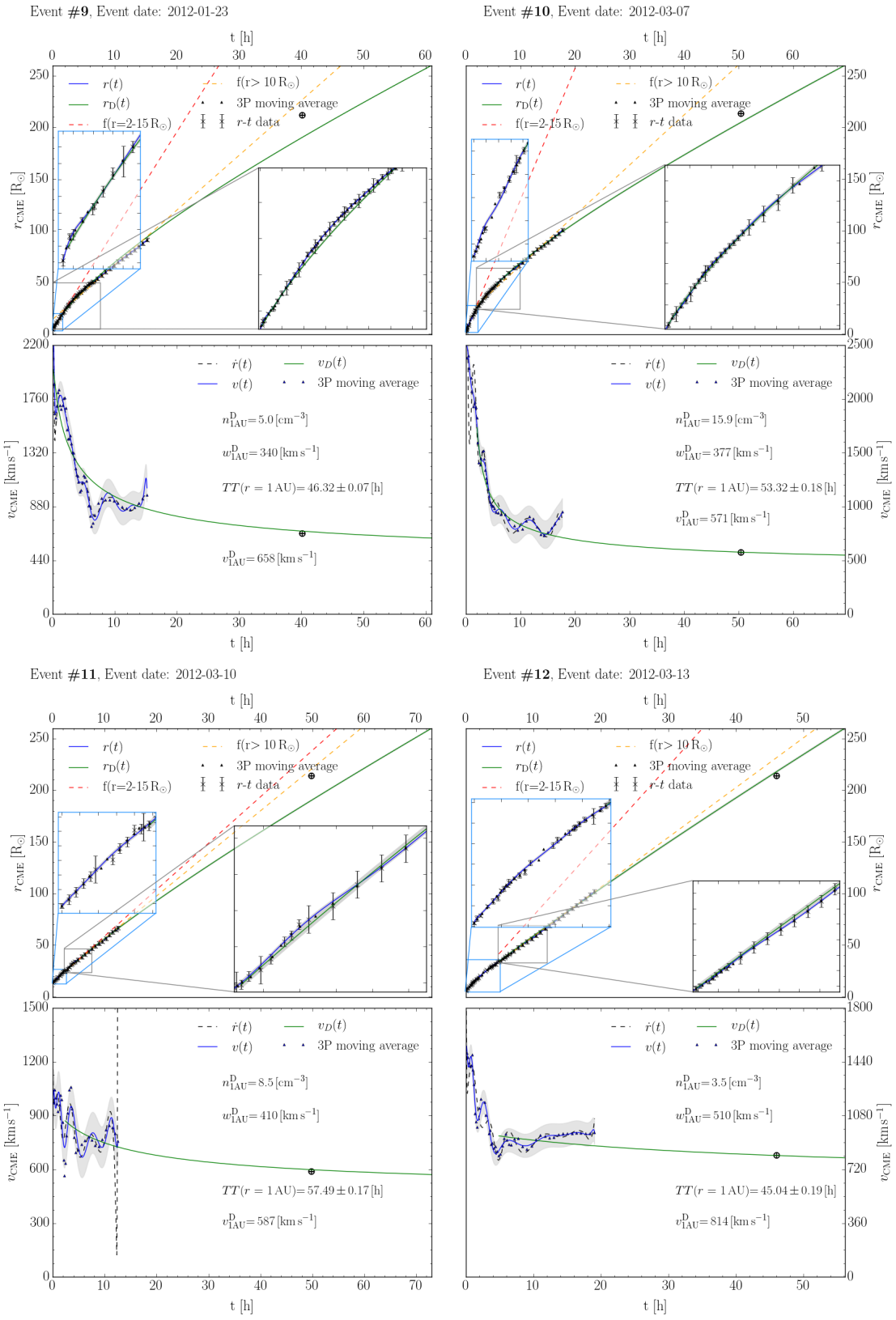

Figure (A.52) Same as Figure 5.29 but for the events #9 to #12.

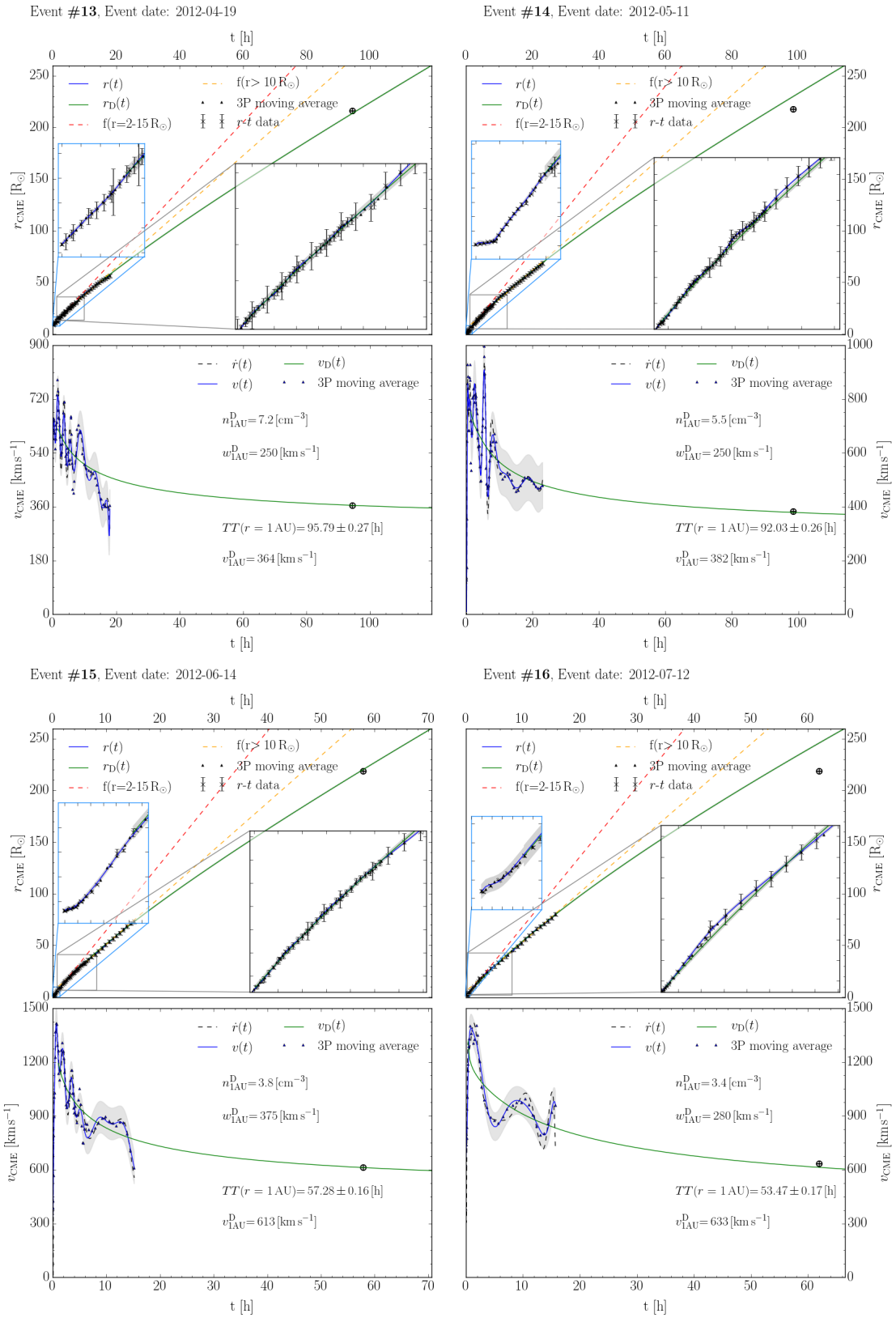

Figure (A.53) Same as Figure 5.29 but for the events #13 to #16.

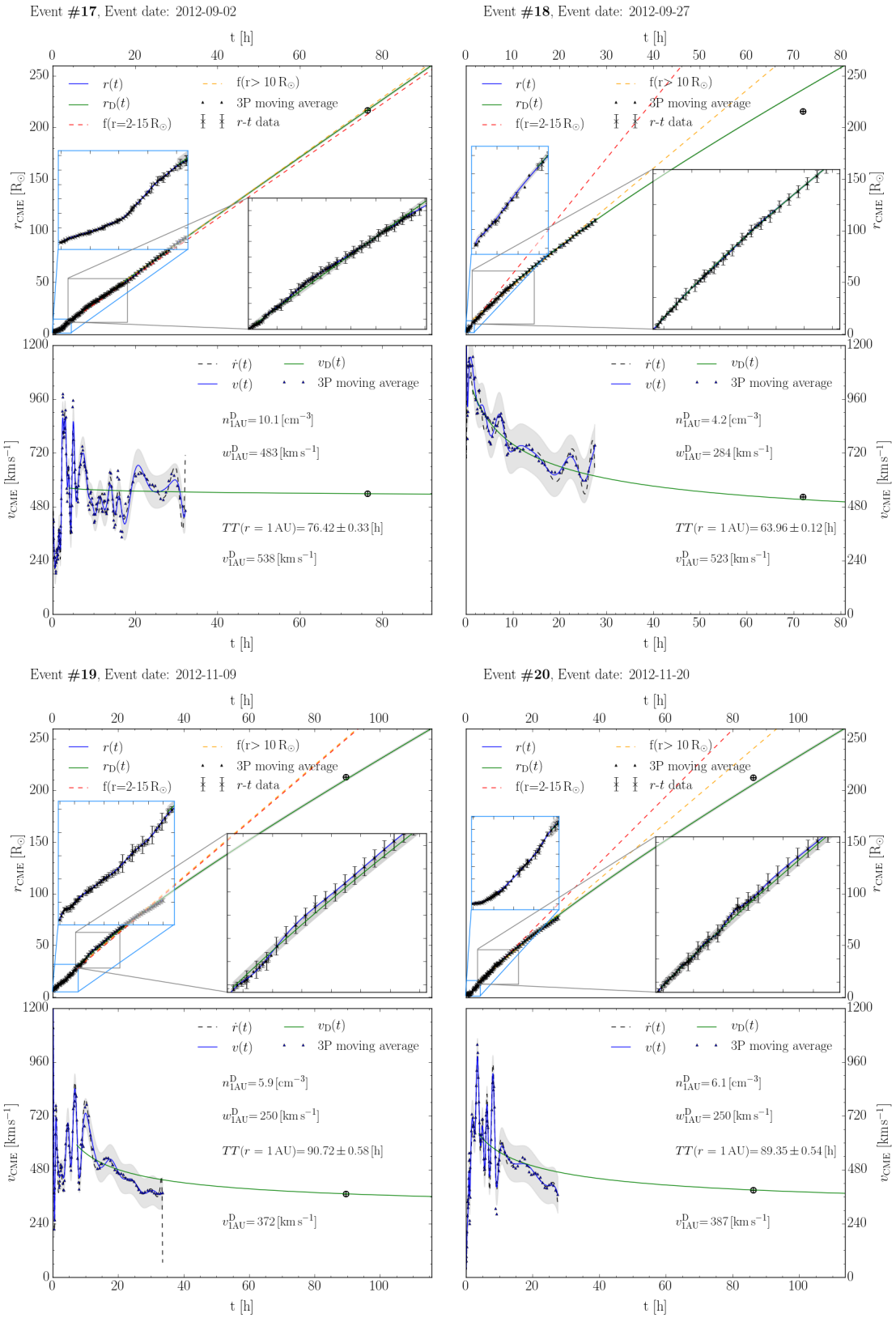

Figure (A.54) Same as Figure 5.29 but for the events #17 to #20.

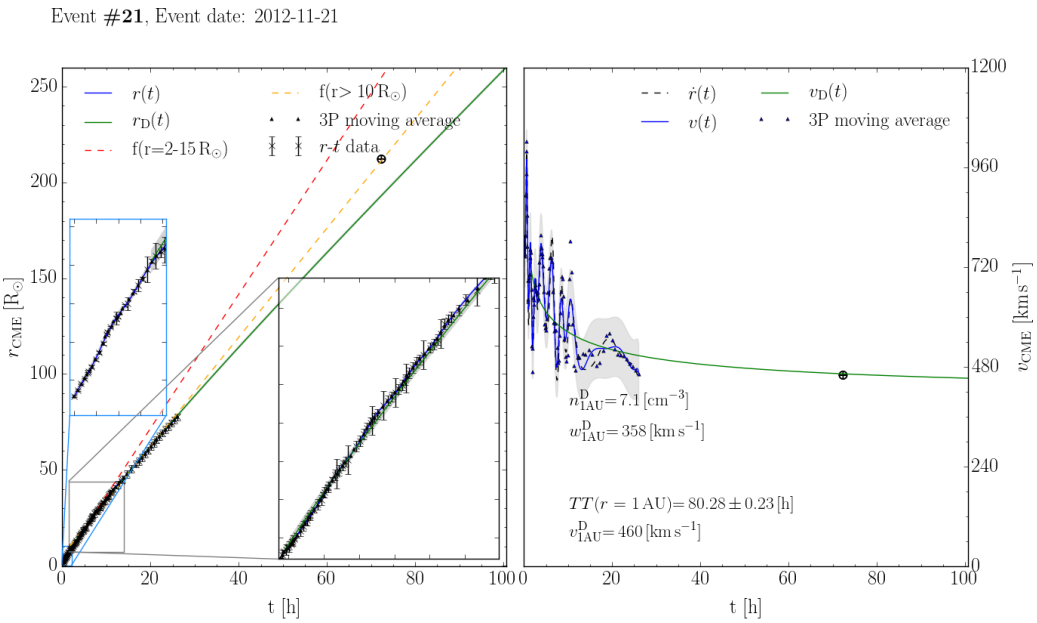

Figure (A.55) Same as Figure 5.29 but for event #21.

A.2.6 Lorentz Force Analysis Results

In the following plots, the TI Lorentz force results of the early CME kinematics r-t-profiles of the CME apex are shown. For a better visibility, the area under the fits of the Lorentz as well as the drag force were filled with blue and green, respectively.

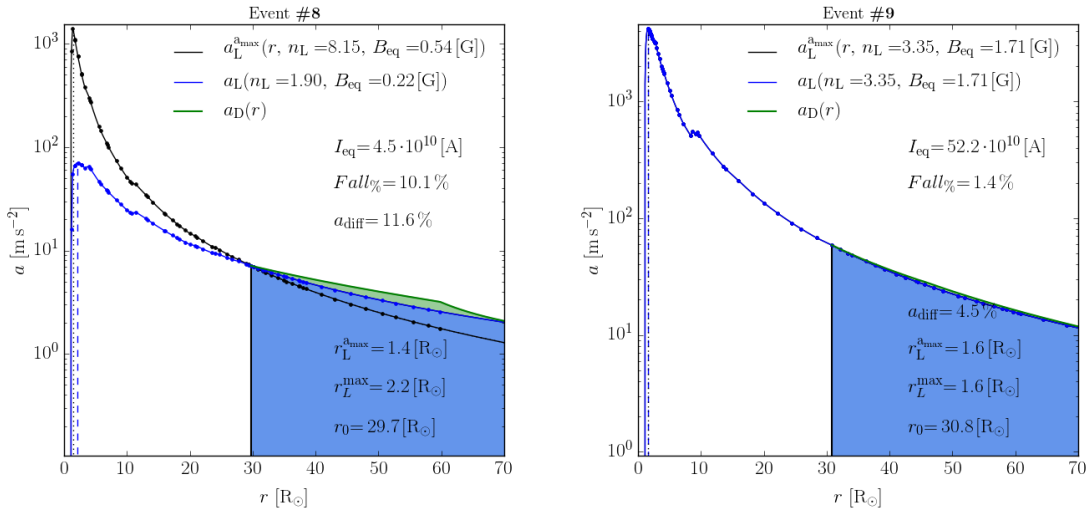

Figure (A.56) Same as Figure 5.33 but for the events #8 and #9.

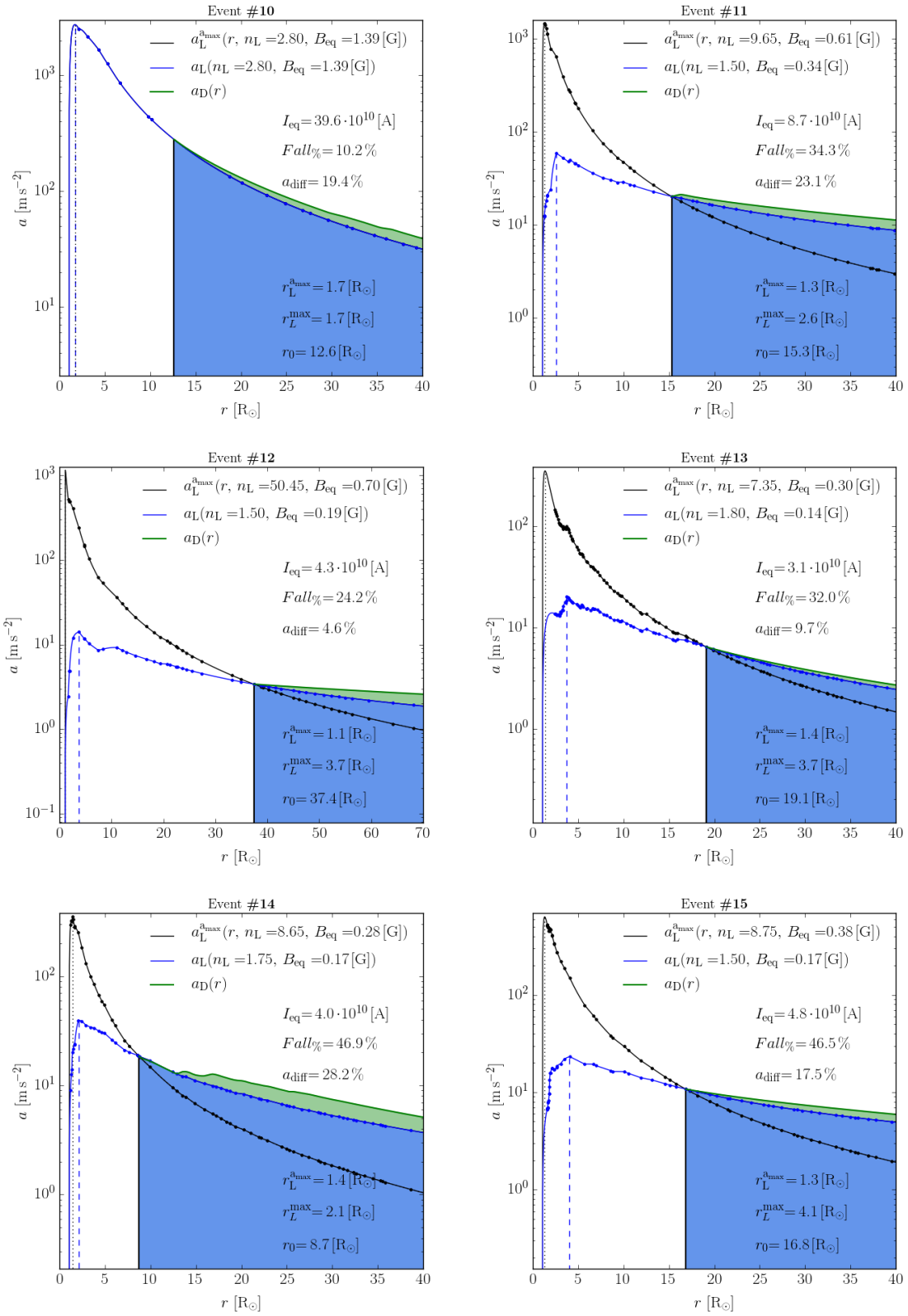

Figure (A.57) Same as Figure 5.33 but for the events #10 to #15.

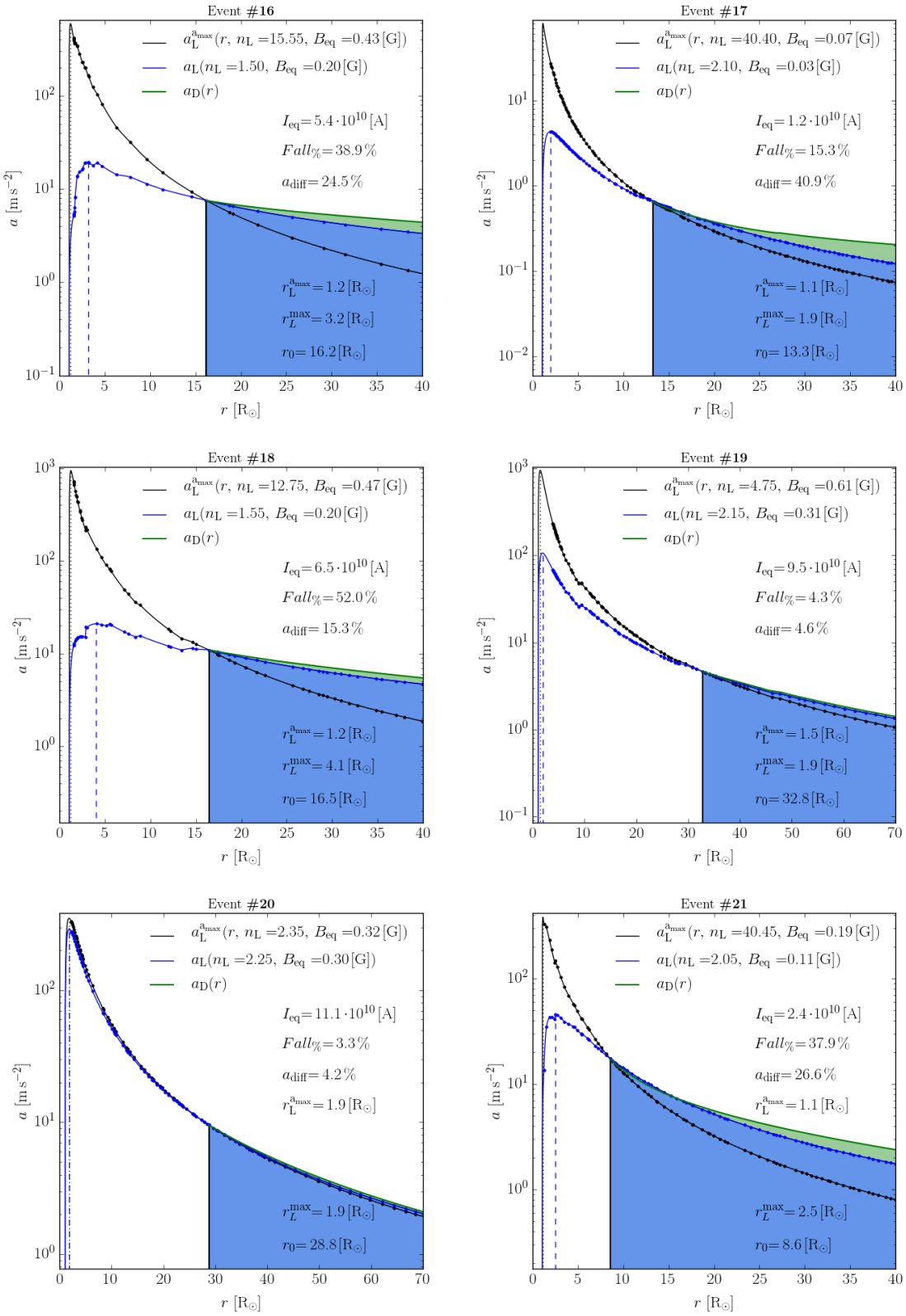

Figure (A.58) Same as Figure 5.33 but for the events #16 to #21.

A.3 Projects

During my time as a PhD I worked in several projects through which this work was possible. Furthermore, the techniques and methods used in this work were developed within the collaborations resulting from the work in this projects. This work is funded by:

- The European Union in the FP7-Project HELCATS (Heliospheric Cataloguing, Analysis and Techniques Service). In the HELCATs project, the team at the Institute for Astrophysics at the University of Göttingen including A. Pluta, E. Bosman and me with the team leader V. Bothmer, developed a kinematic database of CMEs observed with the STEREO/SECCHI suite. My contribution focused on the GCS modelling of CMEs, the determination of CME kinematics and masses as well as the identification of CME SRs.

- The Zentrum für Geoinformationswesen der Bundeswehr in the project OPTIMAP (Operational Tool for Ionosphere Mapping And Prediction). Under the lead of V. Bothmer, and together with J. Hinrichs and M. Venzmer, I studied the affects of Space Weather on Earths Ionosphere and developed techniques to include them in an operational service for the provision and prediction of maps of the vertical electron content. My role within the OPTIMAP project was the GCS modelling of Earth-directed CMEs and the identification of their corresponding in-situ signatures in measurements by ACE in L1.

- The Project "Risikobewertung von Weltraumwetterereignissen" commissioned by the Planungsamt der Bundeswehr Abteilung I 5 Referat Studienmanagement Bundeswehr.

A.4 Publications

This is a list of publications I was involved in during the time of my PhD:

- **Combined geometrical modelling and white-light mass determination of coronal mass ejections**: Adam Pluta, Niclas Mrotzek, Angelos Vourlidas, Volker Bothmer and Neel Savani, *Astronomy & Astrophysics*, **623**, A139

- **Comparison of CME and ICME Structures Derived from Remote-Sensing and In Situ Observations**: V. Bothmer and N. Mrotzek, 2017, *Solar Physics*, **292**, 157

- **An Analysis of Interplanetary Solar Radio Emissions Associated with a Coronal Mass Ejection**: V. Krupar, J. P. Eastwood, O. Kruparova, O. Santolik, J. Magdalenić, A. Vourlidas, M. Maksimovic, X. Bonnin, V. Bothmer, N. Mrotzek, A. Pluta, D. Barnes, J. A. Davis, J. C. Martínez Oliveros and S. D. Bale: 2016, *The Astrophysical Journal Letters*, **23**, 1, article id. L5, 7 pp

A.5 Conferences

This is a list of contributions at conferences I was attended during the time of my PhD:

- **EGU General Assembly 2017**, Vienna, Austria: *A Multi-Model Approach to the Analysis of the Kinematics of CMEs Based on Multi-point Space Observations* , N. Mrotzek, V. Bothmer, J. Davies, R. Harrison
- **EGU General Assembly 2017**, Vienna, Austria: *CME properties and solar source region characteristics - HELCATS results* , V. Bothmer, N. Mrotzek, S. Murray, P. Gallagher, D. Barnes, J. Davies, R. Harrison
- **EGU General Assembly 2017**, Vienna, Austria: *Impacts of Space Weather Effects on the Ionospheric Vertical Total Electron Content* , J. Hinrichs, V. Bothmer, N. Mrotzek, M. Venzmer, E. Erdogan, D. Dettmering, A. Goss, M. Schmidt, F. Seitz, K. Börger, S. Brandert, B. Görres, W. F. Kersten
- **EGU General Assembly 2017**, Vienna Austria: *Radio triangulation of solar radio emissions associated with the 2012 July 23 CME* , V. Krupar, O. Kruparova, O. Santolik, V. Bothmer, N. Mrotzek, J. P. Eastwood
- **EGU General Assembly 2017**, Vienna, Austria: *Modeling of coronal mass ejections with the STEREO heliospheric imagers verified with in situ observations by the Heliophysics System Observatory*, C. Möstl, A. Isavnin, E. Kilpua, V. Bothmer, N. Mrotzek, P. Boakes, L. Rodriguez, V. Krupar, J. Eastwood, J. Davies, R. Harrison, D. Barnes, R Winslow, Helcats Team
- **EGU General Assembly 2017**, Vienna, Austria: *Regional Densification of a Global VTEC Model Based on B-Spline Representations* , E. Erdogan, M. Schmidt, D. Dettmering, A. Goss, F. Seitz, K. Börger, S. Brandert, B. Görres, W. F. Kersten, V. Bothmer, J. Hinrichs, N. Mrotzek
- **ESWW 13 2016**, Oostende, Belgium: *An Aerodynamic Drag Analysis of CMEs from In Situ Measurements and Multipoint Space Observations*, N. Mrotzek, M. Venzmer, V. Bothmer, A. Pluta
- **EGU General Assembly 2016**, Vienna, Austria: *Deriving CME kinematics from multipoint space observations*, N. Mrotzek, A. Pluta, V. Bothmer, J. Davies, R. Harrison
- **EGU General Assembly 2016**, Vienna, Austria: *Impacts of Space Weather Effects on the Ionospheric Vertical Total Electron Content*, J. Hinrichs, V. Bothmer, N. Mrotzek, M Venzmer, E. Erdogan, D. Dettmering, M. Limberger, M. Schmidt, F. Seitz, K. Börger, S. Brandert, B. Görres, W. F. Kersten
- **EGU General Assembly 2016**, Vienna Austria: *Global VTEC-modelling in near real-time based on space geodetic techniques, adapted B-spline expansions and Kalman-filtering including observations of the Sun's radiation*, K. Börger, M. Schmidt, D. Dettmering, M. Limberger, E. Erdogan, F. Seitz, S. Brandert, B. Görres, W. Kersten, V. Bothmer, J. Hinrichs, M. Venzmer, N. Mrotzek
- **ESWW 12 2015**, Oostende, Belgium: *AFFECTS and HELCATS EU Space Weather Visualisation and Dissemination System*, V. Bothmer, N. Mrotzek, J. Hinrichs

Danksagung

"Das Glück bestht nicht darin, dass du tun kannst, was du willst, sondern darin, dass du immer willst, was du tust."

Lew Tolstoi

Abschließend möchte ich die Gelegenheit nutzen, den Menschen zu danken, ohne deren Einsatz diese Arbeit und mein Studium in dieser Form nicht möglich gewesen wären. An erster Stelle möchte ich mich bei meinem Doktorvater, Volker Bothmer, für die Gelegenheit bedanken im Bereich der solar-terrestrischen Physik zu arbeiten und zu promovieren. Unsere Diskussionen bereiteten mir genau so viel Vergnügen wie unserer gemeinsamen Koffeinsucht zu frönen. Weiterhin möchte ich der gesamten Prüfungskommission, vor allem Ansgar Reiners, welcher mich duch alle meine Abschlussarbeiten begleitet hat, danken.

Meinen Kollegen im Institut für Astrophysik danke ich für die lehrreiche und schöne Zeit die ich auf keinen Fall missen möchte. Dies gilt vor allem Stefan Dreizler, Phillip Huke und Heiko Anwand-Heerwart die mir immer mit guten Ratschlägen und einem offenen Ohr zur Seite standen. Klaus Reisch danke ich für seine unschätzbare Unterstützung und Ausdauer in der Bewältigung von Software und Teleskop-Problemen. Ein ganz herzlichen Dank möchte ich den Damen und auch dem Herrn unseres Sekretariats, Daniela Krone, Nicole Böker, Klaudia Wolters, Michaela Ständer und Christian Hartung aussprechen. Ohne euch wäre der Arbeitsaltag nur halb so lustig!

Während meiner Studienzeit als Doktorand und bereits davor hatte ich das Privileg Menschen kennen zu lernen, die fester Bestandteil meines Lebens geworden sind. Meinen langjährigen und guten Freunden Johannes Hinrichs, Giuseppe Nisticò, Kathrin Jacob, Steffen Schwesig, Malte Scherf und Paula Matthies möchte ich besonders dafür danken, dass sie immer für mich da sind und mir zur Seite stehen. Auf das wir noch viele gemeinsame Stunden und Abenteuer erleben werden. Auch meinen Freunden unter den Göttinger Bogenschützen möchte ich für die vielen schönen Jahre und das Vertrauen, was sie in mich setzen, danken.

Meinen Eltern und meiner Schwester kann ich nicht genug dafür danken, dass sie mir das Studium ermöglicht haben und mich mit allen meinen Fehlern akzeptieren und aushalten. Für viele, den Handyakku strapazierende und Seele-baumeln-lassende Telefonate danke ich meiner Lieblingstante und meinem Lieblingsonkel. Meiner Frau danke ich, dass sie mein Leitstern ist und mich immer, und in den letzten Zügen dieser Arbeit im ganz Besonderen, auf Kurs hält.